CD59a – A Novel Role in Bone

Anja Constanze Bloom

A thesis submitted to Cardiff University for the Degree of Doctor of Philosophy

Section of Rheumatology
School of Medicine
Cardiff University 2012

DECLARATION

This work has not previously been accepted in substance for any degree and is not concurrently submitted in candidature for any degree.

Signed …… Date ……

STATEMENTS

This thesis is being submitted in partial fulfillment of the requirements for the degree of PhD.

Signed …… Date ……

This thesis is the result of my own independent work/investigation, except where otherwise stated. Other sources are acknowledged by explicit references.

Signed …… Date ……

I hereby give consent for my thesis, if accepted, to be available for photocopying and for inter-library loan, and for the title and summary to be made available to outside organisations.

Signed …….. Date ……

Anja Constanze Bloom

Acknowledgements

This thesis would not have been possible without the support and guidance of many enthusiastic and inspiring researchers.

I am truly indebted and thankful to my main supervisor Dr Anwen Williams. She encouraged me to do a PhD and taught me many valuable skills, as a researcher and as a person. Furthermore, I owe sincere thankfulness to my co-supervisors Dr Bronwen Evans and Prof Daniel Aeschlimann and their research teams for continuous support and facilitating some of my research.

I would like to show my gratitude to Prof Paul Morgan and his research team for enabling my animal model based research and supplying advice and reagents for all complement related experiments.

Furthermore, I would like to thank Dr Rob van't Hof, University of Edinburgh, for his assistance and training of some MicroCT and histology performed in this project. Thank you to Dr James Matthews, Daryn Michael and Timothy Ashlin for their help in creating and testing of my virus related work.

Fraser Collins has been my friend and lab partner for nearly 3 years and I also want to thank him a lot. He made difficult days easier and good days better. I am obliged to many of my colleagues in the Section of Rheumatology and the Tenovus Building who supported me throughout my PhD with advice and allowing me to use their research facilities.

Finally, I would like to thank Luke Davies and my friends for their patience, support and belief in me.

Summary

The complement system has crucial functions in host defence. Novel data revealed a role for complement components in the pathology of osteoarthritis (OA). CD59a is a regulator of the terminal complement pathway in mice; the purpose of the study was to determine if CD59a$^{-/-}$ mice have an osteoarthritic bone phenotype.

Osteoblast (OB) mineralisation, colony forming unit (CFU) and OCG assays were performed *in vitro* from bone marrow preparations of 8-20 week old mice. Decreased CFU differentiating towards osteoblasts and adipocytes (n=1 only), as well as an increased OCG, was revealed in male CD59a deficient ($^{-/-}$) over wildtype (WT) mice. OCG in females were comparable. A human CD59 knockdown system utilising short hairpin (sh) ribonucleic acid (RNA) delivered by adenoviruses was established but did not differentiate into osteoclasts (OC).

In vivo the bone phenotype of CD59a$^{-/-}$ mice was established for femora and vertebra L6 via X-ray, microcomputed tomography and histology. In male mice femoral length was increased in CD59a$^{-/-}$ versus WT mice at 8-10, 20 and 50 weeks. Cortical bone volume was increased whilst bone mineral density (BMD) was reduced in CD59a$^{-/-}$ versus WT mice at 8-10 and 20 weeks. Trabecular bone analysis of the distal femur (and spine) showed increased trabecular bone ratio, number, thickness, connectivity and total BMD in CD59a$^{-/-}$ over WT at 8-10 (and 20) weeks of age. In female mice there was no difference in femoral length and trabecular bone, but cortical BMD was raised at 50 weeks (CD59a$^{-/-}$ versus WT). Finally, histology revealed enhanced mineral apposition rate and OC surface as well as reduced osteoid surface in male CD59a$^{-/-}$ over WT mice at 8-10 weeks of age.

Increased bone growth and turnover related to CD59a gene deletion were gender specific. These studies highlight CD59a as a potential target for OA treatment.

Contents

List of Figures

List of Tables

Chapter 1

Introduction

1.1 Summary

CD59 is a regulator of the membrane attack complex (MAC) of the complement system. Additionally, it regulates functions that are independent of the complement system e.g. lymphocyte expansion (Kimberley *et al.* 2007). The level of CD59 expression on surfaces has implications for haematological and auto-immune diseases such as Paroxysmal nocturnal hemoglobinuria (PNH), diabetes and Alzheimer's in which CD59 is deficient (Yamashina *et al.* 1990; Yang *et al.* 2000; Qin *et al.* 2004). To identify the functional role in these diseases a number of *in vivo* and *in vitro* experimental models have been utilised. The murine analogue of human CD59 is CD59a, a genetically modified CD59a$^{-/-}$ strain (Holt *et al.* 2001), was created in mice to uncover CD59a's role in age-related macular degeneration (Bora *et al.* 2007), renal thrombotic microangiopahty (Nangaku *et al.* 1998), acute experimental autoimmune encephalomyelitis (Mead *et al.* 2003) as well as experimental models of rheumatoid arthritis (RA) (Williams *et al.* 2004) and osteoarthritis (OA) (Wang *et al.* 2011).

This project specifically concentrates on a role of CD59a in regulating bone homeostasis. Little is known about its actions in bone, but clues are derived from experimental models of arthritis. When CD59a is blocked with monoclonal antibodies joints are more susceptible to damage in arthritis models. Furthermore, CD59a$^{-/-}$ mice exhibit more severe arthritis than wild type (WT) mice (Williams *et al.* 2004). Experimental models of OA also point towards similar modulation of disease. CD59a$^{-/-}$ mice showed worse disease than WT, whereas C3 deficient (C3$^{-/-}$) mice did not show an effect in osteoarthritis progression. C5 deficient (C5$^{-/-}$) and C6 deficient (C6$^{-/-}$) mice showed less osteophyte formation than WT animals (Wang *et al.* 2011). These data demonstrate the relative importance of terminal pathway regulation over the alternative or classical pathway in bone.

Human research is somewhat limited. A study in multiple myeloma patients uncovered a correlation with CD59 and CD55 deficiency and elevation of osteoclast numbers (Terpos *et al.* 2003). In a different study, expression of CD59 in human osteoclasts and osteoblasts was shown (Ignatius *et al.* 2011). These are indicators of CD59's involvement in bone homeostasis, but functional significance of human CD59 or murine CD59a was not established. My study therefore focuses on investigating the role of CD59a in bone remodelling, and its implications in health and disease.

1.2 The Complement System and Historical Perspective

In the 19th century, researchers strove to establish the mechanism of bacterial lysis. Two theories arose to explain the process. The first one suggested that cells in the blood were responsible for bacterial elimination, whereas the second one stated that serum components performed this action. The second theory was proven by an experiment in which animal serum lost its lytic ability when heated, but the activity was restored by adding fresh serum. These investigations led to the discovery of complement proteins that were characteristically heat-labile (Morley and Walport 2000; Walport 2001; Janeway *et al.* 2005). Complement was shown to agglutinate in antibody sensitised ox, human and sheep cells (Gorrill and Hobson 1952), this led to the discovery of the first 4 complement components (C1-4) (Talmage 1957) in the 1950s, followed by C5 (Nilsson and Müller-Eberhard 1965) to C8 (Manni and Müller-Eberhard 1969) characterisation in the 1960s. New components have been identified readily since, and additional players are still discovered today such as β2GPI, a brand new complement regulator (Gropp *et al.* 2011), whose involvement in the complement system was revealed in 2011. This is discussed later in section 1.2.3. Currently, the complement system consists of more than 30 proteins found in plasma and expressed on cell membranes. Soluble complement components are mainly synthesised in the liver, and membrane anchored proteins are present on all circulating and many tissue cells (Walport 2001).

Functionally, the complement system serves to protect the host from pathogens. It is an integral component of the innate immune system and links innate with adaptive immunity. When the complement system works properly it is beneficial for health, but complement dys-regulation can result in tissue damage, pathology and disease (Müller-Eberhard 1988; Morgan and Harris 1999; Walport 2001).

The complement system is subdivided into 3 main activation pathways: classical, alternative and the mannan-binding lectin (MBL) pathway. More recently it has been discovered that different proteases of the coagulation pathway, as well as phagocytic cells, can activate complement components (Ehrnthaller *et al.* 2011).

Consequently, all activation pathways result in the amplification pathway followed by the MAC/lytic pathway. All these will be described in turn in the sections below.

1.2.1 Activation Pathways

Classical Pathway

The classical pathway is activated by complement unit C1 binding to an immune complex made of an antibody attached to an antigen (Janeway *et al.* 2005). C1 is

also able to bind antigens alone on apoptotic cells, viral proteins, gram-negative bacteria (polyanions), β-amyloid, mitochondrial fragments and C-reactive proteins associated with a ligand. Fig. 1.1 provides a pictorial representation of the classical pathway which involves C1, C2 and C4 as well as its negative regulators on host cells: C1 inhibitor (C1-INH), C4 binding protein (C4bp) and complement receptor 1 (CR1) (Müller-Eberhard 1988). At the surface of a pathogen these regulators are missing, and the classical pathway will lead to the generation of the C3 convertase consisting of C4b2a (Kinoshita 1991; Walport 2001; Ehrnthaller *et al.* 2011). Individual complements are tabulated in Tab 1.1.

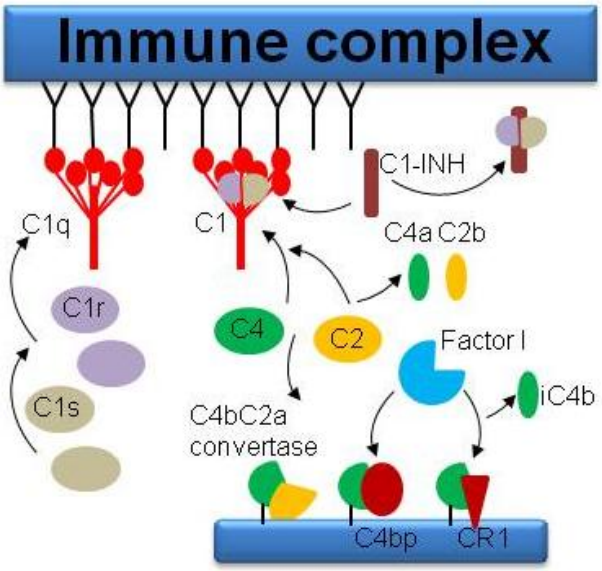

Figure 1.1 Classical Complement Activation Pathway. C1q bound to the immune complex is recognised by C1r and two molecules bind. These activate homeodimers of C1s to form the C1 complex. C1-INH induces C1 complex's irreversible dissociation by removing C1s and C1r subunits, therefore operating as a complement regulator early in the cascade. C4 is cleaved by the C1s subunit to generate C4b which attaches to the surface and releases C4a. Subsequently C1s cleaves C2 and C2a binds to C4b to form the C3 convertase whereas C2b is liberated. C4bp and CR1 can stimulate C4b inactivation by factor I cleavage (Reid and Porter 1981; Müller-Eberhard 1988; Janeway *et al.* 2005; Ehrnthaller *et al.* 2011).

Part of System	ID	Structure	Serum [conc.]	Subunits	Function
Activation	C1	750kD, metallo-protein complex of C1q and C1r2s2	35µg/ml	C1q, C1r, C1s	C1r auto-activates when it recognises C1q binding and activates C1s, which then cleaves C4 to C4a and C4b.
	C4	200kD, zymogen, 3 polypeptide chain (βαγ) - internal thioester bond in α-chain	450-750 µg/ml	C4a, C4b	C4a attaches to cell surfaces to act as weak mediator of inflammation. C4b attaches to cell surfaces with its internal thioester and binds C2a.
	C2	102kD, zymogen	20µg/ml	C2a, C2b	C2b is a precursor of vasoactive C2 kinin and C2a cleaves C3 and C5 as part of the C4b2a convertase.
Regulation	C1-INH	100kD, single-chain glycoprotein with 40% carbohydrate content	240 µg/ml	-	Binds rapidly to active C1s and more slowly to active C1r. It attaches very tightly and therefore causes dissociation.
	C4bp	540-590kD, glycoprotein, contains 2 different polypeptide chains (7α1β)	300 µg/ml	-	Binds up to 4 C4b molecules strongly with α-chain and β-chain associates with anti-coagulant Vitamin K-dependent protein. Can present C3b and C4b to factor I cleavage.

Table 1.1 Classical Pathway Components (Reid and Porter 1981; Sanchez-Corral *et al.* 1995; Caliezi *et al.* 2000; Morley and Walport 2000; Martin *et al.* 2009)**.**

Alternative Pathway

In the alternative pathway C3 from blood plasma activates spontaneously by hydrolysis. This liberates the cell surface binding site, a thioester bond of C3b. Covalent binding to the hydroxyl or amino group of proteins and carbohydrates can now follow at the surface of many bacteria, fungi, viruses and tumour cells. Components of this cascade are called factors and are described in Fig. 1.2 and Tab. 1.2. Properdin can elongate C3bBb's half-life whereas factor H, factor H like protein 1, factor I and β2GPI contribute to the regulation of the pathway which results in the C3 convertase C3bBb (Müller-Eberhard 1988; Zipfel and Skerka 1999; Ehrnthaller *et al.* 2011; Gropp *et al.* 2011).

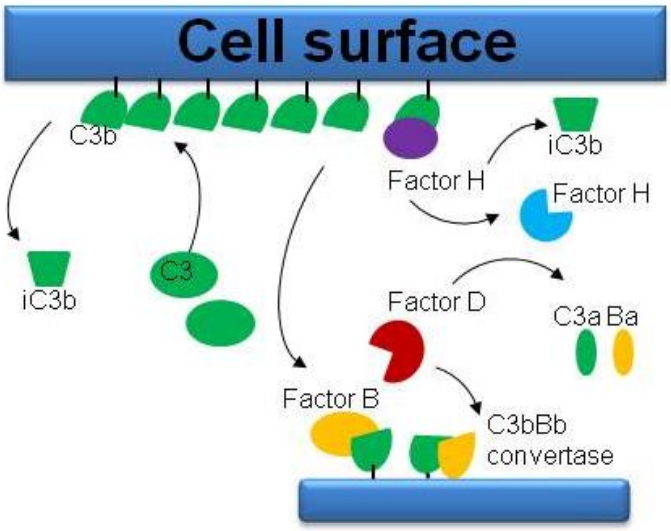

Figure 1.2 Alternative Complement Activation Pathway. In this pathway spontaneously formed C3b inactivates unless factor B (equivalent to C2) binds. Factor D cleaves the complex to create the convertase, C3bBb (Müller-Eberhard 1988; Walport 2001). Factor H competes with factor B for the C3b binding site and inhibits C3 convertase formation. Furthermore bound factor H (and factor H like protein 1) induces C3b inactivation to C3bi by factor I (Müller-Eberhard 1988; Zipfel and Skerka 1999; Ehrnthaller *et al.* 2011). Another complement regulator of C3 is β2GPI, which was recently discovered to control apoptotic cells by binding C3/C3b and can be inactivated by factor I (same mechanism as for factor H) (Gropp *et al.* 2011).

Part of System	ID	Structure	Serum [conc.]	Subunits	Function
Activation	C3	190kD, zymogen, β- and α-chain - internal thioester bond in α-chain	1000-1600µg/ml	C3a, C3b, C3bi and C3dg are the major subunits	C3a triggers local inflammatory response via anaphylatoxin activity. C3b recognises antigens, is subunit of C5 convertases, ligand for CR1 and induces opsonisation. C3bi interacts with CR3 and induces opsonisation whereas C3dg binds to complement receptor 2 (CR2) on B-cells and influences their activation.
	Factor B	90kDa, zymogen	200µg/ml	Ba, Bb	Binds to C3b with Bb.
	Factor D	24kDa, single chain zymogen	1µg/ml	-	Binding specificity to Arg-Lys bond of factor B. Cleaves factor B into its subunits.
Regulation	Factor H	160kD, single chain zymogen	360-550 µg/ml	-	Binds C3b to block convertase formation and acts as factor I co-factor.
	Factor I	88kDa, 2 chain zymogen	35µg/ml	-	Cleaves C3b and C4b in presence of co-factor factor H, CR1, C4bp, MCP and β2GPI.

Table 1.2 Alternative Pathway Components (Müller-Eberhard 1988; Gropp *et al.* 2011).

MBL Pathway

In this pathway MBLs bind to glycans and phospholipids with mannose, glucose, fucose or N-acetylglucosamine as the terminal carbohydrate (Hoffmann *et al.* 1999; Walport 2001; Janeway *et al.* 2005). Additionally the molecule ficolin contains a lectin domain and is able to recognise different carbohydrates (Gadjeva *et al.* 2001). MBL associated proteases 1 and 2 (MASP-1 and MASP-2) and the non-protease small MBL-associated protein (sMAP) are part of the cascade. C1-INH, C4bp and CR1 can also interfere with the MBL pathway. When the cascade forms successfully it results in the formation of the C3 convertase composed of the C4b2a complex as shown in Fig. 1.3 (Ehrnthaller *et al.* 2011).

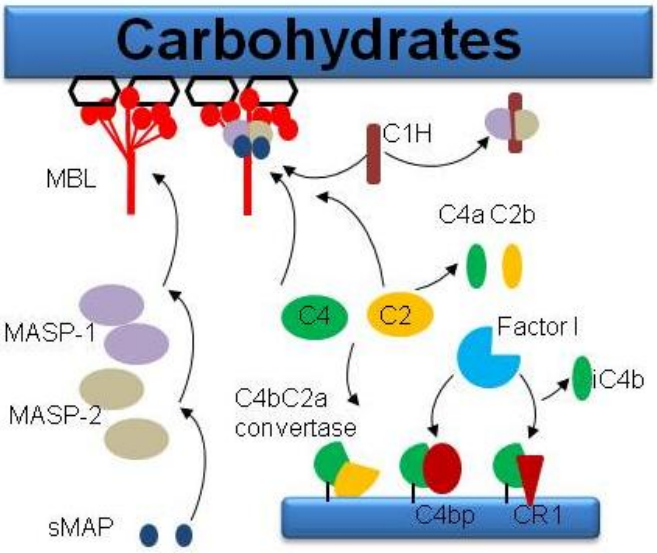

Figure 1.3 MBL Activation Pathway. MBL forms a complex with MASP-1, MASP-2 and sMAP. MASP-2 has the same function as C1s but both, MASP-1 and MASP-2, can activate C2. It is thought that MASP-1 might be able to cleave C3 directly without formation of the convertase (Walport 2001). C1-INH can interfere with the pathway formation by MASP-1 and MASP-2 inactivation. C4bp and CR1 can also inhibit C4b as in the classical pathway.

1.2.2 Amplification Pathway

The classical, alternative and MBL pathway converge at the point of C3 convertase generation, consisting of either C4b2a or C3bBb. These convertases are able to cleave C3 molecules, which attach covalently to the membrane close to the activation site for the accumulation of C3b (Tab. 1.2) (Müller-Eberhard 1988; Janeway *et al.* 2005). Each newly generated C3b molecule can bind to factor B and form another convertase by factor D cleavage. Additionally, C3b can bind to the C3b or C4b of a C3 convertase. This complex acts as C5 convertase as illustrated in Fig. 1.4.

Membrane co-factor protein (MCP) and decay accelerating factor (DAF) are main regulators of the C3 and C5 convertase, but complement receptor of the immunoglobulin superfamily (CRIg), Factor H–related protein 1 (CFHR1) and previously mentioned C3 and C4 regulators are also influencing this pathway.

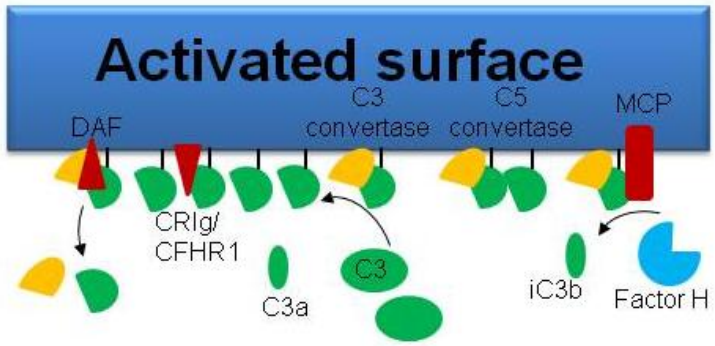

Figure 1.4 Amplification Pathway. Once C3b and convertases are deposited, DAF speeds up the separation of the convertases by attaching to bound C4b, C2a, C3b, Bb. MCP associates with surface bound C3b, C4b and C3bi with 50 times more efficiency than factor H and acts as co-factor for C3b cleavage by factor I (Müller-Eberhard 1988). Furthermore CRIg, found on macrophages, binds to C3b in C3 and C5 convertase and CFHR1 attaches to C3b and C3d (degradation product) to prevent substrate adherence (He *et al.* 2008; Heinen *et al.* 2009).

1.2.3 Terminal Pathway

The C5 convertase generation leads to cleavage of C5. C5b triggers MAC composed of C5b to C9 (Tab. 1.3). This complex creates a transmembrane pore which leads to cell lysis (Davies *et al.* 1989). Its assembly is pictorially illustrated in Fig. 1.5 (Müller-Eberhard 1988; Walport 2001; Janeway *et al.* 2005). MAC is controlled by CFHR1, serumprotein S, clusterin and CD59 (Ehrnthaller *et al.* 2011). CD59 is the final regulator which arrests unwanted complement activation that has

not been controlled at earlier stages (Ruiz-Argüelles and Llorente 2007). It interacts with the α-chain of C8 and binds tightly to the C5-8 complement complex inserted into the cell membrane. It inhibits polymerisation of C9 (Meri *et al.* 1990) and it was shown that one C9 molecule can bind to the C5-8-CD59 complex. CD59 binds to the C9b-fragment and consequently limits C9 unfolding (Meri and Jarva 1998). Therefore the attachment site for further C9 molecules is inaccessible and cell lysis by MAC is prevented (Farkas *et al.* 2002).

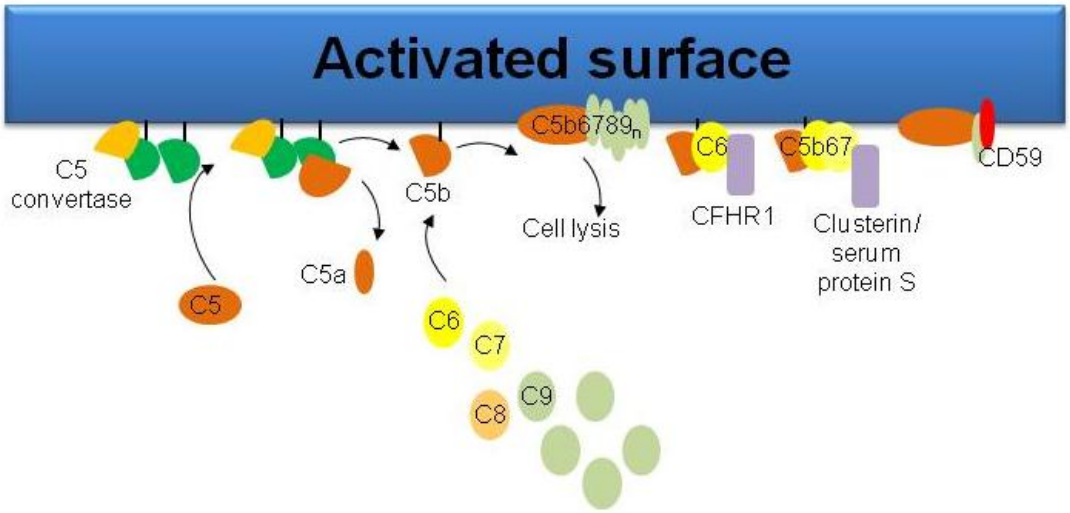

Figure 1.5 Terminal Pathway. When C5 encounters the C5 convertase, it binds to the extra C3b. This changes C5's conformation so it can be readily cleaved into C5a and C5b by Bb/C2a. C6 binds to C5b and C7, C8 and multiple molecules of the C9 bind sequentially to the complex to form the cell lysing MAC. The assembly can be regulated at various steps. CFHR1 can attach to C5, when attached to C3b, and C5b6 therefore inhibiting the C5 convertase generation as well as the MAC assembly (Heinen *et al.* 2009). Additionally serumprotein S and clusterin bind to a lipophilic group of C7 hindering the MAC formation (Ehrnthaller *et al.* 2011). CD59, the final regulator, binds tightly to the C5b-8 or C5b-9 complement complex to inhibit polymerisation of C9 (Farkas *et al.* 2002).

ID	Structure	Serum [conc.]	Subunits	Function
C5	191kD, zymogen, β- and α-chain - linked by disulphide bond	80-340 µg/ml	C5a, C5b	C5a is a peptide mediator of inflammation. C5b is an initiator of MAC, it is meta-stable and attracts C6.
C6	MW 104,800-128,000, single chain glycoproteins	50-70µg/ml		C6 binds to C5b, the complex is still connected to C3b and forms the acceptor for C7.
C7	MW 92,400-121,000, single chain glycoproteins	50-70µg/ml		C7 binds to C5b6. C5b67 induces conformational change of C7 to expose a hydrophobic patch which allows dissociation from the convertase and binds to the membrane layer.
C8	151kD, 3 chain protein, α and γ-chain are linked via a disulphide bond which complex is covalently linked to the β-chain	55µg/ml		The β-chain of C8 has a recognition site for C5b and binding causes structural changes within the complement molecule. This allows the α-chain of C8 to anchor deeper into the lipid bilayer.
C9	71kD, single-chain glycoprotein	50-60µg/ml		C9 binds to C5b678 complex. The first molecule attaches quickly and then undergoes conformational changes which slow down the polymerisation. Between 10 and 16 C9 units are required to create a channel through the membrane which induces cell lysis.

Table 1.3 Membrane Attack Complex formation (Morley and Walport 2000; Gressner *et al.* 2007).

Invading microorganisms do not express complement regulators and are therefore not protected. The way the complement components join to protect host and evading pathogens is demonstrated below in Fig. 1.6. The bioactivity of the complement system is mediated by a series of receptors and inflammatory mediators called anaphylatoxin, C3a and C5a as summarised in Tab. 1.4. The data presented thus far demonstrates that the complement system is tightly regulated. This thesis focuses on CD59 as a major regulator of the terminal pathway. Its function in host defence, health and disease is described in the following sections.

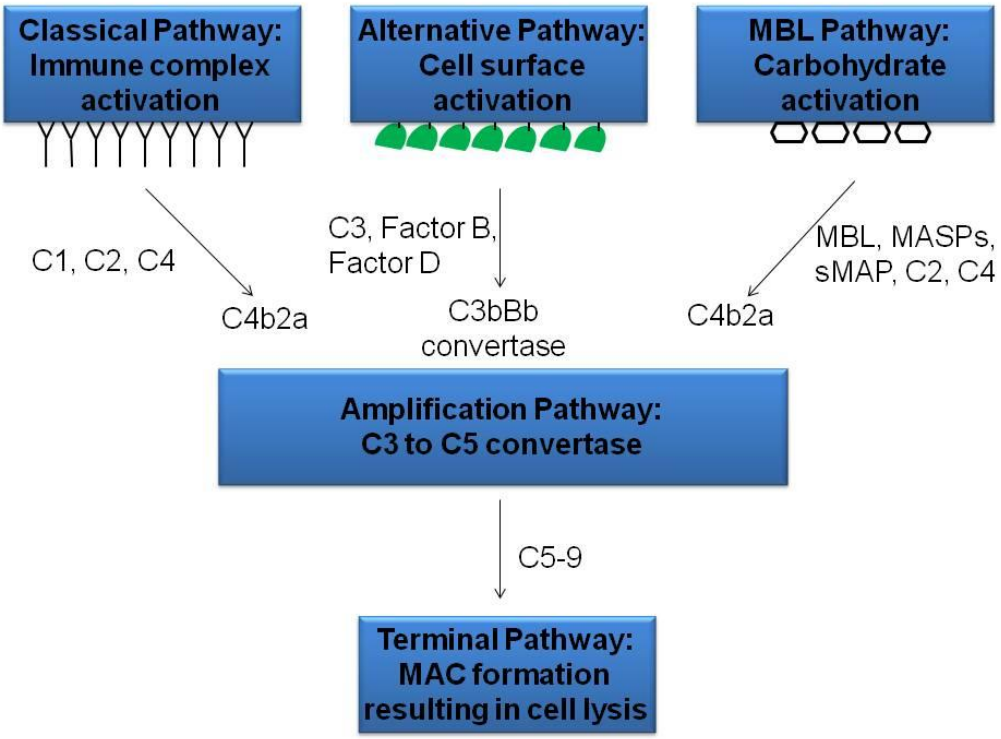

Figure 1.6 The Complement System.

Receptor	Cell expression	Ligand	Pathway Function
CR1	Monocytes, macrophages, neutrophils, erythrocytes, B-cells, polymorphonuclear leukocytes, follicular dendritic cells (FDC)	C4b, C3b, iC3b	Co-factor for factor I inactivation, mediation of phagocytosis, transport of immune complexes to macrophages in the liver for removal from the body.
CR2	B-cells, FDC	C3d, iC3b, C3dg, Epstein-Barr virus	Co-receptor for B-cell component and viral receptor.
Complement receptor 3 (CR3)	Antibody-dependent cytotoxic lymphocytes, neutrophils and macrophages, FDC	iC3b	Binds to C3bi to induce phagocytic removal of foreign fragments.
Complement receptor 4 (CR4)	Macrophages, monocytes, antibody-dependent cytotoxic lymphocytes, dendritic cells	iC3b	Binds to C3bi to induce phagocytic removal of foreign fragments.
C1q receptor (C1qR)	Monocytes, B-cells	C1q	Induces phagocytosis and cell adhesion.
Dendritic cell-specific ICAM3-grabbing non-integrin homologue SIGN-related 1 (SIGNR1)	Dendritic cells, microglial cells	C1q	Induces phagocytosis as well as signalling and inflammation.
C3a receptor (C3aR)	Endothelial cells, mast cells, phagocytes	C3a	Induces migration of phagocytes by activating G protein, regulated by carboxypeptidase N that targets ligand degradation.
C5a receptor (C5aR)	Endothelial cells, mast cells, phagocytes	C5a	Induces migration of phagocytes by activating G protein, regulated by carboxypeptidase N that targets ligand degradation.
C5a receptor-like 2 (C5L2)	Macrophages, neutrophils	C5a	Inhibits phagocyte migration by uncoupling G protein.

Table 1.4 Complement receptors (Müller-Eberhard 1988; Morgan 1990; Morley and Walport 2000; Janeway *et al.* 2005; Zipfel and Skerka 2009).

1.3 CD59 and Historical Perspective

CD59 was discovered as a 20kDa protein by monoclonal antibodies YTH53.1 and MEM43 raised against leukocyte antigens. It obtained its name in the 4th Leukocyte Workshop in 1989. Davies et al. showed that YTH53.1 bound to CD59 causing enhanced cell lysis on erythrocytes and lymphocytes when activated C56 (purified from acute-phase serum) and normal human serum (source of C7-9) were incubated with the cells (Davies *et al.* 1989).

CD59 is ubiquitously expressed on all circulating cells, including erythrocytes and granulocytes as well as lymphocytes, and numerous tissue cells, such as epidermis and endothelia of the skin, vascular endothelia of the liver and glomerular epithelia cells (Davies *et al.* 1989; Meri *et al.* 1991). CD59 is a globular cellular protein consisting of a single polypeptide chain attached to the cell surface via a glycosylphosphatidylinisotol (GPI) anchor. A soluble form of CD59 (sCD59) is also found in urine (MW 13kDa). sCD59 is 200 fold less efficient at protecting cells from MAC lysis but its ability to bind the MAC complex is preserved (Lehto *et al.* 1995). Complement dependent function of CD59 has been discussed in section 1.2.3. However some alternative roles of CD59 have been discovered.

1.3.1 Proposed Complement Independent Roles of CD59

CD59 cross-linking was shown to induce intracellular signalling but a potential ligand to induce cross-linking has not been identified. These functions have been termed complement independent functions as they were observed away from the active site of MAC within the protein structure of CD59a. Proposed ligands for CD59 have been described according to their binding capacity and influence on cell regulation but a mechanism for these alternative roles has not been established yet. Complement independent functions have been demonstrated on a variety of cells such as T-cells, B-cells and Natural Killer (NK) cells. (Kimberley *et al.* 2007).

1.3.1.1 Complement Independent Roles of CD59 in T-Cells

Within cell membranes CD59 is one of multiple GPI anchored proteins located in lipid rafts. GPI-anchors are connected to cytoplasmic protein tyrosine kinase which were thought to alter T-cell activation in humans (Longhi *et al.* 2005). CD59's involvement was tested by generating Fab fragments of 2 anti-CD59 antibodies with different antigen specificity. One of the antibodies blocked complement regulation (MEM-43) whereas the other one did not (HC-1). When incubating $CD4^+$ T-cells with the antigen-specific Fab fragments of antiCD59 antibodies, HC-1 binding resulted in a dose dependent up-regulation of $CD4^+$ T-cell proliferation and interferon (IFN) γ

production, whereas no effect was seen with MEM-43 suggesting CD59 reduces T-cell expansion in a complement independent manner (Sivasankar *et al.* 2009). The effect was confirmed *in vivo* in a mouse model. $CD4^+$ T-cells from $CD59a^{-/-}$ mice proliferated and produced more cytokines than WT mice after *in vivo* infection with a recombinant vaccine virus, confirming down-regulation by CD59a (Longhi *et al.* 2005).

1.3.1.2 Complement Independent Roles of CD59 on B-Cells

CD59 was also suggested to function on $CD4^+$ T-cells in order to stimulate B-cell proliferation. CD59 is only expressed on B-cells in the splenic marginal zone. $CD59a^{-/-}$ mice have a defective humoral response, but their B-cells appeared normal during experiments. It was discovered that when $CD59^+CD4^+$ T-cells interact with B-cells CD59 operated as co-factor to an unknown ligand, resulting in B-cell expansion. This function was identified as complement independent when lymphocytes were cultured *ex vivo* in presence and absence of CD59a (Kimberley *et al.* 2007). As these cultures are performed in heat inactivated serum, no MAC activation should have occurred.

1.3.1.3 Complement Independent Roles of CD59 on NK Cells

Additionally, subpopulations of NK cells expressing CD59 were found to be more active at cell killing than $CD59^-$ NK cells. The mechanism was thought to involve CD59 acting via natural cytotoxicity receptors NKp46 and NKp30. These receptors signal through a tyrosine kinase phosphorylation. CD59 was cross-linked by antibodies which induced tyrosine phosphorylation through the GPI-anchor (Marcenaro *et al.* 2003). This mechanism was also seen in T-cell expansion (section 1.3.1.1) and was confirmed as complement independent in T-cells. Therefore it was proposed that CD59 signalling in NK cells was utilising an alternative mechanism to MAC activation (Kimberley *et al.* 2007).

CD59 is not only important on NK cells but also on NK target cells. U937, a $CD59^-$ cell line, was transfected with CD59 expressing plasmids with different membrane anchors. Cells, expressing GPI-anchored CD59, were more susceptible to NK cytotoxicity probably due to interactions with the NK receptor. To determine if the effect was complement independent, antibodies targeting the C8/C9 binding site and antibodies against a different isotope were tested. Only antibodies against the alternative epitope affected cytotoxicity (Omidvar *et al.* 2006; Kimberley *et al.* 2007).

CD59 is also involved in a number of other functions. These are described in the Tab. 1.5.

Function	Interaction	Mechanism
Lipopolysaccharide (LPS) receptor	CD59 blocking antibody and anti-sense oligonucleotides caused reduced LPS signalling and cytokine generation on $CD14^-$ keratinocytes.	Utilising GPI-anchor for nuclear factor (NF)-κB signalling, interleukin (IL)-6, Granulocyte macrophage-colony stimulating factor and tumour necrosis factor (TNF) α secretion.
Apoptosis	Cross-linking of CD59 induced apoptosis of Jurkat cells and T-cell-blasts which could be blocked by anti-TNF-related apoptosis-inducing ligand (TRAIL) antibodies.	Activation induced cell death (AICD) regulates lymphocyte maturation and is stimulated by cross-linked CD59 to signal via TRAIL instead of Fas ligand.
Cell surface interactions	CD59 was found to weakly bind CD2 on T-cells and NK cells. Anti-CD59 antibodies were identified to inhibit erythrocyte interaction with T-cells.	CD2 is an adhesion and signalling protein that binds mainly CD58 on target cells as co-stimulatory signal to activate T-cells and induce NK- and cytotoxic T-cell lysis. CD59 interaction was proposed to be indirect maybe via a protein complex.
	CD59 has a receptor function for intermedilysin (ILY), a pore-forming bacterial toxin of *Streptococcus intermedius*. Its attachment site is the same as for C8α and C9.	Once ILY is bound to CD59 it will form a lytic pore.
	Binding of CD59 to calreticulin (CRT) was shown. PNH patients showed decreased binding of CRT.	CRT, a calcium binding receptor on neutrophils, does not have a transmembrane domain and uses GPI-anchored proteins, including CD59, to signal.
Reproduction	CD59 is present in large quantities on cells of the reproductive system and in seminal plasma.	CD59 prevents complement lysis via the transit into the female tract. It adds to immune tolerance to ensure fertilisation and pregnancy. CD59 might also support cell adhesion when egg and sperm interact.
Development	A GPI-anchored homologous of CD59 was identified as Prod 1 in newt.	Prod 1 is required in limb generation during development. Location of free Prod 1 at the proximal end helps cell identification.

Table 1.5 Alternative Roles of CD59 (Monleon *et al.* 2000; Kimberley *et al.* 2007).

1.3.2 Human Diseases Correlated with CD59 Deficiency

CD59 is involved in numerous processes throughout the body but the regulation of MAC is most pronounced. The main disease linked to CD59 deficiency is PNH. It is a rare, acquired disorder in which blood cells are subjected to complement lysis. In PNH patients' erythrocyte and platelet lysis causes haemolytic anaemia and thrombosis that can result in strokes (Holguin *et al.* 1989; Yamashina *et al.* 1990). PNH develops due to somatic mutations of the *PIG-A* gene in dividing bone marrow cells. The mutations result in a loss of GPI-anchored proteins including DAF and CD59. It was shown that DAF is not responsible for the increased susceptibility to complement lysis in PNH because in add-back experiments DAF could only partly reduce the haemolysis (Medof *et al.* 1987).

Reduced CD59 expression has also been linked with other haematological disorders as well as autoimmune diseases such as diabetes, Alzheimer's and inflammatory arthritis (Alegretti *et al.* 2009). Diabetes patients suffer from vascular damage and this pathology was linked to CD59. Patients' CD59 can be inactivated by glycation in the vascular endothelia. In this process glucose binds the active domain of CD59 resulting in an increased MAC deposition (Qin *et al.* 2004).

In Alzheimer's' disease MAC assembly and subsequent neuritic losses were revealed. During the disease CD59 was found to be reduced in the frontal cortex and hippocampus. CD59 was discovered to be down-regulated by amyloid β-peptide at the mRNA level causing increased susceptibility to cell lysis (Yang *et al.* 2000).

Furthermore, in RA, increased MAC assembly was identified to contribute to synovitis. This was probably due to the reduced expression of CD59 discovered in synovial membrane of patients (Konttinen *et al.* 1996). Similarly in OA increased MAC expression in synovium and around chondrocytes was revealed (Wang *et al.* 2011). In Psoriatic Arthritis (PsA) increased MAC deposition was found on erythrocytes which might have contributed to synovitis and inflammation. Again, impaired CD59 expression on erythrocytes was identified as a possible cause of disease (Triolo *et al.* 2003).

Inflammatory arthritic disorders have distinct patterns of bone pathology, in which too much bone is produced or eroded, affecting joint function. The significance of CD59's effect on bone is not known but clues can be derived from inflammatory studies in rodents, which have been well characterised.

1.3.3 CD59 in Experimental Disease Models

Experiments with mice revealed gene duplication - CD59a and CD59b. These proteins were found to share 63% sequence homology. CD59b is only expressed in the testis, whereas CD59a is more widely expressed and proven to be the main regulator of the terminal pathway. The CD59a gene was characterised, cloned and 4 exons were identified, of which the major coding region is located in the third exon. $CD59a^{-/-}$ mice were created by homologous recombination, replacing the third exon with a neomycin resistance gene in mouse embryonic stem cells (Holt *et al.* 2001).

$CD59a^{-/-}$ mice only show a mild PNH phenotype, which is probably due to protection by the additional murine complement regulator complement receptor-1 related gene/protein Y. The spontaneous intravascular haemolysis was shown to be higher in male over female mice. Interestingly, male mice also presented an increased complement activity which might explain the enhanced susceptibility. CD59 has been studied in various disease models, and the $CD59a^{-/-}$ mouse model was utilised frequently (Holt *et al.* 2001; Baalasubramanian *et al.* 2004).

1.3.3.1 Inflammatory Arthritis Models

A number of inflammatory arthritis studies have demonstrated the terminal pathway to be a major player in pathology and regulation of CD59. During these studies effects on joint swelling as well as the synovium, cartilage and bone were investigated, which will be described in detail below.

1.3.3.1.1 Swelling and Synovitis

Clinical features of inflammation manifest as joint swelling and erythema, which can be scored according to severity. In murine models, paw diameters and volume are also measures for quantitative analysis. Goodfellow et al. established a rat collagen induced arthritis (CIA) model, and proved that the onset of inflammation was delayed when complement was depleted with cobra venom factor (CVF). This highlighted the importance of complement in arthritis development. Treatment of CIA with C3 inhibitor soluble CR1 (sCR1) showed a stronger suppression of disease onset than CVF (Goodfellow *et al.* 2000).

To uncover if CR1 was blocking C3 and C4, Solomon et al. studied joint swelling in the K/BxN serum-induced RA model. When using C4 deficient ($C4^{-/-}$) mice, it was discovered that arthritis progression was not affected. This took the classical and MBL activation pathways out of the equation for complement involvement in arthritis development (Solomon *et al.* 2002).

On the other hand $C3^{-/-}$ mice, studied by Wang et al., showed that a single hit of bovine type II collagen (BCII) did not cause arthritis in comparison to WT mice. Multiple hits resulted in mild joint swelling in $C3^{-/-}$ mice but less severe than in WT mice (Hietala *et al.* 2002).

The role of C5 in arthritis has been studied in various papers and the most recent on using $C5^{-/-}$ DBA/1 mice in a CIA model showed resistance to inflammation onset in single and multiple hit experiments (Wang *et al.* 2000).

To further investigate the involvement of MAC Mizuno et al. used the Fab fraction of a monoclonal CD59 blocking antibody (6D1) to study complement in the synovium. Rats were injected with 6D1 and presented acute, transient arthritis characterised by joint swelling at day 1 which ceased by day 3, suggesting uncontrolled MAC deposition (Mizuno *et al.* 1997).

In antigen induced arthritis (AIA) Williams et al. revealed that knee swelling was increased in $CD59a^{-/-}$ mice over age-matched WT mice 1 day after disease initiation, which stayed increased until day 7. This effect was reversible by addition of recombinant membrane targeted CD59 (sCD59-APT542), confirming a CD59a deficiency effect and the importance of MAC activation in arthritic inflammation (Williams *et al.* 2004).

When looking closer at the synovium by histological analysis, Hietala identified pannus formation and synovial thickening with a single dose of BCII in WT animals, which resulted in vast infiltration of inflammatory cells during boosting. This inflammation was not seen in $C3^{-/-}$ animals (Hietala *et al.* 2002).

Wang et al. showed that $C5^{-/-}$ mice were also resistant to synovial cell proliferation, infiltration by neutrophils, lymphocytes, and plasma cells as well as pannus development. This was despite IgG and C3 binding to collagen and cartilage as well as specific TNFα secreting T-cells within the nearby lymph nodes (Wang *et al.* 2000).

When looking at the terminal pathway, histological processing of 6D1 treated rat joints uncovered that 6D1 was bound to CD59 at the synovial lining, surrounding tissue and blood vessels. It caused synovial infiltrate and thickening which exacerbated between 6 and 24h after injection. MAC deposition was identified at the synovial surface in 6D1 treated rats (Mizuno *et al.* 1997).

To confirm this data, AIA histological sections were stained for MAC deposition. $CD59a^{-/-}$ mice showed exacerbated cellular infiltrate and larger MAC deposition at the synovial lining, whereas only patches were stained in the WT control group (Williams *et al.* 2004).

OA is another disease which has recently been found to be inflammatory with up-regulated complement activation in synovial fluid of patients. Wang et al. induced murine OA models by medial meniscectomy, meniscal tearing and aging. He identified that $C3^{-/-}$ mice showed synovitis development similar to WT animals but $C5^{-/-}$ and $C6^{-/-}$ mice were protected. $CD59a^{-/-}$ mice showed worse disease highlighting CD59's role in MAC regulation (Wang *et al.* 2011). All these are evidence for the terminal pathway contribution in development of synovitis.

1.3.3.1.2 Cartilage Pathology

Other components of the joint, such as cartilage, are also affected in the above described models. During BCII boosting WT animals showed cartilage destruction, an effect not seen in $C3^{-/-}$ or $C5^{-/-}$ mice (Wang *et al.* 2000; Hietala *et al.* 2002).

Additionally, joint erosion was visible earlier in $CD59a^{-/-}$ compared to WT animals in the AIA model. This was caused by MAC deposition, as MAC staining was discovered in the connective tissue adjacent to the synovial lining in $CD59a^{-/-}$ mice only (Williams *et al.* 2004).

$CD59a^{-/-}$ mice also showed enhanced proteoglycan loss and cartilage degradation in comparison to WT and $C3^{-/-}$ mice in OA models. $C5^{-/-}$ and $C6^{-/-}$ mice were protected from any cartilage degradation (Wang *et al.* 2011). Very often when joint destruction is described, cartilage and bone changes are reported together.

1.3.3.1.3 Bone Pathology

Bone destruction was identified in BCII boosted WT animals but not in $C3^{-/-}$ or $C5^{-/-}$ mice (Wang *et al.* 2000; Hietala *et al.* 2002). This was comparable to the OA model in which $C5^{-/-}$ and $C6^{-/-}$ mice were protected from bone erosion and osteophyte development over WT animals. $C3^{-/-}$ mice did not show alteration to the bone phenotype in comparison to WT mice, but $CD59a^{-/-}$ mice showed enhanced osteophyte formation and bone erosion in these models (Wang *et al.* 2011).

These data demonstrate the relative importance of terminal pathway regulation over activation pathways in bone. CD59 expression has been shown on normal human mesenchymal stem cells (MSCs), OCs and OBs (Ignatius *et al.* 2011). In a clinical study of 43 newly diagnosed multiple myeloma patients, 56% of patients showed CD55 and/or CD59 deficiency on their erythrocytes and the deficiency correlated to elevated resorption markers. This association suggests that CD55 and CD59 regulate osteoclast activity (Terpos *et al.* 2003). This has not been intensively studied and was therefore chosen for this project.

CD59 has been investigated in further disease models of which some are described in Tab. 1.6.

Disease Model	Experiments	Mechanism
Renal allograft transplantation in miniature pigs	Rejected kidneys showed MAC and C3 presence at the time of rejection. In accommodated kidneys CD59 level was increased which was not seen in rejected organs. Accommodated kidneys were re-transplanted and low MAC deposition was found on these organs supporting a CD59 effect.	Increased CD59 expression protects from allografts rejection by blocking MAC mediated cell lysis (Griesemer *et al.* 2009).
Age-related macular degeneration (AMD)	During this eye disease new blood vessels are formed by chorodial neovascularisation (CNV). In the animal model a membrane of the choroid is disrupted with laser photocoagulation resulting in MAC deposition. CD59a was found to be down-regulated during CNV. CD59a$^{-/-}$ mice developed CNV early, more severe and showed increased MAC deposition in comparison to WT mice. CNV was prevented when sCD59a, fused to the Fc region of an antibody, was added.	Decreased CD59 expression leads to increased MAC mediated cell lysis and angiogenic growth factor secretion to form CNV. sCD59-Fc can reverse AMD development (Bora *et al.* 2007).
Experimental renal thromboitic microangiopahty (TMA).	Auto-antibodies against glomerular endothelial cells (GEN) are generated. Fab fragment of anti-CD59 and anti-GEN antibodies were introduced into rats via renal artery perfusion. In TMA treated with anti-CD59 increased MAC deposition and endothelial injury developed in comparison to TMA without anti-CD59.	CD59 protects from MAC dependent lysis in glomerular endothelium (Nangaku *et al.* 1998).
Acute experimental autoimmune encephalomyeli-tis (EAE)	This mouse model of multiple sclerosis resembles demyelination and axonal injury of neurons. Disease was induced with recombinant MOG, a glycoprotein important for myelination. CD59a$^{-/-}$ mice exhibited more severe pathology and cellular infiltrate than WT mice. MAC deposition overlaid with the sites of inflammation and injury.	In the brain CD59 is expressed at low level and might either be depleted after chronic complement activation or auto-antibodies block its activity (Mead *et al.* 2003) .
Myasthenia gravis (MG)	During MG auto-antibodies against the acetylcholine receptor (AChR) cause loss of neuromuscular transmission. Complement was activated at AchR, CD59a$^{-/-}$ and DAF deficient (DAF$^{-/-}$) showed a mild MG whereas CD59a$^{-/-}$DAF$^{-/-}$ mice presented severe disease. Anti-C5 blocking antibodies administrated to CD59a$^{-/-}$DAF$^{-/-}$ mice revealed that disease progression was arrested.	MAC formation plays a major role in MG development (Morgan *et al.* 2006).
Wallerian degeneration	Neurons were exposed surgically and crushed with forceps. CD59a$^{-/-}$ mice showed increased MAC deposition and damage to the nerve axon as well as increased macrophage infiltration over WT mice early after surgery.	CD59 is thought to protect from early MAC dependent axon destruction after lesion (Ramaglia *et al.* 2009).

Table 1.6 Role of CD59 in experimental disease models.

The role of CD59 in age related joint degeneration and bone pathology has not been described. To appreciate the effect, the structure and function of bone, as well as its homeostasis, has to be outlined.

1.4 Structure and Function of Bone in the Human Skeleton

The skeleton consists of different types of bone: the skull, exoskeleton and long bones. Each type has a distinct structure and function, and develops in different ways. The skull and exoskeleton provide organ protection whereas long bones provide strength and allow for motility. The majority of this project deals with the long bones and these will be covered in further detail below.

1.4.1 Embryonic Development of Long Bones

Long bones develop via endochondral ossification. Here chondrocytes are formed which proliferate to form a cartilage model of the developing bone. Chondrocytes become hypertrophic, which means they stop proliferating but enlarge in size and produce a different matrix which allows calcification and invasion by blood vessels. Chondrocytes eventually undergo apoptosis to make space for the bone marrow cavity and OBs which secrete bone matrix (Fig. 1.7) (Ham and Cormack 1979; Gilbert 2000a; Rosen 2008).

Not all cartilage has turned into bone at birth. Bones continue to grow from ossification fronts (growth plates) in which chondrocytes proliferated throughout childhood and turn into mineralised bone gradually (Gilbert 2000b).

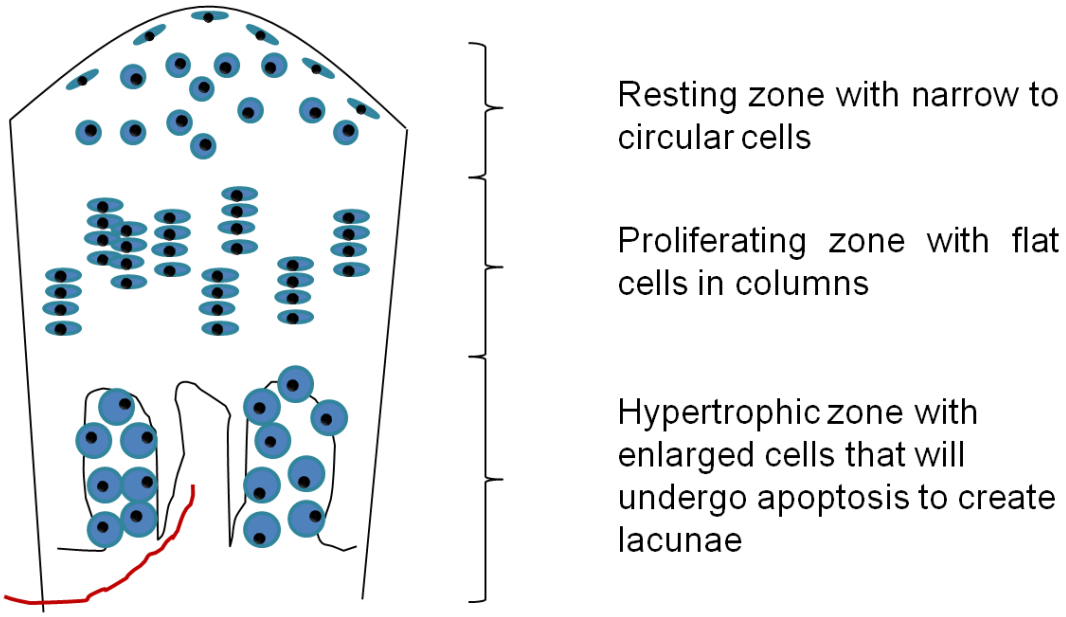

Figure 1.7 Endochondral cartilage. Blood vessels enter cartilage to deliver chondrocytes, which degrade cartilage, and MSCs that differentiate into OBs to synthesise bone (Andrades *et al.* 1996; Abad *et al.* 2002).

1.4.2 Bone Structure

The bone matrix of an adult has a much larger connective tissue mass than any other organ. It consists of 50-70% of calcium and phosphate minerals called hydroxyapatite crystals and 20-40% of protein. The main protein component is type I collagen (Col1), but small amounts of other collagens and non-collagenous proteins reside in bone as shown in Tab. 1.7 (Favus 2006).

Mineralised matrix can be divided into 2 types, woven and lamellar. Woven bone is the immature form found in bone development and fracture repair. It has a high turnover rate and shows a random pattern of collagen fibres and mineralisation; hence it is more flexible. Lamellar mature bone consists of tightly packed collagen fibres. Neighbouring lamellae run in different directions, interconnect and give strength to the bone (Buckwalter and Cooper 1987).

Protein	Function
Aggrecan	Arranges matrix, stores water and ions for mechanical integrity.
Albumin	Blocks hydroxyapatite expansion.
Alkaline phosphatase (ALP)	Transports Ca^{2+}, hydrolysis pyrophosphates and other mineralization inhibitors as phosphate source.
Asporin	Modulates collagen arrangement.
Biglycan	Associates with collagen and growth factor, present at peak of bone mass.
Bone sialoprotein (BSP)	Associates with cells, may induce mineralisation.
Decorin	Associates with collagen (for modulating fibre thickness), transforming growth factor (TGF) β (to control function) and blocks cell binding to fibronectin.
Fibrillin 1 and 2	May modulate elastic fibre assembly.
Fibromodulin	Associates with collagen and TGFβ, may control fibril assembly.
Fibronectin	Associates with cells, fibrin heparin, gelatin and collagen.
Glypican	Modulates bone morphogenic protein (BMP)-SMAD (intracellular transcription factors) signalling and cell differentiation.
Lumican	Associates with collagen, may control fibril assembly.
Matrix Gla protein	Inhibitor of mineralisation.
MEPE	Modulates mineralisation and hormone function.
Osteoadherin	May induce cell binding.
Osteocalcin (OCL)	May modulate OC precursor and OC function, may induce reversal of remodelling, and blocks mineralisation.
Osteoglycin/Mimecan	Associates with TGFβ and controls collagen fibre formation.
Osteonectin (ON)	Controls collagen assembly and maybe hydroxyapatite storage, associates with growth factors and favours bone formation signalling.
Osteopontin (OPN)	Associates with cells, may modulate mineralisation and proliferation, blocks nitric oxide synthase.
Perlecan	Modulates cell communication in conjunction with other matrix proteins.
Protein S	May be produced by OB lineage cells.
Secreted phosphoprotein 24	May modulate thiol proteases.
Tenascin-C	Inhibits cell-fibronectin binding.
Tenascin-X	Controls cell-matrix associations.
Tetranectin	May modulate mineralisation.

Protein	Function
Thrombospondin	Associates cells to matrix, binds collagen, histidine rich glycoproteins and coagulation cascade proteins.
Type III and V collagen	Small amounts in bone to regulate collagen fibre width.
Vitronectin	Associates cells to matrix, binds coagulation cascade proteins.
α2HS glycoprotein	Blocks calcification and stimulates endocytosis, acts as opsonin/chemokine.

Table 1.7 Bone matrix proteins (Rosen 2008).

Once long bones have reached maturity they consist of 3 sections: epiphysis, metaphysis and the shaft. Each of these is further divided into cortical and trabecular bone (Fig. 1.9) (Buckwalter and Cooper 1987; Favus 2006).

1.4.2.1 Structure and Function of Cortical Bone

Cortical bone is dense, solid and builds the outer layer of each bone with a thickness of approximately (approx.) 1-5mm (Wehrli 2007). It makes up 80% of adult bone and is composed of osteons or Haversian system, which is the basic structural element of mineralised bone (Fig. 1.8) (Hall 2005). The human osteon is 2,000 μm in length, up to 200 μm wide and forms at a speed of 20-40 μm/day (Raisz 1999). Cortical bone is covered by an outer fibrous connective tissue layer, the periosteum. The inside of cortical bone is coated by the endosteum (Fig. 1.9). The periosteum contains nerve endings, and both layers possess blood vessels and bone cells (Favus 2006). Cortical bone is essential for mechanical functions as it is much more tightly packed than trabecular bone. Its tubular and stiff structure in the shaft allows for efficient counteracting to torsion and bending (Buckwalter and Cooper 1987; Favus 2006).

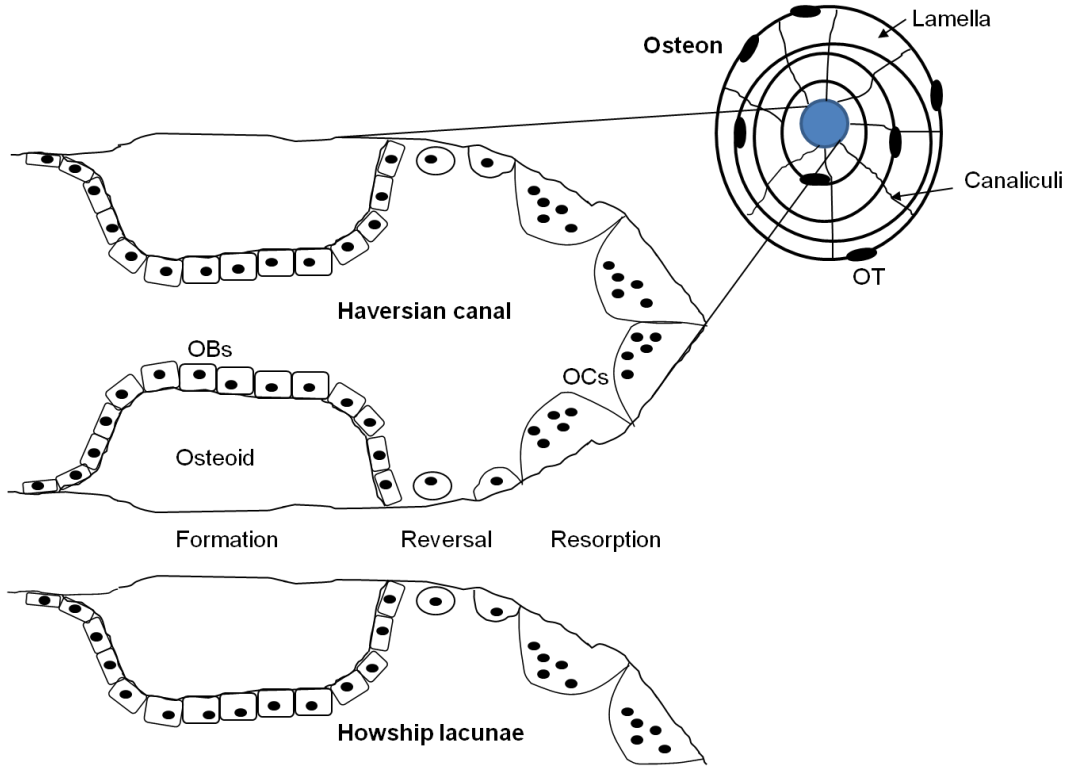

Figure 1.8 Osteon. The Haversian canal is surrounded by lamella of extracellular matrix (ECM) and osteocytes. Canaliculi connect osteocytes (OT) and osteon surfaces. Bone remodelling takes place in the Haversian canal (Enlow 1962; Buckwalter and Cooper 1987; Favus 2006).

1.4.2.2 The Structure and Function of Trabecular Bone

Trabecular bone is a spacious network of thin bone plates and bars of approx. 0.1-0.15mm thickness (Wehrli 2007). Its structure is orientated to support mechanical resistance (Keaveny *et al.* 2001) but its low density also allows for some degree of elasticity. When load is applied to a long bone the metaphysis, which is predominately made of trabecular bone, allows for deformation. Trabecular bone is composed similarly to cortical bone but bone marrow runs through its interconnected structure (Fig. 1.9). Its osteons are only half the size of the Haversian channel. It forms a thinner saucer-shaped channel called Howship lacunae (Fig. 1.8) (Raisz 1999; Hadjidakis and Androulakis 2006). Trabecular bone has a large surface covered by bone cells which allows for fast resorption or apposition according to the body's requirements. Trabecular bone therefore regulates acid-base levels as well as calcium and phosphate haemostasis. Extra-cellular fluids contain constant calcium (8.5-10.5 mg/decilitre (dl)), phosphorus (2.5-4.5 mg/dl) and pH (7.4) levels which are regulated by a variety of hormones controlling bone turnover, further described in Tab. 1.10 (Buckwalter and Cooper 1987; Levi and Popovtzer 1999; Yarbro *et al.* 2004; de Baat *et al.* 2005).

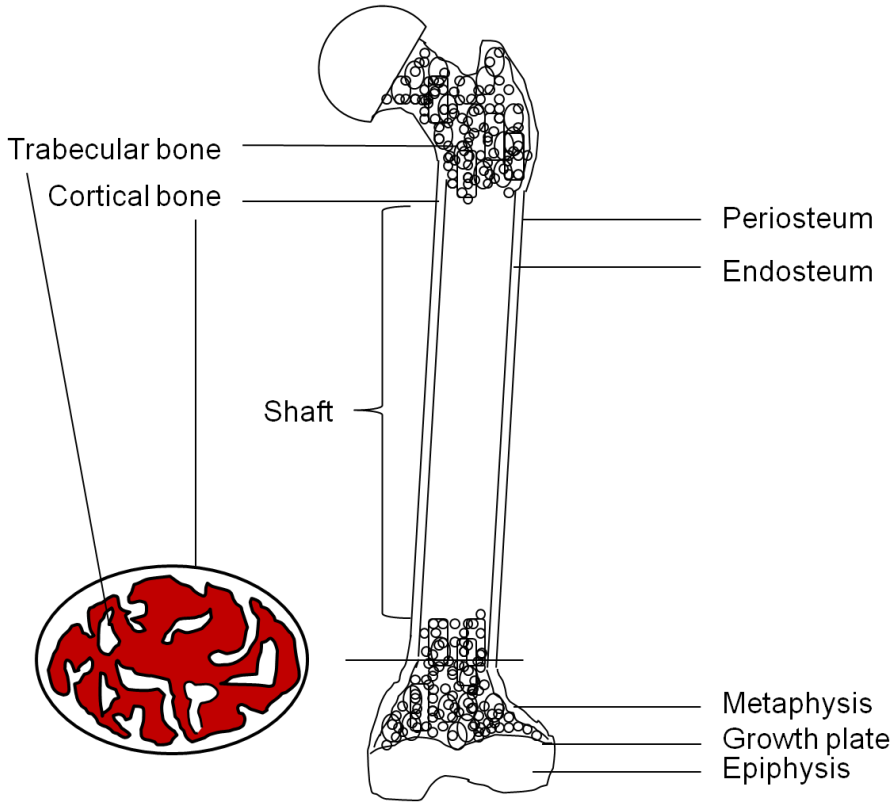

Figure 1.9 Architecture of a long bone.

1.4.3 The Biology of Bone Cells

Mature bones are remodelled by OCs, OBs and OT. The individual cell types are discussed in detail below.

1.4.3.1 The Biology of Osteoclasts

The OC originates from myeloid lineage of the bone marrow or blood. Human peripheral blood OC precursor cells express a variety of markers such as CD14 (monocyte marker), CD33 (myeloid marker) and CD45 (leukocyte marker) as well as some markers shared with murine precursor cells listed in Tab. 1.8 (Filgueira 2009).

Marker (human/mouse)	Description	Human blood	Mouse primary cells
CX3CR1	chemokine receptor for adhesion of leukocytes	Low	+
CR3	Macrophage differentiation marker	+	negative to dull
RANK	Receptor activator of NFκB	+	Low (Muto *et al.* 2011)
c-Fms	Macrophage colony stimulating factor (M-CSF) receptor	+	+
OSCAR	Osteoclast associated receptor (IgG-like receptor)	+	- (Kim *et al.* 2002)

Table 1.8 Osteoclast precursor marker expression (Lorenzo *et al.* 2010).

OC differentiation requires two cytokines: RANK ligand (RANKL) and M-CSF. Both are produced in membrane bound and soluble form by bone lining cells and stromal cells. This allows cell-to-cell and paracrine communication between haematopoietic and non-haematopoietic cells. Both mediators are essential for all stages of OC differentiation as depicted in Fig. 1.10.

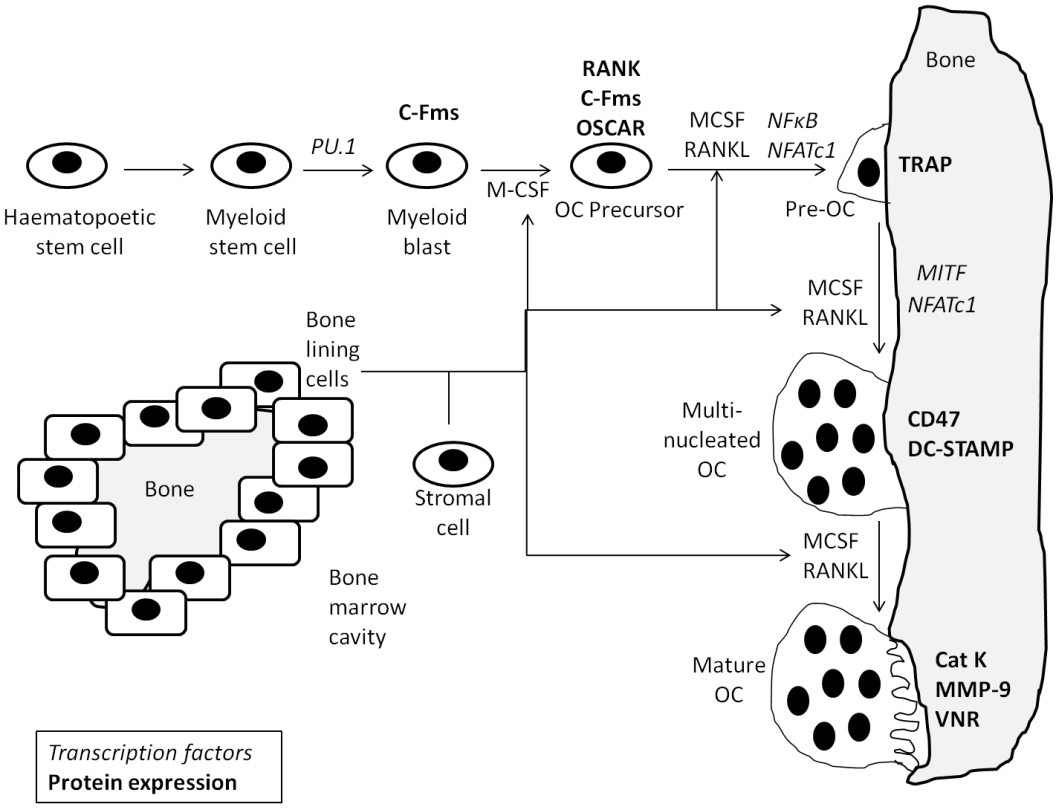

Figure 1.10 Osteoclastogenesis (OCG). OC precursors become c-Fms positive after activation of transcription factor PU.1. This enables M-CSF stimulation that initiates RANK expression. RANKL binding activates different pathways, including NFκB and, with OSCAR as co-activator, nuclear factor of activated T cells (NFATc1). The latter modulates expression of Cathepsin K (Cat K), tartrate-resistant acid phosphatase (TRAP), calcitonin receptor (CTR) and dendritic cell specific transmembrane protein (DC-STAMP) (Athanasou 2011). Microphthalmia transcription factor (MITF), DC-STAMP and CD47 are essential for cell fusion. Once vitronectin receptor αvβ3 (VNR) is expressed additional survival and differentiation signals are induced and functional proteins such as Cat K and matrix metalloproteinase 9 (MMP-9) are produced (Favus 2006; Filgueira 2009; Knowles and Athanasou 2009; Athanasou 2011).

Mature OCs are terminally differentiated, multinucleated cells (≥2 nuclei) attached to calcified bone lining (Morriss-Kay *et al.* 2001; Amoui *et al.* 2004; Teitelbaum 2004; Favus 2006). They are bone 'breaker' cells and are essential for bone remodelling as is portrayed in detail in section 1.5.

1.4.3.2 The Biology of Osteoblasts

OBs originate from MSCs which can be isolated from bone marrow, explants, fat tissue, blood and Wharton's Jelly (a fluid within the umbilical cord). MSCs develop colonies of stromal bone marrow cells. Stroma defines non-haematopoietic

connective tissue milieu that is essential for haematopoiesis. Stromal colonies develop from a single precursor cell and are called colony forming unit fibroblasts (CFU-F) which have been identified in many species. Human and mouse CFU-F can be identified in bone marrow as myeloid lineage marker negative. Mouse CFU-F are stem cell antigen-1 (Sca-1) positive whereas human CFU-F are stem cell factor (CD34) and STRO-1 positive. They can also express vascular cell adhesion molecule -1 (CD106), receptor for TGF-beta superfamily ligands (CD105) and other markers (Short *et al.* 2003; De Schauwer *et al.* 2011).

Runx2 is a transcription factor and the main regulator of bone formation as shown in Fig. 1.11 (Bianco 2011). Once matured, OBs look like round to polygonal cells sandwiched between an osteoid and the bone surface. They do not proliferate (Ham and Cormack 1979; Buckwalter and Cooper 1987; Favus 2006; Lorenzo *et al.* 2010). OBs are bone 'makers' and are also required for bone remodelling as explained in section 1.5.

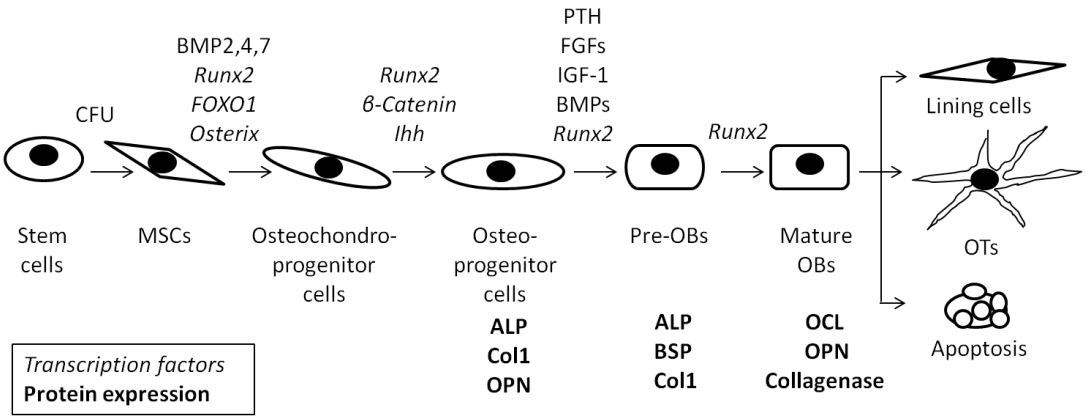

Figure 1.11 Bone formation. Runx2 acts through osterix and FOXO1 to initiate MSC differentiation which results in a common progenitor with chondrocytes. This early process is also supported by BMPs. Next β-catenin, part of the Wnt signalling pathway, is the transcription factor that guarantees differentiation of osteochondrogenic precursors towards osteoprogenitors. Indian hedgehog (Ihh) also induces Runx2 expression in favour for bone formation. Resulting ostoeprogenitor populations proliferate due to PTH stimulation. Further differentiation is achieved by fibroblast growth factors (FGFs) and insulin-like growth factor 1 (IGF-1) signalling via protein kinase C (PKC) pathway-dependent Runx2. BMPs and TGFβ support this action by signalling through SMADs. They associate with Runx2 to induce further BMP, Runx2 and osterix expression and cells turn into pre-osteoblasts. Runx2 then regulates expression of Col1, ALP, OPN, BSP, OCL) and ON (Rosen 2008; Lorenzo *et al.* 2010). These matrix proteins can be used as markers for different stages of bone formation. Whereas ALP is expressed early in differentiation; Col1, BSP, OPN appear later on and OCL is a marker of mineralising OBs (Buckwalter and Cooper 1987; Favus 2006; Rosen 2008; Bianco 2011).

1.4.3.3 The Biology of Osteocytes

About 30-50% of all OBs terminally differentiate into OTs. They are buried within the osteon but keep secreting matrix proteins such as OCL and dentin matrix protein. OTs are oval shaped cells with spikes that lose cell volume and organelles upon aging. They are mechanosensor cells that initiate and control bone remodelling as explained in section 1.5 (Buckwalter and Cooper 1987; Favus 2006; Hadjidakis and Androulakis 2006; Rosen 2008; Lorenzo *et al.* 2010).

1.5 Bone Modelling and Remodelling

In bone all 3 cells work in harmony to maintain healthy and strong bones. There are 2 mechanisms of renewal: bone modelling and remodelling. Bone utilises the mechanism of modelling when structural changes are required, for example, during growth and increased load. In this process bone resorption by OCs and bone formation by OBs are uncoupled (Favus 2006). Bone remodelling, on the other hand, is a coupled process of constant replacement of old and fractured bone by newly synthesised one. It is performed by the bone remodelling unit (BRU), in which a variety of cell types interact with each other and work sequentially in four stages: activation, resorption, reversal and bone formation (Fig. 1.8). These will be covered in detail below.

1.5.1 Activation of Bone Remodelling

OCs are implicitly involved in the activation phase of remodelling which consists of 2 phases. Firstly the identification of a remodelling surface is covered followed by osteoclast recruitment.

<u>Identification of Remodelling Surface</u>

The process starts with the activation of a resting bone surface into a remodelling one. The selection of a new remodelling surface is mainly non-specific and not fully understood but it has been shown to be activated in fractured areas. OTs are thought to be involved in the initiation. OTs have long microfilaments creating a system of processes encapsulated in canaliculi that extend throughout the whole bone matrix connecting each other and the bone surface via gap junctions consisting of connexion 43 (Fig. 1.8). Alterations in biomechanics might trigger signalling to bone lining and stromal cells (Buckwalter and Cooper 1987; Hadjidakis and Androulakis 2006; Rosen 2008; Lorenzo *et al.* 2010).

Osteoclast Recruitment

Stromal cell signalling is essential for differentiation and survival of haematopoietic stem cells (HSCs). The bone marrow consists of numerous niches of stem cells. The HSC niche contains bone lining cells that keep HSCs in a resting undifferentiated stage. When stromal or bone lining cells are activated, their morphology changes and this causes HSC recruitment by Notch and stromal cell-derived factor (SDF)-1, as well as by mediators they release. This includes secretion of the chemokine (C-C motif) ligand 9 (CCL9/MIP-1γ) and RANKL. OC precursor cells express RANK as well as CCR1 (receptor for CCL9/MIP-1γ), and are attracted not only from the niche but the circulation to the bone surface where they enter the bone lining. Here they adhere via N-cadherin, β-catenin and vascular cell adhesion molecule (VCAM) and differentiate into mature OCs, which is described in section 1.4.3.1 (Raisz 1999; Favus 2006; Hadjidakis and Androulakis 2006; Filgueira 2009; Lorenzo *et al.* 2010).

1.5.2 Bone Resorption

Mature OCs adhere tightly to the bone surface to allow for resorption to occur and for removal of degradation products (explained below).

Generation of Resorption Pit

Mature OCs polarise towards their basal membrane and obtain physical contact with bone matrix. To strengthen the attachment, VNR triggers adherence to the bone by connecting to the Arginine-Glycine-Aspartic acid motive of OPN and other matrix proteins. VNR also activates ontogenic protein-tyrosine Src kinase which causes establishment of the actin ring. This is a sub-membrane, circular shaped cytoskeleton organisation which results in a tight sealing zone that produces a separate compartment called the resorption pit (Xu and Lindquist 1993; Favus 2006).

Vesicle Transport and Resorption

The basal membrane within the resorption pit is a dynamic ruffled border in which secretion and phagocytosis are taking place simultaneously. Vesicles of continuously produced enzymes and vacuolar proton pumps (H^+-ATPase) move towards the pit. Protons are produced by carbonic anhydrase II (Ca II) within the cell and when released generate an acidic pH of 4.5 within the compartment to decalcify hydroxyapatite (see section 1.5.4) underneath. At the same time lysosomal proteins such as MMP-9, Cat K and TRAP work efficiently at low pH to digest organic parts

of the matrix (Filgueira 2009; Lorenzo *et al.* 2010). Additionally, digested products and some freed OTs are phagocytosed from the pit and transported inside the OC via phagolysomal vesicles. Acidic intracellular compartments contain enzymes such as TRAP to further degrade collagen. Digests and enzymes such as Cat K are transcytosed towards the apical membrane and secreted into the blood stream, from which they are further excreted into the urine. End-products of resorption, such as Col1 cross-linked N-telopeptide, are detectable in urine and blood fluids (Favus 2006; Hadjidakis and Androulakis 2006; Filgueira 2009; Proff and Römer 2009). OCs are terminated by osteoprotegerin (OPG), a soluble decoy receptor of RANKL, and undergo apoptosis. At the same time mononucleated cells finish off the resorption process (Favus 2006; Hadjidakis and Androulakis 2006).

1.5.3 Reversal of Bone Remodelling

Resorption is succeeded by the reversal stage of the BRU. The cavities created by OCs are filled with monocytes and freed OTs. These attract pre-OB which provide signals for OB migration and differentiation. The process of recruitment is unknown but some evidence has shown that coupling factors produced by OCs, or freed during resorption, may be involved. For example, TGF-β, released from the matrix, was found to induce bone formation. Furthermore ephrinB2, secreted by OCs, has been identified to modulate OB differentiation (Favus 2006; Okamoto *et al.* 2011).

1.5.4 Bone Formation

The final stage of remodelling is formation. Once OBs have differentiated they secrete the organic matrix, which is then followed by mineralisation. The osteoid is secreted first and mainly consists of Col1 organised in long thick fibres to arrange matrix which then determines flexibility. Consequently, non-collagenous proteins bind to the collagen. Microfibrils made of fibrillin sit between the collagen fibres and bind growth factors such as TGF-β and BMPs to regulate cell signalling.

Once the osteoid has matured it undergoes mineralisation. For this OBs liberate small, membrane-bound vesicles with calcium and phosphate ions as well as degrading inhibitors of mineralisation (pyrophosphate and proteoglycans). The secreted hydroxyapatite ($Ca_{10}(PO_4)_6(OH)_2$) is very small and contains impurities such as carbonate, magnesium and acid phosphate. Impurities make the structure weaker, which allows readily resorption when needed. Minerals are deposited at various collagen sites, starting off small but growing with matrix maturation and as they do so contain fewer impurities. Minerals then start accumulating to fill the spaces between collagen bundles to finish the process (Favus 2006; Hadjidakis and

Androulakis 2006; Rosen 2008). The surface is then covered by bone lining cells and seen as a resting surface whilst other osteons are remodelled. Bone remodelling is controlled by a range of factors – biochemical, mechanical and environmental as described in Tab. 1.9 (Favus 2006; Hadjidakis and Androulakis 2006).

	Factor	Produced by	Causal Effect
Break down	Peroxisome proliferators-activated receptor (PPAR)γ	Haematopoietic lineage cells including OCs	Inhibits MSC differentiation via transcriptional modulation of positive (eg. BMP4) and negative (eg. Transducer of ErbB-2 (Tob) 1) regulators (Shockley *et al.* 2009).
	Sclerostin	OT	Inhibits Wnt signalling resulting in reduced OB differentiation.
	OF45	OT	Inhibitor of bone formation, modulates phosphate metabolism (Marie 2009).
	Pro-inflammatory cytokines (eg. TNFα, IL-6)	Stromal cells	Induces RANKL expression or gives co-stimulatory effects to OCs (Take *et al.* 2005; Favus 2006; Hadjidakis and Androulakis 2006; Filgueira 2009; Proff and Römer 2009; Athanasou 2011).
	Prostaglandin E2	OB	Enhances RANKL expression.
	Glucocorticoids	OC	Inhibits BMP and Wnt signalling and enhance parathyroid hormone (PTH) signalling resulting in reduced bone formation.
Formation	OPG	Stromal cells/OBs	Soluble decoy receptor for RANKL, inhibits OCG and resorption.
	Calcitonin (CT)	Thyroidal C-cells	Calcium sensor that blocks OC fusion and resorption by removing the ruffled border, blocking OC movement and proteins secretion (Favus 2006; Hadjidakis and Androulakis 2006; Filgueira 2009; Proff and Römer 2009).
	TGFβ	Stromal cells	Inhibits OC differentiation.
	Dentin matrix protein (DMP)-1	OT	Regulates phosphate metabolism and mineralisation.
	Phex and Fimbrin	OT	Controls phosphate metabolism.
	PTH-related protein (PTHrP)	Many tissues	Regulates chondrocyte proliferation during endochondral ossification.
	Androgens	Glands	Induces periosteum and trabecular bone generation by increasing β-catenin and reducing Axin and Axin2.
	Oestrogen	Glands	Induces OPG and diminished production of IL-6, TNFα and IL-1 by circulating macrophages and modulates RANKL and TNFα expression of T-cells. Induces TGFβ by dendritic cells/macrophages to reduce resorption.
	Growth factors (eg. IGF, BMPs)	Hepatocytes, stromal cells	Control mineralisation. IGF-1 supports PTH anabolic effect. Platelet-derived growth factor (PDGF) is required for migration and proliferation.
	Toll-like receptor (TLR) 2 and 4	Macrophages	Inhibits resorption by down-regulating RANK expression in OCs (Ferrari-Lacraz and Burger 2010).

	Factor	Produced by	Causal Effect
Dual activities	PTH	Parathyroid cells (Suva 2006)	Induces bone resorption (constant signal) and controls mineral homeostasis (anabolic intermittent signal). It promotes Runx2 expression via PKC pathway or inhibits Runx2 and osterix. Runx2 can be further regulated by its inhibitor Notch to determine when OB mineralisation is saturated (Rosen 2008; Lorenzo *et al.* 2010).
	1,25-dihydroxyvitamin D3 (Vit D)	Not made in the body but converted by liver and kidney to its active form.	Stimulates OCG and also favours bone formation by inhibiting PTH. Induces secreting of OPN, OCL and matrix Gla protein in favour of mineralisation (Sato *et al.* 1993).
	Leptin	Adipocytes	Dose dependent: low dose favours bone formation over adipogenesis, induce OPG in OBs; high dose induces MSC and adipocyte apoptosis and blocks bone formation via neuropeptide in hypothalamus (Cirmanova *et al.* 2008).
Environ-ment	Diet		Different diets can influence bone health. High calcium diet, for example, supports bone health whereas a diet high in protein leads to loss of calcium from the body (Bowen *et al.* 2004).
	Age		OBs and adipocytes originate from the same precursor (MSC), reciprocally regulated, adipocyte number increases with age where as OB number declines.
	Sex		In women menopause causes oestrogen level drop resulting in low bone mineral density.
	Weight		Increased weight also stimulates increased bone apposition but rapid weight loss in obese persons can result in drastic bone loss.
	Physical activity		Exercise that leads to increased muscle mass also has an anabolic effect on bone.

Table 1.9 Mediators of bone remodelling (Rosen 2008).

When the dynamic is distorted the healthy bone becomes diseased. A variety of diseases characterised by too much or too little bone matrix are described in Tab. 1.10.

	Disease	Cells implicated/mechanism	Treatment
Reduced bone formation	Osteoporosis	In post menopausal women, oestrogen deficiency induces up-regulation of OC numbers and resorption. Osteoblasts can also be dysfunctional due to aberrant regulation of hormones such as IGF-1 and PTH (Raisz 1999; Rodan and Martin 2000).	Calcium and Vit D supplements, oestrogens and progestin, selective oestrogen receptor modulators (SERMs) (eg. Raloxifene), bisphosphonates (eg. Alendronate), teripartide (recombinant PTH), strontium ranelate, CT and Cathepsin K inhibitor (Rodan and Martin 2000; Rosen 2008).
	Solid tumours and haematopoietic malignancies	Enhancing OCG and resorption. Bone resorption releases TGFβ and with the help of pro-inflammatory cytokines allows seeding of local bone metastases (Rodan and Martin 2000).	Bisphosphonates (eg. Zoledronic acid).
	Hyperparathyroidism	PTH overproduction leads to up-regulation of OCs, bone remodelling and hypercalcaemia (Raisz 1999; Rosen 2008).	Surgical removal of parathyroid glands, controlled calcium and Vit D intake.
	Non-union fracture	Caused by low numbers of osteoprogenitor cells and mal-regulation of OBs (Griffin *et al.* 2008; Hofmann *et al.* 2008).	Surgical removal of scar tissue and placing metal plates, autogenous bone graft or tissue engineered bone into the wound (Yoshikawa *et al.* 2011).
Increased bone formation	Paget's disease	Viral infection or genetic mutation leads to atypical OCs. Irregular resorption by OCs leads to enhanced bone formation of woven bone weakening the skeleton (Raisz 1999; Rosen 2008; Saluja *et al.* 2009; Michou and Brown 2011).	Bisphosphonates (eg. Etidronate), synthetic salmon CT as well as analgesics (eg. Aspirin), anti-inflammatory drugs, orthopaedic and neurosurgical treatments.
	Osteopetrosis	Rare genetic disease in which mutations in OC leads to increased bone formation resulting in thickening of bone (Raisz 1999; Rosen 2008; Saluja *et al.* 2009; Michou and Brown 2011).	Bone marrow transplantation, calcium deficient diet, high glucocorticoid treatment.

	Disease	Cells implicated/mechanism	Treatment
Inflammatory arthritis	RA	Chronic inflammation of synovial joints leads to local production of pro-inflammatory cytokines as well as RANKL production by synovial fibroblasts and T-cells. These fuel the OC activity and cause cartilage and subchondral bone erosion (Rodan and Martin 2000; Piccoli *et al.* 2011).	TNF-blocker (eg. Infliximab), IL6-blocker (eg. Tocilizumab), CD20- (Retuximab) and CD22-blockers (Epratuzumab), non-steroidal anti-inflammatory drugs (NSAIDs) (eg. Ibuprofen), anti-rheumatic drugs (DMARD) (eg. Methotrexate), corticosteroids (Prednisolone) (NHS-Choices 2010a; Mizuno and Morgan 2011).
	OA	Mechanical and osmotic stresses alter metabolism resulting in cytokine production, cartilage degradation. This causes blood vessel invasion and microfractures resulting in osteophytes and subchondral sclerosis due to up-regulated OC activity and changes of OB phenotype to produce more RANKL and MMPs (Karsdal *et al.* 2008; Abramson and Attur 2009).	Exercise, weight loss, pain killers (paracetamol, NSAIDs, opioids, capsaicin cream), intra-articular injection of corticosteroids (NHS-Choices 2010b).
	PsA	Synovitis causes invasive OC precursor development and recruitment to the joint due to TNFα. High concentrations of RANKL and TNFα in the joint causes increased OCG and extensive bone erosion (Ritchlin *et al.* 2003).	Physiotherapy, DMARD (eg. Methotrexate), NSAIDs (eg. Ibuprofen), TNF-blocker (eg.Etanercept), steroid injection (The-Psoriasis-Association).
	Ankylosing Spondylitis	Inflammation triggers increased OC activity and extensive bone formation in the spine due to BMP signalling that leads to fusion of vertebrae (Braun and Sieper 2007).	NSAIDs (eg. Indocin), DMARD (eg. Sulfasalazine) and TNF-blocker (eg. Infliximab) (Braun and Sieper 2007; Spondylitis-Association-of-America 2011).

Table 1.10 Bone diseases (Rosen 2008).

The interplay between the complement system and bone diseases such as RA and OA has been investigated, but each arthritic disease demonstrated variable bone phenotypes. Dynamics between complement components and bone homeostasis have also been established.

1.6 The Role of Complement Regulating Bone in Health and Disease

The complement system's involvement in OCG and bone formation has been investigated in a number of *in vitro* and *in vivo* studies which are described in detail below.

1.6.1 Role of Complement on OCG

OCG regulation has been discovered to depend on C3 when stimulated with Vit. D. This opened up research into C3 and C5 receptors. Findings from initial differentiation assays were supported by studies into different knockout models.

1.6.1.1 *In Vitro* Role of Complement on OCG

In the early 90s a Japanese group was the first to publish complement involvement in bone cells. Initially they discovered that cultured murine stromal cells and calvarial primary osteoblasts stimulated with Vit D produced a 190kDa protein which they identified as C3. Next the authors prepared co-cultures from bone marrow supplemented with Vit D which produced ALP^+ colonies and $TRAP^+$ multinucleated cells adjacent to each other. When C3 was blocked no colonies or $TRAP^+$ cells appeared. In cultures with added C3 and no Vit D stimulation $TRAP^+$ cells were not detectable, suggesting that C3 is working together with other factors stimulated by Vit D to induce OCG (Sato *et al.* 1991).

During OCG, Sato et al. (1993) identified that C3 was stimulating macrophage-like cells, mononuclear $TRAP^+$ cells and small multinucleated (up to 5 nuclei) $TRAP^+$ cells. These cells were found to have multiple C3 receptors. Blocking antibodies against these receptors revealed that C3 produced by OBs and stromal cells binds mainly CR3, which disappears during OCs maturation. When blocking C3 at different time points of OCG, C3 was found to be most important during late proliferation and early differentiation (Sato *et al.* 1993).

In 2 human studies OBs and OCs were shown to activate C5. C3a/C5a, in synergy with IL-1β, could induce IL-6, IL-8, RANKL and OPG release by OBs. Furthermore C3a and C5a were supposedly able to induce OCG in absence of RANKL and M-CSF (Pobanz *et al.* 2000; Ignatius *et al.* 2011). Recently, C1q

expression was also discovered in OC cultures derived from human peripheral blood monocytes. C1q expression was most pronounced in immature osteoclasts and C1q supplementation increased OCG, suggesting that the classical pathway is also playing a role (Boon *et al.* 2012).

1.6.1.2 *In Vivo* Role of Complement on OCG

To obtain an *in vivo* appreciation of complement on OCG, C3 production was studied in Vit D-deficient (Vit $D^{-/-}$) animals. Calvarial levels of C3 were much lower in Vit $D^{-/-}$ animals than in controls. When Vit D was administered C3 production was stimulated in bone. $C3^{+}$ cells were located in the peristeum and tibial metaphyses co-localised with OB precursor cells (Jin *et al.* 1992; Sato *et al.* 1993).

This data was confirmed by Mangham et al. who showed that C3 deposited to the hydroxyapatite of trabecular surfaces of human foetuses. $TRAP^{+}$ mononuclear cells expressing CR3 and CR4 were localised to the same area. When multinucleated cells were formed, expression of these receptors was lost, showing that complement was needed for the recruitment of OC precursor cells to the site of resorption (Mangham *et al.* 1993).

Furthermore, $C3^{-/-}$ mice were found to express lower RANKL and OPG levels, which resulted in reduced production of M-CSF and IL-6 as well as fewer OCs being present (Tu *et al.* 2010).

Recent research has also concentrated on the anaphylatoxins, C5a and C3a, and their receptors. In an abstract Ehrnthaller et al. described that C5aR was hardly detectable in MSC but readily expressed by OTs, OBs and OCs in trabecular bone (Ehrnthaller *et al.* 2009). It was identified that components of the alternative pathway were produced locally to activate C3, and released C3a/C5a where required for optimal OC generation by controlling IL-6 levels (Tu *et al.* 2010).

1.6.2 Role of Complement on Bone Formation

In order to characterise OB in more detail murine calvaria cultures were analysed via the Affymetrix Gene-Chip array. When looking at 27,000 genes prominent complement expression was discovered. All 3 chains of C1q were expressed the most, followed by C4, C3aR, properdin, C1 inhibitor and factor H (Roman-Roman *et al.* 2003).

Around the same time another group performed an Affymetrix gene chip on adult human cell lines from different stages of the OB differentiation, starting with a pre-OB line to a pre-OT line. C1r, C1s and factor H were among the 47 genes that changed in a consistent down-regulation between all cell lines. The authors

suggested that this mechanism causes inhibition of OCG in the area of newly generated bone (Billiard *et al.* 2003).

Most of the research has concentrated on the complement components and their cleavage products, however, the role of complement regulators in bone is unclear.

1.7 Hypothesis and Aims of the Project

Preliminary data by Dr Anwen Williams revealed a spontaneously induced bone disease when histologically examining joint tissue from 19 month old CD59a$^{-/-}$ mice compared to age matched WT mice. The pathology was featured by enhanced OC localisation and disorganised bone resorption in the epiphysis. Inflammation was not identified in synovium of either CD59a$^{-/-}$ or WT mice. The articular cartilage of the joint was replaced by bone and aberrant endochondral ossification and osteophyte formation was observed. These features are characteristic for OA.

This evidence allowed constructing the hypothesis that CD59a$^{-/-}$ mice have an osteoarthritic bone phenotype. Currently no treatments are available to inhibit the development of osteoarthritis (Wang *et al.* 2011) therefore the following research question arose: Would CD59 be suitable for osteoarthritis treatment? In order to investigate the hypothesis 4 specific aims were derived which are investigated in the following chapters.

Aim 1: Determining the role in OB differentiation and maturation.

Aim 2: Assessing the impact of CD59a on OCG.

Aim 3: Investigating the role of human CD59 in resorption assays.

Aim 4: Phenotypic analysis of bone structure in CD59a$^{-/-}$ mice.

Chapter 2

Materials and Methods

2.1 Materials

Acids and solvents were obtained from Fisher Scientific. Other reagents were supplied by Sigma-Aldrich unless stated otherwise. A comprehensive, alphabetical list of suppliers is provided in **Appendix 1**.

2.2 Solutions

A number of solutions, stains and buffers were used throughout the thesis, they are listed alphabetically below:-

(i) Acetate Solution - 3.5 ml Sodium acetate (1.64 mg/ml (w/v)), 1.5 ml glacial acetic acid (1.5% (v/v)) were added to distilled water (dH_2O) to a final volume of 10 ml.

(ii) Alkaline Phosphatase (ALP) stain – 3.34 µl BCIP solution (see *(ix)*) and 4.4 µl NBT solution (see *(xxxvi)*) were added to 2-Amino-2-hydroxymethyl-propane-1,3-diol buffered hydrogen chloride (Tris-HCl) solution (see *(lii)*) to a final volume of 1 ml.

(iii) Alizarin red - The stain (10 g/l (w/v)) was prepared in dH_2O at pH 4.2. The solution was filtered (Fisherbrand QT 260 filter paper (Fisher)) before use.

(iv) Ammonium persulfate solution - A fresh solution (10%, w/v) was prepared every time by dissolving Ammonium persulfate in dH_2O.

(v) Ampicillin plate - Autoclaved lysogeny broth (see below) containing ampicillin (Fisher Scientific, 50 mg/ml (v/v)) and Ultrapure-agar (Invitrogen, 3.75 g) was poured into sterile Petri-dishes before surfaces were flamed to keep aseptic.

(vi) Aniline blue acid – Aniline blue (0.3 mg/ml) and Phosphotungstic acid (10 mg/ml) were dissolved in dH_2O.

(vii) l-ascorbic acid 2-phosphate sesquimagnesium salt hydrate (ASP) stock solution – ASP (12.5 mg/ml (w/v)) was prepared in sterile phosphate buffered saline (PBS, Invitrogen) and stored at -20°C.

(viii) Assay buffer – A solution of Bovine serum albumin (BSA, 1% (w/v)) was prepared by dissolving BSA in PBS (see (*xliii*), pH 7.3) containing Tween 20 (0.05% (v/v)).

(ix) 5-bromo-4-chloro-3 indolyphosphate (BCIP) solution - BCIP (75 µg) was diluted in 1 µl of dimethylformamide (DMF from Fisher, 70% (v/v)).

(x) Buffer A - A solution of Tris-HCl (100 mM, pH 7.4) was prepared in dH_2O that contained calcium chloride ($CaCl_2$, 5 mM).

(xi) Buffer B – A Sodium acetate (NaOAc, 50 mM) solution (pH 5.5) was prepared, ethylenediaminetetraacetic acid (EDTA, 2 mM), Dithiothreitol (DTT, 2 mM), NaCl (350 mM) and chondroitin 4-sulfate sodium salt (0.15% (w/v)) were then added.

(xii) Buffered formalin - A stock solution (4% (v/v)) of tissue fixative was prepared by adding 100 ml Formaldehyde solution (37%) to 900 ml of PBS (see *(xliii)*, pH7.3).

(xiii) Blocking buffer – BSA (1% (w/v)) was dissolved in PBS (see *(xliii),* pH7.3).

(xiv) Calcein solution – Calcein (1.75 mg/ml) was dissolved in sterile PBS containing sodium bicarbonate ($NaHCO_3$, 2% (w/v)).

(xv) Citrate buffer - Hydrogen peroxide (H_2O_2, 1 µl/ml (v/v)) was mixed with citric acid solution (42 g/l (w/v), pH 3.95) immediately before use.

(xvi) Chloramphenicol plate – Bacto-tryptone (BD Biosciences, 10 g), Bacto-yeast extract (Merck, 5 g), Ultrapure-agar (15 g) were prepared in 1 l sucrose solution (see *(xlviii)*, 5%). Solution was autoclaved, cooled and chloramphenicol (12.5 µg/ml), 5-bromo-4-chloro-3-indolyl β-D-galactoside (X-gal, 80 µg/ml) and isopropyl-beta-D-thiogalactopyranoside (IPTG, 200 µM) were added. Plates were poured into sterile Petri-dishes under aseptic conditions.

(xvii) Col1 (calf skin) – A stock solution of Col1 (2.5 mg/ml (w/v)) was prepared in acetic acid solution (50 mM) with agitation over night. The solution was buffered with Tris (1.5 M) to pH 8.8 and a concentration of 2 mg/ml.

(xviii) Collagenase (Clostridiopeptidase A) Type I - A stock solution of collagenase (1mg/ml (w/v)) was prepared in dH_2O.

(xix) Complete medium for HEK 293T cells – Heat-inactivated foetal calf serum (FCS from Lonza, 10% (v/v)), penicillin-streptomycin (Gibco, 50 units/ml - 50 µg/ml),

sodium pyruvate (1mM) and L-glutamine (Gibco, 2 mM) were added to Dulbecco's modified eagle medium (Invitrogen).

(xx) Complete medium for human cell cultures - Heat-inactivated FCS (Biosera, 10% (v/v)), penicillin-streptomycin (Gibco, 50 units/ml - 50 µg/ml) and L-glutamine (Gibco, 2 mM) were added to Roswell Park Memorial Institute 1640 basal medium (RPMI, Invitrogen).

(xxi) Complete medium for murine cell cultures – α-minimum essential medium (αMEM, Invitrogen, 100 g) and $NaHCO_3$ (2.2 g) were dissolved in dH_2O to a final volume of 10 l. The solution was sterile filtered (0.22 µm pore size) and autoclaved before use. Penicillin-streptomycin (Lonza) was added to the medium to achieve a final concentration of 50 units/ml/ 50 µg/ml (v/v), and heat-inactivated FCS (Lonza) was added to the medium for a final concentration of 10% (v/v) for OC cultures whereas the treatment for FCS in OB cultures varied.

(xxii) Dexamethasone (DEX) stock solution – DEX (10 mM) was prepared in ethanol (100%). This was used as stock solution for CFU-AD medium. The solution was further diluted to 0.5 mM in sterile PBS as a stock solution for CFU and mineralisation medium. All stock solutions were aliquoted and stored at -20°C.

(xxiii) Eosin solution - Eosin tetrabromo fluorescein 225 (Fisher Scientific, 1% (w/v)) was prepared in dH_2O.

(xxiv) FACS buffer - FCS (2% (v/v)) was dissolved in PBS (see *(xlii)*, pH 7.3).

(xxv) Giemsa stain – This commercially available stain was diluted (1:10) using PBS (see *(xlii)*, pH 6.8) to a final concentration of 0.04% (v/v).

(xxvi) Glacial acetic acid solution – Glacial acetic acid (2% (v/v)) was prepared in dH_2O.

(xxvii) Glutaraldehyde solution – A fresh solution (40% (v/v)) was prepared in dH_2O.

(xxviii) Glycerol buffer – Glycerol (65% (v/v), Mg SO_4 (0.1 M) and Tris-HCl (0.025 M, pH 8) were prepared in dH_2O.

(xxix) β-Glycerophosphate (βGP) stock solution - βGP (1 M) was dissolved in sterile PBS and stored at -20°C.

(xxx) Indomethacin stock solution – Indomethacin (50 mM) was dissolved in ethanol (100%) and stored at -20°C.

(xxxi) Insulin stock solution – Insulin (2 mg/ml (w/v)) was prepared in glacial acetic acid (1% (v/v)) and stored at -20°C.

(xxxii) 3-isobutyl-1-1methylxanthine (IBMX) stock solution – IBMX (1 M) was dissolved in warm dimethyl sulfoxide (DMSO, 100%) and stored at -20°C.

(xxxiii) Kodak GBX developer and replenisher solution – The reagent was diluted 1:5 in tap H_2O.

(xxxiv) Kodak GBX fixer and replenisher solution – The reagent was diluted 1:5 in tap H_2O.

(xxxv) Lysogeny Broth (LB) medium - Bacto-tryptone (BD Biosciences, 10 g), Bacto-yeast extract (Merck, 5 g) and NaCl (10 g) were dissolved in dH_2O and the pH was adjusted to 7 before further dilution in dH_2O to 1 l. The mixture was then autoclaved.

(xxxvi) Nitro blue tetrazolium (NBT) solution - NBT (50 µg) was dissolved in 1µl of DMF (100% (v/v)).

(xxxvii) MACS buffer - A solution was prepared containing BSA (0.5% (w/v)) and EDTA (2 mM) in sterile PBS.

(xxxviii) May-Grünwald - The stain, which is commercially available, was diluted (1:2) in PBS (see *(xliii)*, pH 6.8) to a final concentration of 0.2% (w/v).

(xxxix) Milk buffer - Fat free milk powder (5% (w/v)) was dissolved in PBS (see *(xliii)*, pH 7.3).

(xl) Mount for resin sections - AnalaR Normapur saccharose (VWR, 100 g), gum Arabic (100 g) and Thymol (1 crystal) were added to 120 ml of dH_2O. The mixture

was dissolved in a water bath (80°C), centrifuged briefly and stored in 5 ml syringes at 4°C.

(xli) Oil red O stock solution - Oil red O (0.5 g) was dissolved in isopropanol (Fluka) to a final volume of 100 ml. The solution was stored away from light at room temperature.

(xlii) Oil red O working solution – A fresh solution was prepared every time by diluting Oil red O stock (see *(xli)*) 1:1.5 in dH_2O. The solution was stirred for 15 min and filtered before use.

(xliii) Phosphate buffered saline (PBS) - One tablet PBS (Oxoid, pH 7.3) was dissolved in 100 ml of dH_2O. For Giemsa staining only, one tablet of PBS (Merck, pH 6.8) was dissolved in 100 ml of dH_2O.

(xliv) Refolding buffer - Triton x100 (2.5% (v/v)) was diluted in dH_2O.

(xlv) Resin solution - Dibuthyl phthalate (10 g), Perkadox 16 (Akzo Nobel, 1 g) and Novoscave (Novochem, 0.01 g) were dissolved in methyl-methaxcrylate (MMA, 89 ml).

(xlvi) Silver nitrate stock solution – Silver nitrate (15% (w/v)) was diluted in dH_2O and stored away from light.

(xlvii) Sodium dodecyl sulphate (SDS) solution – SDS (10% (w/v)) was diluted in dH_2O.

(xlviii) Sucrose solution – 50 g sucrose was added to 1 l of dH_2O before being dissolved at 37°C for 30 min.

(xlix) Tartrate Resistant Acid Phosphatase (TRAP) stain 1 – 5 ml acetate solution (section 2.2, *(i)*), 1 ml sodium tartrate (0.3 M), 100 µl naphthol AS-MX phosphate disodium salt (10 mg/ml) and 10 µl Triton X-100 were added to 4.39 ml dH_2O. The buffer was incubated at 37°C for 15 min before fast red violet LB (3 mg) was added and kept at 37°C until used.

(l) TRAP stain 2 – 140 mg naphthol AS-TR phosphate (Apollo) was dissolved in 500 µl N-N dimethyl formanide. 100 ml sodium acetate (0.2 M, pH 5.2) was added and 230 mg sodium tartrate dehydrate. Finally, 140mg fast red salt TR were dissolved in the solution.

(li) 3,3'5,5' Tetramethybenzidine (TMB) solution - TMB (240 mg) was dissolved in 10 ml DMSO-ethanol solution (5 ml DMSO was added to 5ml ethanol).

(lii) 2-amino-2-hydroxymethyl-propane-1,3-diol buffered hydrogen chloride (Tris-HCl) solution – Tris-HCl (100 mM, pH 9.5), sodium chloride (NaCl, 100 mM) and magnesium chloride ($MgCl_2$, 5 mM)) were prepared in dH_2O.

(liii) Tris-acetate-EDTA (TAE) buffer - Tris (40 mM), Acetic acid (20 mM), EDTA (2.5 mM), Ethidium Bromide (0.0005% (v/v)) were prepared in dH_2O.

(liv) Trypsin-EDTA (TE) buffer - Trypsin-EDTA, which is commercially available as 0.5% solution (Gibco), was diluted to 1:2 or 1:10 in sterile PBS (pH 7.3).

(lv) Trypan Blue solution – Trypan Blue (0.4% (w/v)) was prepared in PBS (see *(xliii)*, pH 7.3) and filtered before use.

(lvi) Wash buffer – Tween-20 was diluted in PBS (see *(xliii)*) to achieve a final concentration of 0.05% (v/v) at pH 7.3.

(lvii) Western blot transfer buffer - Glycine (2.93 g), Tris (5.81 g), SDS (0.375 g) and methanol (200 ml) were made up to 1 l in dH_2O.

(lviii) Zymography destain – Methanol (450 ml) and glacial acetic acid (100 ml) were prepared in dH_2O to a final volume of 1 l.

(lix) Zymography digestion buffer A – DTT (2.5 mM) and EDTA (2.5 mM) were added to NaOAc solution (50 mM, pH 5.5).

(lx) Zymography digestion buffer B – Tris-HCl (50 mM, pH 7.4), $CaCl_2$ (5 mM), NaCl (120 mM) and Triton X-100 (2.5% (v/v)) were prepared in dH_2O.

(lxi) Zymography digestion buffer C – Tris-HCl (50 mM, pH 8), NaCl (50 mM), $CaCl_2$ (10 mM) and Triton X-100 (2.5% (v/v)) were prepared in dH_2O.

(lxii) Zymography loading buffer – Tris-HCl (70 mM, pH 6.8), glyerol (10% (v/v)), SDS (2% (w/v)) and bromophenol blue (0.001% (w/v)) were prepared in dH_2O.

(lxiii) Zymography running buffer - Tris (3 g), glycine (14.4 g) and SDS (1 g) were dissolved in dH_2O to a final volume of 1 l at pH 8.3.

(lxiv) Zymography stain - Brilliant blue R Coomassie (0.25% (w/v)) was dissolved in zymography destain (see *(lviii)*).

(lxv) Zymography wash buffer A - NaOAc (50 mM, pH 5.5), NaCl (100 mM), cysteine (10 mM) and Triton X-100 (2.5% (v/v)) were prepared in dH_2O.

(lxvi) Zymography wash buffer B – Tris-HCl (50 mM, pH 7.4), $CaCl_2$ (5 mM) and NaCl (120 mM) were prepared in dH_2O.

(lxvii) Zymography wash buffer C – Tris-HCl (50 mM, pH 8), NaCl (50 mM) and $CaCl_2$ (10 mM) were prepared in dH_2O.

2.3 Determining the Role of CD59a in Osteoblast Differentiation and Maturation

The main aim of this chapter was to identify the effect of CD59a on osteoblast (OB) differentiation and mineralisation. Before this could be established, an *in vitro* differentiation assay was developed. Firstly a source of OBs had to be determined. For the purpose of these experiments and because of the availability of gene deficient mice, murine primary mesenchymal stem cells (MSCs) and OBs were used to specifically examine the function of CD59a. OBs are commonly extracted from explants of the calvaria and MSCs or OBs from long bones (Hu *et al.* 2009). In this study explants and bone marrow cultures were prepared from long bones and compared to each other. Varied culture conditions, such as cell concentrations and time courses, were investigated to decide on the best method to test the hypothesis that CD59a regulates OB differentiation and mineralisation.

2.3.1 Animals and Housing

CD59a$^{-/-}$ mice that were used in this thesis were bred onto a C57BL/6J background (more than eight generations). They were kindly supplied by Prof B Paul Morgan (Holt *et al.* 2001; Bhole and Stahl 2004). WT C57BL/6J mice were purchased from an in-house colony that was maintained by Dr Awen Gallimore. The colonies were kept in the Joint Biological Service Unit (Cardiff University). All animals were held in conventional housing at stable temperature and humidity on a 12 h light/dark cycle with food and water available *ad libitum*.

2.3.2 Tissue Culture Materials

The following tissue culture consumables were utilised in this thesis:-

(i) Nunc tissue culture plates (12 wells) and Nunc tissue culture flasks (25 cm^2 and 75 cm^2). They were purchased from VWR.

(ii) Petri-dishes were purchased from Fisher Scientific.

(iii) BD falcon tubes (15 ml and 50 ml) were purchased from SLS.

(iv) Universal tubes (20 ml) and Eppendorfs (0.5 ml and 1.5 ml) were bought from Greiner.

(v) Syringes (5 ml) and 21-gauge hypodermic needles were purchased from BD Pharmingen.

All cell cultures were kept in a humidified atmosphere at constant temperature (37°C) with a regulated supply of CO_2 that was maintained at 5% in air.

2.3.3 Establishment of Bone Cell Cultures and a Mineralisation Assay

To prepare for mineralisation assays, MSCs and OBs first had to be harvested, expanded and finally seeded onto plates containing medium that induced differentiation and mineralisation. Bone marrow and explant cultures were prepared from male mouse bones. All animals were killed by Schedule I method. Both femora and humeri were dissected and stored dry in a 20 ml universal tube on ice prior to isolation of the bone marrow cells.

To obtain MSCs from the bone marrow, the top of each bone was cut open under aseptic conditions and transferred into a sterile 0.5 ml Eppendorf with the open end facing down (a 2 mm^2 hole was cut in the bottom of each Eppendorf). The 0.5 ml Eppendorf was fitted into a 1.5 ml Eppendorf as shown in Fig. 2.1.

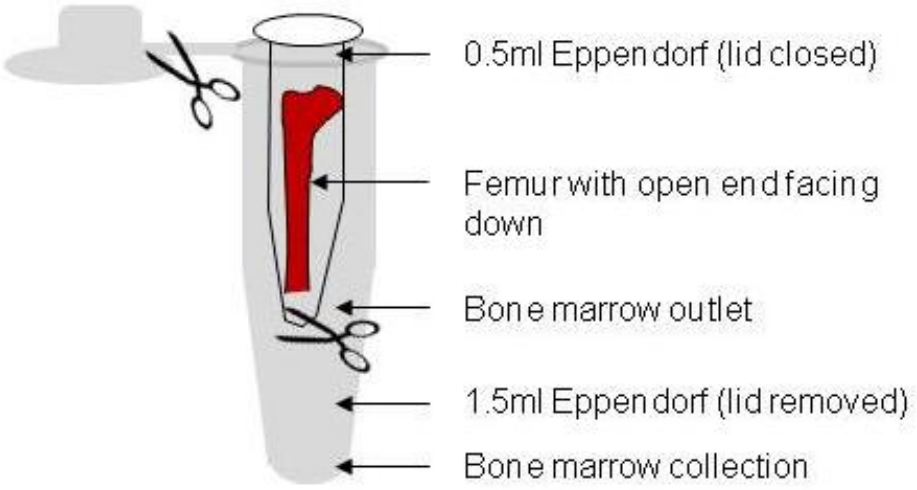

Figure 2.1 Eppendorf assemblies for bone marrow harvesting. Diagram showing the protocol for bone marrow extraction.

The tube assembly was centrifuged at 3,000 x g for 1 min in a conventional tabletop micro-centrifuge. The resultant bone marrow pellet was collected in the base of the 1.5 ml Eppendorf. The bone marrow from each mouse was pooled (femora and humeri) into a single 1.5 ml Eppendorf by recurrent resuspension in 1 ml complete medium for murine cell cultures (section 2.2, *(xxi)*). A single cell suspension was generated by careful and repeated mixing in a 5 ml syringe fitted with a 21-gauge hypodermic needle.

Once the bone marrow was removed, explants from both femora and humeri were used as source of OBs. For this, cartilage was discarded from subchondral bone and bone fragments were placed into a Petri-dish containing sterile PBS. Shafts were separated from all other bone components and transferred into a

separate Petri-dish. This was required as the growth plate containing fragments accommodated stem cells and chondrocytes which did not provide pure OB cultures.

All bone fragments (from shaft and epiphysis/metaphysis) were cleaved into explants (maximum length of 3 mm) and placed in 1.5 ml Eppendorfs with sterile PBS. Solutions were agitated thoroughly to remove bone marrow cells still attached to the bone, which was visible as red staining. To remove unwanted cellular debris Eppendorfs were centrifuged at 3000 x g briefly. Explants were collected at the bottom, the solution was discarded and fresh PBS was added. This washing procedure was repeated until all bone fragments appeared white.

2.3.3.1 Bone Cell Cultures

Once bone marrow and explants were prepared, they were set up to test cell number, cell source, FCS treatment, β-Glycerophosphate (βGP, section 2.2, *(xxix)*) concentration and a time course. For this, cells were expanded in 25 cm^2 or 75 cm^2 flasks containing 4 or 10 ml medium supplemented with FCS that was tested untreated and heat-inactivated (56°C for 30 min) (Tab. 2.1).

Test condition	Cell source	Flask size in cm^2	FCS
Cell density/ Cell source	Bone marrow	2x25	Untreated
	Shaft explants		
	Epiphysis/metaphysis explants		
FCS/ βGP supplementation	Bone marrow	1x75	Untreated
			Inactivated
Time course	Bone marrow	2x75	Inactivated

Table 2.1 Testing parameters of proliferation.

If multiple flasks were used for the same condition then cells and explants were equally split. Explants also had to be spread evenly throughout the flask with a sterile pipette tip.

Fresh complete medium for murine cell cultures was added after 3 days to allow MSCs to proliferate and non-adherent cells to be removed. Explant cultures were left undisturbed for 6 days to enable cells from the bone surface to proliferate onto the plastic. In both conditions, medium was then changed every 3 to 4 days until confluence was reached (7-14 days). MSCs and their progeny were identified as elongated to spindle-shaped cells that were termed confluent when all cells were touching as illustrated in Fig. 2.2. Once 100% confluence was reached cells were passaged or processed for mineralisation assays.

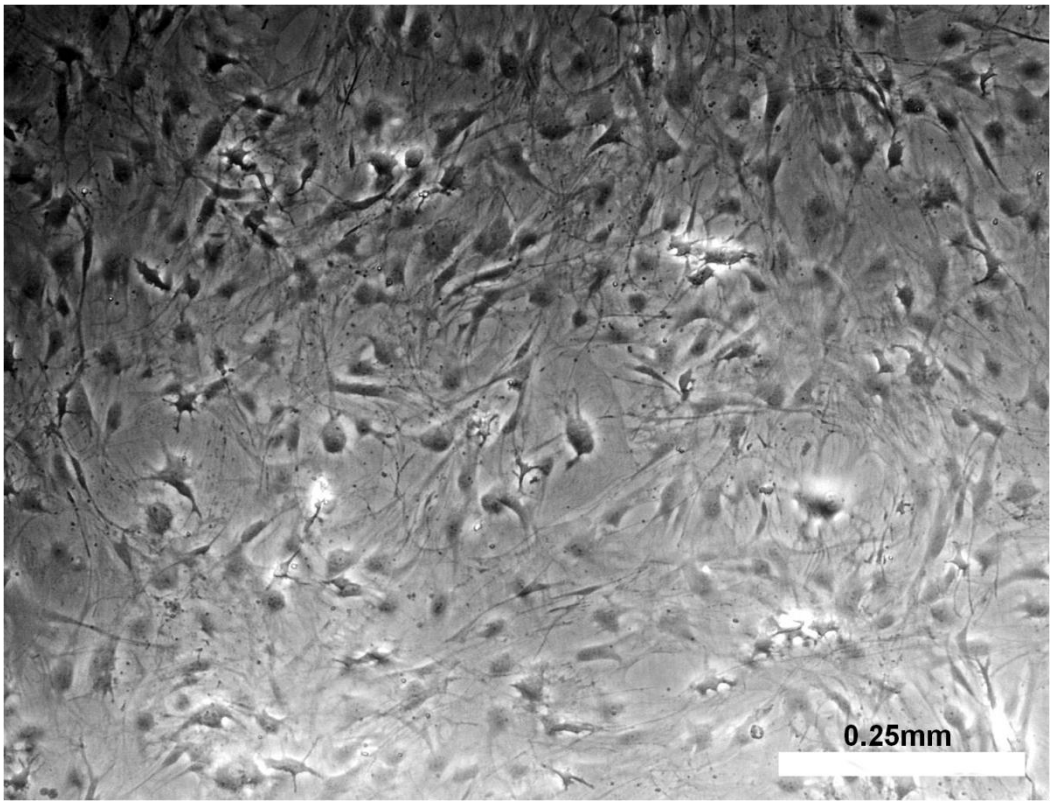

Figure 2.2 Illustration of confluent MSCs under the inverted microscope.

2.3.3.2 Establishing Conditions for a Mineralisation Assay

Expanded MSCs and OBs were plated to establish appropriate cell densities, supplements and time course of mineralisation (Tab. 2.2).

Test condition	Cell source	Passage	FCS	β-GP [mM]	Cells/well
Cell density	Bone marrow	Primary	Untreated	10	$1x10^4$
					$2x10^4$
		1			$3x10^4$
					$4x10^4$
Cell source	Bone marrow	1	Untreated	10	$4x10^4$
	Explants (shaft and epiphysis/metaphysis)		Untreated		$4x10^4$
FCS supplementation	Bone marrow	Primary	Untreated	10	$4x10^4$
			Inactivated		
β-GP concentration	Bone marrow	Primary	Inactivated	2	$4x10^4$
				10	
Time course	Bone marrow	Primary	Inactivated	10	$4x10^4$

Table 2.2 Testing parameters of to obtain mineral deposition.

As MSCs adhered strongly they were detached from the plastic flask using the following method. Medium was removed and cells were washed with 1 ml PBS. Trypsin-EDTA (0.25%) was utilised as dislodgement reagent by adding 300 µl or 500 µl per (25 cm^2 or 75 cm^2) flask. The solution was distributed to cover the bottom of the flask and incubated at 37°C for 3 min before agitation at room temperature until the majority of cells were detached as observed microscopically. Complete medium for murine cell cultures (1 ml) was added to each flask to dilute out and block Trypsin-EDTA. The cell suspension was transferred into a universal tube and flasks were washed with 1 ml complete medium for murine cell cultures to collect all dislodged cells. The solution was transferred into the same universal tube already containing detached cells and centrifuged at 300 x g for 5 min to collect cells. Supernatant was discarded and cells were re-suspended in 1 ml complete medium for murine cell cultures.

Initially an aliquot was diluted 1:2 in trypan blue solution (section 2.2, *(iv)*) to observe and quantify viable cells utilising the haemocytometer as explained in Fig. 2.3. In this method, only dead cells are able to take up the stain and were excluded from the haemocytometer count. Cell concentration was determined according to the formula stated in Fig. 2.3. In further experiments cells were diluted 1:2 in complete medium for murine cell cultures to calculate cell density.

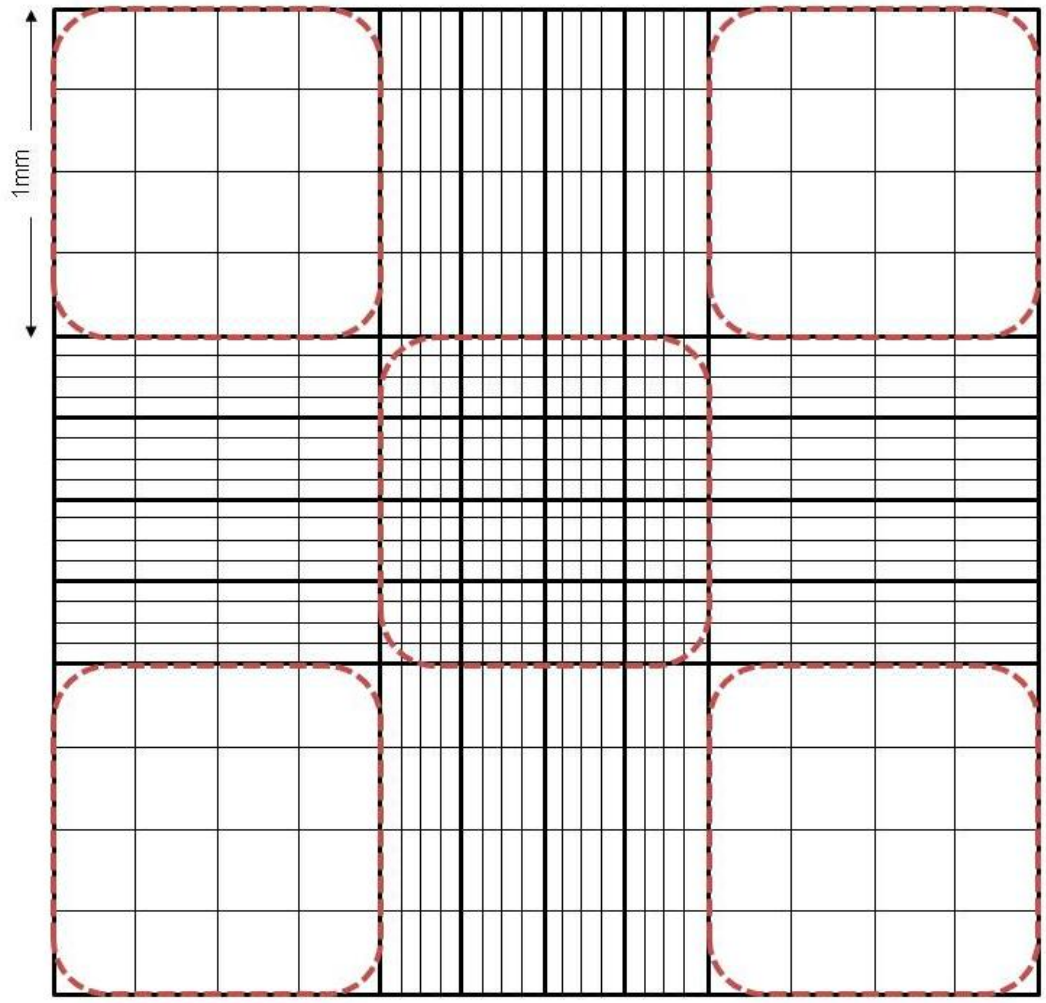

$$\text{Cells/ml} = \left(\frac{\text{Total number of cells counted}}{\text{number of 1mm}^2 \text{ squares counted}} \right) \text{x dilution x } 10^4$$

Figure 2.3 Demonstration of haemocytometer grid. Diagram illustrating square for counting procedure. The outer and centre squares were counted as indicated by the dashed lines. Cells touching the top and left line were included in the count, whereas cells touching the right or bottom line were excluded. Between 20 and 50 cells were counted per square. If the variation between squares was greater than 20%, the cells were re-suspended and the count repeated. Once counted, cell concentration was determined. Each square has an area of $1mm^2$ and a depth of 0.1 mm; therefore the space holds 0.1 µl (Sigma-Aldrich 2010). The cell concentration was calculated according to the equation displayed.

The cell concentration was adjusted according to the requirements of each mineralisation assay, as described in Tab. 2.2. Diluted cell suspension (1 ml) was added to each well of a 12 well plate and each condition was tested in triplicates.

Plated cells were left to adhere overnight before medium was discarded and replaced by complete medium for murine cell cultures supplemented with dexamethasone (DEX, stock solution described in section 2.2., *(xxii)*, 10 nM), l-ascorbic acid 2-phosphate sesquimagnesium salt hydrate *(*ASP, stock solution described section 2.2., *(vii)*, 50 µg/ml) and the appropriate βGP concentration. This day was defined as day 0. Fresh mineralisation medium was added every 3 to 4 days and mineralisation was observed microscopically as brown precipitate resting on top of cells. Cells were left to differentiate for up to 28 days. Alizarin red staining was used to identify the development of mature OBs within each well (section 2.3.3.3).

Cells that were not plated were cultured further to passage one. For this, bone marrow derived cells were added into 25 cm^2 flasks containing complete medium for murine cell cultures. Explants were left in flasks after trypsin-EDTA digest and supplemented with fresh medium to allow for further cell expansion.

2.3.3.3 Identification and Quantification of Mineralisation

Alizarin red was used to stain for OBs, it binds to the hydroxyapatite deposited by OBs in culture. Alizarin red staining was performed on day 10, 14, 17, 21, 24 and 28. Briefly, cells were washed with PBS (section 2.2, *(xliii)*, 1 ml/well), fixed in buffered formalin (section 2.2, *(xii)*, 1 ml/well) for 15 min and washed in dH_2O (1 ml/well). Alizarin red (section 2.2, *(iii)*, 0.5 ml/well) was added to each well for 5 min, then non-specific unbound stain was removed by washing in 50% ethanol (5x). The last wash was incubated for 15 min at room temperature. Finally all stained wells were left to dry.

Plates were transferred into a Hewlett-Packard (HP) scanner to obtain high resolution images (600 dpi). The amount of Alizarin red staining per well was determined by utilising Coral Paint Shop Photo ProX3 (ProX3), where a greyscale was applied and Image J software to quantify the total area of stain per well for each condition.

2.3.4 Establishment of a Colony Forming Unit Assay

The next objective was to determine the ability of bone marrow cells to establish colony forming units (CFU) of cells entering the OB fate. Bone marrow cells were harvested as described in section 2.3.3. An aliquot (10 µl) of the cell suspension was diluted 1:100. A high number of erythrocytes were identified which were then lysed by a 1:2 dilution in glacial acetic acid solution (section 2.2, *(xxvi)*). Haemocytometer counts were performed as described in section 2.3.3.2.

Bone marrow cells were diluted in complete medium for murine cell cultures to the appropriate cell concentrations (Tab. 2.3). Cells (1 ml/well) were added in triplicates to a 12 well plate and incubated overnight to adhere. Medium and non-adherent cells were discarded and replaced with the complete medium for murine cell cultures supplemented with DEX (10 nM) and ASP (50 µg/ml) to initiate cell differentiation. This day was defined as day 0. Fresh medium was added on day 3 and 7.

Test condition	Cells/well
Cell density	$2x10^5$, $4x10^5$, $8x10^5$
Time point	$8x10^5$, $1.2x10^6$
Evaluation of the quantification procedure	$1.2x10^6$

Table 2.3 Testing parameters of CFU.

2.3.4.1 Identification and Quantification of Cells Entering CFU

Alkaline phosphatase (ALP) staining was used to identify osteogenic lineage cells in cultures on day 7 and 10. For this, cells were rinsed in PBS (1 ml/well) and fixed in buffered formalin (1 ml/ml) for 15 min. This was followed by washing in dH_2O (1 ml/well) and cells were stained in ALP stain (see section 2.2, *(ii)*, 1 ml/well) overnight; storing plates in the dark at room temperature. Cells were washed in dH_2O (1 ml/well) and counter stained in Eosin solution (section 2.2., *(xxiii)*, 0.5 ml/well) for 90 s. Plates were washed with 1 ml/well dH_2O twice and left to dry.

Colonies were defined as ALP^+ if a cluster of 20 or more cells contained ALP stained (blue) cells (Vidal *et al.* 2007). These were microscopically counted for each well in turn. Plates were processed for quantification as described in section 2.3.3.3.

2.3.5 Quantification of CFU in WT and CD59a$^{-/-}$ Mice

After optimisation of CFU assays, bone marrow cultures from WT and CD59a$^{-/-}$ mice were examined for their differentiation potential. Bone marrow cells were harvested as described in section 2.3.3 and plated at $1.2x10^6$ cells/well. Cells were incubated for 10 days in complete medium supplemented with DEX (10 nM) and ASP (50 µg/ml) and medium was replaced on day 3 and 10. ALP^+ staining surface area was quantified as described in section 2.3.3.3.

2.3.6 Testing Reproducibility of Mineralisation in WT and CD59a$^{-/-}$ Mice

To evaluate the reproducibility of the established mineralisation assay, experiments were set up sequentially. For this, MCS from bone marrow (2 femora, 2 humeri and

2 tibiae) of WT and CD59$^{-/-}$ mice (n=7) were harvested and expanded in 2x75 cm^2 flasks per mouse as described in section 2.3.3. After confluence was reached MSCs were plated at 8x10^4 cells/well and were differentiated in complete medium for murine cell cultures supplemented with DEX (10 nM), ASP (50 µg/ml) and β-GP (10 mM) for 21 days. Mineralisation by mature OBs was identified utilising Alizarin red (section 2.3.3.3) and ALP (section 2.3.4.1) staining.

2.3.7 Comparison of CFU of Adipocytes in WT and CD59a$^{-/-}$ Mice

In order to assess whether changes identified in CFU are due to differential regulation of MSCs, adipocyte colony (CFU-AD) generation was tested. Bone marrow cells were harvested (section 2.3.3), plated (sections 2.3.5) and stimulated with complete medium for murine cell cultures supplemented with insulin (section 2.2, *(xxxi)*, 5 µg/ml), indomethacin (section 2.2, *(xxx)*, 50 µM), DEX (1 µM) and IBMX (section 2.2, *(xxxii)*, 0.5 µM) for 10 days according to Ripoll et al. (Ripoll and Bunnell 2009). Fresh medium was supplied on day 3 and 7.

2.3.7.1 Identification and Quantification of Adipocytes

Oil red O staining was utilised to identify lipid droplets of adipocytes. Cells were washed in PBS (1 ml/well) before fixation in buffered formalin (1 ml/well) for 10 min. This was followed by washing in dH_2O (1 ml/well) and staining in Oil red O working solution (section 2.2, *(xlii)*, 1 ml/well) for 15 min. Cells were washed in isopropanol (60% (v/v), 1 ml/well) and then in PBS (1 ml/well). Haematoxylin (300 µl/well) was utilised for counter staining before wells were washed with dH_2O (1 ml/well) and covered with sterile PBS (1 ml/well) for storage.

Plates were analysed immediately as lipids could not be identified once wells were dry. Lipids appeared as red droplets within cells and as only a small number of adipocytes were present, the methodology of Crisp et al. was adapted for my study (Crisp *et al.* 2000). Adipocytes were grouped according to their proximity as 1 adipocyte, colonies of 2-5 adipocytes or colonies containing more than 5 adipocytes.

2.3.8 Statistics

All statistical analysis was performed with Graphpad Prism software. A student T-Test was performed when comparing 2 unpaired groups. One-way ANOVA was utilised when studying more than 2 unpaired groups. Two-way ANOVAs were performed when assessing more than 2 groups with 2 independent variables respectively. Mean and standard error are stated throughout the result section.

2.4 Assessing the Impact of CD59a on Osteoclastogenesis

A number of precursor cells have previously been utilised for osteoclastogenesis (OCG) *in vitro*, including primary cells (such as bone marrow preparations or blood monocytes) (de Vries *et al.* 2009) and cell lines (such as RAW 264.7 cells) (Galal *et al.* 2007). Again, as genetically modified mice were available on site, bone marrow preparations were selected as an appropriate precursor cell source to test the working hypothesis. They were grown and differentiated into osteoclasts (OCs) in medium containing M-CSF and RANKL on glass coverslips. Phenotypic analysis was performed on OC generated from WT, CD59a$^{-/-}$ and C6$^{-/-}$ bone marrow preparations.

2.4.1 Animals and Housing

CD59a$^{-/-}$ and C6$^{-/-}$ mice on a C57BL/6J background were kindly supplied by Prof B Paul Morgan and WT mice were purchased as described in section 2.3.1.

2.4.2 Tissue Culture Materials

Nunc tissue culture plates (containing 24 and 96 wells) were purchased from VWR. Petri-dishes were obtained from Fisher Scientific. Round glass coverslips (6 mm and 13 mm diameter) and rectangular coverslips for microscopy (22x26 mm) were ordered from Knittel Gläser. The coverslips that were used for cell culture purposes were sterilised by soaking in ethanol (100%) and dried thoroughly before use. Other consumable and culture conditions are described in section 2.3.2.

2.4.3 Harvesting Bone Marrow Cells

Murine bone marrow cells were obtained from the femora of female and male 8-10 week old mice (WT, CD59a$^{-/-}$ and C6$^{-/-}$) as described in section 2.3.3. The bone marrow cell pellet was re-suspended in complete medium for murine cell cultures (up to 3 ml). A single cell suspension was generated by careful and repeated mixing in a 5 ml syringe fitted with a 21 gauge hypodermic needle. Glacial acetic acid solution was used at a 1:2 dilution to lyse red cells in the suspension. The cell suspension obtained from each femur was combined and cell concentration determined using a haemocytometer as depicted in Fig. 2.3. The concentration of the bone marrow cells was adjusted according to requirements of each OCG assay (section 2.4.4).

2.4.4 Optimisation of Murine OCG on Glass Coverslips

The first objective was to establish a reproducible method of OCG that allowed for accurate evaluation of OC function. In the preliminary experiments the following coverslip sizes, cell densities and RANKL concentrations were tested (Tab. 2.4).

Coverslip size (mm)	Cells/coverslip	Volume (µl)	RANKL [ng/ml]	Adherence
13	$3x10^5$ or $5x10^5$	500	2 or 5	Cell suspension added onto coverslip within 24 well plate
6	$6.4x10^4$	100	2	Cells suspension added onto coverslip within 96 well plate
6	$6.4x10^4$	10	2	Cell suspension added onto coverslip spread within Petri-dish

Table 2.4 Parameters that were tested during optimisation of OCG assays.

Bone marrow preparations were adhered at 37°C for 2 h in complete medium for murine cell cultures. The coverslips were then washed carefully to remove the non-adherent cells. One 13 mm coverslip or three 6 mm coverslips were transferred into 1 well of a 24 well plate containing complete medium for murine cell cultures (section 2.2, 500 µl) supplemented with M-CSF (R&D Systems, 25 ng/ml) and RANKL (R&D Systems, concentrations in Tab. 2.4). The OC culture supernatants were harvested on day 3 and stored for subsequent analysis, fresh differentiation medium was then added. Supernatants were also harvested on day 5 and day 7 (end point). All supernatants were stored at -70°C until needed for subsequent analysis (section 2.4.7). Tartrate Leukocyte Acid Phosphatase (TRAP) staining was used to identify OC on the coverslips (section 2.4.5.1).

2.4.5 Identification of Multinucleated OCs

A commercially available kit (Sigma) was utilised and the methodology used was as described in the manufacturer's instructions. Briefly, 0.25 ml citrate concentrate and 1.25 ml dH_2O were added to 3.75 ml acetone. Cells were fixed with 400 µl/well of the solution for 30 s. Cells were washed in dH_2O and wells were air-dried for 15 min. Meanwhile 0.4 ml acetate solution, 0.4 ml tartrate solution, 0.4 ml naphthol AS-BI phosphoric acid solution (12.5 mg/ml) and fast garnet (3 mg) were added to 8.8 ml of warm dH_2O. The staining solution was stirred for 60 s and filtered before use. Cells were stained (500 µl/well) in the dark at 37°C for 1 h and consequently washed in dH_2O for 3 min. This was followed by counter staining with 200 µl/well

haematoxylin acid for 5 min and washing in dH_2O twice. Glycerol gelatine was liquidised for mounting in a waterbath (100°C). Each coverslip was mounted onto a microscope slide (Menzel-Gläser).

OC were identified microscopically (x10 object magnification utilising an Olympus BX41 microscope with a Camedia C-3030 digital camera attached) on days 3, 5 and 7.

Finally, multinucleated $TRAP^+$ cells (containing 2 or more nuclei) were counted for each condition; these were defined as OCs. The definition of OCs varies in the literature, but the minimum number of nuclei for an OC lies in the range of 2 to 4 (Burgess *et al.* 1999; Shevde *et al.* 2000; Amoui *et al.* 2004). In accepting these criteria high number of OCs were counted in each field of view (FoV) and small changes could be monitored. The perimeters of the nuclei were defined by light maroon rings within the cells. Nucleoli (dark purple) were observed after the coverslips were gently counter-stained with haematoxylin.

2.4.5.1 Morphological Assessment of Bone Marrow Preparations on Day 0

The phenotype of the cell population within the bone marrow preparation at assay initiation was assessed as an internal control for the OC assays. Bone marrow preparations were stained with Giemsa/May-Grünwald on day 0 and differential cell counts were performed.

To obtain sufficient cell density for counting, bone marrow cells were initially adhered to a microscope slide using a cytospin. Briefly, bone marrow cells were diluted to $1x10^6$ cells/ml. The cell suspensions (100 µl) were pipetted into the cytospin megafunnels that were attached to a filter card and Shandon cytoslide (all Thermo Scientific). The megafunnel-cytoslide assembly was centrifuged in the Shandon Cytospin 3 (Thermo Scientific) at 115 x g for 10 min.

For all further experiments $6.4x10^3$ cells were seeded onto 6 mm coverslips. Slides and coverslips were left to air dry prior to staining.

2.4.5.2 Giemsa/May-Grünwald Staining Procedure

Cells were fixed in methanol (300 µl/well) for 15 min before being stained in May-Grünwald (section 2.2, *(xxxviii)*, 300 µl/well) for 15 min. The cells were then counterstained in Giemsa stain (section 2.2, *(xxv)*, 300 µl/well) for 15 min. Excess stain was removed by first washing in PBS pH 6.8 (section 2.2, *(xliii)*, 300 µl/well) and then in dH_2O (300 µl/well, 1 min in each solution). The stained cells were left to air-dry before they were mounted under a coverslip with a distyrene-plasticizer-xylene mixture (DPX, Fisher Scientific).

The following cell types and their precursors were identified and grouped using this staining procedure; erythrocytes (light pink cytoplasm, no nucleus), lymphocytes (small cells with a round dark purple nucleus), monocytes (U-shaped purple nucleus), mesenchymal stem cells (large round purple nucleus with one nucleolus, only present 0.01-0.001% of bone marrow population (Siemionow 2006)) and megakaryocytes (proportionally larger than other cells with lobed purple nucleus). Five random areas (at x40 object magnification) were selected on each coverslip, cells were counted and their phenotype noted.

2.4.6 Measuring CD59a Expression in OCG Assays Using Quantitative Polymerase Chain Reaction (qPCR)

Initially, locally produced antibodies (Professor B Paul Morgan's Complement Biology Group) were utilised to assess the level of CD59a expression on the surface of the bone marrow preparations. Unfortunately, and after numerous attempts, the antibodies failed to bind specifically to the murine cells. Antibodies were tested using flow cytometry and immunocytochemical methods and always provided unsatisfactory high background when compared against a relevant control antibody (data not shown). A qPCR method was therefore established as an alternative method to check CD59a expression in bone marrow preparations and on cells over the time course of the OCG assays.

2.4.6.1 RNA Extraction

WT bone marrow cells were recovered and the OCG assay initiated as described in sections 2.4.3 and 2.4.4. In order to assure that an adequate amount of RNA was recovered at each step of the OCG assay, $1.45x10^6$ bone marrow cells were plated on 22x26 mm coverslips in 1.5 ml complete medium for murine cell cultures. For these studies, 6 well plates were utilised as carriers for the coverslips. After a 2 h adherence step and washing, the cells were differentiated in complete medium for murine cell cultures containing M-CSF (25 ng/ml) and RANKL (2 ng/ml) for 7 days. Cell cultures were sampled on day 0, 1, 3, 5 and 7. RNA was extracted as described below.

All steps were performed in a clean room and all solutions and plastics were RNase free. Wells were washed with warm, sterile PBS before cells were lysed in ice-cold TRIzol reagent (Invitrogen, 500 µl/well). Cell lysis was supported by gentle agitation using a pipette. The resultant lysate was left at room temperature for 5 min before being transferred into 1.5 ml Eppendorfs (SLS, Safe-lock). Chloroform (230 µl/ml of lysate) was added, the contents of the Eppendorfs mixed and then left at

room temperature for a further 3 min to precipitate proteins. Meanwhile, heavy-phase lock gel Eppendorfs (SLS) were centrifuged at 12,000 x g for 30 s to pellet the gel. RNA containing aqueous extract was transferred onto the gel within the heavy-phase lock gel Eppendorf and centrifuged at 13,000 x g for 2 min as illustrated in Fig. 2.4. The upper aqueous phase was added to new Eppendorfs. Isopropanol (same volume as extract) was mixed into each Eppendorf and RNA was precipitated at -20°C for 20 min. After thawing, solutions were centrifuged at 12,000 x g at 4°C for 10 min. Supernatants were discarded and pellets washed with 750 µl of 75% ethanol. Pellets were dislodged by carefully mixing before centrifugation at 7,500 x g at 4°C for 5 min. Supernatants were removed and pellets were air-dried before resuspension in 200 µl of RNAse free H_2O (Promega). Eppendorfs containing RNA were heated to 65°C for 5 min (to help re-suspend the RNA pellet), vortexed and incubated on ice for 1 h. RNA concentration (260 nm) and purity (260/280 nm) was measured with the nanodrop (NanoVue, GE Healthcare). If the concentration was less than 100 ng/µl the following steps were performed. Total RNA was ethanol precipitated for storage by addition of 1 µl of Ambion glycogen (Invitrogen, 5mg/ml), $1/10^{th}$ of the total volume of sodium acetate (3 M, pH 5.2) and 2.5 volumes of ethanol (100%). Samples were allowed to precipitate at -80°C for at least 1 h. Precipitates were collected by centrifugation at 12,000 x g at 4°C for 20 min, washed with 80% ethanol and re-centrifuged at 12,000 x g at 4°C for 10 min. Pellets were air-dried and reconstituted in an appropriate volume of nuclease-free H_2O.

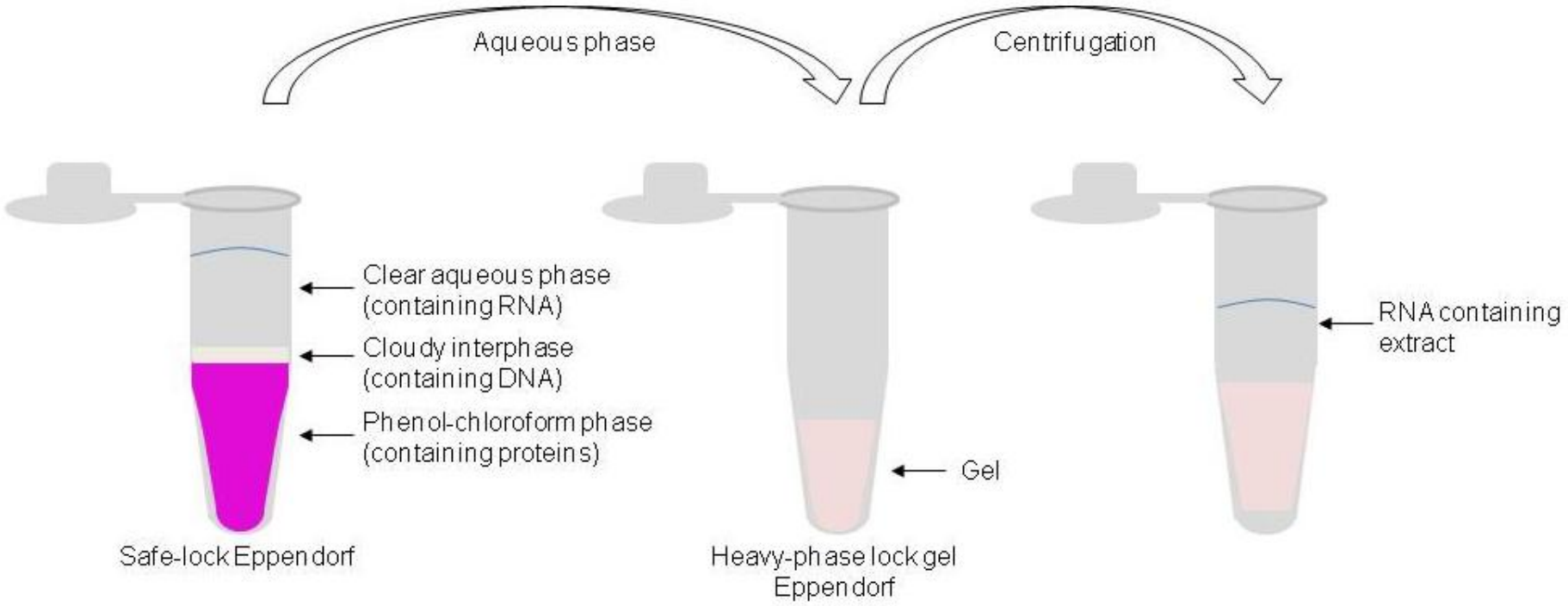

Figure 2.4 Demonstration of RNA purification.

2.4.6.2 Reverse Transcription

Extracted RNA was processed to generate complementary deoxyribonucleic acid (cDNA). cDNA was produced via a reverse transcription reaction on the Gene Amp PCR System 9700 (Applied Biosystems) using the Superscript II TM Reverse Transcriptase (Invitrogen) with the following 2-step protocol for high cDNA yield. Firstly 1 µl of Oligo (deoxy-thymine nucleotides (dT)) Primer (0.5 µg/µl; Promega), 1 µl of deoxy-nucleotide-tri-phospates (dNTPs, 10 mM; Promega) and 1-5 µg RNA were mixed to a final volume of 13.5 µl in RNase free dH_2O. The solution was incubated at 65°C for 5 min to denature RNA, chilled on ice and centrifuged briefly at 3,000 x g to pool the contents to the bottom of the tube. Subsequently 4 µl first strand buffer and 2 µl DTT were added and the solution incubated at 42°C for 2 min to optimise conditions for the enzyme. Each reaction was started by addition of 0.5 µl Superscript II TM Reverse Transcriptase and was incubated at 42°C for 50 min to generate cDNA. The temperature was raised to 95°C for 2 min to inactivate the enzyme. Solutions were chilled on ice again and centrifuged as before. The temperature was returned to 42°C for 2 min before adding fresh 0.5 µl Superscript II Reverse Transcriptase. Reactions were incubated at 42°C for an additional 50 min and Superscript II Reserve Transcriptase was heat inactivated at 70°C for 15 min. Finally cDNA was cooled to 4°C and stored at -20°C.

2.4.6.3 Primer Design

In order to amplify cDNA present in the sample and identify CD59a expression, primer sequences unique to the cDNA molecules had to be designed. A sequence for a probe was also required as the TaqMan method (Invitrogen) was utilised. The probe contains a fluorophore and a quencher. It attaches to the cDNA and is degraded by the polymerase during transcription. This results in a fluorescent signal corresponding to the number of templates during qPCR. Primers and probes were designed with Oligo Primer Analysis Software 4.0 and ordered from BEurofins MWG Operon. Murine acid ribosomal phosphoprotein P0 (H36B4) was used as housekeeping gene. All primers and probes are as stated in Tab. 2.5.

Product	Sequence	Concentration [nM]
Primers for H36B4	5’ AGA TGC AGC AGA TCC GCA T 3’ 5’ ATA TGA GGC AGC AGT TTC TCC AG 3’	300 300
Probe for H36B4	5’FAM AGG CTG TGG TGC TGA TGG GCA AGA AC TAMRA 3’	100
Primers for murine CD59a	5’ GCT ACC ACT GTT TCC AAC CG 3’ 5’ GTC CAT AAT GAT CTC ACC ATG AC 3’	300 600
Probe for CD59	5’ FAM TCC TGT CTC TAT GCT GTA GCC GGA ATG C TAMRA 3’	150

Table 2.5 Primers and Probes for qPCR.

2.4.6.4 Quantification of CD59a

qPCR was performed on the Abi Prism 7000 (Applied Biosystems). CD59a primers were tested between 150 and 600 nM whereas probes were tested between 100 and 200 nM. The optimised concentrations are displayed in Tab. 2.5. For the reaction the TaqMan PCR core reagents kit was employed. AmpliTaq Gold was supplied with all required buffers and dNTPs and added to obtain the final concentrations stated in Tab. 2.6. The AmpErase UNG, which is supplied to protect from RNA amplification, but caused product degradation, was not used. Reactions (25 µl) containing forward and reverse primer, probe, TaqMan reagents and cDNA (1-100 ng) were prepared in duplicates. For each primer pair the control consisted of qPCR reactions lacking the cDNA component.

Component	Final Concentrations
x 10 TaqMan PCR Buffer	x 1
Deoxy-adenosine triphosphate (dATP)	200 µM
Deoxy-cytosine triphosphate (dCTP)	200 µM
Deoxy-guanine triphosphate (dGTP)	200 µM
Deoxy-uracile triphosphate (dUTP)	200 µM
$MgCl_2$	2 mM
AmpliTaq Gold DNA Polymerase	0.025 U/µL

Table 2.6 Concentrations of TaqMan components.

Solutions were pipetted into ABgene Thermo-Fast 96, semi-skirted plates (Thermo Scientific) and sealed with an adhesive PCR film (Thermo Scientific). The thermocyclic reaction to amplify cDNA products was as follows:

Initial denaturation:	95°C	10 min	
Denaturation:	95°C	15 s	x 40
Annealing/extension:	60°C	1 min	
Hold:	4°C		

Reactions were analysed with ABI Prism supplied software and cycle threshold (Ct) of H36B4 reactions were subtracted from CD59a reactions to obtain ΔCt value. One time point was then determined as 1 and all others were made relative to it by a further subtraction (ΔΔCt). These values were then used to calculate fold changes ($2^{-\Delta\Delta Ct}$).

2.4.7 Evaluation of Supernatants Harvested from OCG Assays

Cat K, MMP-9 and cytokine/chemokine concentrations were measured in the supernatants that had been harvested at each step of the OCG procedure. A number of techniques were adopted (enzyme-linked immunosorbent assays (ELISA), bioassay and zymography) to analyse the activity of the mediators.

2.4.7.1 Quantification of Cat K using an ELISA

Cat K is the major protease produced by OCs. It provides an indication of the functional activity of OCs as it is required to degrade the organic matrix of bone. In the first instance, an ELISA that was developed to quantify human Cat K (Biomedica) was tested. The manufacturer's datasheet stated that there was cross reactivity with rodent Cat K. The kit had been successfully utilised for rat samples (Wada *et al.* 2005) and was provided free of charge to evaluate my murine supernatants. A human recombinant Cat K source (300 pmol/l) from Enzo Life Sciences was included as positive control. The ELISA was performed according to manufacturer's instructions. Briefly, the assay was carried out at room temperature. Pre-coated microtitre strips were filled with 50µl/well of sample (neat) and standard (top standard = 300 pmol/l), 200 µl/well polyclonal anti-Cathepsin K-HRP was added and the solutions were incubated for 20 h in the dark. Strips were washed in wash buffer (section 2.2, *(lvi)*, x5) by adding 300 µl/well and all solution was removed. Substrate (200 µl/well) was dispensed and incubated for 30 min in the dark before terminating the reaction with stop solution (50 µl/well). Colorimetric change in the assay was measured at 450 nm using a Wallac Victor^2 microplate reader.

2.4.7.2 Development of a Cat K Bioassay

The objective was to develop a functional assay to assess Cat K activity in the supernatants harvested from the OCG. The bioassay for type I collagen (Col1) was

set up on the principal that if tissue culture plates were coated with known concentrations of Col1, then collagenase (contained within the OCG supernatants) would degrade the collagen, and the changes in collagen binding would be measured using a collagen-specific antibody. The detection principles of an ELISA could then be applied to measure the changes in collagen colorimetrically.

A 96 well ELISA plate was loaded with a solution of Col1 (section 2.2, *(xvii)*, 10 µg/ml, 50 µl per well). The plate was left at 4°C overnight; with gentle agitation to facilitate the coating process. The collagen solution was discarded and the plate was blocked with blocking buffer (section 2.2, *(xiii)*, 200 µl/well) for 1 h at room temperature. The plate was washed 5 times in wash buffer before adding the mouse monoclonal anti-collagen type I (bovine) antibody. A concentration of antibody was not given, but recommended dilutions were included in the dilution range tested (1:1,000 to 1:128,000). 100 µl of each dilution was added to each well and incubated (with agitation) at room temperature for 1 h. The plate was washed as before and the secondary antibody (anti-mouse IgG peroxidase conjugated) was loaded onto the plate (100 µl/well). A dilution range was also suggested by the manufacturer and consequently a number of dilutions were examined from 1:2,000 to 1:128,000. The plate was once more left at room temperature for 1 h. The colorimetric phase of the assay was triggered using streptavidin-horseradish peroxidase (R&D Systems). It was diluted in assay buffer (section 2.2, *(viii)*, 1:200); 100 µl of this solution was added to each well and left for 20 min at room temperature. After a final wash step, TMB solution (section 2.2, *(li)*) was diluted (1:100) in citrate buffer (section 2.2., *(xv)*). 100 µl of the solution was added to each well. After 10 min in the dark, a sufficient surface area of blue stain was achieved, the colorimetric reaction was then stopped by adding 12% sulphuric acid (100 µl/well). The optical density of each well was determined at 450 nm using a Wallac Victor^2 microplate reader.

Bacterial Clostridiopeptidase A (mixture of enzyme purified from *Clostridium histolyticum* bacteria that contains collagenases, section 2.2., *(xviii)*) was used as the reference collagenase standard for the bioassay. It was added in triplicate (100 µl/well) to collagen coated wells (top standard = 1,000 ng/ml) and a standard curve was plotted at end point to calculate absolute collagenase concentrations in each test sample.

In order to test the specificity of the bioassay, other collagenases were examined alongside Clostridiopeptidase A : -

(i) MMP-1 (105 µg/ml, kindly supplied by Dr Vera Knäuper, Dental School, Cardiff University). This enzyme is active at neutral pH, for this reason it was diluted in

Buffer A (section 2.2, *(x)*, pH 7.4) for optimal function in the bioassay (top standard = 500 ng/ml).

(ii) Human recombinant Cat K (23 µg/ml, Enzo Life Sciences). This enzyme is functional at low pH, for this reason it was diluted in Buffer B (section 2.2, *(xi)*, pH 5.5) for optimal function in the bioassay (top standard = 5000 ng/ml).

2.4.7.3 Analysis of Cat K by Col1 Zymography

Col1 zymography was also used as an alternative method to detect active Cat K in OCG supernatants. 4 ml of 30% Acrylamide/bis-Acrylamide solution (Bio-Rad), 1 ml Col1 stock solution and 2.5 ml Tris (1.5 M, pH 8.8), 0.1 ml SDS solution (section 2.2, *(xlvii)*) were added to 2.35 ml dH_2O to generate a 12% polyacrylamide gel. The mixture was inverted gently and supplemented with ammonium persulfate solution (section 2.2, *(iv)*, 50 µl) and tetramethylethylenediamine (TEMED, Bio-Rad, 20 µl) immediately before pouring to induce gel setting. The gel was pipetted carefully into a Mini-Protean electrophoresis casting system (Biorad), the assembly of which is demonstrated in Fig. 2.5. The gel mixture was not added to the top of the casting plates in order to leave space for the comb. A 10-well Teflon comb was inserted and trapped air was removed. The gel was left to set for 1 h before being removed from the holding device and secured in an electrode construction. The gel was immersed in running buffer (section 2.2, *(lxiii)*) within a Mini Protean II (Bio-Rad) tank (Fig. 2.5). The comb was removed and the wells were cleaned with running buffer. 5 µl of pre-stained SDS-polyacrylamide gel electrophoresis (PAGE) Broad Range Standards (Bio-Rad) or 10 µl of each sample (diluted to 80% (v/v) in loading buffer (section 2.2, *(lxii)*)) were loaded into each well. The electrophoresis apparatus was connected to a BioRad Model 500/200 Power Supply; the gel was run at 100 V for 90 min.

After electrophoresis the gel was removed from the tank and carefully transferred into a washing tray. The gel was incubated in refolding buffer (section 2.2, *(xliv)*, twice for 15 min) and rinsed in zymography wash buffer A or B (section 2.2, *(lxv)* and *(lxvi)*) according to Giusti et al. ; this step re-activated the collagenases in the samples (Giusti *et al.* 2008). The enzyme was finally left to degrade the substrate in the gel for 20 h in digestion buffer A or B (section 2.2, *(lix)* and *(lx)*) at 37°C.

To visualise the degraded areas of the gel, digestion buffer was discarded and zymography destain (section 2.2, *(lviii)*) was added to the gel for 10 min. It was then removed, replaced by zymography stain (section 2.2, *(lxiv)*) and incubated (with agitation) at room temperature for 60 min. Zymography destain was added to the gel once again until the blue colour was faded sufficiently to observe clear white

‘digested’ bands. Gels were rinsed in water and then placed onto filter paper and transferred into a *Hewlett-Packard* (HP) scanner whilst wet to obtain a high resolution image.

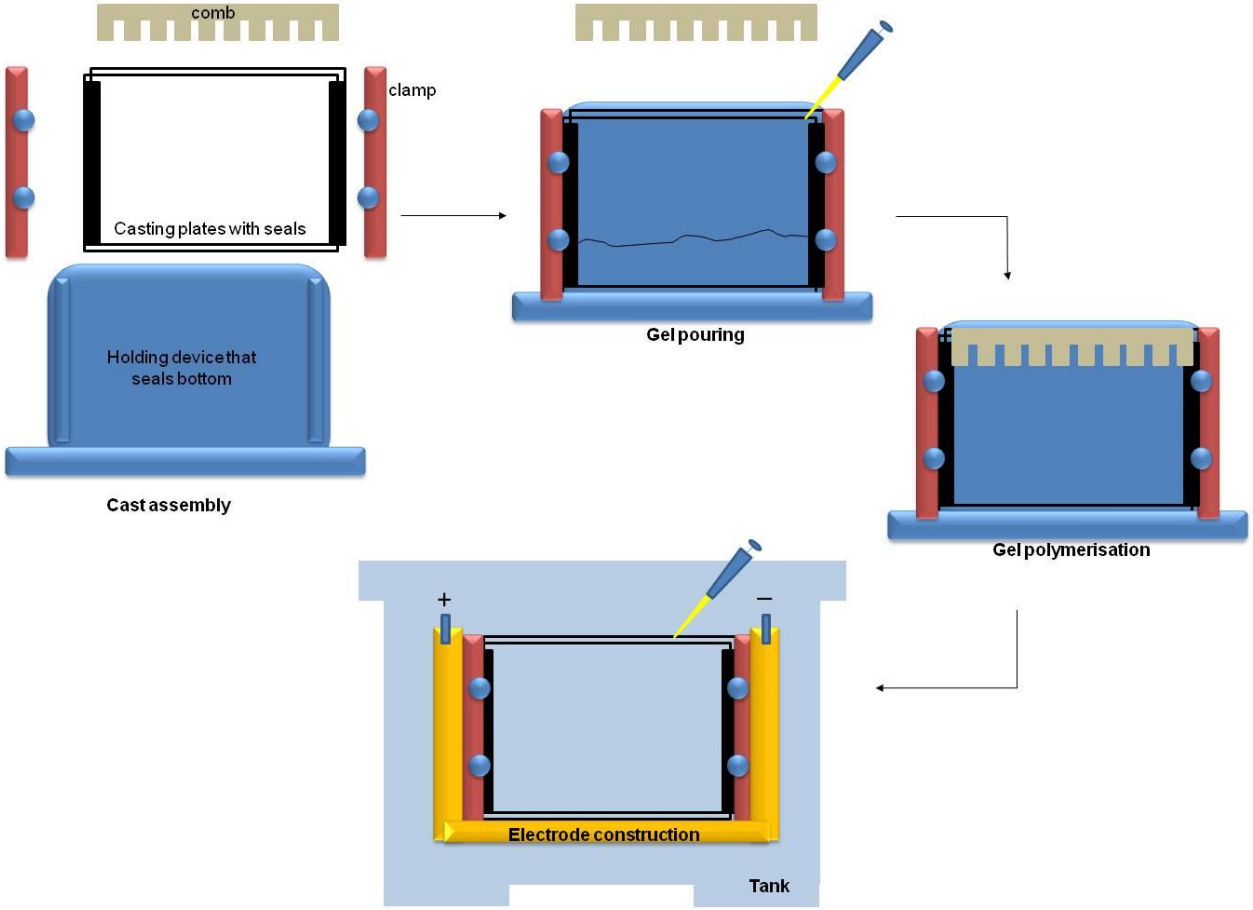

Figure 2.5 Mini-Protean electrophoresis casting system.
Black sealing strips (2) were sandwiched between 2 glass casting plates. These were clamped at each side to create a tight seal and clipped into the holding device. The gel was carefully poured between the casting plates and the comb was added on top to create wells before polymerisation. The sealed gel was carefully removed from holding device and transferred onto an electrode construction; which was placed into an electrophoresis tank.

2.4.7.4 Quantification of MMP-9 by Gelatin Zymography

MMP-9 is a gelatinase that is secreted by OCs. MMP-9's functional activity can be established in solution by using gelatin zymography, this method is routinely used in the literature to investigate MMP-9 bioactivity (Achilli *et al.* 2011). Gelatin zymography was performed as described in section 2.4.7.3 with the following changes; 7.5% polyacrylamide gel was prepared with 2% gelatin (0.2% final concentration) as substrate. After the refolding, gels were rinsed in zymography wash buffer C (section 2.2, *(lxvii)*) and digestion was performed with zymography digestion buffer C (section 2.2, *(lxi)*).

2.4.7.5 Western Blot to Confirm MMP-9 Bio-Activity

In order to confirm that MMP-9 was responsible for the degraded areas of the gelatin zymograph western blotting was performed. Proteins were blotted onto a Hybond-P polyvinylidene fluoride (PVDF) membrane (GE Healthcare). The membrane was washed in 100% methanol before use. It was then soaked in transfer buffer (section 2.2, *(lvii)*) together with several pieces of Whatman filter paper. The zymography gel, PVDF membrane and filter paper were arranged according to the schematic in Fig. 2.6. The protein blotting was performed at 80 mA for 2 h. After the transfer procedure was complete, non-specific protein interactions were blocked by immersion of the membrane in milk buffer (section 2.2, *(xxxix)*, for 30 min at 4°C). The membrane was then rinsed with wash buffer for 5 min. Goat polyclonal MMP-9 antibody (0.4 µg/ml, Santa Cruz) was diluted in wash buffer, applied to the membrane and was incubated overnight at 4°C. The membrane was thoroughly (3 times) rinsed with wash buffer before the secondary antibody (Donkey anti-goat IgG-HRP diluted in wash buffer (0.4 µg/ml)) was added. The membrane was incubated for a further 2 h at 4°C and washed before detection of protein by chemiluminescence. An Amersham Detection Reagents (GE Healthcare) was used for this purpose. The membrane was added onto a piece of cling film and excess buffer was removed. Equal volumes of Detection Reagent 1 and 2 were mixed and pipetted onto the membrane until it was covered. After 1 min incubation excess solution was discarded and the membrane was turned upside down onto a fresh piece of cling film. The membrane was then completely wrapped in cling film and placed into a hypercassette. The procedure was finished in a darkroom. Here, Amersham Hyperfilm TM ECL (GE Healthcare) was placed on top of the membrane; it was exposed for 1 min in the dark. Finally the film was developed with Kodak GBX development reagents (Sigma). The film was placed into Kodak GBX developer and replenisher solution (section 2.2, *(xxxiii)*) until bands were visible under the red light.

This was followed by washing in tap water and transferring the film into the Kodak GBX fixer and replenisher solution (section 2.2, *(xxxiv)*) until it became clear. Once finished the film was left to dry in an upright position.

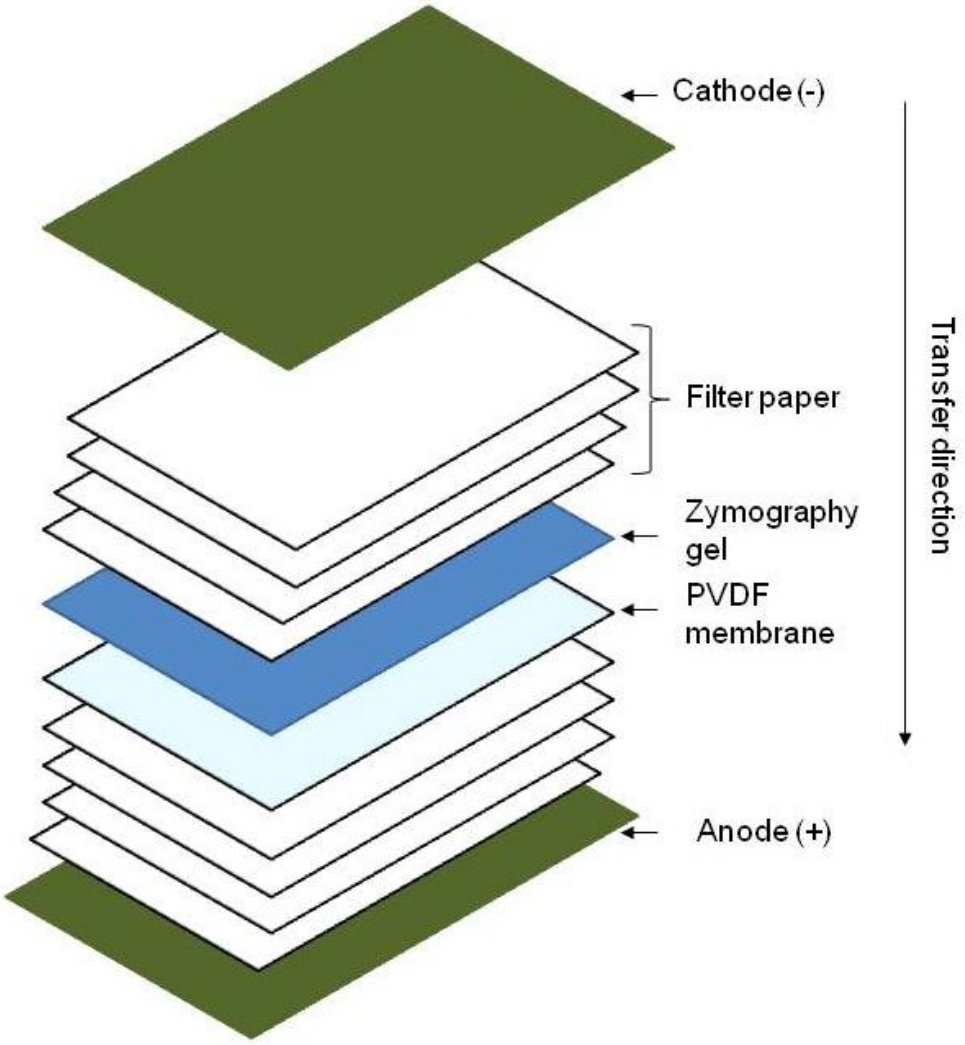

Figure 2.6 Assembly of transfer components (Fermentas-International-Inc 2011).

2.4.7.6 Measuring ProMMP-9 by ELISA

ProMMP-9 concentrations were measured using an ELISA that was developed in-house applying ProMMP-9 capture reagent, recombinant mouse MMP-9 and biotinylated anti-mouse ProMMP-9 antibody for detection (all purchased from R&D Systems). Several antibody concentrations were tested in a matrix formation; the following method was most sensitive.

A 96 well ELISA plate (Nunc) was coated with 1 µg/ml capture antibody (diluted in sterile PBS); it was incubated at room temperature overnight. After being washed thoroughly, blocking buffer (300 µl/well) was added to each well. The plate was left at room temperature for 2 h before being washed again and the diluted

standard (doubling dilutions in assay buffer with a top standard of 20 ng/ml) or samples (diluted in the range between 1:10 and 1:100 in assay buffer) loaded in duplicate (100 µl per well). Samples were incubated at room temperature for a further 2 h, after an additional wash step the detection antibody (0.625 µg/ml in assay buffer) was added to each well (100 µl). After a 1 h incubation period the plate was washed and developed colorimetrically as described in section 2.4.7.2.

2.4.7.7 Quantification of Cytokines/Chemokines

In order to access cytokines, supernatants were firstly screened via a multiplex assay. The Multiplex cytokine assay kit for murine pro-inflammatory mediators (Mesoscale Discovery) was performed by Dr Bronwen Evans (Co-supervisor). The assay measured IFNγ, IL-10, IL-12 p70, IL-1β, IL-6, murine keratinocyte-derived cytokine (mKc) and TNFα.

After discovering that mKc was highly expressed in OC cultures over other pro-inflammatory cytokines (eg. IFNγ), mKc levels were determined in all OCG supernatants by a specific ELISA kit (R&D Systems). The mouse CXC chemokine KC DuoSet was used and the ELISA was performed as described in section 2.4.7.6 with the following changes; rat anti-mouse Kc (2 µg/ml) was utilised as capture and 200 ng/ml biotinylated goat anti-mouse Kc as detection antibody, recombinant murine Kc was used as standard and samples were measured neat.

2.4.8 Statistics

All statistical analysis was performed with Graphpad Prism software. GraphPad QuickCal Outlier test was utilised to determine single, extreme outliers via the Grubbs' test. Student T-Test was performed when comparing 2 unpaired groups. One-way ANOVAs were used when studying more than 2 unpaired groups and Two-way ANOVAs were utilised when assessing more than 2 groups with 2 independent variables respectively. Mean and standard error (SEM) are stated throughout the result section.

2.5 Investigating the Role of Human CD59 in Bone Resorption

In order to study the impact of CD59 insufficiency on OCG in humans it was necessary to establish an OCG assay *in vitro*. Subsequently a system to block the biological activity of CD59 was also developed. These steps were essential to our understanding of the translational value of observations from the mouse to human bone health and disease. CD59 deficiency in humans has only been reported in a single case (Yamashina *et al.* 1990) and therefore the study of CD59 cannot be supported by patient samples. CD59 blocking antibodies have been used previously in the Complement Biology Group (Cardiff University) (Sivasankar *et al.* 2009). Unpublished data demonstrated that antibodies were unsuitable for long term CD59 blockade due to the rapid turnover of GPI-anchored proteins on the cell surface (half-life= 4 h) (Bojkowska *et al.* 2011).

The predicted timeframe of the human OCG assays was in excess of 2 weeks therefore a strategy that allowed a more complete and more stable suppression of CD59 production was considered most appropriate. For this reason, an antisense nucleic acid that induced the degradation of CD59 mRNA molecules was utilised. Antisense oligonucleotides, ribozymes, DNAzymes and RNA interference (RNAi) are commonly used to knockdown gene expression (Scherer and Rossi 2003). RNAi sequences against CD59 were tested in this study and a number of delivering strategies were examined to obtain optimal infection before OCG assays were commenced.

2.5.1 Tissue Culture Materials

Materials and culture conditions are described in section 2.4.2. Additionally, 30 µm pre-separation filters, MiniMACS columns and magnetic separator were purchased from Miltenyi Biotec. Ultracentrifuge tubes were obtained from Beckman and cell scrapers from Corning. Elephant ivory was kindly donated for research use by HM Customs and Excise (Heathrow, London, UK). The acquisition of the ivory was led by Dr Bronwen AJ Evans. Discs were cut in house (approx. 6 mm diameter) using an IsoMet Low Speed Saw (Buehler).

In order to remove excess dust and obtain smooth differentiation surfaces, the ivory discs were immersed in tap water and sonicated for 1 min. This process was repeated 10 times before each disc was sterilised in 100% ethanol and dried before use.

2.5.2 Cell Line Maintenance

Human embryonic kidney (HEK) 293T cells (kindly supplied by Dr R James Matthews) were grown in complete medium for HEK 293T cells (section 2.2, *(xix)*) and passaged at a dilution of 1:9 once a week. Jurkat EB.1 cells (kindly supplied by Dr R James Matthews) were grown in complete medium for human cultures (section 2.2, (*xx*)) and passaged when 100% confluent at a dilution of 1:30 twice a week. Both cell lines were maintained in 75 cm^2 tissue culture flasks.

2.5.3 $CD14^+$ Monocyte Purification from Human Blood

Initially human OC precursor cells were obtained to set up resorption assays. Precursor cells ($CD14^+$ monocytes) were isolated from human peripheral blood by adapting a published method (Nicholson *et al.* 2000). Blood was collected after approval of the project by the local ethics committee. Blood (50 ml) was obtained from consented healthy donors. Heparin sodium (1 unit/ml, Cardiff & Vale University Health Board Pharmacy, University Hospital of Wales) was used in each preparation to prevent clotting. Histopaque (1.077 g/ml, 5 ml) was added into 15 ml falcon tubes and 10ml of blood was carefully dispensed onto its surface. In order to separate cell populations, the tubes were centrifuged at 400 x g (without brake) for 30 min as shown in Fig. 2.7. Plasma was discarded and peripheral blood mononuclear cells (PBMCs) were transferred into clean tubes. PBMCs were diluted to 10 ml with Hank's balanced salt solution (HBSS, Invitrogen) and then centrifuged at 300 x g for 10 min. Supernatants were removed and this wash step was repeated twice. Cells from 50 ml of blood of the same donor were pooled, washed once more in fresh HBSS (10ml) and re-suspended in complete human medium (section 2.2, 5 ml). The cell suspension and reagents required for all subsequent steps were kept on ice. The cell concentration was determined utilising a haemocytometer as described in section 2.3.3.3. The PBMC suspension was passed through a 30 µm pre-separation filter to remove any aggregates. PBMCs were pelleted once again before being mixed with MACS buffer (section 2.2, *(xxxvii)*, 80 µl per $1x10^7$ cells) and CD14 MACS beads (20 µl per $1x10^7$ cells Miltenyi Biotec). The suspension was left for 15 min on ice before a MiniMACS column was utilised to purify $CD14^+$ cells according to manufacturer's instructions. Briefly, a column was placed on a magnetic separator and rinsed with MACS buffer (500 µl) before cell-beads suspension was applied to the column. The MiniMACS column was washed 3 times with MACS buffer before elution with MACS buffer (1 ml each). The eluted cell suspension was diluted 1:2 into complete medium for human cell cultures (section 2.2, *(xx)*) to keep cells viable. The final cell density was determined utilising the haemocytometer (section 2.3.3.3).

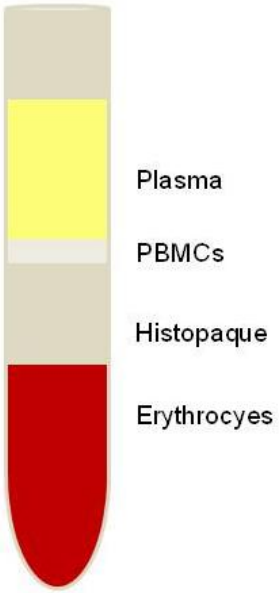

Figure 2.7 Separation of PBMCs using Histopaque.

2.5.4 Resorption Assay

To set up the resorption assay, purified human $CD14^+$ monocytes were diluted to $3.2x10^6$ cells/ml and 20 µl (final $6.4x10^4$ cells) were applied to ivory discs that were placed in a Petri-dish. Cells were left to adhere for 2 h at 37°C. Ivory discs were washed in complete human medium and transferred into 48 well plates containing 500 µl/well complete medium for human cell cultures supplemented with recombinant human M-CSF (5 ng/ml), RANKL (2 ng/ml) and protein cross-linking antibody, murine polyHistidine (R&D Systems, 2.5 µg/ml, Clone AD.1.1.10, IgG1) to support RANKL signalling. Cells were grown in this differentiation medium for 14 days. Fresh medium was added every 3 to 4 days.

2.5.5 Identification of Multinucleated OCs and Resorption Pits

TRAP staining was performed on day 14 to reveal the presence of OCs. Cells were washed in PBS (300 µl/well) before fixation in glutaraldehyde solution (section 2.2, *(xxvii)*, 300 µl/well) for 15 min at 37°C. Excess fixative was removed by washing in PBS (300 µl/well) twice and air drying for 5 min. Cells were stained with TRAP stain 1 (see section, 2.2, *(xlix)*, 300 µl/well) for 6min at 37°C before washing in PBS and dH_2O as before. Finally plates were left to dry. Representative images were obtained at x10 object magnification utilising an Olympus BX41 microscope with a Camedia C-3030 digital camera attached.

Subsequently, all cells were removed in order to assess resorption pits. Cells were incubated in hydrogen peroxide (1%, 300 µl/well) over night with agitation. Ivory discs were sonicated for 90 s and the solution was replaced by tap

water. Wet cotton swaps were used to gently remove cells and debris from ivory discs. The cleaning procedure was monitored microscopically. Once all cells were removed, ivory discs were stained with Toluidine blue (0.5%, 300 µl/well) for 2 min with agitation and rinsed in tap water. Resorption pits appeared in a darker purple than the ivory disc surface as more negatively charged proteoglycans are available for the stain to bind.

2.5.6 Lentiviral Delivery System

Once a resorption assay was established a CD59 knockdown system had to be developed. A lentivirus system that allowed for stable knockdown of transcripts in non-dividing cells had been established by Dr Sivasankar Baalasubramanian (Complement Biology Group, Cardiff University School of Medicine); this was tested in the first instance. In this system, a plasmid was utilised which produced shRNA. When the plasmid was transcribed, a 19-29 bp complementary RNA sequence with a loop was produced to create a double stranded RNA (Mittal 2004). shRNA is processed by various enzymes, transported into the cytoplasm where the loop is cleaved by the RNase III enzyme, DICER, and one strand of RNA binds to Argonaute. Along with other proteins the RNA molecule and Argonaute formed the RNA induced silencing complex (RISC). The RISC complex binds to the complementary CD59 mRNAs, which are then degraded by Argonaute induced mRNA cleavage (Rao *et al.* 2009).

2.5.6.1 Testing Competence of $CD14^+$ Monocytes for Lentiviral Infection

In order to test the efficiency of the lentiviral delivery system, a recombinant lentivirus (kindly supplied by Dr Liam Morgan), containing a green fluorescent protein (GFP), but not encoding for any shRNA, was utilised. Infection was tested in Jurkat EB.1 cells (a positive control cell line previously utilised by Dr Sivasankar Baalasubramanian) and compared to $CD14^+$ monocytes. $2x10^4$ of confluent Jurkat EB.1 cells were seeded per well (96 well plates, 200 µl). GFP encoding-lentivirus was added to cultures at a multiplicity of infection (MOI) of 8 (Fig. 2.8).

$$\text{Volume of viral stock added to cultures (ml)} = \frac{\text{Cells plated x MOI desired}}{\text{Plaque forming unit (Pfu)/ml determined during virus titration}}$$

Figure 2.8 Formula to calculate dilution of virus for infection.

$CD14^+$ monocytes were purified as described in section 2.5.3. Cells were diluted in complete medium for human cell cultures supplemented with M-CSF (5ng/ml) to

obtain $3.2x10^4$ cells in 200 µl. Polybrene (Millipore, 6µg/ml) and GFP-encoding lentivirus (MOI 8) were mixed with $CD14^+$ monocytes and transferred into a 96 well plate. All cells were incubated with lentivirus at 37°C for 2 days.

2.5.6.2 Infection Analysis Utilising Flow Cytometry

Flow cytometry was performed to analyse GFP expression. Initially, adherent cells were removed from the bottom of the well with a cell scraper. Cell solutions were transferred into 5 ml Falcon Polystyrene round-bottom tubes (BD Biosciences) and pooled from multiple wells to obtain between $1x10^5$ to $1x10^6$ cells/sample. Cells were collected by centrifugation at 800 x g for 3 min and re-suspended in FACS buffer (section 2.2, *(xxiv)*, 200 µl). An equal amount of buffered formalin was added to fix all samples.

Flow cytometry was performed on the FACSCalibur (BD Biosciences). CellQuest Pro software (BD Biosciences) was utilised. A dot plot (forward scatter (FSC) versus side scatter (SSC)) and a histogram, displaying FL1-H to visualise GFP, were created. Cell populations and autofluorescence was adjusted by altering the SSC voltage, FSC Amp/Gain and threshold using non-infected cells. Cells were applied and 10,000 events were counted for all samples.

For the analysis, viable cells were gated and the gate was applied to the histogram of all samples. The autofluorescence histogram of non-infected cells was overlaid onto the GFP expressing cell population and the GFP positive cell population was determined by drawing a marker on the histogram from the tail of the autofluorescence in the non-infected cell population to the tail of the GFP positive cell population.

2.5.6.3 Plasmid Replication

Once the protocol of infection was established, the virus was generated from commercial available shRNA containing plasmids (Sigma). Dr Baalasubramanian tested a variety of CD59-shRNA targets and a non-target control in a pLKO.1-puro vector (Sigma) containing ampicillin (bacterial selection) and puromycin (mammalian selection) resistance genes. He identified CD59-shRNA target-1 as most effective in Jurkats EB.1 via flow cytometry and supplied the plasmid containing target-1. DNA sequence:

> 5’ CCG GCC GTC AAT TGT TCA TCT GAT TCT CGA GAA TCA GAT GAA CAA TTG ACG GTT TTT G 3’).

Blotting papers containing control and shRNA plasmids were obtained from Singapore as no virus was available in Cardiff. It was placed into Eppendorfs with 100 µl TAE buffer (section 2.2, *(liii)*) to stabilise plasmids. Plasmids were transformed into competent DH5α (Invitrogen). Eppendorfs containing frozen DH5α (50 µl aliquots) were placed into a container with ice and mixed with plasmids at either 1:50 or 1:10 dilution. Cells were kept on ice for a further 10 min and then heat-shocked for 20 s at 42°C. Cells were diluted to 1 ml with LB medium (section 2.2, *(xxxv)*) and Eppendorfs were incubated at 37°C and 220 rpm for 1 h. This was followed by centrifugation at 6,000 x g for 30 s to pellet cells. Excess medium was removed leaving behind 50-100 µl solution which was used to re-suspend the pellet and the solution was dispersed onto ampicillin plates (section 2.2, *(v)*). Plates were incubated at 37°C overnight.

A colony from each agar plate was inoculated in LB medium (10 ml) containing ampicillin (100 µg/ml). Cultures were incubated at 37°C and 220 rpm for 6 h. A glycerol stock was prepared by adding 0.5 ml of each culture to 0.5 ml glycerol buffer (section 2.2, *(xxviii)*) which was stored in a Styrofoam box at -80°C. The remaining cultures were inoculated 1:100 in LB medium (500 ml) containing ampicillin (100 µg/ml). Cultures were incubated at 37°C and 220 rpm for 16 h before harvesting bacteria by centrifugation at 11,000 x g for 10 min at 4°C.

A PureLink HiPure Plasmid Filter Purification Kit (Invitrogen) was used to purify plasmid DNA (low copy number) according to manufacturer's instructions. Briefly, columns were prepared by allowing equilibration buffer (30 ml; 0.1 M Sodium acetate, pH 5, 0.5 M NaCl, 0.15% (v/v) Triton X-100) to drain through the filter cartridge within the columns. Meanwhile cell pellets were re-suspended in resuspension buffer (20 ml; 50 mM Tris-HCl, pH 8, 10 mM EDTA) with RNase A (20mg/ml in resuspension buffer) before lysis buffer (10 ml; 0.2 M NaOH, 1% (w/v) SDS) was added and tubes were inverted gently until a homogenous solution formed. The cell lysate was then incubated for 5 min and precipitation buffer (10 ml, 3.1 M potassium acetate, pH 5.5) added. This was followed by gently mixing by inversion. The lysate was applied to the column and the flow through discarded. The filter cartridge was removed and the column washed with wash buffer (50 ml; 0.1 M Sodium acetate, pH 5, 825 mM NaCl). The flow through was removed again and a fresh 50 ml falcon tube placed underneath the column. Elution buffer (15 ml; 100 mM Tris-HCl, pH 8.5, 1.25 M NaCl) was added to the solution to precipitate the DNA. Isopropanol (10.5 ml) was added to the DNA and the solution mixed. DNA was precipitated by centrifugation at 12,000 x g for 30 min at 4°C. The DNA pellet was re-suspended in 70% ethanol (5 ml) before centrifugation as above. Ethanol

was discarded and the falcon tube air-dried for 10 min before re-suspending the plasmid DNA in TE Buffer (section 2.2, *(liv)*, 200 µl). Finally, concentrations of plasmids were determined on the Nanodrop Spectrophotometer (260 nm) and plasmids stored at -20°C.

2.5.6.4 Generation of Lentivirus

Virus was generated via transfection of HEK 293T cells with the construct using the Effectene transfection reagent (Qiagen). Purified transfer shRNA containing vector plasmid target-1 (1 µg) was mixed with pΔ8.91 plasmid (encodes for capsid proteins and reverse transcriptase, 0.75 µg) and pMD2G plasmid (encodes for envelope protein, 0.5 µg). The solution was diluted to 300 µl with DNA-condensation buffer before Enhancer (16 µl) was added. The solution was vortexed and incubated at room temperature for 5 min. Effectene (60 µl) was added and mixed well with the pipette. The transfection complex was incubated at room temperature for 10 min and complete medium for HEK 293T cells (3 ml) added. HEK 293T cells were 75% confluent and received fresh DMEM medium (8 ml). Plasmid-lipid complexes (3.3 ml) were slowly applied to the cells and incubated for 72 h at 37°C.

Cell supernatant containing virus was harvested in 50 ml falcon tubes and cleared from the cell debris by centrifugation at 3,000 x g for 5 min. The supernatant was transferred into ultracentrifuge tubes and centrifuged at 80,000 x g at 4°C for 2 h. The supernatant was removed and the virus pellet re-suspended in 900 µl serum free DMEM, dispensed in aliquots (60 µl) and stored at -80°C.

2.5.6.5 Infection with shRNA Containing Lentivirus

To compare viral infection efficiency to previously obtained data by Dr Baalasubramanian (unpublished), $2x10^5$ Jurkat EB.1 cells were seeded per well (500 µl) into a 24 well plate. GFP-lentivirus was added at a MOI of 8, non-shRNA control virus and CD59 shRNA containing lentivirus were added at a 1:100 dilution (n=3). Cells were cultured with virus for 2 days before analysis.

2.5.6.6 Monitoring Infection Efficiency of Lentiviruses

Flow cytometry was performed to identify GFP and CD59 expression. Cells were removed from wells and re-suspended into FACS buffer as described in section 2.5.6.2. The sample that did not contain any virus was re-suspended in 600 µl FACS buffer and was divided into unstained, isotype control and CD59 staining sample (200 µl each). Antibodies were utilised according to manufacturer's recommendations and are described in Tab. 2.7. Non-labelled primary antibody

MEM43 (anti-CD59) and the DD7 (isotype control) were added to appropriate samples. All samples were incubated on ice for 30 min before centrifugation at 800 x g for 3 min. Buffers were then discarded and cell pellets were re-suspended in fresh FACS buffer (200 µl). This wash step was repeated. Secondary antibody (anti-mouse IgG - Fluorescein isothiocyanate (FITC)) was added to appropriate samples and incubated on ice for 30 min. All samples were washed twice as before. Buffered formalin (200 µl) was added to all suspensions to fix cells and analysis was performed either with FACSCalibur (section 2.5.6.2) or with the Accuri C6 Cytometer and CFlow Plus software (BD Biosciences).

	Antibody/labelling proteins	Supplier	Raised in	Concentration	Dilution used
Primary	MEM43, anti-human CD59	Supplied by Dr Claire Harris	Mouse	280mg/ml	1:280
Secondary	Anti-mouse IgG-FITC	Vector Laboratories	Horse	1mg/ml	1:100
	$F(ab')_2$ fragment of anti-mouse IgG (H+L)- Alexa Fluor 647	Invitrogen	Goat	2mg/ml	1:100
Directly conjugated	MEM15, anti-human CD14-FITC	Abcam	Mouse	0.004mg/ml	1:100
Isotype control	DD7, Anti-human IgG1	Chemicon (Millipore)	Mouse	0.1mg/ml	1:100
	Anti-human IgG1-FITC	BD Pharmingen	Mouse	Not supplied	1:100

Table 2.7 Antibodies used in flow cytometry.

A flow rate of 66 µl/min was chosen and 10,000 events were acquired. No further adjustment was needed as the Accuri has a 7 log range to capture cell parameters. To analyse samples gates, overlays and markers were applied as described in section 2.5.6.2.

2.5.7 Adenovirus Delivery System

Transient adenovirus infection was established as an alternative vector delivery system. Dr Daryn Michael and Tim Ashlin generated 3 viruses with different shRNA sequences targeting CD59. Briefly, Invitrogen BLOCK-iT RNAi Designer was utilised to generate sequences. miR RNAi was chosen and the accession number of mature CD59 from GenBank (X16447) was entered. Targets were identified for the 3' untranslated region which were assessed utilising a BLAST search in Pubmed against the human genome. Sequences that did not match any other mRNA than CD59 and showed only 20% homology to non-transcribed sequences were selected as shRNA targets:

1: 5' CTA ACT GAC TAC ATC CAA GGA 3'
2: 5' ACA TAT GGA ACA TTT GGC ATG 3'
3: 5' TTC ATG CCC TGC TAT CTG GAA 3'

The AdZ-mIR155 vector was utilised to generate shRNA and adenovirus was generated according to Dr Richard Stanton's protocol (Stanton 2008). Oligonucleotides (oligos) were purchased from Invitrogen (Fig. 2.9).

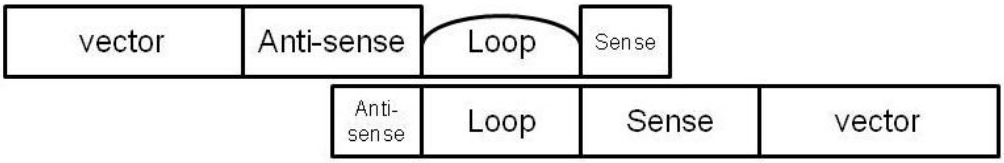

Figure 2.9 Oligo design. The forward oligo contained 40 bp vector sequence, 21 bp anti-sense, 19 bp loop and 3 bp sense sequence whereas the reverse oligo started with 3 bp anti-sense, 19 bp loop and 19 bp sense sequence (forms internal loop) followed by 40 bp vector sequence. This created overlapping oligos that could be integrated into the plasmid via homologous recombination.

SW102 *Escherichia coli* containing AdZ-mIR155 vector were utilised for transformation. Once SW102 cells were cultured to the appropriate density, a temperature shift for activation (42°C) of the *bet* (single stranded DNA annealing protein) and *exo* (5'-3' double stranded DNA exonuclease) genes was performed

(Murphy and Campellone 2003). These proteins enabled homologous recombination of oligos with the overlapping vector sequence after transformation with oligos utilising electroporation (2.5kV in 0.2ml cuvettes (BioRad)). SW102 cells were spread onto chloramphenicol plates (section 2.2, *(xvi)*) supplemented with sucrose, Isopropyl βD-1 thiogalactopyranoside (induces *lacZ*) and X-gal (galactose and indole containing compound). Colonies were grown at 32°C for 48 h. To generate recombinant vectors an ampicillin-*lacZ* (β-Galactosidase) - *sacB* (sensitivity to sucrose) cassette had to be removed. Colonies were grown on sucrose, therefore, cells which did not undergo recombination and still contained the *sacB* gene would not grow. SW102 cells that contained mutated *sacB*, but still had functional *lacZ* resulted in blue colonies as X-gal was cleaved. Colonies appearing transparent to white carried the vector with correctly inserted oligos.

The latter colonies were selected and cultured to carry out Miniprep to purify plasmids. After confirmation of the correct insert via restriction digestion and sequencing, a Maxiprep (Macherey-Nagel) was performed and adenoviruses were prepared in 293TREx cells (Invitrogen) utilising Polyfect kit from Qiagen. Supernatants were titred according to Bewig and Schmidt and number of plaques were counted in 3 fields of view and pfu/ml was generated (Bewig and Schmidt 2000):

$$\text{Pfu/ml} = \frac{\text{Infected cells/field x fields/well}}{\text{Volume of virus (ml) x dilution factor}}$$

2.5.7.1 Infection with Adenoviruses and Testing of OCG

In order to establish infection and knockdown ability of adenoviruses, human $CD14^+$ monocytes were purified as described in section 2.5.3. Monocytes were cultured in 48 well plates (500 µl/well) in complete medium for human cell cultures supplemented with M-CSF (5 ng/ml). Fresh medium was added every 2 to 4 days. Different viruses, virus load, cell densities and incubation times were tested to determine CD59 knockdown as described in Tab. 2.8.

Testing Condition	Cells seeded (cells/well)	Viral source	MOI	Incubation (days)
Infection efficacy	$1x10^5$	GFP expressing	50, 100, 500	5 days in M-CSF and 2 days with infection
Virus selection	$1x10^5$	shRNA1, shRNA2, shRNA3	50, 100, 500	5 days in M-CSF and 2 days with infection
Incubation time	$1x10^5$	Empty vector, shRNA3, shRNA1+3	100 and 200	5 days in M-CSF and either 2 or 4 with days infection or 7 days with 2 day infection
Cell density	$1x10^5$, $3x10^5$	Empty vector, shRNA3	100, 200	1 day in M-CSF and 2 days infection

Table 2.8 Parameters that were tested to obtain CD59 knockdown.

2.5.7.2 Monitoring Infection Efficiency of Adenoviruses

Flow cytometry was utilised to determine GFP, CD14 and CD59 expression as well as cell viability. Cells were removed from wells and re-suspended into FACS buffer as described in section 2.5.6.2. The sample that did not encounter any virus was divided into 6 to 7 samples (unstained, CD14 single staining, CD14 isotype control, CD59, CD59 isotype control, double staining and/or 7-amino-actinomycin D (7AAD) viability staining sample (200 µl each)). MEM43 (anti-CD59) and DD7 (isotype control) antibodies (Tab. 2.7) were added to the appropriate samples. All samples were incubated on ice for 30 min before centrifugation at 800 x g for 3 min. Buffer was discarded and FACS buffer (200µl) was utilised to re-suspend each cell pellet. This wash step was repeated. Alexa Fluor 647 conjugated secondary antibody (Tab. 2.7) was added to corresponding samples and incubation followed for 30 min on ice before washing was performed as above. Samples utilised for double staining were blocked with mouse serum (in-house, 1:50). All samples were incubated for 15 min on ice. Directly conjugated MEM15 and the according FITC isotype control (Tab. 2.7) was mixed into the appropriate samples. This was followed by incubation and washing as before. Cells were either fixed by adding an equal amount of formal saline or 7AAD (eBioscience, 25 µg/test) was added 10 min before the flow cytometry procedure to all appropriate samples. All samples were acquired by the Accuri as described in section 2.5.6.6.

2.6 Phenotypic Analysis of Bone Structure in CD59a$^{-/-}$ Mice

A number of imaging techniques have been utilised in the literature to investigate skeletal changes in rodents including X-ray, dual energy X-ray absorptiometry (DXA), microcomputed tomography (MicroCT) and magnetic resonance imaging (MRI) (Swartz and Loevner 2008). In this study X-ray and digital caliper assessment was selected for prominent morphological changes and subsequent MicroCT allowed for high resolution analysis to identify subtle alterations in bone structure and BMD (van't Hof 2012). Finally, methylmethacrylate (MMA)-embedded bone sections were stained for OB and OC activity *in vivo*.

2.6.1 Animals and Harvesting of Femora and Vertebrae

CD59a$^{-/-}$ mice were kindly supplied by Prof B Paul Morgan and WT mice were purchased as described in section 2.3.1. Femora and vertebrae were obtained from female and male 8-10, 20 and 50 week old CD59a$^{-/-}$ and WT mice. All animals were killed by the Schedule I method. Hindlimbs and vertebrae from the neck to the onset of the tail were dissected and fixed in 70% alcohol.

2.6.2 Femoral Length and Shaft Diameter Assessment

Hindlimbs from 8-10, 20 and 50 week old CD59a$^{-/-}$ and WT mice were examined for femoral length utilising the X-ray setting of a Kodak In-vivo Imaging System FX Pro (Carestream). Samples were aligned in a Petri-dish (3.5cm diameter) before being transferred into a plastic container (15x10 cm). This assembly was placed into the top pocket of the machine to allow for high resolution images. The Kodak MI SE software was applied to acquire images. Firstly, X-ray projections were previewed to adjust sample position and focus. Final settings utilised X-ray as the illumination source at 35 peak kV and 149 µA. The camera lens was adjusted to an f-stop (degree of aperture opening) of 4.96, field of view was utilised at 90.3 mm, an exposure time of 60 s were chosen to obtain a single image and an illumination correction was applied. Once images were collected, femoral length was obtained by changing the field of view to 49 to correct for the camera zoom. Shaft diameter was determined in midshaft utilising a digital caliper.

2.6.3 Histomorphometric and BMD Analysis of Cortical and Trabecular Bone in Femora

MicroCT (Skyscan-1072), a 3 dimensional (3D) X-ray technique, was exploited to obtain BMD and morphological parameters of cortical and trabecular bone obtained from 8-10, 20 and 50 week old WT and CD59a$^{-/-}$ mice.

2.6.3.1 Acquisition of X-ray Projections

The X-ray source was set to 49.6 KV and 200.8 µA and 7.952 s exposure was selected with a gain of 1. The stage to which the sample was attached was set to rotate 180°, 0.45° (rotation step) between each X-ray image. Frame averaging was set to 1, meaning that only one picture per angle was taken. Random movement was chosen at 10 to correct eventual movement of specimen. The X-ray beam went through a 1 mm aluminium filter and the magnification was chosen to give a 10.8 µm pixel size. Before samples could be tested, a flat field of the empty chamber was generated to subtract background noise. After the set-up of the Skyscan machine, hindlimbs were prepared as described in Fig. 2.10.

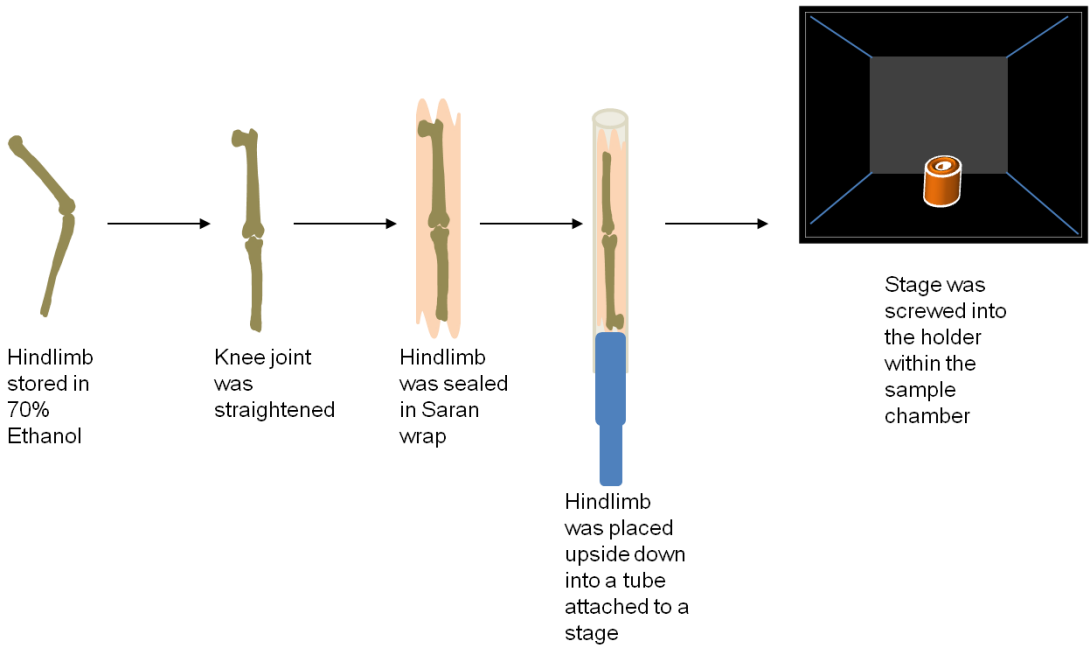

Figure 2.10 Sample preparation for MicroCT scanning. Figure illustrating joint preparation to enter the X-ray sample chamber. Joints were straightened and covered in cling film to prevent drying out. Next they were inserted into a plastic tube (0.4cm radius) attached to a stage. The femur was facing down to allow for straight alignment. The sample chamber was opened and the stage was screwed tightly into the holder within the MicroCT scanner.

Once samples were placed into the MicroCT scanner, a preview was generated and the sample stage was lifted to position the joint and rotated to confirm straightness of the femur at all angles. Finally, X-ray projections (413 vertical images/samples) were acquired.

2.6.3.2 Reconstruction and Adjustment of Acquired Projection Datasets

X-ray projections were applied to NRecon (Skyscan) software in which a reconstruction algorithm generated crossectional images that enabled 3D analysis. To initiate reconstruction, the axial reconstruction range was set between 8 and 1008. X-ray projections cause artefacts, such as beam hardening and ring artefacts. Beam hardening is caused when X-rays pass higher and lower energy photons creating dark streaks or skewing the shape of the object. It was corrected by 1%. Ring artefacts, appearing when the stage rotates, were not reduced (0). A threshold to remove soft-tissue noise and enhance bone structure was set to 0.005946-0.095366. To obtain a defined, clear bone area the projections from all angles have to be aligned accurately by fine tuning at 3 positions within the projection before reconstruction created 1001 BMP files.

BMP files were opened in CTAnalyzer (CTAn, Skyscan) and the femur was selected (500 images) and saved as a new dataset. Initially, femora that were not completely straight were corrected in the software Dataviewer (Skyscan). Datasets were opened (without resizing) and loaded for 3D viewing. Once straightened, datasets were saved as VOI TRA.

2.6.3.3 Histomorphometry of Cortical Bone

The adjusted datasets were analysed in CTAn. A reference point within the growth plate was determined in each femur as shown in Fig. 2.11. To measure cortical bone the shaft was selected 3 mm below the growth plate. Here a length of 1 mm, comprised of 100 images, was investigated (Fig. 2.11). A doughnut region of interest (ROI) was drawn around the cortical bone (Fig. 2.11). The greyscale index was set between 111 and 255 to highlight cortical bone. From this a 3D analysis was performed to obtain bone volume (BV) and crossectional thickness (CsTh).

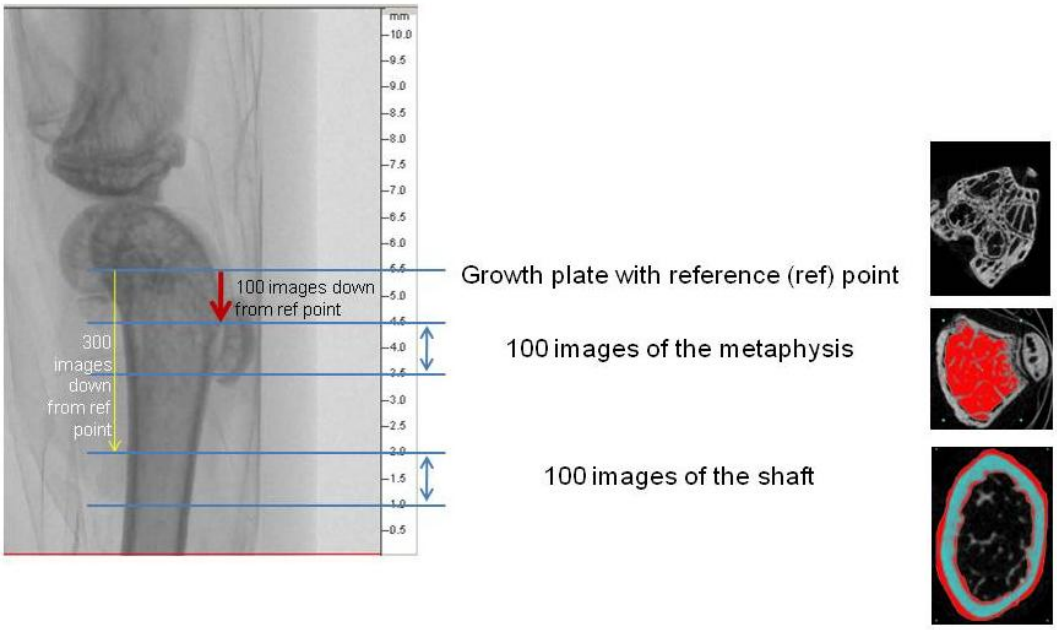

Figure 2.11 MicroCT of a femur. Figure illustrates reference point and areas of interest selected for cortical and trabecular bone analysis.

2.6.3.4 Determination of Bone Mineral Density

To obtain bone mineral density (BMD), the Skyscan 1072 had to be calibrated. Mouse phantoms of 0.25 g/cm^3 and 0.75 g/cm^3 density were obtained from Skyscan. The phantoms were added on top of each other into the tube attached to the stage. The same settings for projection acquisition and reconstructions were used as described in section 2.6.3.1 and 2.6.3.2. The dataset was opened in CtAn and 2 mm were selected of the 0.25 g/cm^3 phantom. A circular ROI was chosen of the core of the phantom containing minimal irregularities. From this the Attenuation coefficient mean was determined. This was repeated for the other phantom. BMD calibration was performed as described in Fig. 2.12. BMD was obtained for the cortical bone within the doughnut selection.

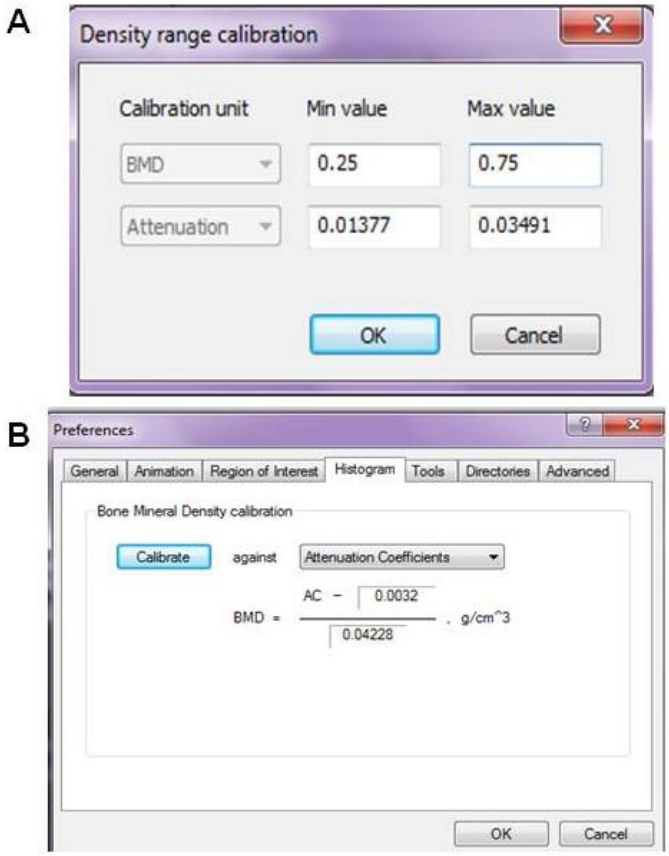

Figure 2.12 BMD calibration. Figure shows BMD and attenuation coefficient of mouse bone phantoms (**A**). Equation for bone samples with unknown BMD was determined from calibration in A (**B**).

2.6.3.5 Generation of 3D Representative Images

Datasets of cortical bone selections were re-opened in CTAn and the doughnut shaped ROI applied to create a 3D Model. The model was saved as a STL file. Consequently, the Skyscan software CTVolume (CTVol) was opened and the STL file chosen. Zoom and orientation of the model was adjusted and screen prints were saved.

2.6.3.6 Histomorphometry and BMD of Trabecular Bone

Trabecular bone consists of small bone structures (trabeculae) in rod and plate shapes. To characterise trabeculae, parameters, such as BV/tissue volume (TV) trabecular number (TbN) and trabecular thickness (TbTh), trabecular separation (TbSp), trabecular pattern factor (TbPf) and structure model index (SMI) were measured. These are indicators of the amount of bone present and how it is shaped and distributed. Characterisation of trabecular bone according to these parameters allows for interpretation of bone quality (Skyscan 2009).

For trabecular bone analysis Dataviewer adjusted datasets were opened in CTAn. An area of 1 mm below the reference point was selected and 1 mm of bone was analysed as pictorially illustrated in Fig. 2.11. The area within the cortical ring was selected before choosing the greyscale index between 80 and 226. This was followed by a 3D analysis to obtain BV/TV, TbTh, TbN, TbSp, TbPf and SMI. Finally the volumetric (total) BMD was determined. It was chosen to take into account the space between trabeculae, not just the actual density of the bone structure. Generation of 3D models for Tb bone followed the methodology of section 2.6.3.5.

To create representative images of trabecular bone, femoral datasets (created in section 2.6.3.2) were opened in CtAn and vertical images were generated by cutting the horizontal view within the reference image as shown in Fig. 2.13. Images were saved and edited in Pro X3.

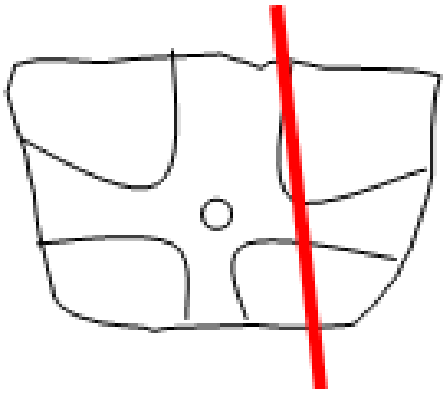

Figure 2.13 Generation of vertical view of trabecular bone within femora. Growth plate reference point is shown and red line represents how bone was cut to create a vertical image.

2.6.4 Histomorphometric Analysis of Trabecular Bone in Vertebrae

In order to identify if phenotypical changes were localised to the long bones or extended to other areas in the body, vertebrae of 8-10 and 20 week old male WT and CD59a$^{-/-}$ specimens were analysed. Vertebrae of the lumbar spine are a major trabecular bone location (Turner *et al.* 2000) and are a recommended area for clinical densitometry (Lewiecki *et al.* 2008). MicroCT of lumbar vertebrae was performed in collaboration with Dr Rob van't Hof at Edinburgh University.

X-ray projections of vertebrae were generated utilising the Skyscan 1172. Parameters that changed from the previous analysis (section 2.6.3.1) were the following: The X-ray source was 60 kV and 167 µA with a 0.5 mm aluminium filter. Magnification was set to 7 µm pixel size and no random movements were corrected. Specimens were prepared for scanning as described in Fig. 2.10, but the tube and stage utilised had a larger radius (0.75 cm) to accommodate spines safely.

The lumbar spine of mice contain 6 vertebrae (Bab *et al.* 2007). The main body of vertebra 6 (L6) was scanned. Reconstruction was performed in NRecon as before (section 2.6.3.2) with the following alterations: Quality of projection datasets was monitored utilising the profiling function. It presents a graph plotting the pixels per mm of aligned images. If the 2 lines follow the same path then the scan was successful and the alignment has been calculated correctly by the software making fine-tuning redundant. Beam hardening was set to 18% and ring artefacts reduction to 12. An ROI was employed to reconstruct only the bone occupying area and the threshold ranged from 0 to 0.11. After reconstruction, Dataviewer (section 2.6.3.2) was used to straighten the vertebra L6 to the position illustrated in Fig. 2.14.

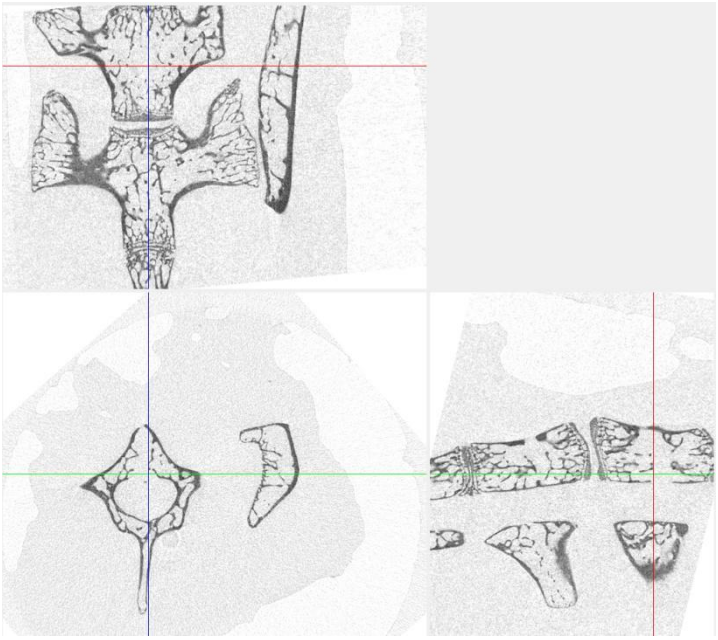

Figure 2.14 3 orientational views of L6.

Adjusted datasets were opened in CTAn and only a limited area of trabecular bone was analysed because of the complex shape of vertebrae. The ROI started after the cartilage disappeared on the distal and proximal end of L6 and the shape of the vertebra's main body was followed as shown in Fig. 2.15. The greyscale index was set from 70 to 255 and before 3D analysis was carried out, datasets were filtered (median, 2D space, radius 1), a threshold (global, low 70, high 255) determined and datasets were despeckled (remove white speckles, 3D space, remove less than 50 voxels, apply to image). Analysis then determined BV/TV, TbN, TbTh, TbSp, TbPf and SMI.

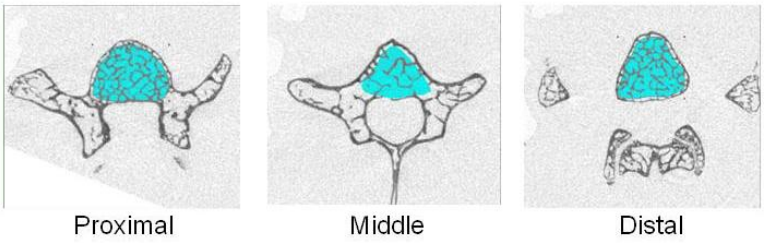

Figure 2.15 Selection of trabecular bone of L6.

Adjusted femoral datasets were opened in CtAn and according to the illustration in Fig. 2.16, vertical images were created as explained in section 2.6.7. Additionally, 3D models were prepared (section 2.6.3.5).

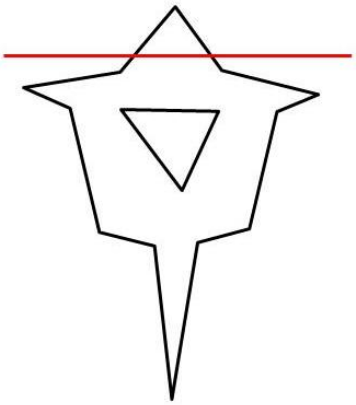

Figure 2.16 Generation of vertical view of trabecular bone within L6. Mid-section of vertebra is shown and the red line represents how bone was cut to create a vertical image.

2.6.5 Investigation of OB Activity *In Vivo*

Femora of 8-10 and 20 week old male WT and CD59a$^{-/-}$ mice were histologically processed after MicroCT analysis in collaboration with Dr Rob van't Hof. All femora were MMA-embedded to allow for analysis of calcified bone. MMA is a hydrophobic resin which was used because of 1) fast infiltration of the resin, 2) polymerisation at low temperature, 4) morphological preservation and 5) high-quality image analysis.

2.6.5.1 Tissue Processing

In order to process femora, they were separated from the tibia at the knee joints and cut in half using a scalpel. Distal femora were placed into disposable baskets (small, 4 divisions, Leica) with PBS. Baskets were added to a holder and transferred into a vial containing PBS.

The Leica Tissue processor (EM TP4C) was prepared with 100 ml reagent vials containing solutions described in Tab 2.9. Samples were agitated during the incubation for full penetration and incubated at 4°C utilising a vacuum.

Step	Reagent	Time (h)
Dehydration		
1	PBS	3/4
2	50% ethanol	2
3	70% ethanol	2
4	80% ethanol	2
5	96% ethanol	2
6	100% ethanol	3
7	100% ethanol	3
Defatting		
8	xylene	1
9	xylene	12

Table 2.9 Tissue processing.

After processing, excess xylene was removed from baskets and the holder was transferred to a vial containing a freshly prepared resin solution (section 2.2, *(xlv)*). This vial was transferred into a vacuum container which was sealed with Parafilm. An air-inlet on top of the container was opened to pump out all oxygen (approx. 5min). After the air-inlet was resealed, resin infiltrated the femora during 7 day incubation at 4°C. Excess resin solution prepared for infiltration was stored in the fridge for embedding.

2.6.5.2 Embedding of Femora

Histobloc N molds (TAAB) were filled with stored resin solution and samples were added straight after their removal from baskets. Femora were positioned and sealed as illustrated in Fig. 2.17 before molds were immersed into a water bath at 29°C for 9 h to polymerise resin. Polymerised blocks were mounted onto a universal holder for Histobloc N (TAAB). 1 part of cold-serving resin (Technovit) was added to 2 parts of HistoResin mounting medium (Leica) and the resulting solution was poured on top of the holder as described in Fig. 2.18. Resin hardened within 30 min and blocks were removed.

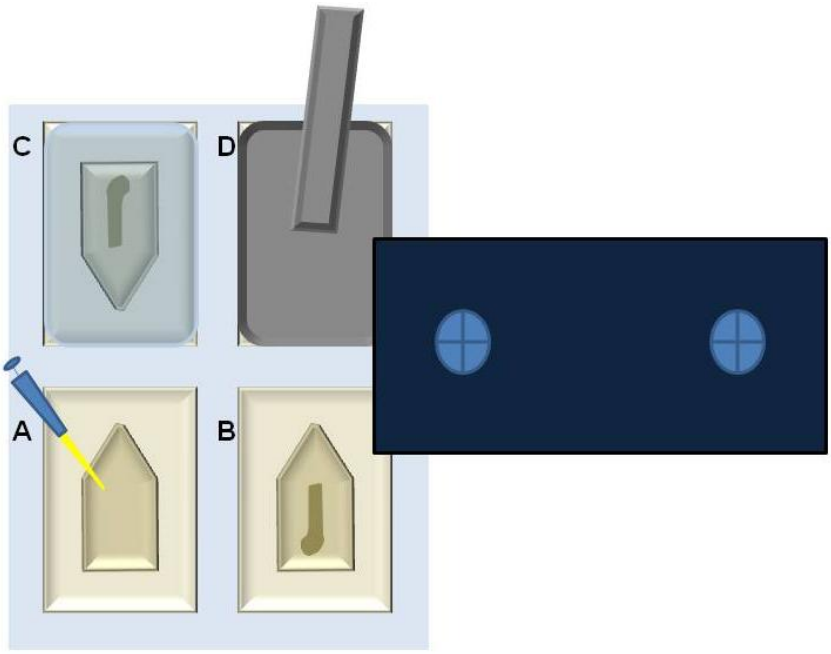

Figure 2.17 Sample preparation for polymerisation. Resin solution was added into molds utilising a pipette until molds were filled 90% (**A**). A femur was placed sideways into each mold with the shaft pointing towards the triangular end, but keeping this area free of bone (**B**). Molds were sealed airtight with a cover foil (**C**) and a metal holder (**D**). All 4 covered molds were screwed tightly into a metal device.

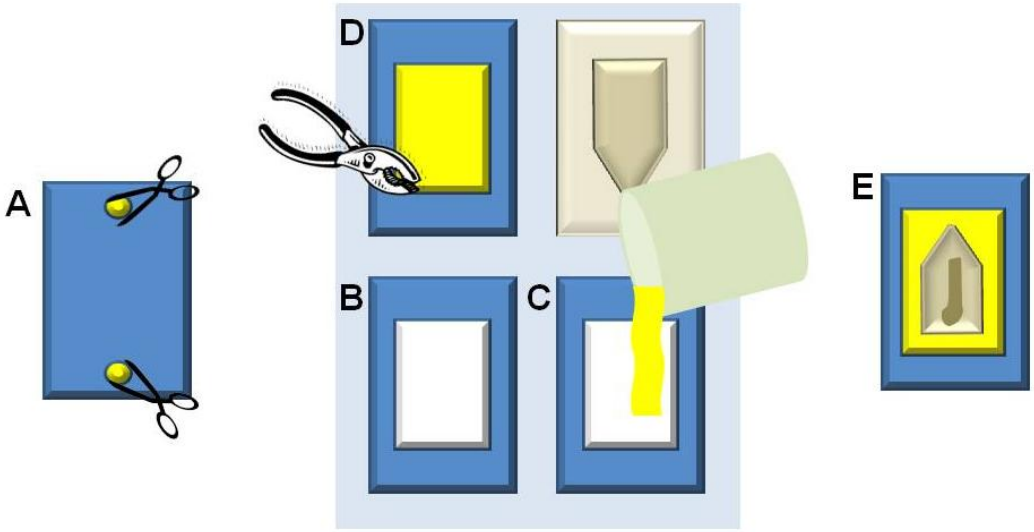

Figure 2.18 Mounting of polymerised blocks. Raised surfaces on the holders were removed to prevent leakage (**A**) and polymerised surfaces cleaned before mounting. Holders were placed on top of the polymerised blocks (**B**) and mounting solution was added (**C**). When the mount became solid, holders were removed from the mold with pliers (**D**). This also freed polymerised blocks which were attached to the holder for sectioning (**E**).

2.6.5.3 Trimming of Resin Embedded Blocks

A motorised drive microtome (Leica, RM2265) was utilised. Disposable blades (Leica) were applied for trimming and adjusted to the clearance angle of 5°. A block was clamped into the holder and to reduce the cutting force it was oriented with the triangular side facing the blade. A block was trimmed until a considerable amount of shaft was visible on the surface.

2.6.5.4 Sectioning of Resin Embedded Blocks

Once all femora were trimmed, smooth sectioning was achieved by replacing the blade with a D profile tungsten carbide knife 12 or 16 cm (Leica). The section thickness was adjusted to 5 µm. During sectioning, the block surface was moistened with 30% ethanol. A section was collected using a brush wetted with 30% ethanol. The brush caught a section at the triangular part which appeared first. Once enough sections were collected from a single block, they were transferred to labelled tissue tack microscope slides (Polysciences, coated with saline) that were covered with 96% ethanol. Sections were stretched with a brush and cover foils (TAAB) were immersed in 96% ethanol and placed on top of the sections. Excess ethanol was dried off and slides were sandwiched into a pressure clamp. The clamp was tightened and incubated at 37°C for 2 days to support drying and adhesion of sections. Finally the clamp was cooled for 30 min and slowly released before removing slides.

2.6.5.5 Identification of Osteoids

To identify osteoblast activity von Kossa/van Gieson staining procedure was performed to quantify osteoids. Von Kossa stained for mineralised matrix whereas van Gieson highlighted the OB secreted collagen-rich osteoids (Yadav *et al.* 2011; Lindhe *et al.* 2012).

For this procedure sections were initially stained on slides. Before staining, resins had to be removed by immersion in 3 changes of methozyethyl acetate (MEA) for 20 min each time. Sections were transferred to xylene for 2 changes (10 min each time) and dried for 30 s. This was followed by hydration of sections by rinsing them in 2 changes of 100% ethanol and then once in 96%, 80%, 70% and 50% ethanol. Hydration was finished by immersion of slides in 2 changes of dH_2O.

Von Kossa staining was initiated by incubation of slides in 1.5% silver nitrate, diluted from the silver nitrate stock solution (section 2.2, *(xlvi)*), for 5 min in the dark. The excess solution was removed by brief washing in dH_2O for 3 changes. To induce a colour change of the mineralised backbone to black, sections were

reduced in 0.5% hydroquinone (TAAB) for 2 min and rinsed again in dH_2O for 2 changes. Sections were counterstained in van Gieson (filtered, TAAB) for 5 min and washed in dH_2O for 2 changes before being dried on a hot plate at 45°C. Sections were dehydrated in xylene for 5 min and 22x50 mm coverslips (VWR) were mounted onto the slides. For this DPX (Fluka) was dropped onto the coverslip and xylene soaked sections were carefully moved onto the coverslip with the sections facing down. Once the coverslip attached to the slide it was turned over again and left to dry over night.

Staining on slides did not always produce sections suitable for analysis. Some polymerised blocks resulted in poorly attaching sections. Therefore more sections were removed from the corresponding blocks as described in section 2.6.5.4. Sections were subjected to the floating method in which the resin was not removed to give sections support and the stain was allowed to penetrate sections from both sides. For this, sections were added into ice cube trays (holding 10 ml per slot). One section was added to individual compartments and each section was washed in dH_2O. Von Kossa and van Gieson staining were carried out as described above. Sections were dehydrated in 70% ethanol and unfolded with forceps. After 3 sections were transferred onto slides, all sections were straightened with forceps. Excess resin around the bone containing area was removed utilising a scalpel. The mount for resin sections (section 2.2, *(xl)*) was melted in a water bath (65°C). Coverslips were mounted onto sections by dripping the resin mount next to the section and adding the coverslip on top. Finally slides were left to dry.

2.6.5.6 Quantification of Osteoids

Trabecular bone was chosen for osteoid analysis as its remodelling rate is higher than in cortical bone (see section 1.4.2.2) and small changes could be monitored. Slides stained with von Kossa/van Gieson were scanned with a ScanScope CS slide scanner (Aperio) to digitalise complete slides. A summary of the generation of high quality images is illustrated in Fig. 2.19.

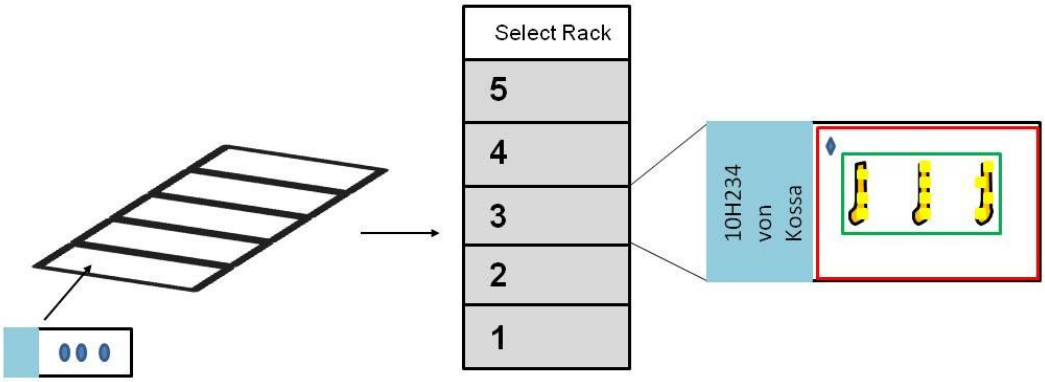

Figure 2.19 ScanScope illustration. Figure demonstrates how slides were loaded into the rack. They were then selected to obtain a snapshot which enabled adjusting the area of interest (red), scan area (green), calibration point on a white background (blue diamond) and focus points (yellow squares) on femoral sections.

ImageScope was then used to process images. As exporting images as TIF files did not result in the desired magnification for osteoid quantification, snapshots of the trabecular bone area within each femoral section were taken at x20 object magnification as described in Fig. 2.20. The scanned area width was utilised to determine the µm/pixel (0.49875) which was required for further analysis.

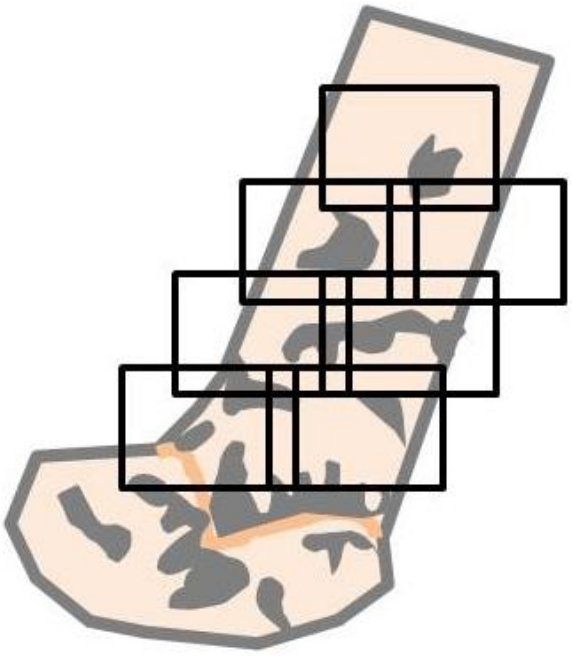

Figure 2.20 Illustration of overlapping images. Figure demonstrates snapshots were taken to capture the trabecular bone in the shaft.

The Fiji-Win64 image J program was used applying a Macro developed by Stephan Preibisch to stitch individual images together to create a single image. This was

supported by the Macro ‘StitchFromFile’ developed by Dr Rob van’t Hof and a demonstration can be viewed in Fig. 2.21.

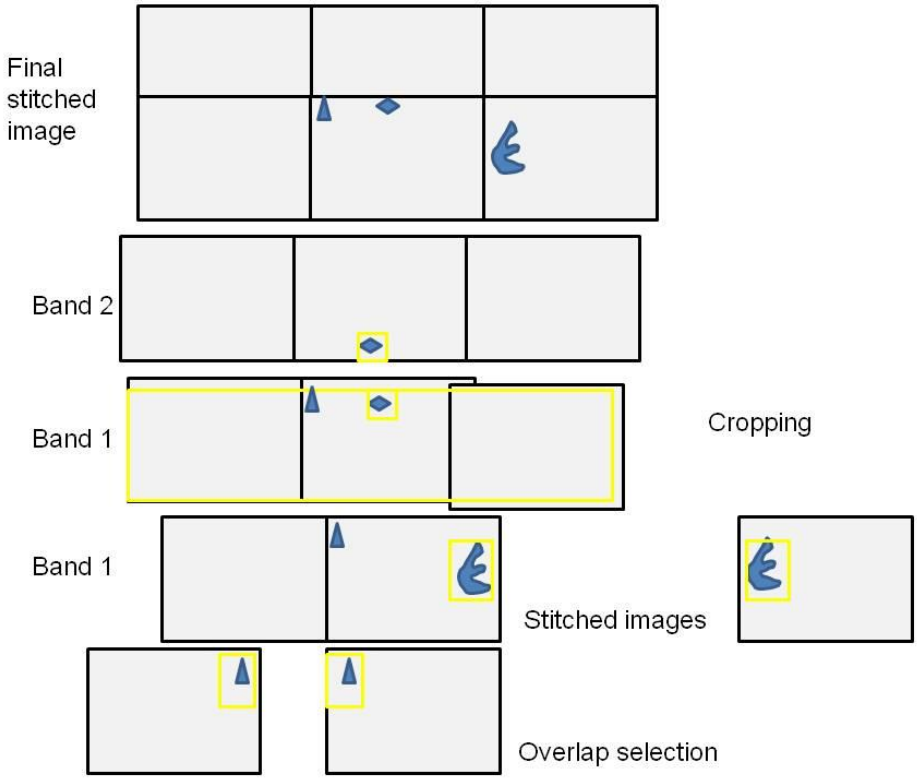

Figure 2.21 Stitching of high resolution images. Figure illustrates how overlaps of images are selected to generate a merged image. This is performed in bands to allow stitching in 2 dimensions. Once a band is finished, cropping allows for better overlap to stitch individual bands together.

All sections were analysed with an additional custom designed Image J Macro also developed by Dr Rob van’t Hof. In the program TRAPHisto the calculated 0.49875 µm/pixel was entered to calibrate the program (Fig. 2.22). Analysis resulted in TV, BV, bone surface (BS), osteoid numbers (OSN) and osteoid surface (OSS) quantification.

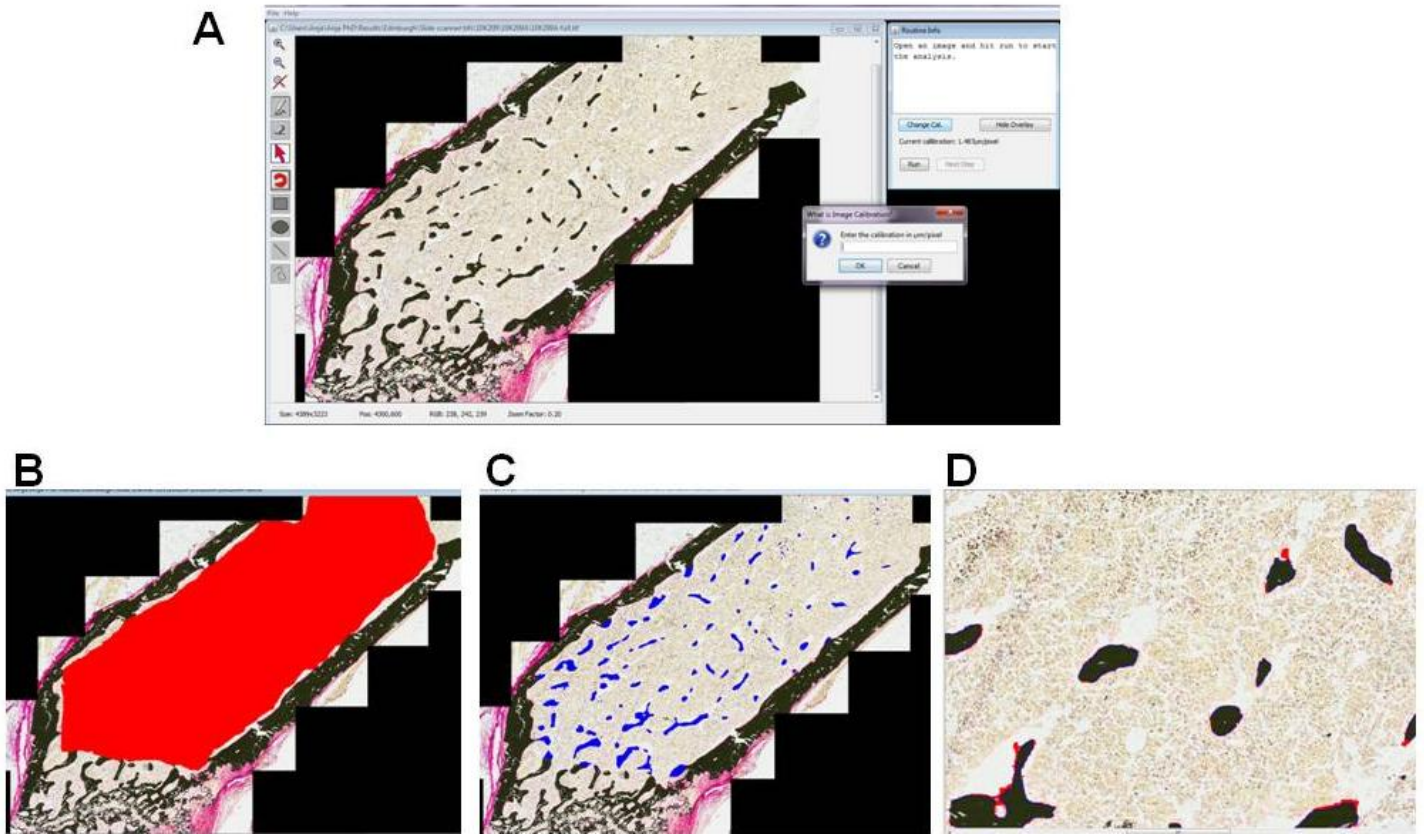

Figure 2.22 TRAPHisto program. A demonstration of assessment stages is shown. Initially a stitched image was opened and the program was calibrated (**A**). The TV containing the trabecular bone was selected in red (**B**) before the trabeculae was highlighted in blue (**C**). Finally osteoids on the bone surface were identified in red (**D**).

2.6.5.7 Calcein Labelling *In Vivo*

In vivo staining with the fluorophore calcein allowed for monitoring of calcium deposition by OBs over time. For this an additional cohort of four 8-10 week old WT mice and 4 age matched CD59a$^{-/-}$ mice were treated by intra-peritoneal injections with calcein solution (section 2.2, *(xiv)*) 4 and 1 days before sacrifice (Home Office license 30/2361). Femora were histologically processed as described in section 2.6.5.1 to 2.6.5.4. Generated sections only required counterstaining by immersion in Aniline blue (0.3 mg/ml, pH 7.5) for 20 min to identify position of the trabecular bone. Slides were washed in tap water twice, air dried, mounted with DPX as described in section 2.6.5.5 and dried again.

2.6.5.8 Assessment of Mineral Apposition

Images of Calcein/Aniline blue labelling slides were taken with the Leica Q5501W microscope. In the Leica QWinV3 software, images of trabecular bone, stained with Aniline blue, were taken with white light at x20 object magnification. For this the exposure was adjusted to 5.48 ms, the image was grey-scaled, and white balance and shading correction was applied. The microscope was changed to FITC (515 nm) without moving the slide. A fluorescent image was taken at 303 ms exposure. A total of 4 non-overlapping images (white and fluorescent light) were generated per section. After all sections were processed an image was taken of the haemocytometer at the same magnification to calculate the pixel/mm as described in section 2.3.5. This was converted to µm/pixel.

White light and fluorescent images of the same area were stacked utilising Fiji-Win64 Image J program to locate trabecular BS on fluorescent images. All stacks were analysed with 'CalceinHisto' macro developed by Dr Rob van't Hof. The calculation was set to 0.1407µm/pixel (Fig. 2.23) and parameters described in Fig. 2.23 were selected. TV, BV, BS, single label (OB mineralised at one timepoints only at a specific BS), double label (OB mineralised at both time points at a specific BS) and width of double label were quantified. From this the mineral apposition rate (MAR) was generated by dividing the width of the double label by the number of days between injections (3) in µm/day. Bone formation rate (BFR/BS) was calculated by multiplying the MAR by the sum of double and half of the single label. These were then divided by the BS ($\mu m^3/\mu m^2$/day).

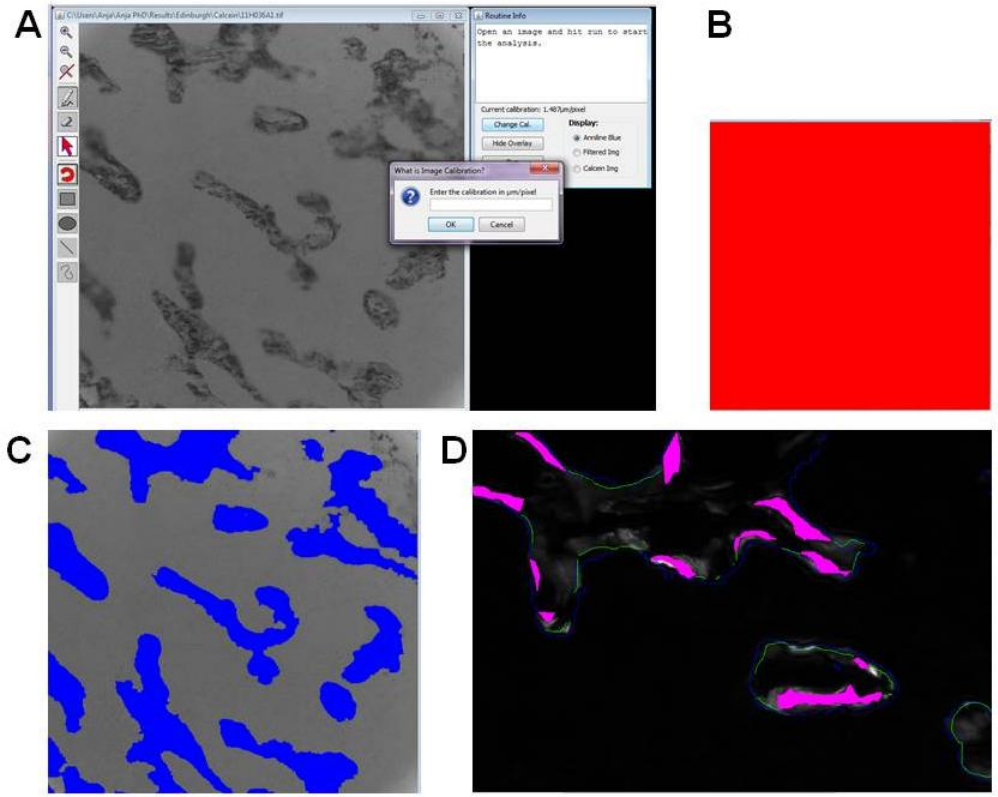

Figure 2.23 CalceinHisto program. Stacked white light and fluorescent images were opened. White light image in grey scale was displayed and software was calibrated (**A**). As only trabecular bone was selected the total area was chosen as TV (**B**). Trabeculae were highlighted in blue (**C**) and BS was converted into a blue line on the fluorescent image (**D**). Area of parallel double labelling of calcein was selected in purple and single label around the bone surface was depicted as green line.

2.6.6 Investigation of OC Localisation *In Vivo*

Slides generated in section 2.6.5.4 were also assessed for OC localisation in WT and CD59a$^{-/-}$ samples utilising TRAP/Aniline blue staining. Again, sections adhered to slides were initially stained via the following protocol. Resin removal and dehydration was performed as described in section 2.6.5.5. Sections were transferred into the TRAP stain 2 (section 2.2, *(l)*) which was filtered (Whatman, grade 230) before use. Sections were stained for 2 h at 37°C, but the development of maroon colour was monitored and the time adjusted accordingly to avoid background staining. Sections were rinsed in dH_2O twice and counterstained in Aniline blue acid (section 2.2, *(vi)*) for 20 min. Subsequently, sections were washed twice in tap water, left to dry, mounted with resin mount as described in section 2.6.5.5 and were dried again.

Similarly, stained sections of low quality were re-stained via the floating section method. Sections from different blocks were added into sealable glass containers (50 ml). Initially all sections were washed in dH_2O before 10 ml TRAP stain 2 was added per container and incubated on the agitator at 37°C for approx. 2 h. Sections were washed with 3 changes of dH_2O and counterstained with Aniline blue acid for 20 min. After another 2 changes of washing in dH_2O, sections were mounted as described in section 2.6.5.5.

Slides stained with TRAP/Aniline blue were scanned in ScanScope CS slide scanner, processed in Image Scope and stitched together in the Image J as described in section 2.6.5.6. The program TRAPHisto was utilised for OC quantification as also explained in section 2.6.5.6. When parameters were calculated, OC numbers (OCNr) and OC surface (OCS) was determined instead of osteoids.

2.6.7 Statistics

All statistical analysis was performed with Graphpad Prism software. The GraphPad QuickCal Outlier test was utilised to determine single, extreme outliers via the Grubbs' test. A Student T-Test was performed when comparing 2 unpaired groups. Two-way ANOVA was utilised when assessing more than 2 groups with 2 independent variables respectively. Mean and standard error (SEM) are stated throughout the result section.

Chapter 3

Determining the Role of CD59a in Osteoblast Differentiation and Maturation

3.1 Introduction

CD59 is expressed on human mesenchymal stem cells (MSCs) and osteogenic lineage cells (Tian *et al.* 2007; Hu *et al.* 2009; Trentz *et al.* 2010), therefore it is likely that murine MSCs express CD59a. Whether CD59a affects osteoblast (OB) formation or function has not been investigated previously.

3.2 Aim and Objectives

The purpose of this chapter was to evaluate the role of CD59a in OB differentiation and function, by measuring OB generation from precursor cells and assessing the capacity of the OB to form a mineralized matrix *in vitro*.

To accomplish this aim the following key objectives were identified:

1. To establish a reproducible OB mineralisation and colony forming unit (CFU) assay.
2. Assess the impact of CD59a on MSC differentiation and mineralisation using mouse MSCs or OBs as the favoured cell source.

3.3 Results

Initially, an OB mineralisation assay was established *in vitro*, before the role of CD59a in OB differentiation and mineralisation was evaluated. Femora and humeri were harvested from 7 to 20 week old mice. Bone marrow and explant cultures were prepared as explained in section 2.3.3. Assay conditions were tested to obtain the optimum 1) cell density, 2) cell source, 3) foetal calf serum (FCS) supplement, 4) β-Glycerophosphate (βGP) concentration and 5) time points for evaluation. Once established WT and CD59a$^{-/-}$ samples were compared during OB differentiation, mineralisation and adipocyte generation. The findings of these studies are described in detail below.

3.3.1 Establishing a Cell Concentration Sufficient to Support OB Mineralisation

To determine the optimum cell density for the mineralisation assay, cells were cultured in medium supplemented with dexamethasone (DEX) and ascorbic acid (ASP) to induce OB differentiation and βGP (for mineralisation) for 28 days (Bellows *et al.* 1992; Peter *et al.* 1998; Coelho and Fernandes 2000). At end point the wells were stained with Alizarin red as a positive marker (Fig. 3.1) demonstrating that the conditions were sufficient to support OB differentiation and function *in vitro*.

MSCs were seeded at various concentrations ranging from $1x10^4$ and $4x10^4$ cells/well. The surface area of the Alizarin red staining was shown to gradually

increase with cell density, with the highest level of staining being observed at $4x10^4$ cells/well (Fig. 3.1D).

Mineralised nodule formation between cells has been reported as a measure of functional mineralisation by OBs in the literature (Idris *et al.* 2008). Mineralised nodule size was slightly increased in those cultures seeded at $4x10^4$ cells over the other cell densities (Fig. 3.2). Hence, $4x10^4$ cells/well was chosen as the optimal cell density to obtain highest yield of functional OBs in subsequent assays.

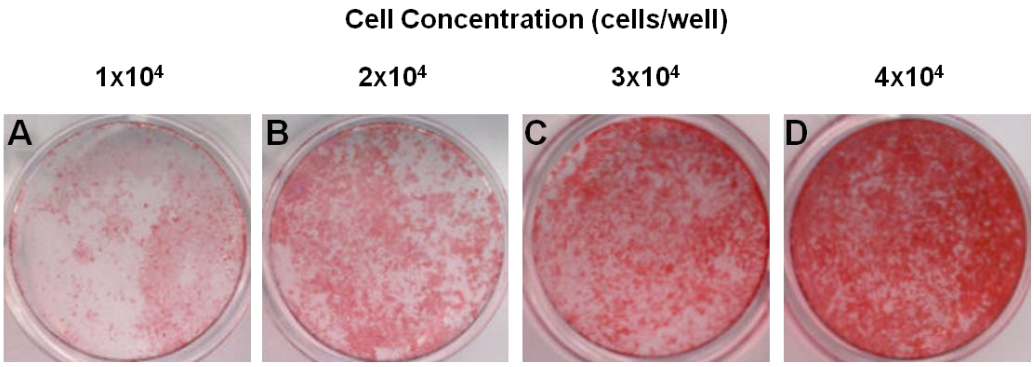

Figure 3.1 Mineralisation of cultures from bone marrow derived MSCs to determine cell density. A pool of bone marrow cells from 2 femora and 2 humeri of an 8 week old male mouse was obtained (n=1 mouse). MSCs were cultured until confluent before seeding at $1x10^4$ (**A**), $2x10^4$ (**B**), $3x10^4$ (**C**) and $4x10^4$ (**D**) cells/well (n=3 wells per cell density) in 12 well plates. After overnight adherence, medium supplemented with DEX (10 nM), ASP (50 µg/ml) and βGP (10 mM) was added to induce mineralisation. Cells were cultured for 28 days and Alizarin red staining was performed at end point to visualise mineralisation. Representative wells are shown.

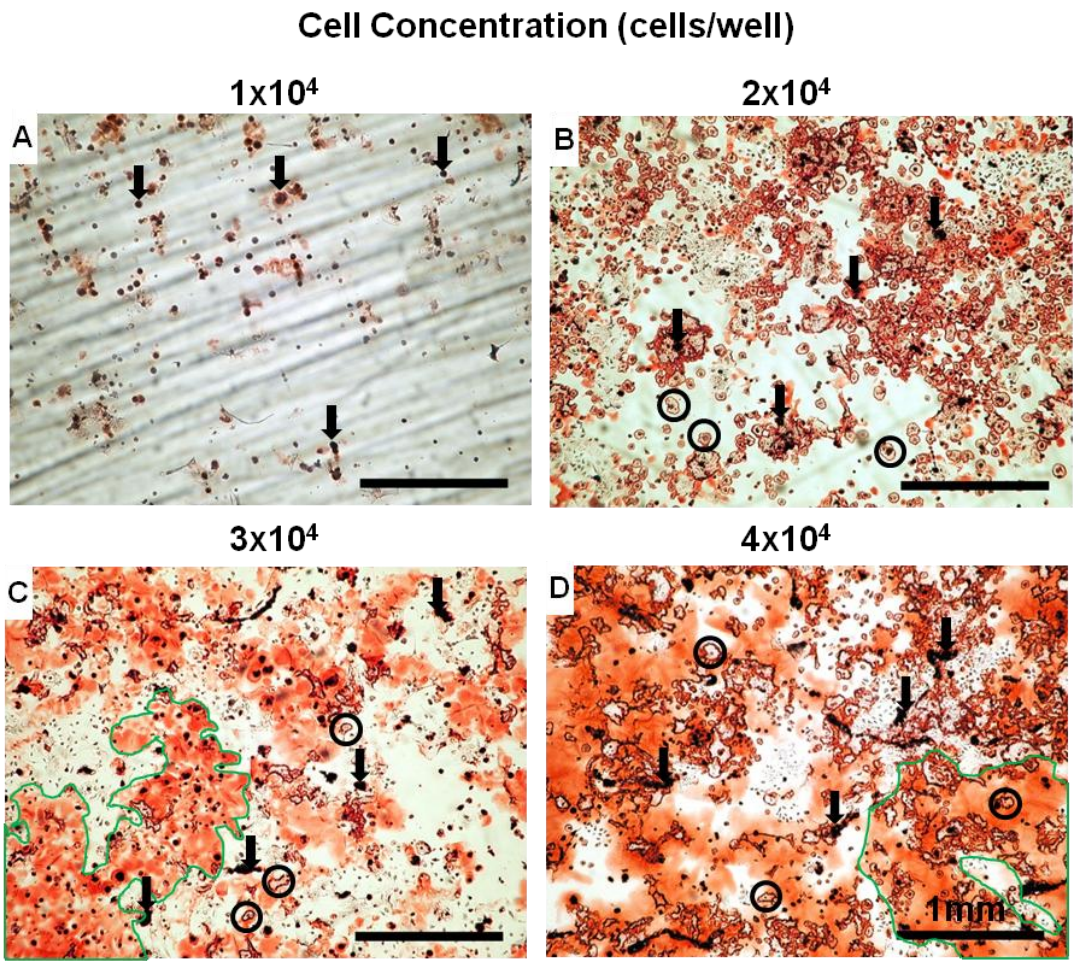

Figure 3.2 Morphological assessment of mineralisation. Cultures seeded at $1x10^4$ (**A**), $2x10^4$ (**B**), $3x10^4$ (**C**) and $4x10^4$ (**D**) cell/well were examined microscopically to determine the quality of mineralisation. Examples of mineralised nodules (⬇), mineralisation encircling cells (O) and diffused mineralisation (area denoted in green line) are indicated.

3.3.2 Assessment of Cell Source for Differentiation of Functional OBs

To test the most suitable OB precursor cell source, cells were either harvested from the bone marrow or grown from shaft and epiphysis/metaphysis explants before being expanded according to the procedure outlined in section 2.3.3. After expansion cells were seeded at $4x10^4$ cells/well and left to differentiate and mineralise for 28 days before Alizarin red staining. Cells cultured from the bone marrow showed increased Alizarin red staining (Fig. 3.3) and presented with more medium sized mineralised nodules than cells obtained from the explants of the shaft or epiphysis/metaphysis (Fig. 3.4). Hence bone marrow cultures had more capacity to differentiate into functional OBs than explant cultures and were utilised in subsequent experiments.

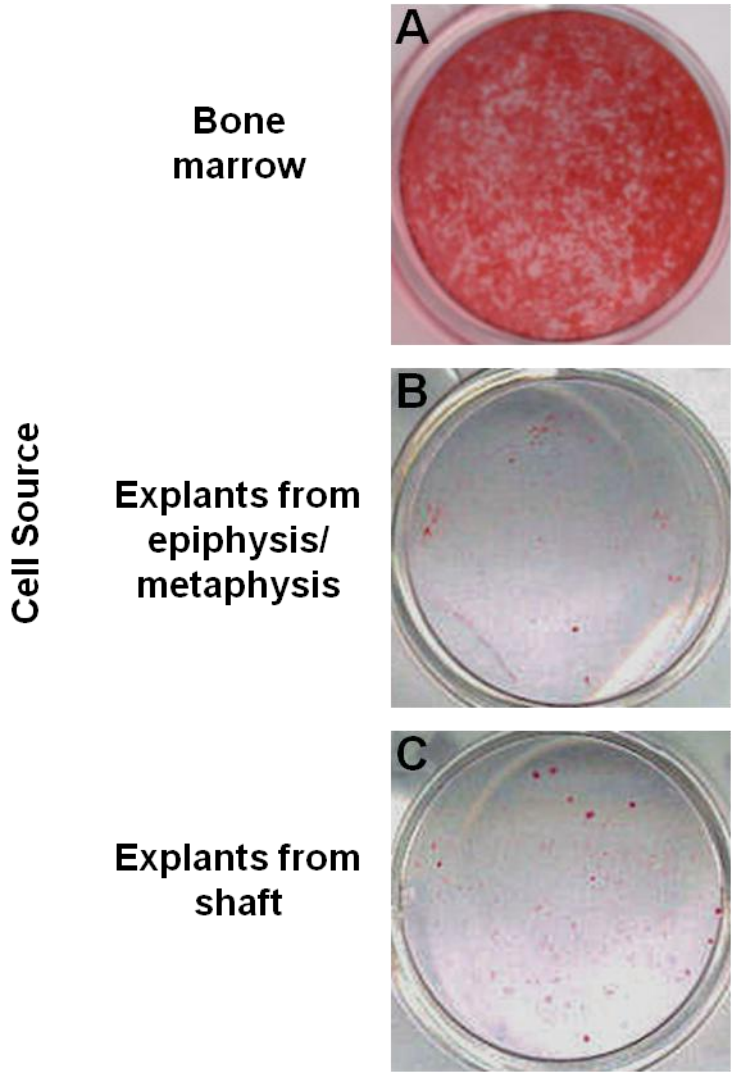

Figure 3.3 Mineralisation of cultures established from bone marrow derived MSCs and explant cultures. A pool of bone marrow cells and bone explant derived cells from 2 femora and 2 humeri of an 8 week old male mouse were used (n=1 mouse of which 3 wells were cultured per cell source). Cells were cultured and stained as outlined in Fig. 3.1. Representative wells from bone marrow cultures (**A**), explant cultures from the epiphysis/metaphysis (**B**) and shaft (**C**) are shown.

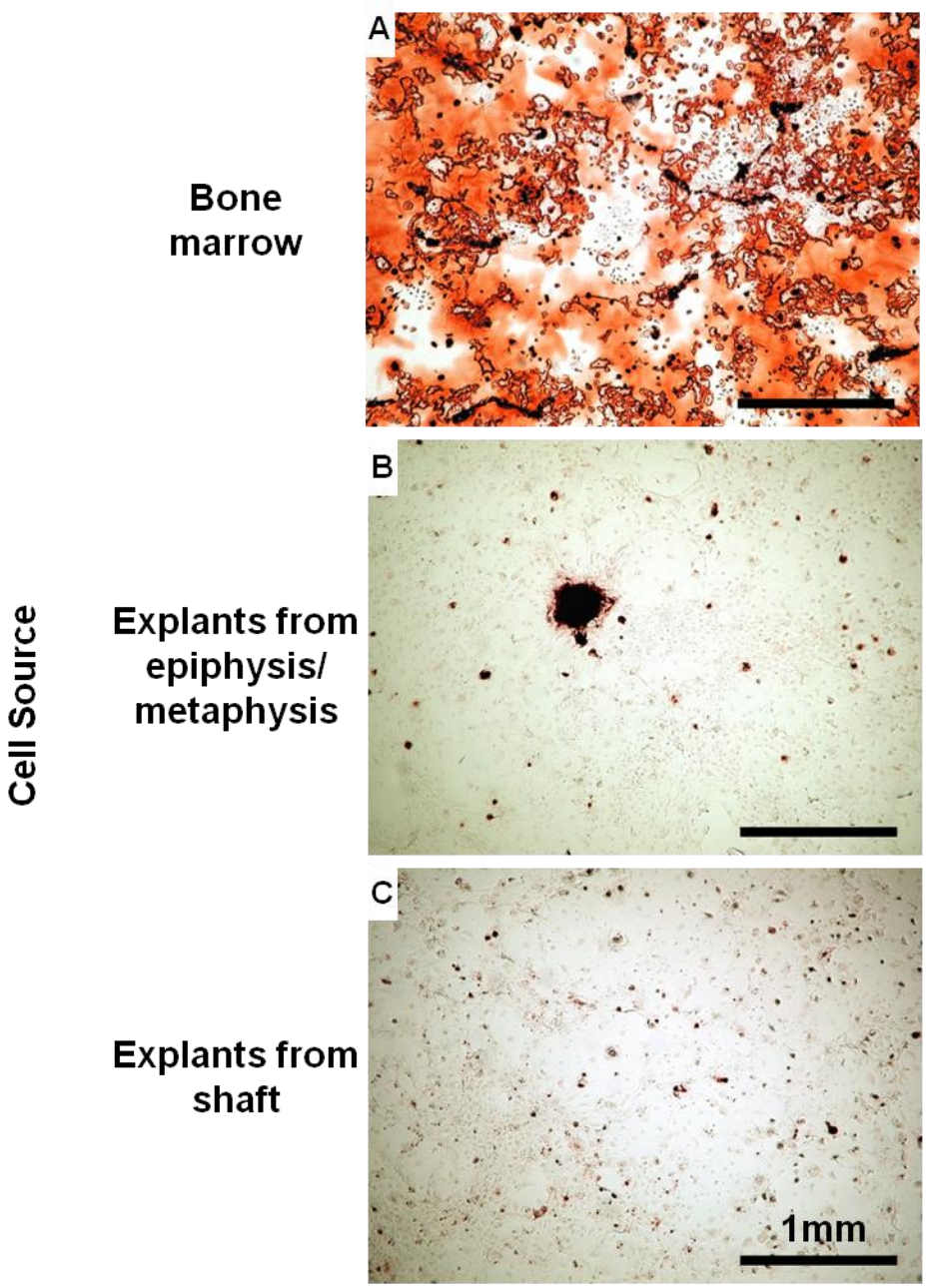

Figure 3.4 Morphological examination of mineralisation in cultures established with different cell sources. Bone marrow cultures (**A**), explant cultures from the epiphysis/metaphysis (**B**) and shaft (**C**) were examined microscopically at higher magnification to analyse the mineral deposits morphologically.

3.3.3 Examination of the Effect of FCS Supplements on Mineralisation of OB Cultures

FCS (as supplied by the manufacturer) was routinely used for OB mineralisation assays by our research group. An *in vitro* system without external complement was desired for this study to investigate the effect of CD59a on OBs. Hence FCS versus heat-inactivated FCS was compared in the OB assays.

Bone marrow cells were expanded in complete medium for murine cell cultures with FCS or heat-inactivated FCS (Tab. 2.1). Once plated, MSCs were left to differentiate in medium supplemented with the corresponding FCS and mediators for 21 days. Alizarin red staining was performed and mineralisation was observed microscopically.

Mineralised nodules formed in cultures grown in both FCS and heat-inactivated FCS (Fig. 3.5). Mineralised nodules were slightly smaller in heat-inactivated FCS (Fig. 3.5B), but occurred with the same frequency as in untreated FCS (Fig. 3.5A). Consequently heat-inactivated FCS was adopted for all subsequent experiments.

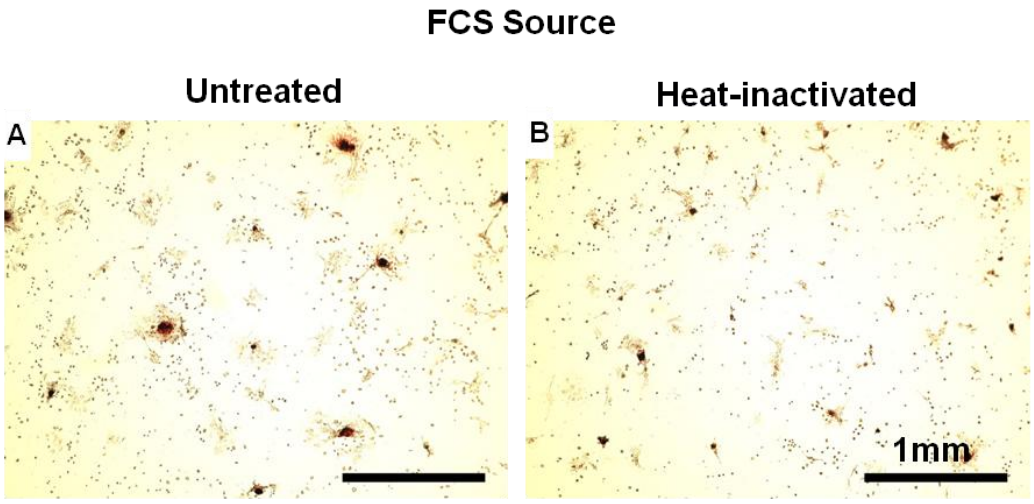

Figure 3.5 Morphological assessment of mineralisation utilising different types of FCS. A pool of bone marrow cells from 2 femora and 2 humeri of an 8 week old male mouse were used (n=1 mouse). Bone marrow MSCs were cultured until confluent in medium supplemented with untreated or heat-inactivated FCS (10%). MSCs ($4x10^4$ cells/well, n=3 wells per FCS type) were seeded and after overnight adherence, placed in medium containing DEX (10 nM), ASP (50 µg/ml), βGP (10 mM) and untreated (**A**) or heat-inactivated (**B**) FCS (10%) to induce mineralisation. On day 21 Alizarin red staining was performed to visualise mineralisation.

3.3.4 Identification of Optimal βGP Concentration for Mineralisation of Bone Marrow Cell Cultures

For OB to undergo the process of mineralisation, *in vitro*, βGP is required in the culture medium. High βGP concentration (10 mM) within the medium has been reported to precipitate calcium and phosphate mineral spontaneously giving an apparent false positive result (Khouja *et al.* 1990; Chang *et al.* 2000). To avoid this mineralisation assays were performed with medium containing 2 or 10 mM βGP to determine the concentration of βGP necessary for mineralisation (Tab. 2.2). Cultures were left to differentiate for 21 days and Alizarin red staining revealed mineralisation nodules in cultures stimulated with 10 mM βGP only (Fig. 3.6). Therefore βGP concentration of 10 mM was continued for subsequent assays.

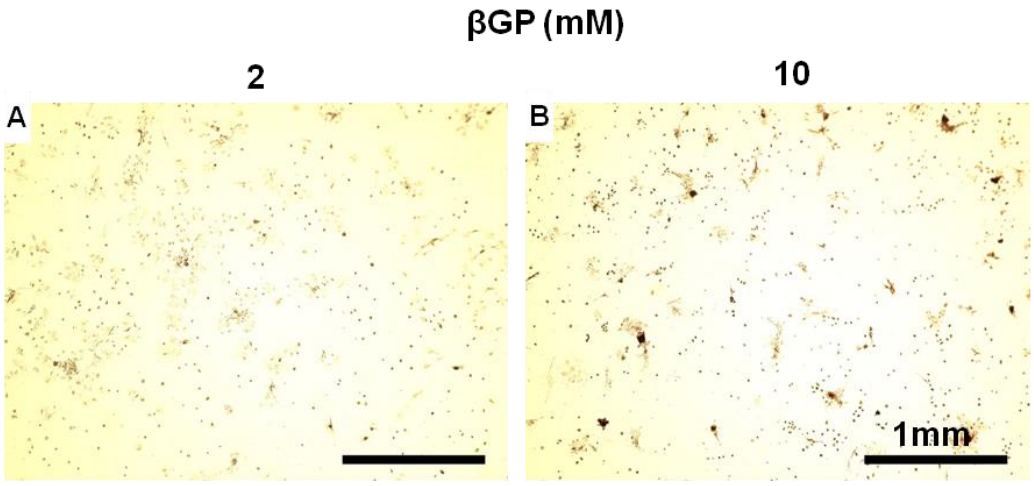

Figure 3.6 Assessment of the effect of βGP concentration on mineral nodule formation. Cells were harvested and seeded as described in Fig. 3.5 (n=1 mouse of which 3 wells were plated per βGP concentration). After overnight adherence, medium containing DEX (10 nM), ASP (50 µg/ml) and 2 (**A**) or 10 mM βGP (**B**) was added to induce mineralisation. On day 21 Alizarin red staining was performed to visualise mineralisation.

3.3.5 Assessment of Time Course of Mineral Deposition in WT and CD59a$^{-/-}$ Cultures

In order to establish if cultures derived from WT and CD59a$^{-/-}$ bone marrow cells mineralise at the same rate, mineralisation was monitored on day 14, 21 and 28. Alizarin red staining was negligible in cultures on day 14 (Fig. 3.7). Levels of mineralisation significantly increased over the duration of the time course. However this rise was more pronounced in the CD59a$^{-/-}$ samples. Minimal Alizarin red staining was identified in WT samples which was inconsistent with data obtained in section 3.3.3 and 3.3.4. A significant difference ($p<0.001$) between WT and CD59a$^{-/-}$

samples was observed (WT=9.0±6.9 and CD59a$^{-/-}$=171.7±66.3 mm^2/well (results in this format = Mean±SEM unless stated otherwise)) on day 28 as illustrated in Fig. 3.8.

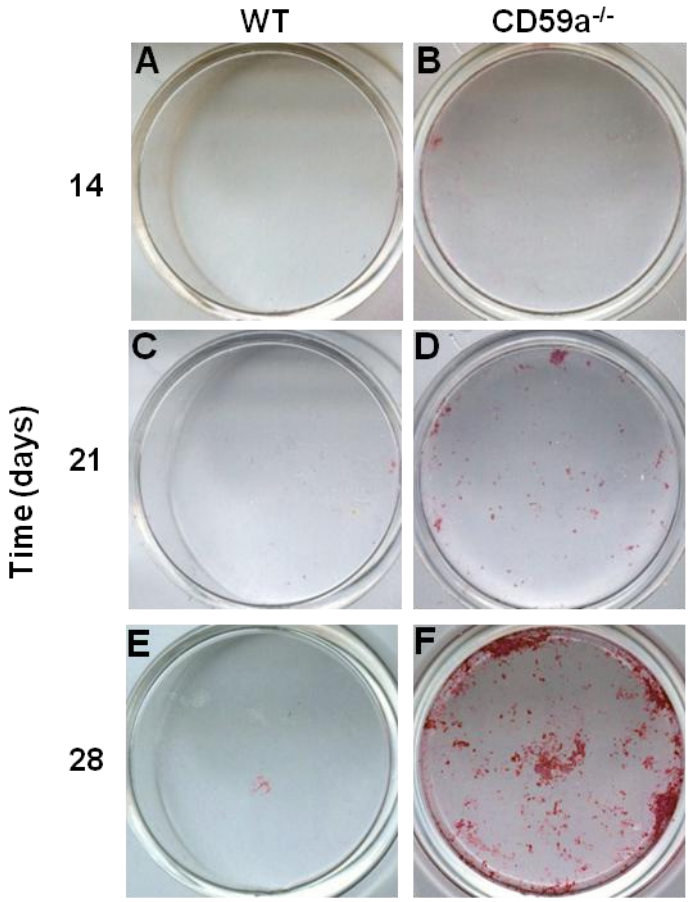

Figure 3.7 Assessment of mineralisation at different time points during culture. A pool of bone marrow cells from 2 femora and 2 humeri was obtained from a 7 week old WT (**A**, **C** and **E**) and CD59a$^{-/-}$ (**B**, **D** and **F**) mouse and cultured until confluence in complete medium for murine cell cultures (n=1 mouse per group). MSCs (4x10^4 cells/well, n=3 wells per condition) were seeded and after overnight adherence cultured in complete medium for murine cell cultures containing DEX (10 nM), ASP (50 µg/ml) and βGP (10 mM) to induce mineralisation. Alizarin red staining was performed to visualise mineralisation on day 14 (**A** and **B**), 21 (**C** and **D**) and 28 (**E** and **F**). Representative wells are shown.

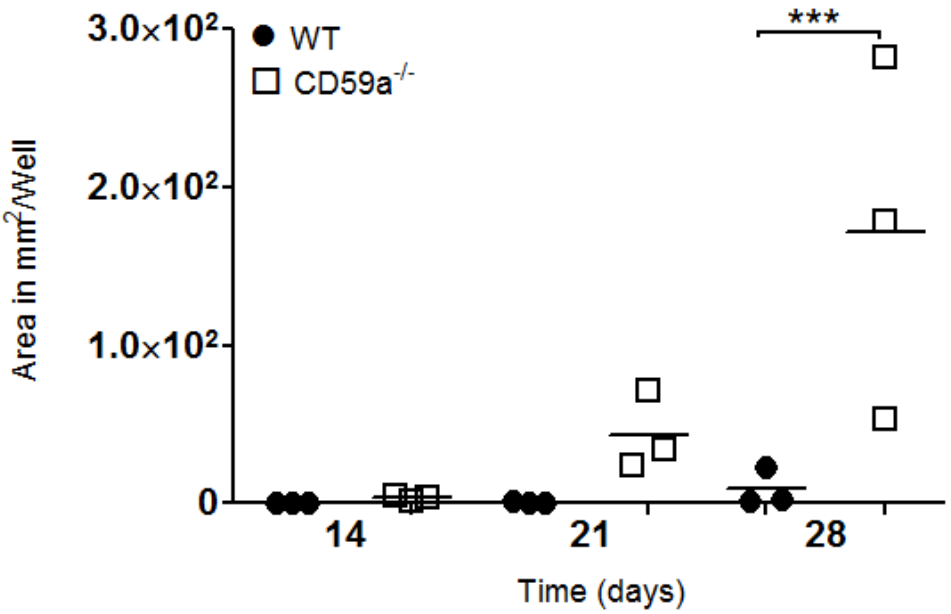

Figure 3.8 Quantification of mineralisation at different time points of culture. Cells were cultured as outlined in Fig. 3.7 (n=1 mouse per group of which 3 wells were analysed at each time point). Alizarin red staining was performed to visualise mineralisation. Surface area of Alizarin red staining was quantified utilising Image J on day 14, 21 and 28. Two-way ANOVA was performed (strain: p=0.0100, time: 0.0195, interaction: p=0.0360) and Bonferroni post-tests are indicated (***(p<0.001)).

3.3.6 Identification of Optimal Cell Seeding Density for Colony Forming Units Assays

In order to establish OB differentiation potential, murine bone marrow cultures were set up to evaluate CFU (more than 20 cells) (Vidal *et al.* 2007). Initially, cell concentrations were examined to generate high numbers of CFU. Bone marrow cells were plated at $2x10^5$, $4x10^5$ and $8x10^5$ cells/well and left to adhere overnight. Cultures were stimulated with OB differentiation medium (complete medium for murine cell cultures supplemented with DEX (10 nM) and ASP (50 µg/ml)) which was non-mineralising. After 7 days alkaline phosphatase (ALP) staining was carried out to identify CFU (section 2.3.4).

ALP staining was low in cultures at $2x10^5$ cells/well (Fig. 3.9A). As cell density was increased ALP staining became more intense and more colonies were visible (Fig. 3.9C). When the number of colonies were quantified, values significantly rose (p=0.0007) from 0 to 11±2 at $8x10^5$ cells/well (Fig. 3.10).

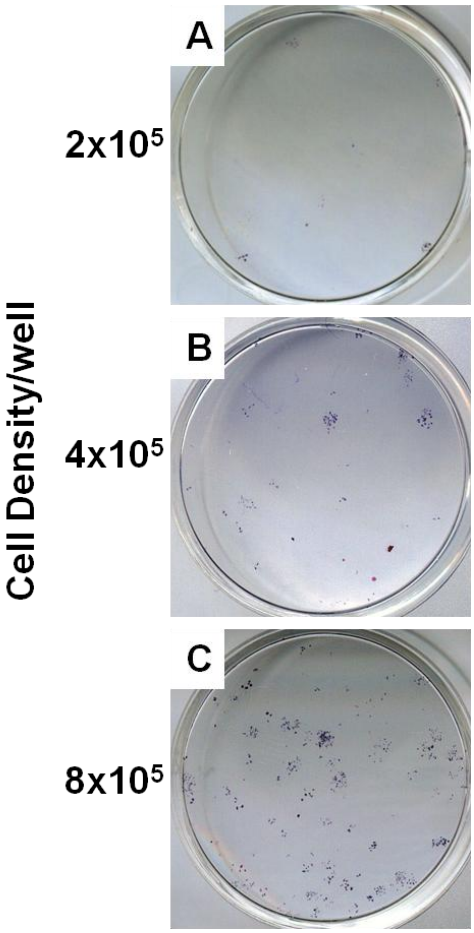

Figure 3.9 Representative images of ALP$^+$ cells in cultures grown at different cell densities. Bone marrow preparations were obtained from a 9 week old WT mouse (n=1 mouse). Cells were seeded at 2x10^5 (**A**), 4x10^5 (**B**) and 8x10^5 (**C**) cells/well (n=3 wells per cell density) and grown in the presence of OB expansion medium. After 7 days, ALP staining (blue) was performed in order to visualise CFU.

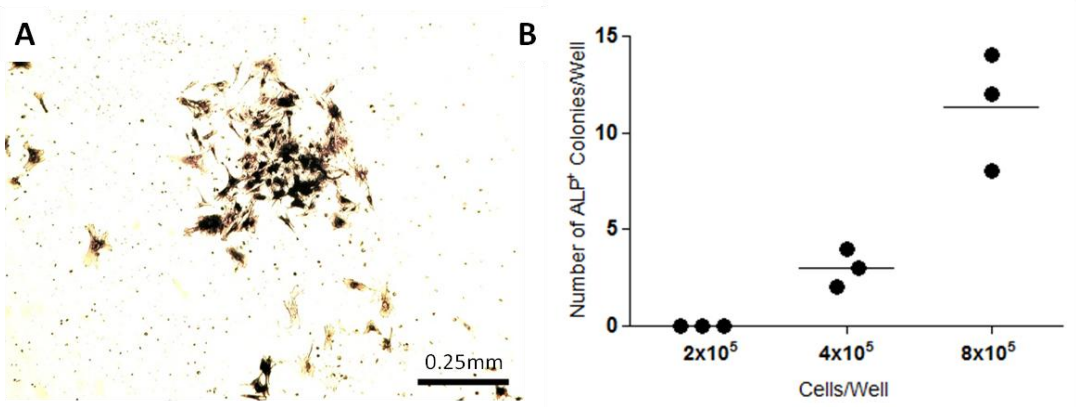

Figure 3.10 Quantification of CFU grown in cultures at different cell densities. A pool of cells from 2 femora and 2 humeri was used (n=1 mouse of which 3 wells were analysed per cell density). Representative image illustrating an ALP$^+$ colony containing more than 20 cells (**A**). Number of ALP$^+$ colonies grown at 2x10^5, 4x10^5 and 8x10^5 cells/well were counted (**B**). A One-way ANOVA (p=0.0007) was performed.

3.3.7 Establishment of an Optimised Time Point for CFU Assays

To determine whether a further increase in cell density would lead to a rise in CFU bone marrow was obtained from a 20 week old WT mouse. Cells were seeded at $8x10^5$ cells/well and $1.2x10^6$ cells/well. ALP^+ CFU was determined on day 7 and 10. When comparing CFU at $8x10^5$ cells/well quantified after 7 days to the previous WT sample, CFU significantly rose ($p<0.0001$) from 11.3±1.8 to 82±4.4 colonies/well (Fig. 3.11A). Numbers of CFU demonstrated no significant difference between $8x10^5$ cells/well (82±4 ALP^+ colonies/well) and $1.2x10^6$ cells/well (84±3 ALP^+ colonies/well) after 7 days in culture, but the colony size was increased in the $1.2x10^6$ cells/well cultures. By day 10 colonies started to merge which may have contributed to a lower number of colonies in cultures of $8x10^5$ cells/well on day 10 as illustrated in Fig. 3.11B. Therefore $1.2x10^6$ cells/well incubated for 7 days was chosen as the optimised CFU assay condition.

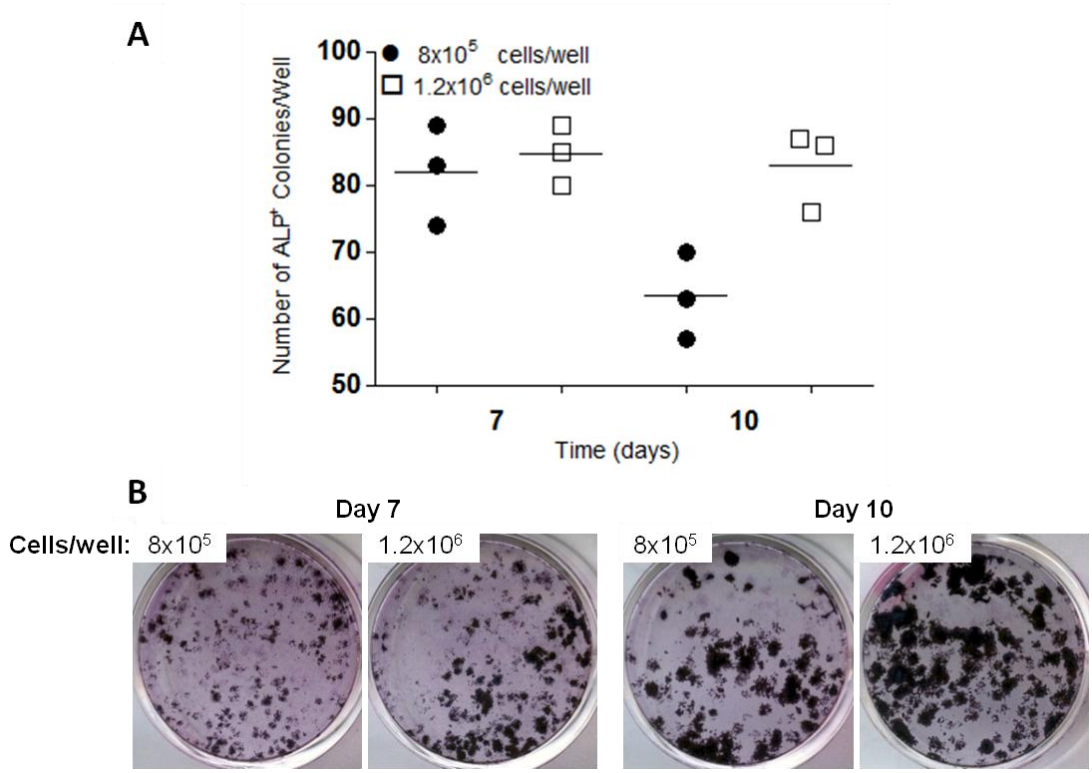

Figure 3.11 CFU re-evaluation at different cell densities and 2 time points. Bone marrow preparations were obtained from 2 femora and 2 humeri of a 20 week old WT mouse (n=1 mouse). The number of ALP^+ colonies grown at $8x10^5$ and $1.2x10^6$ cells/well (n=3 wells per group) was determined on 7 and 10 days (**A**). Representative images are shown in **B**.

3.3.8 Development of a Quantification Procedure for CFU

To establish if quantification of CFU could be simplified numbers of ALP^+ colonies were compared to ALP staining surface area. At $1.2x10^6$ cells/well the number of ALP^+ colonies was significantly greater in WT (100±8 ALP^+ colonies/well) than $CD59a^{-/-}$ (65±7 ALP^+ colonies/well) cultures (Fig. 3.12). Comparable differences were found by computer added image analysis of each well using the Image J package to quantify stained surface area (section 2.3.3.3). Hence image analysis is a reliable measure to quantify ALP stain. ALP staining measured computationally was faster and was therefore adopted for studies.

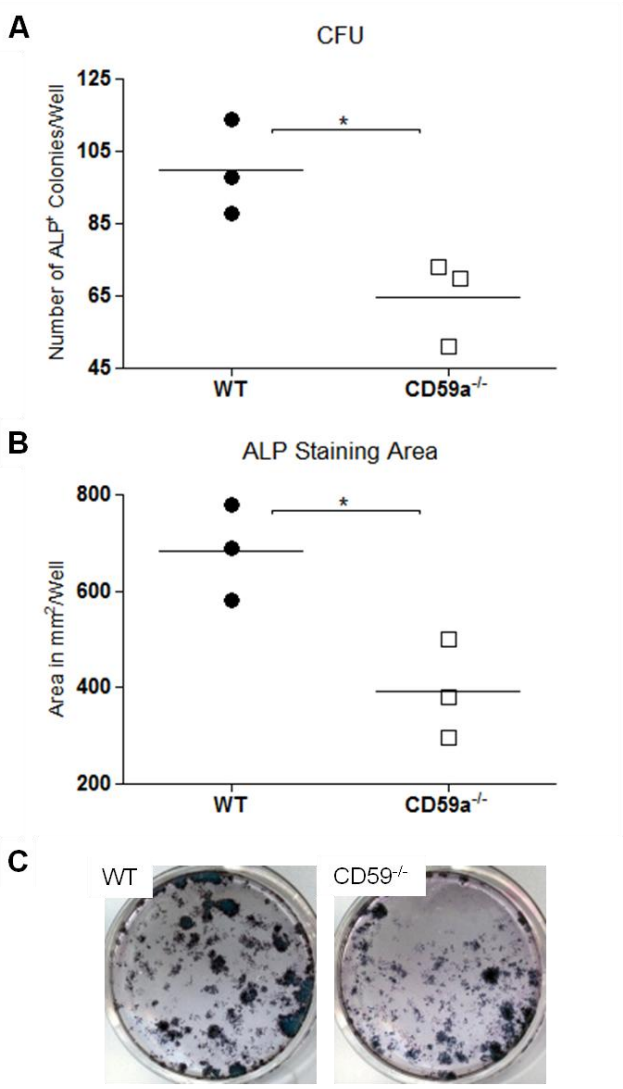

Figure 3.12 CFU in bone marrow cultures of WT and $CD59a^{-/-}$ mice on day 7. Bone marrow preparations were obtained from 2 femora and 2 humeri of an 8 week old WT and $CD59a^{-/-}$ mouse (n=1 mouse per group). $1.2x10^6$ cells/well (n=3 wells per mouse) were grown in medium for supplemented with DEX (10 nM) and ASP (50 µg/ml) for 7 days. The number of ALP^+ colonies (**A**) was determined and ALP staining surface area was quantified utilising Image J (**B**). Unpaired T-test was performed as indicated (*($p<0.05$)). Representative images are displayed (**C**).

3.3.9 Reproducibility of Mineralisation Assays

To determine the reproducibility of the mineralisation assays, 7 repetitions of WT versus CD59a$^{-/-}$ samples at 8-10 weeks were performed; in some cases 2 repeats (samples from 2 mice) were carried out at the same time. As the mineralisation assay established in section 3.3.5 did not produce adequate mineralisation in WT samples, expanded MSCs were seeded at 8x10^4 cells/well. This increase in cell density required the adjustment of time points to 14 and 17 days. A further alteration was introduced by quantifying ALP staining surface area of mineralising OBs rather than CFU from expanded bone marrow cultures. This was employed to monitor OB differentiation during mineralisation assays.

Although ALP staining surface area was consistent within experiments, between experiments as well as in WT and CD59a$^{-/-}$ samples, it varied greatly (Fig. 3.13). For example, in experiment 1 staining of CD59$^{-/-}$ samples at 1225.5±71.1 mm^2/well was reduced compared to the WT samples at 1948.5±23.3 mm^2/well (Fig. 3.13A). In experiment 2 the CD59a$^{-/-}$ staining covered an area of 293.7±20.3 mm^2/well which was raised over the WT staining (236.1±24.5 mm^2/well) on day 14 (Fig. 3.13B).

Similarly, when quantifying Alizarin red, in experiment 1 the staining surface area of CD59a$^{-/-}$ (119.5±24.1 mm^2/well) was higher than in WT (42.1±25.2 mm^2/well) samples on day 14 (Fig. 14). In contrast in experiment 6 and 7, WT and CD59a$^{-/-}$ samples stained more intensely than in experiment 1, but were comparable to each other with 1099.0±101.4 and 971.5±166.8 mm^2/well respectively. Furthermore, ALP and Alizarin red surface area were strongly correlated (p=0.0004) to each other (Fig 3.15). Therefore, in *in vitro* OB mineralisation assays the variation between mice/individual experiments was too large to reproducibly identify potential differences between WT and CD59a$^{-/-}$ mice.

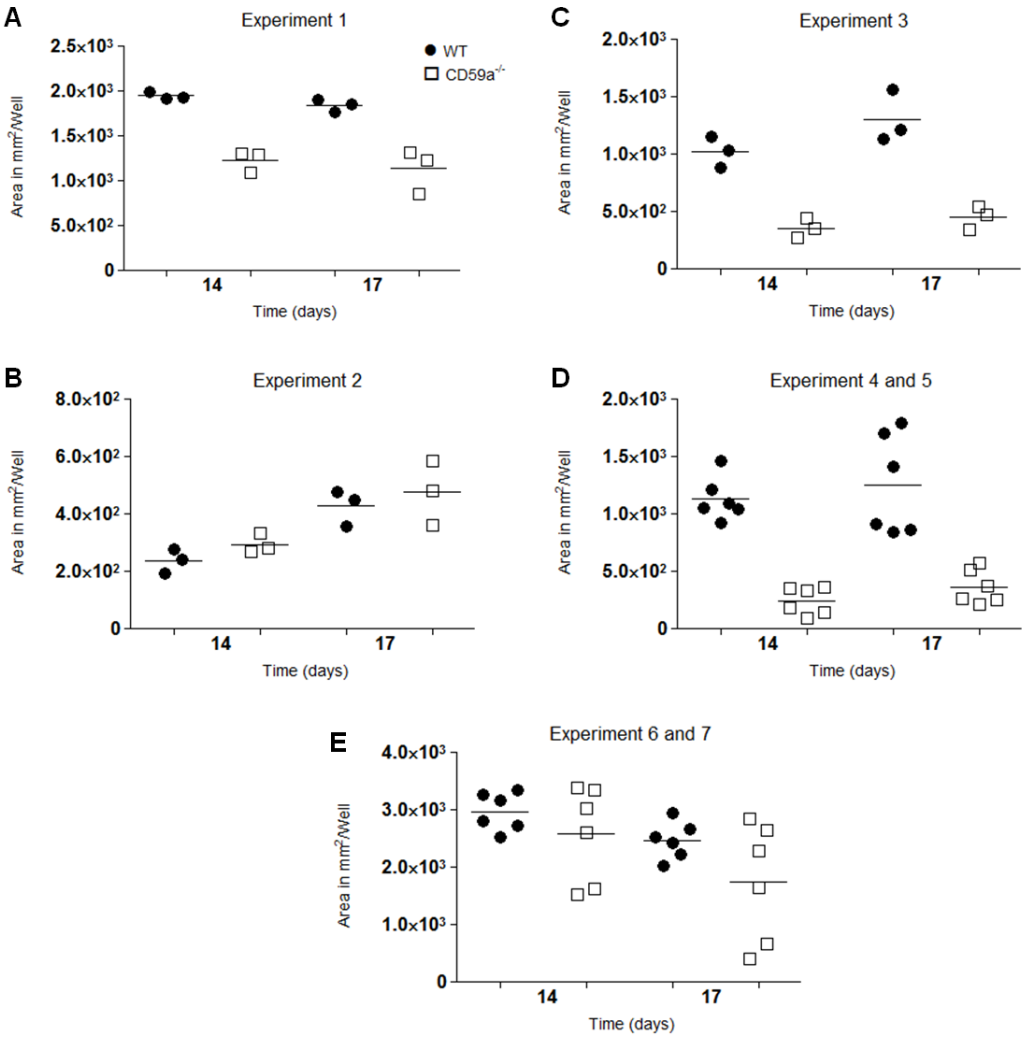

Figure 3.13 Quantification of OB differentiation. A pool of bone marrow cells from 2 femora, 2 tibiae and 2 humeri was obtained from 8-10 week old WT and CD59a$^{-/-}$ mice (n=7 mice per strain). Cells were cultured and MSCs (8x10^4 cells/well, n=3 wells per group) were subsequently seeded. After overnight adherence, cells were cultured in medium containing DEX (10 nM), ASP (50 µg/ml) and βGP (10 mM) to induce mineralisation. Surface area of ALP staining was quantified utilising Image J on day 14 and 17. Experiments 1-7 were performed over a time frame of 11 months. After experiment 1 (**A**) the FCS batch was changed. Following experiment 2 and 3 (**B** and **C**) a building move interrupted the procedure before carrying out experiment 4 to 7 (**D** and **E**).

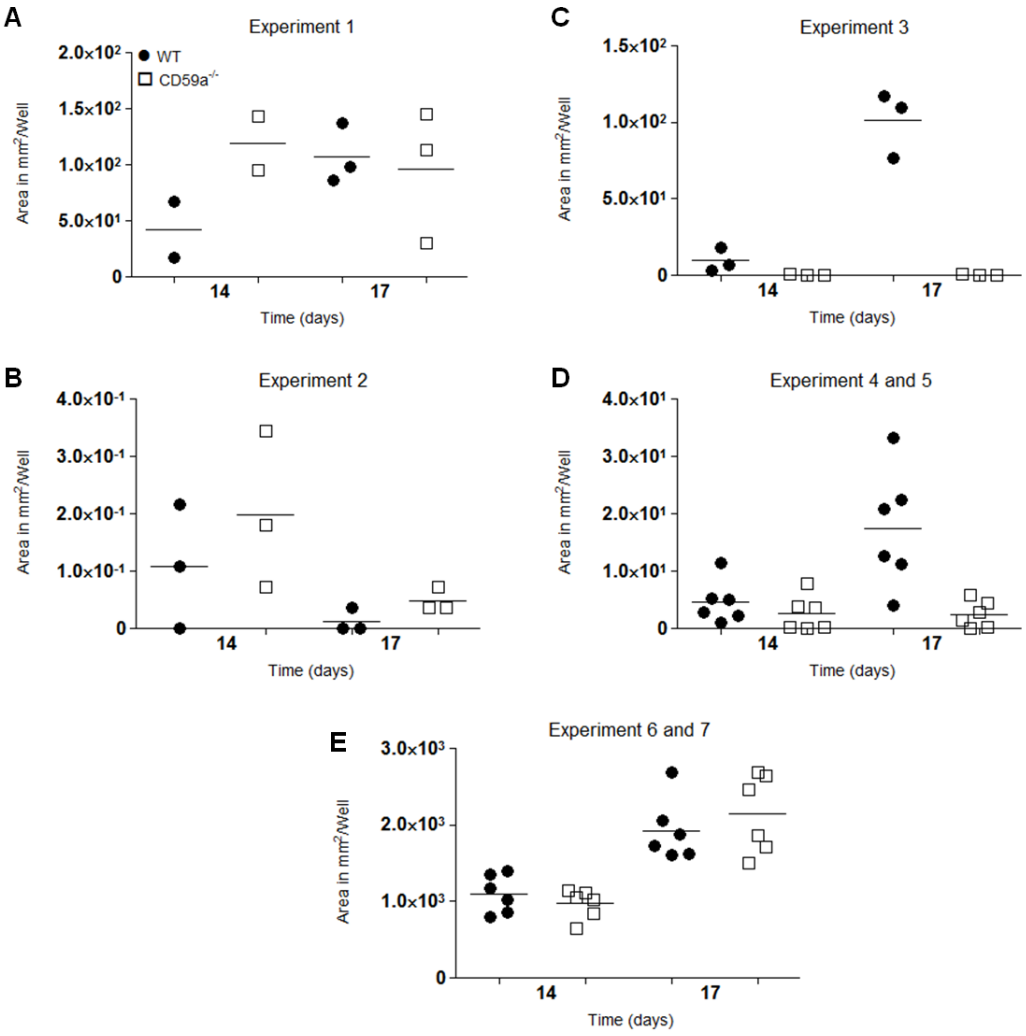

Figure 3.14 Quantification of mineralisation. A pool of bone marrow cells from 2 femora, 2 tibiae and 2 humeri was obtained from 8-10 week old WT and CD59a$^{-/-}$ mice (n=7 mice per strain of which 3 wells were analysed per group). Cells were cultured as outlined in Fig. 3.13. Surface area of Alizarin red staining was quantified utilising Image J on day 14 and 17. Experiments 1-7 were performed over a time frame of 11 months. After experiment 1 (**A**) the FCS batch was changed. Following experiment 2 and 3 (**B** and **C**) a building move interrupted the procedure before carrying out experiment 4 to 7 (**D** and **E**).

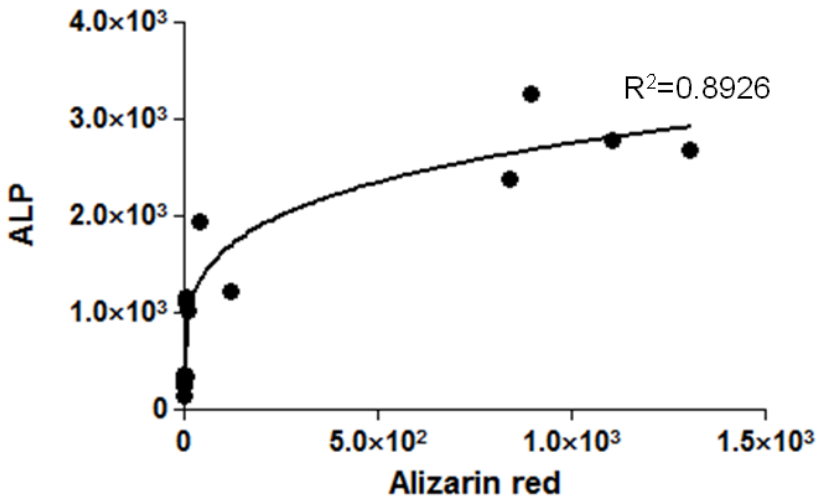

Figure 3.15 Correlation of ALP and Alizarin Red staining on day 14. Data displayed in Fig. 3.13 and 3.14 were plotted against each other to determine correlation (r^2) (n=7 mice per strain). One sample T-test was performed (p=0.0004).

3.3.10 Establishment of Cell Seeding Density and Time Course for Assessment of CFU of Adipocytes

Since MSCs also have the capacity to differentiate into adipocytes and in Fig. 3.12 and some experiments in Fig. 3.13, decreases in osteogenic CFU in CD59a$^{-/-}$ cultures were noted, I questioned whether the smaller number of osteogenic CFU drop was accompanied by increased CFU of adipocytes (AD). In order to investigate this further I set up a CFU-AD *in vitro* assay. Bone marrow cells were plated and run parallel with osteogenic CFU assays as described in section 2.3.7. Unlike the osteogenic assays which were incubated in complete medium for murine cell cultures supplemented with DEX (10nM) and ASP (50µg/ml), cultures for CFU-AD analysis were grown in DEX (1 µM, induces differentiation via CCAAT/enhancer protein-β and PPARγ), insulin (5 µg/ml, induces differentiation via IGF-1), indomethacin (50 µM, induces differentiation via PPARγ) and IBMX (0.5 µM, induces production of adipogenic and lipogenic proteins) (Lehmann *et al.* 1997; Novakofski 2004). The number of adipocyte forming colonies was counted after day 7 and 10 using Oil red O staining.

Fig. 3.16 illustrates that CFU-AD developed at $8x10^5$ and $1.2x10^6$ cells/well on day 7 and 10. When quantifying numbers of colonies, increase in cell seeding density from $8x10^5$ (14±0.3 colonies) to $1.2x10^6$ (25±5 colonies) cells/well resulted in significantly more ($p<0.05$) colonies containing 2-5 adipocytes on day 7 (Fig. 3.17). This pattern continued on day 10 and was also present in colonies

containing more than 5 adipocytes for both time points. Additionally, CFU-AD (>5 adipocytes) significantly rose at $8x10^5$ between day 7 and 10 with 6±1 and 17±1 colonies respectively; this finding also applied to $1.2x10^6$ cells/well. Consequently, $1.2x10^6$ cells/well were chosen as plating concentration and 10 days as the optimal time point for subsequent CFU-AD assays.

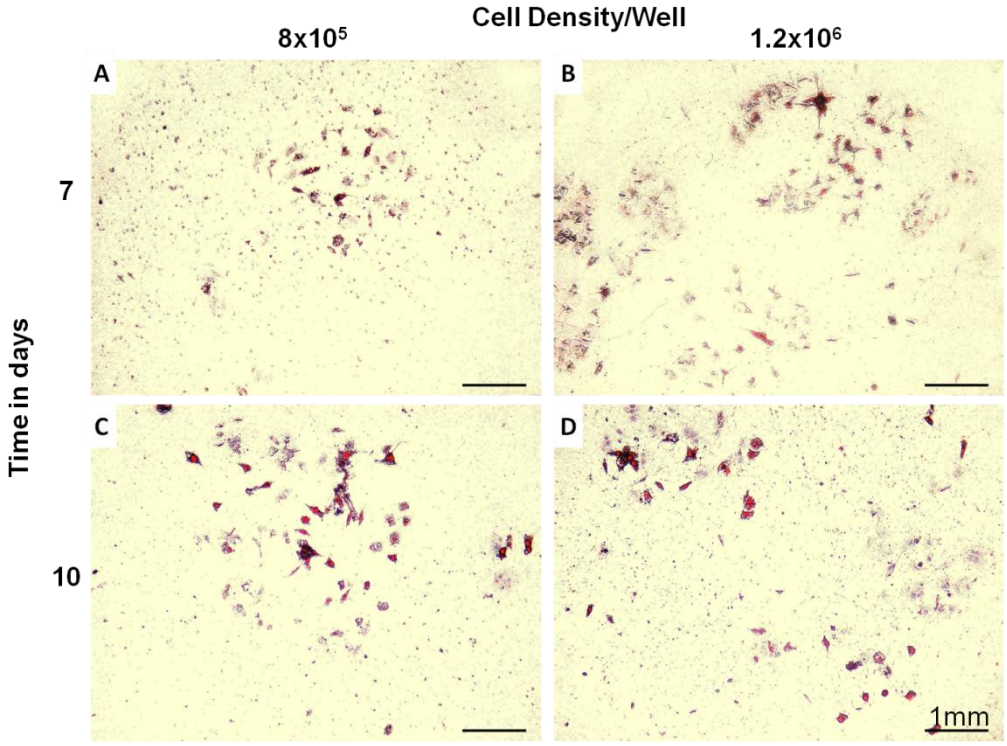

Figure 3.16 Representative images of CFU-AD using different cell seeding densities. Bone marrow preparations were obtained from a 20 week old WT mouse. Cell concentrations of $8x10^5$ (**A** and **C**) and $1.2x10^6$ (**B** and **D**) cells/well were tested. Cells were cultured in complete medium for murine cell cultures containing insulin (5 µg/ml), indomethacin (50 µM), DEX (1 µM) and IBMX (0.5 µM). Oil red O staining was performed after day 7 (**A** and **B**) and 10 (**C** and **D**).

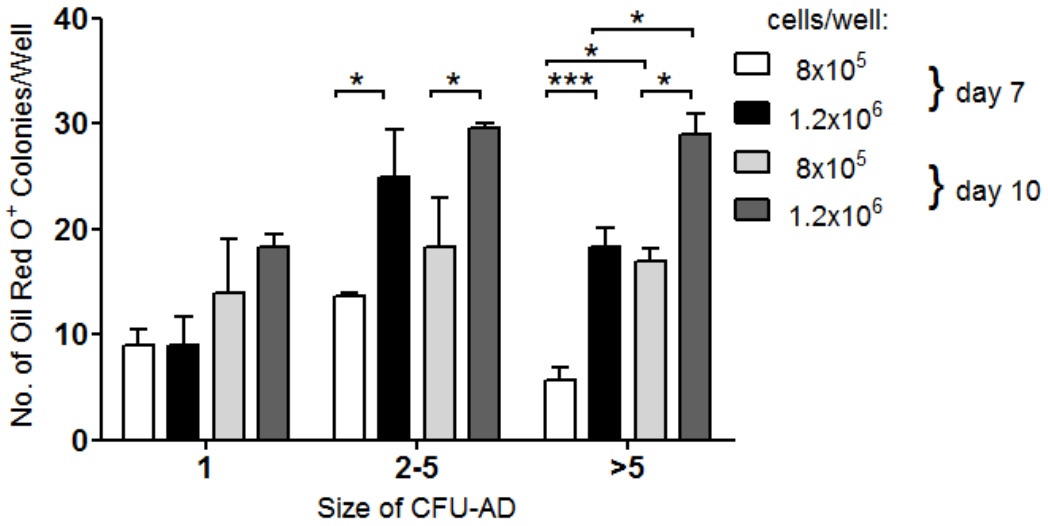

Figure 3.17 Quantification of CFU-AD. Bone marrow preparations were obtained from 2 femora and 2 humeri (n=1 mouse). Number and size of Oil red O^+ colonies (CFU-AD) grown at $8x10^5$ and $1.2x10^6$ cells/well (n=3 wells per group) for 7 and 10 days was determined. A two-way ANOVA was performed (cell density over time: $p<0.0001$, colony size: $p= 0.0003$, interaction: $p=0.1083$) and significance of Bonferroni post-tests are indicated (*($p<0.05$), ***($p<0.001$)).

3.3.11 Quantification of CFU-AD in WT and CD59a$^{-/-}$ Samples

The adipogenesis potential of WT and CD59a$^{-/-}$ bone marrow cells was investigated. Oil red O staining on day 10 revealed, significantly reduced ($p<0.001$) number of single adipocytes in CD59a$^{-/-}$ (5±1) over WT (15±1) samples (Fig. 3.18). This pattern also emerged for colonies containing 2-5 adipocytes. A similar trend was present for larger colonies (>5 adipocytes) and as visualised in Fig. 3.18B and C. However, only a single animal was analysed for each group.

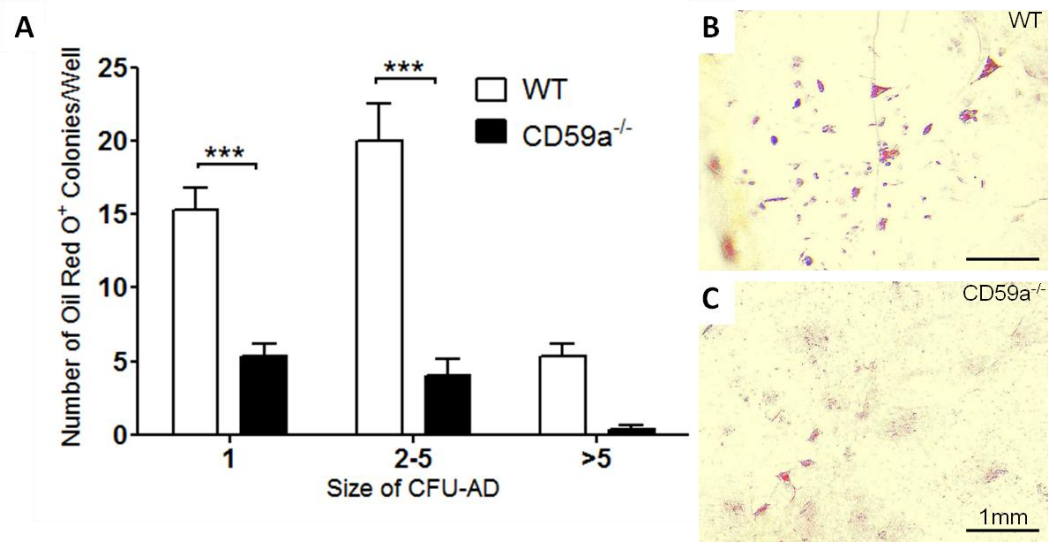

Figure 3.18 CFU-AD formation in WT and CD59$^{-/-}$ samples on day 10. Bone marrow preparations were obtained from an 8 week old WT and CD59a$^{-/-}$ mouse (n=1 mouse per strain). 1.2x10^{6} cells/well (n=3 wells per group) were grown in medium supplemented with insulin (5 µg/ml), indomethacin (50 µM), DEX (1 µM) and IBMX (0.5 µM) for 10 days (**A**). The number and size of Oil red O^{+} colonies was quantified. A two-way ANOVA was performed (strain: p<0.0001, colony size: p<0.0001, interaction: p=0.0063) and Bonferroni post-tests are indicated (***(p<0.001)). Representative images of adipocytes for WT (**B**) and CD59a$^{-/-}$ (**C**) samples are illustrated.

3.4 Discussion

The establishment of a reproducible *in vitro* OB mineralisation assay was necessary to examine OB differentiation and functionality. This chapter presents a sequential account of the method development. Additionally, *in vitro* osteogenic and adipogenic CFU assays were set up to evaluate the capacity of bone marrow cell populations to differentiate into OBs and adipocytes. These methods were then applied to analyse potential differences in bone marrow cells derived from WT and CD59a$^{-/-}$ mice.

3.4.1 Establishing a Cell Concentration Sufficient to Support OB Mineralisation

Mineralisation was induced by medium containing ASP, DEX and βGP. These mediators are commonly utilised in mineralisation assays in the literature. Inorganic phosphate was reported in some studies to induce mineralisation instead of βGP. DEX was added less frequently to cultures and was found to be substituted with mediators such as BMP-2 or Vit D to enhance ALP expression. ASP supplementation was found most consistently, especially in combination with αMEM

(Fromigué *et al.* 2008; Hoemann *et al.* 2009). These data supported our choice of mediators, but other combinations should be investigated.

For successful mineralisation the concentration of the mediators used has been shown to play an important role. In this study mediators were used at 50 µg/ml (ASP), 10 nM (DEX) and 10 mM (βGP). In the literature, mineralisation from mouse MSCs differed in their ASP concentration (14.5 µg/ml to 50mg/ml) (Choudhary *et al.* 2008; Scheller *et al.* 2010; Zhang *et al.* 2011a). According to Hoemann et al. in mineralisation assays the concentration of DEX varied between 10 and 100nM and between 5 and 10mM for βGP (Hoemann *et al.* 2009). Therefore the concentrations chosen here were comparable to published research.

In order to compare cell plating density, $1x10^4$ to $4x10^4$ cells were seeded per well ($2.6x10^3$ to $1x10^4$ cells/cm^2) and mineralisation was induced. Cells seeded at $1x10^4$ cells/cm^2 were observed to produce the highest level of mineralisation with a slightly increased size of mineralised nodules. Rajalin et al. plated $5x10^3$ cells/cm^2 expanded MSCs to induce mineralisation via the same mediators as used in this study (Rajalin *et al.* 2010). In contrast Zhang et al. preferred $5.2x10^5$ cells/cm^2 and Choudhary et al. seeded $1x10^5$ cells/cm^2 (Choudhary *et al.* 2008; Zhang *et al.* 2011a). These studies did not add DEX to their cultures. As Purpura et al. demonstrated, higher cell density makes DEX redundant in order to commit cells to the osteogenic phenotype (Purpura *et al.* 2004). Hence, the cell concentration in combination with mediators selected was in agreement with the relevant literature.

3.4.2 Assessment of Cell Source for Differentiation of Functional OBs

Bone marrow derived cultures produced more mineralised nodules than explant cultures. A search of current literature did not provide any examples of a murine study on this topic, however, a study performed by Yameen et al. in a human system provided results consistent with what was observed in the murine system. The authors compared human bone marrow derived MSC to explant cultures obtained from trabecular bone of tibiae and concluded that mineralised nodule formation was greater in bone marrow derived precursor cells (Yameen *et al.* 2009). This suggested that my study had the potential to translate to a human culture system.

3.4.3 Examination of the Effect of FCS Supplements on Mineralisation of OB Cultures

Next a source of FCS was established. Heat-inactivated FCS produced slightly smaller mineralised nodules, but at the same frequency as untreated FCS. Nimura

et al. tested human synovial MSC differentiation in untreated and heat-inactivated FCS and revealed that treatment of FCS affected proliferation of cells, but mineralisation potential was comparable (Nimura *et al.* 2010). Bruinink et al. also examined OB differentiation (utilising ALP as a read-out) from human bone marrow MSCs by supplementing medium with untreated and heat-inactivated human serum. In this study the type of serum was critical to the outcome, heat-inactivated serum resulted in less ALP staining (Bruinink *et al.* 2004). ALP activity in cultures supplemented with untreated FCS led to non-physiological mineralisation according to Hamlin and Price (Hamlin and Price 2004). In my study heat-inactivated FCS was preferred as a source to rule out exogenic complement effects and these findings from the literature supports the choice of FCS used.

3.4.4 Identification of Optimal βGP Concentration for Mineralisation of Bone Marrow Cell Cultures

When determining βGP concentration, mineralisation was found to occur at 10 mM, but not at 2 mM supplementation after 21 days in culture. Mineralised nodule formation is dependent on the presence of ALP and βGP. ALP is the enzyme that hydrolysis βGP to generate phosphate for hydroxyapatite production (Coelho and Fernandes 2000) with low levels of ALP required to convert large amounts of βGP. Supplementation of cell line cultures with 2 mM phosphate and 2 mM calcium was shown to be insufficient for induction of mineralisation (Hoemann *et al.* 2009). However, Chang et al. found that the presence of ALP and βGP in cultures causes mineral deposition on top of collagen fibrils in a manner that is not found *in vivo* (Chang et al. 2000). Therefore, the authors recommend reducing βGP to 2 mM. This concentration has been successfully used, for example, when rat calvariae derived precursor cells were stimulated for 21 days (Brandao-Burch *et al.* 2005). In my system only 10 mM produced distinct mineralised nodules when comparing βGP concentrations.

3.4.5 Assessment of Time Course of Mineral Deposition in WT and CD59a$^{-/-}$ Cultures

To establish if mineralisation occurs at the same rate in WT and CD59a$^{-/-}$ samples a time course was generated. In Fig. 3.8 mineralisation increased between day 14 and 28 in CD59a$^{-/-}$ samples whereas little staining was observed in WT samples. Collected data from different murine and human studies by Hoemann et al. reveals that mineralisation generally appeared within 2 to 3 weeks of stimulation with ASP, DEX and βGP (Hoemann *et al.* 2009). De Sauza Malaspina et al. tracked OB

differentiation over a 35 day time course when utilising the foetal human cell line hFOB 1.19. The authors observed cell proliferation within the first 7 days and formation of cell colonies by day 21. Matrix vesicles, which are responsible for initiating mineral apposition, were identified on day 21 as well. Finally, mineralisation appeared sporadically on day 28, but established itself by day 35 (de Souza Malaspina *et al.* 2009). Similarly, my study showed little mineralisation in WT samples on day 28 and might have required longer incubation in mineralisation medium to obtain larger mineralised nodules.

3.4.6 Development of a CFU Assay

CFU were established next in order to identify OB differentiation characteristics. When optimising cell concentration, CFU significantly increased between $2x10^5$ and $8x10^5$ cells plated per well ($5x10^4$ and $2x10^5$ cells/cm^2). In the literature, the comparison of cell densities for CFU from bone marrow is not routinely reported. In a study by Zhang et al. bone marrow MSCs were isolated before plating 50, 200 and 1000 cells per 60 mm diameter dishes. This was called secondary CFU as stimulation of other cell types of the bone marrow to obtain ALP^+ colonies was removed. The authors identified small number of colonies at 50 cells/dish, at 1000 cells/dish identification of individual colonies was not possible. Quantification was therefore performed at 200 cells/well (Zhang *et al.* 2011b). Scutt et al. recommended keeping cell seeding density low to enable individual CFU to adhere and proliferate to represent clonal expansion from a single precursor cell. The authors suggested to seed $3.6x10^4$ cells/cm^2 (Scutt *et al.* 2003). Other papers utilise 0.5 to $1.5x10^5$ cells/cm^2 which is close to the range used in my study (Isogai *et al.* 1996; Chou *et al.* 2009). $2x10^5$ cells/cm^2 produced a small number of CFU in my study when quantification was performed after 7 day incubation. Published data, utilising these seeding densities, analysed osteogenic CFU after 10 to 18 days (Dimai *et al.* 1998; Scutt *et al.* 2003; Chou *et al.* 2009), therefore larger colonies would have been obtained upon longer incubation in my study.

Consequently, $8x10^6$ and $1.2x10^6$ cells were seeded per well ($2x10^5$ and $3x10^5$ cells/cm^2) and incubated for 7 and 10 days. $3x10^5$ cells/cm^2 produced the highest density of large, non-merging CFU after 7 days in culture. Therefore my study proved that a higher cell concentration allows for a shorter incubation period to obtain efficient colony formation.

When comparing the number of CFU at $8x10^5$ cells/well quantified after 7 days between a 9 and 20 week old mouse, CFU were up-regulated in the latter. This could have resulted from variation between assays, but Zhang et el. studied

differentiation potential of C57BL/6 bone marrow cells at 3-6, 12-18 and 24 month old mice and data revealed that CFU increased between 3 to 18 month before declining at 24 month (Zhang *et al.* 2008). Therefore it was likely that increased CFU resulted from an enhanced differentiation potential in the 20 week old mice utilised in my study. Furthermore it highlighted the importance of comparing age matched mice. These were used in all subsequent experiments.

ALP is a marker for early OB differentiation (Rosen 2008) and therefore ALP^+ colonies containing more than 20 cells were quantified initially in this method as CFU. When comparing this to quantification methods in the literature, Chou et al. differentiated between ALP^+ and total number of colonies (Chou *et al.* 2009). Similarly, Dimai et al. utilised the same methodology, but included the number of ALP^+ cells within each colony (Dimai *et al.* 1998). This analysis was not performed here because most cells were ALP^+ cells. Additionally some studies determined $calcium^+$ and $collagen^+$ colonies (Still and Scutt 2001; Holmes *et al.* 2004), a method that should be considered for future studies as it is an efficient mean to identify cell differentiation and functionality within the same assay.

As ALP^+ cells were the predominant cell type in my assays, evaluation of ALP staining was considered. Quantification of ALP staining surface area produced a comparable result to the number of ALP^+ colonies counted. Counting colonies is the predominant method of analysis in the literature, either microscopically or via computer software (eg. IQ software using Photoshop) (Stenderup *et al.* 2001; Scutt *et al.* 2003). Other groups analysed ALP activity by adding *p*-nitrophenylphosphate to cultures and measuring the absorbance of formed *p*-nitrophenyl at 405 nm (Evans *et al.* 2000; Baksh *et al.* 2007). Kamalia et al. demonstrated quantification of endogenous ALP by flow cytometry after trypsin-EDTA digestion of OBs and staining with fast violet lb salt or fast red tr salt (fluorescent) (Kamalia *et al.* 1992). Hence the literature either focused on the number of colonies or the quantification of ALP. The methodology applied in this study allowed for ALP quantification while retaining colony and cell morphology.

3.4.7 Quantification of CFU in WT and $CD59a^{-/-}$ Bone Marrow Cultures

When applying the optimised methodology to samples, ALP staining surface area was raised in WT over $CD59a^{-/-}$ samples, but this experiment needs to be repeated. Human CD59 is expressed on MSCs and used as the surrogate marker in many studies to identify MSCs from primary cell sources and long term cultures (Izadpanah *et al.* 2006; Lange *et al.* 2007; Watson *et al.* 2010). Javazon et al.

monitored and compared CD59 expression on human and rat expanded MSCs in colony forming assays without stimulation by DEX and ASP. CD59 was expressed on all mature MSC colonies in human and rat cultures (Javazon *et al.* 2001). Consistent expression of CD59 on mature MSCs suggests that CD59 might be involved in MSC differentiation. If the down-regulation of ALP^+ colonies in $CD59a^{-/-}$ mice can be repeated, the effects of the complement system need to be considered. Moll et al. studied the interaction of MSCs and the complement system. MSCs were shown to suppress acute immune response when activated and recruited to the site of injury by C3a and C5a. When MSCs were injected into blood, deposition of iC3b and C3dg, but not C1q was noted. Additionally, MSCs were shown to express CD59 as the sole complement regulator that efficiently prevented complement mediated lysis (Moll *et al.* 2011). The effect of MAC on MSCs has not been identified yet, but from the collated research it can be predicted that CD59 signalling and protection from complement mediated lysis may be involved in OB differentiation.

3.4.8 Reproducibility of Mineralisation Assays

When quantifying ALP and Alizarin red staining surface area of the mineralisation assays, experiments were internally consistent, but assays showed a large degree of variation between animals or individual experiments. During the study numerous environmental factors were altered. Initially a batch change in FCS had to be performed. Anselme et al. performed a batch test with 6 different FCS to choose the one which produced most ALP^+ colonies, demonstrating the variability caused by this supplement (Anselme *et al.* 1999). Here only 3 batches were tested to obtain comparable mineralisation to the present batch. Additionally, our laboratories moved building after experiment 3 and an incubator change was performed. Successful bone marrow cell cultures depend on temperature, pH and humidity (Till and McCulloch 1961) which should be regulated by the incubator, but might have been affected by the new environmental conditions.

Further variables arose as these were primary cultures derived from mice. The mice encountered infections (pinworm, protozoa, Novovirus, *Helicobacter species*) within the Joint Biomedical Service Unit. *Helicobacter species*, for example, are gram-negative bacteria that infect the gastrointestinal tract. These bacteria can cause gastritis, inflammatory bowel diseases as well as hepatitis and liver lesions (Laboratory 1997). The resulting inflammatory response might have led to activation and release of numerous leukocytes from the bone marrow (Hermesh *et al.* 2010) possibly affecting starting cell populations.

On some occasions, these infections were treated with antibiotics in the drinking water. Bruckner et al. highlighted that treatment of mice with antibiotics can alter gastrointestinal bacteria leading to antibiotic resistance (Bruckner 1976). Alterations in gastrointestinal flora might have also induced inflammation. Additionally, antibiotics could have caused toxicity to murine cells. Hu et al. identified that when porcine heart valves were stored in RPMI with Streptomycin it caused a reduction of cell viability by 60% within 12 h (HU *et al.* 1989). Consequently, reduced viability might have altered the bone marrow environment. Various exogenous factors contributed to assay variability and should be kept constant in future experiments to obtain more consistent results.

3.4.9 Establishment of Cell Density and Time Course for CFU-AD

To investigate MSCs' capacity of WT and CD59a$^{-/-}$ samples to differentiate into adipocytes, a CFU-AD assay was established. 1.2x10^6 cells were plated per well (3x10^5 cell/cm^2) and incubated for 10 days in presence of DEX (1 µM), Insulin (5 µg/ml), Indomethacin (50 µM) and IBMX (0.5 µM) to obtain the highest possible yield of CFU-AD. Stimulation with these mediators is most common in the literature, but is also performed by other mediators such as hydrocortisone, rosiglitazone and netolgitazone. Furthermore, the cell density of 3x10^5 cell/cm^2 used in this chapter is in agreement with published data (Moerman *et al.* 2004; Novakofski 2004; Lazarenko *et al.* 2006).

3.4.10 Quantification of CFU-AD in WT and CD59a$^{-/-}$ Samples

CFU-AD were reduced in one CD59a$^{-/-}$ over WT samples and also requires repeating. However, Festy et al. identified expression of CD59 on mature adipocytes and linked CD59 to obesity (Festy *et al.* 2005). Misso et al. studied aromatase knockout mice which developed obesity featured by hypertrophy of adipocytes. When these mice were fed with cholesterol weight loss was induced and, amongst the mediators monitored, CD59 expression levels were altered (Misso *et al.* 2005). This evidence highlights not only the continued expression of CD59 once differentiated, but also its diverse involvement in different tissue mechanisms. As OB and adipocyte differentiation could be reduced in CD59a$^{-/-}$ mice, MSCs differentiation capacities should be investigated.

3.5 Conclusion

To conclude, *in vitro* investigation of the effect of CD59a on OB differentiation revealed the subsequent findings:

- Internally consistent mineralisation and CFU assay were successful established.
- The impact of CD59a on mineralisation was not revealed due to assay variability.
- However, CD59a may be involved in regulation of CFU.

With regard to the effect of CD59a upon mineral apposition, my data was inconclusive. Since the function of OBs is dynamically related to the functions of OCs in bone I next investigated the impact of CD59a upon OC differentiation and function.

Chapter 4

Assessing the Impact of CD59a on Osteoclastogenesis

4.1 Introduction

The possible changes seen in osteoblast (OB) differentiation in the absence of CD59 in chapter 3 add further weight to the hypothesis that CD59a could exert an important function in bone in mice. Evidence for this notion comes from observations in experimental models of arthritis. In a murine model of rheumatoid arthritis (RA) CD59a insufficiency caused an increase in erosive bone pathology (Williams *et al.* 2004). Unpublished preliminary data of Dr Anwen Williams revealed that 19 month old CD59a$^{-/-}$ mice presented with a spontaneous bone disease characterised by excessive osteoclast (OC) expression in joint tissues, which was not seen in WT mice. At the same time the synovial joint was clear of inflammatory cells. This data led us to my hypothesis that this effect might be independent of inflammation. This also led to the question: is CD59a's functionality in bone uncoupled from or dependent upon MAC? To address this question C6$^{-/-}$ mice were included in this study. C6 is an essential component of the MAC complex. C6$^{-/-}$ mice cannot therefore assemble the MAC complex and all functions performed by CD59a should be uncoupled from the complement system in these mice. If C6$^{-/-}$ mice behave like WT mice, than the signalling of CD59a in bone would be complement independent. If C6$^{-/-}$ act like CD59a$^{-/-}$ mice than both components (MAC and CD59) are required for signalling and disruption of either component would prevent regulation of OCs. Complement independent function of CD59a has been reported previously in T-cells and other areas of biology, these are described in detail in section 1.3.1. The mechanisms that might explain the protective effect of CD59a on bone in mice (with or without arthritis) have not been evaluated previously.

4.2 Aim and Objectives

The aim of this chapter was to study the impact of CD59a and MAC upon OCG from mouse bone marrow preparations. In order to achieve this aim I identified 3 key objectives; they were:

1. To develop a reproducible OCG assay.
2. To perform phenotypic analysis of bone marrow cells in WT, CD59a$^{-/-}$ and C6$^{-/-}$ mice, in order to determine whether any differences in OCG might be attributed to variability in the starting cell population.
3. To measure OCG under controlled conditions *in vitro* in WT, CD59a$^{-/-}$ and C6$^{-/-}$ mice.

4.3 Results

In the first instance, a reproducible system for monitoring OC differentiation *in vitro* had to be established in the laboratory. Only then could the role of MAC and CD59a be determined during OCG. Murine bone marrow cells were obtained from WT, $C6^{-/-}$ and $CD59a^{-/-}$ mice. All mice were aged between 8 and 10 weeks at time of sacrifice. Bone marrow cells were harvested as described in section 2.4.3. Initially, OCG was established using WT bone marrow cell cultures. Assay conditions were optimised to obtain 1) uniform OC coverage on glass coverslips, 2) reproducible OC titres between assays, and 3) sufficient OC yields for counting and mechanistic studies. OCG assays were then established in $C6^{-/-}$ and $CD59a^{-/-}$ and all outcome measures (Cat K, MMP-9, mKc) compared against WT data. The results of these studies are reported herein.

4.3.1 Morphological Assessment of Bone Marrow Preparations

When bone marrow preparations were adhered to glass coverslips, they were densely populated (Fig. 4.1A). Hence cytospins of bone marrow samples were prepared in order to conduct differential cell counts on the bone marrow cell populations (Fig. 4.1B and C). The Giemsa/May-Grünwald stain was used to differentiate between leukocyte cell populations (section 2.4.5.2). From the initial investigations, the following groups were identified: erythrocytes, lymphocytes, monocytes, megakaryocytes and others (including small numbers of MSCs). All leukocyte subsets were of an equivalent number in WT and $CD59a^{-/-}$ cell populations on day 0. Samples contained monocytes (50-60%), megakaryocytes (20%) and lymphocytes (8-10%). Erythrocyte counts varied somewhat between WT (18%) and $CD59a^{-/-}$ (6%) samples (Fig. 4.1B and C).

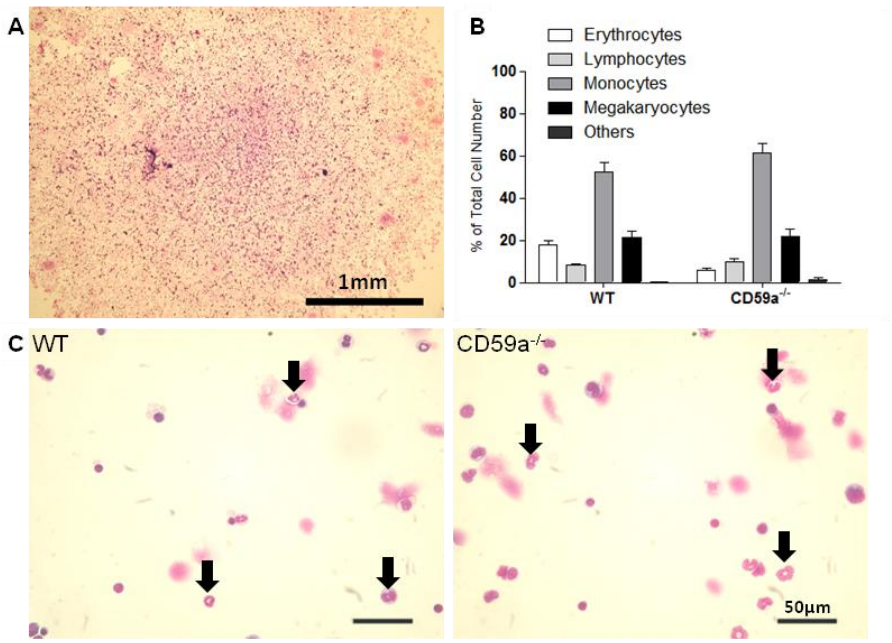

Figure 4.1 Characterisation of bone marrow preparation at day 0. Cell preparations obtained from the bone marrow of 8-10 week old female WT and CD59a$^{-/-}$ mice were cultured on 6 mm glass coverslips (n=1 mouse per strain of which 3 coverslips were set up). Cells were seeded at a density of 6.4x10^4 cells/10 µl and stained for Giemsa/May-Grünwald after 2 h adherence (**A**). Bone marrow cells prepared using cytospin (6.4x10^4/100 µl) and stained with Giemsa/May-Grünwald for differential cell counts (n=5 random FoV per coverslip). Graph illustrating percentage of total cell number of grouped populations (**B**). Representative images of cytospin are shown and arrows point to examples of monocytes (**C**).

4.3.2 Differentiation of WT Mouse Bone Marrow Preparations into OCs

WT bone marrow cells (3x10^5 and 5x10^5 per well) were adhered to 13 mm glass coverslips that were cultured in M-CSF (25 ng/ml) alone or in combination with RANKL (2 and 5 ng/ml) for 7 days. Pre-OCs and OCs stained maroon with TRAP and were counted using light microscopy (section 2.4.5).

No TRAP$^+$ cells were observed in cultures grown in M-CSF alone (Fig. 4.2 A and B). The addition of RANKL was required to generate TRAP$^+$ cells (Fig. 4.2 C to E). For each test condition studied, 1) the average number of cells, 2) average number of TRAP$^+$ cells and 3) average number of TRAP$^+$ multinucleated cells per FoV (n=5 per coverslip) was determined.

Total cell numbers were higher in cultures containing M-CSF over those containing M-CSF and RANKL (Fig. 4.3A). There was no significant difference in the number of TRAP$^+$ cells at RANKL concentrations of 2 ng/ml compared to 5 ng/ml (Fig. 4.3B and D).

In the literature, OC differentiation was shown to be dependent on starting cell number (Ishida *et al.* 2002), hence OC yield were compared at initial bone marrow cell densities of $3x10^5$ cells/well and $5x10^5$ cells/well. Multinucleated $TRAP^+$ cells (OCs) were counted for each condition as defined in section 2.4.5 (Fig. 4.3C). OCs (expressed as a percentage of total cells) were significant higher ($p<0.01$ and $p<0.001$) when cells were seeded at $3x10^5$ cells/well (42.8±2.1% and 44.2±2.8% (results in this format = Mean±SEM unless stated otherwise)) compared to $5x10^5$cells/well (32.5±2.4% and 29.8±2.4%) with RANKL at 2ng/ml and 5ng/ml respectively (Fig. 4.3D). There was no significant difference in the percentage of multinucleated $TRAP^+$ cells in cultures containing RANKL at 2ng/ml versus 5ng/ml seeded at the same initial cell density. Therefore, in succeeding experiments $3x10^5$cells/well was selected as the optimal starting cell density with M-CSF (25ng/ml) and RANKL (2ng/ml) chosen as optimal conditions to achieve the highest OC yields.

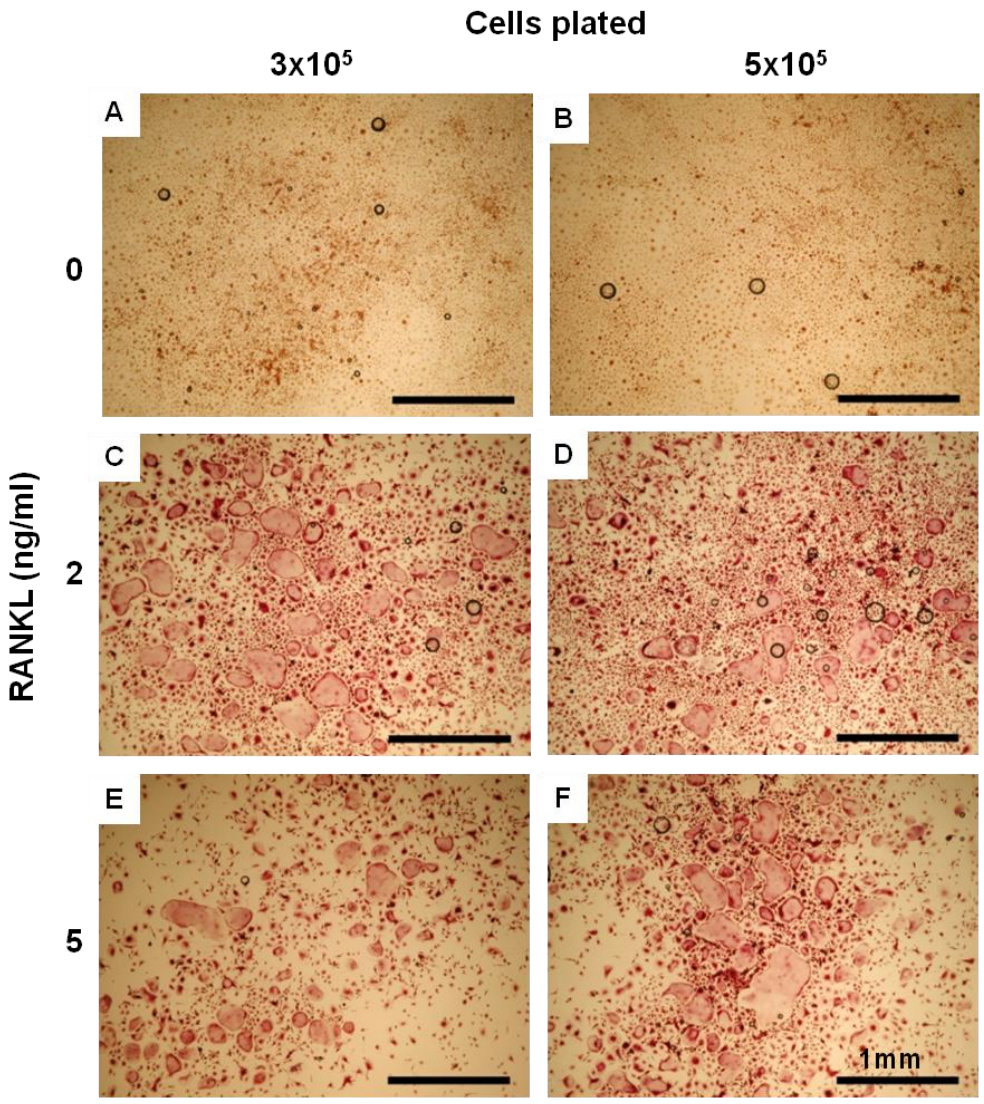

Figure 4.2 Representative images of OCs grown on 13 mm glass coverslips. Bone marrow preparations were obtained from an 8 week old male WT mouse. Cell concentrations $3x10^5$ (**A**, **C**, **E**) and $5x10^5$ (**B**, **D**, **F**) were tested. Cells were cultured in presence of M-CSF (25ng/ml) with and without RANKL on 13 mm glass coverslips. After 7 days, TRAP staining was performed. Cells were stimulated with M-CSF only (**A** and **B**), M-CSF and 2ng/ml RANKL (**C** and **D**), M-CSF and 5ng/ml RANKL (**E** and **F**).

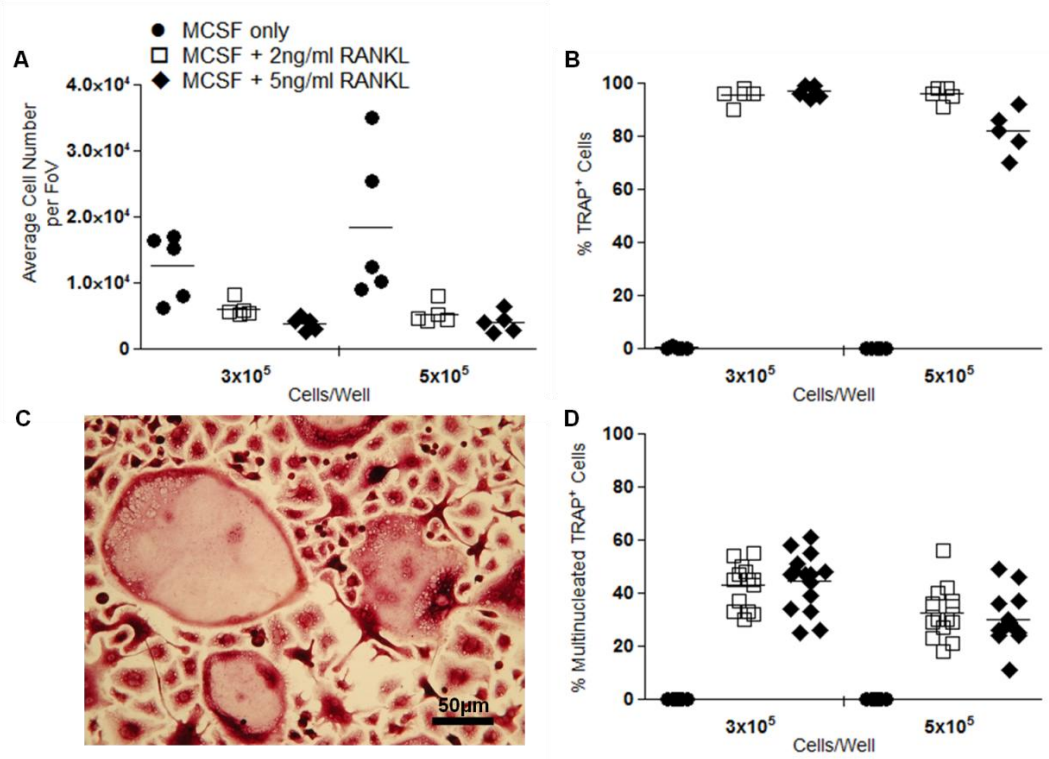

Figure 4.3 Quantification of OC on 13 mm glass coverslips. A pool of cells from 2 femora for each mouse was used (n=1 mouse of which 3 coverslips were prepared). Cells grown in M-CSF only (●), M-CSF and 2ng/ml RANKL (□) and M-CSF and 5ng/ml RANKL (♦) were quantified. Total cells (**A**), TRAP$^+$ (**B**) (maroon stained) cells and multinucleated TRAP$^+$ (**D**) cells were counted. Multinucleated cells were defined as 2 or more nuclei containing cells (**C**). Data are shown as total cells counted in 5 FoV (a) and % TRAP$^+$ cells (b, c) determined at end point (5-15 FoV). Two-way ANOVAs (and Bonferroni post-tests (see in text) were performed for **A** (cell density: $p<0.3703$, RANKL concentration: $p<0.0001$, interaction: $p=0.3231$), **B** (cell density: $p<0.0021$, RANKL concentration: $p<0.0001$, interaction: $p=0.0002$) and **D** (cell density: $p<0.0001$, RANKL concentration: $p<0.0001$, interaction: $p=0.0016$).

4.3.3 Improving OC Coverage on Coverslips

Although OC yields were adequate using 13 mm coverslips, I frequently observed inconsistency in cell coverage and a patchy appearance to the cells at end point. In order to overcome this problem, 6 mm coverslips were trialled as shown in Tab. 2.4. The cell density was adjusted accordingly from $3x10^5$ cells/coverslip to $6.4x10^4$ cells/coverslip. These smaller coverslips also allowed for capture of more than 80% of the total surface area of the coverslip in 5 FoV at x10 object magnification under the microscope. The total cell number and $TRAP^+$ multinucleated cells were determined in order to calculate OC differentiation (%) on each coverslip. Cells were distributed evenly over the coverslips; average cell numbers ranged from 310 to 385 cells/FoV as summarised in Fig. 4.4A. Multinucleated $TRAP^+$ cells were compared in 3 separate wells, the values were comparable at 15.8±1.1%, 16.0±1.4% and 15.3±1.1% (Fig. 4.4B).

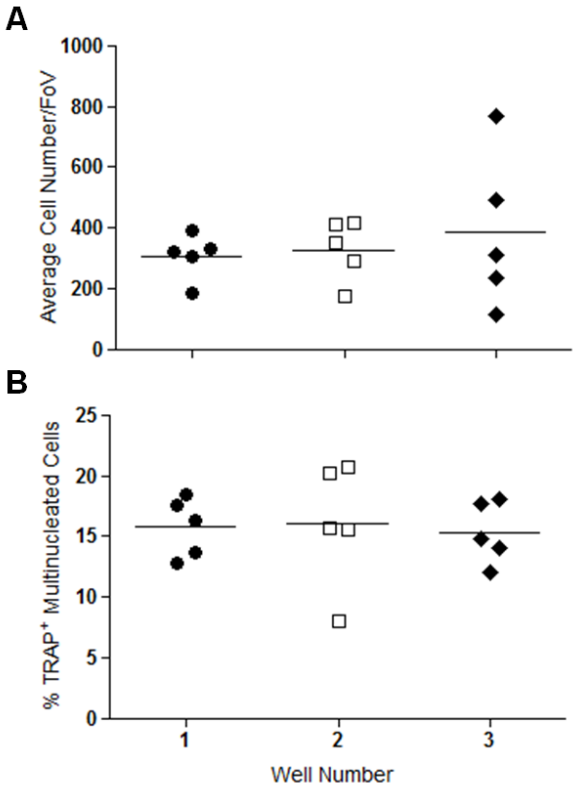

Figure 4.4 OC coverage on coverslips. $6.4x10^4$ bone marrow cells from an 8 week old female mouse were plated onto 6 mm glass coverslips (n=1 mouse). After adherence 3 coverslips were added into single wells (n=3 wells) of a 24 well plate containing differentiation medium (M-CSF and RANKL). One coverslip/well was removed on day 3, 5 and 7. After 7 days, TRAP staining was performed on one coverslip/well. Total cells (**A**) and multinucleated $TRAP^+$ cells were counted for a 5 FoV/coverslip to determine variation between wells. Percentage multinucleated $TRAP^+$ cells was calculated (**B**).

4.3.4 Assessing the OCG Assay over a Seven Day Time Course

OCG assays were initiated using WT and CD59a$^{-/-}$ bone marrow preparations as described in section 2.4.4. Cells were incubated in M-CSF (25 ng/ml) alone or M-CSF and RANKL (2 ng/ml). OC differentiation was monitored on day 3, 5 and 7 of the assay using TRAP staining.

On day 3 (Fig. 4.5A), total cells per FoV in samples grown in M-CSF were higher in CD59a$^{-/-}$ (156±77 cells/FoV) than WT (42±12 cells/FoV). The trend was unchanged on day 5; the total cell number rose in CD59a$^{-/-}$ to 499±92 cells/FoV and in WT to 117±33 cells/FoV. By day 7 the total cells per FoV were significantly different in CD59a$^{-/-}$ (1975±483 cells/FoV) versus WT (381±70 cells/FoV) cultures ($p<0.001$). Proliferation between day 3 and 7 was comparable in WT and CD59a$^{-/-}$ samples. Representative images of the changes in TRAP^{-} cell number are shown in Fig. 4.5B.

Counts of cells (WT and CD59a$^{-/-}$) grown in M-CSF and RANKL were comparable to samples cultured in M-CSF alone at day 3 (Fig. 4.6A). By day 7 the total cell per FoV in CD59a$^{-/-}$ was 401±63 cells/FoV which was significantly higher ($p<0.001$) than day 3 counts. In contrast, WT cell expansion was stagnated giving total cell counts of 100±41 cells/FoV. Cell counts were therefore significantly higher in CD59a$^{-/-}$ than WT cultures on day 5 ($p<0.05$) and on day 7 ($p<0.001$).

Multinucleated TRAP^{+} cells or OCs (expressed as percentage of total cells) increased significantly in both WT ($p<0.01$) and CD59a$^{-/-}$ ($p<0.001$) cultures over time (Fig. 4.6B). On day 3 only a small number of OCs were observed in WT (0.1±0.1%) and CD59a$^{-/-}$ (0.4±0.3%) samples (Fig. 4.6C). By day 5, OCG had increased slightly to 3.3±0.1% in CD59a$^{-/-}$ and 1.8±0.5% in WT samples. By day 7 the majority of cells stained positive for TRAP. OCs were significantly increased (versus day 3) in both CD59a$^{-/-}$ (17.3±1.6%) and WT (5.2±0.5%) samples ($p<0.001$, $p<0.01$), however, OC numbers were significantly greater for CD59a$^{-/-}$ versus WT cells ($p<0.001$).

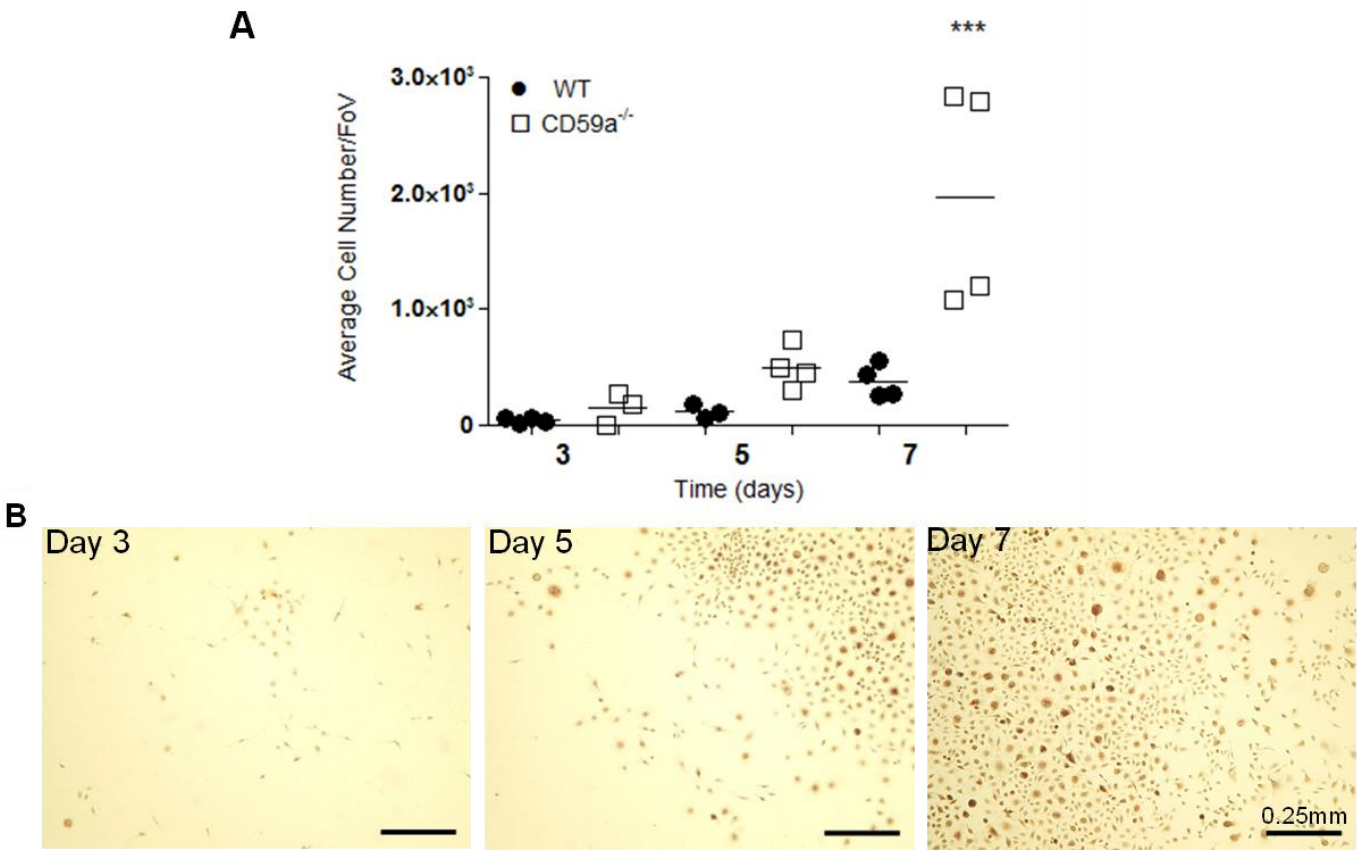

Figure 4.5 Time course testing to evaluate cell proliferation. $6.4x10^4$ bone marrow cells from an 8 week old female WT (●) and $CD59a^{-/-}$ (□) were plated onto 6 mm glass coverslips. A pool of cells from 1 femur for each mouse was used (n=1 mouse per strain). All coverslips were placed in triplicates into wells (n=4 wells per condition) of a 24 well plate containing medium supplemented with M-CSF. TRAP staining was performed after 3, 5 and 7 days. Total cells per FoV was determined for 5 FoV per coverslip (**A**). A two-way ANOVA was performed (strain: p=0.0018, time: p=0.0004, interaction: p=0.0098) and Bonferroni post-tests were indicated (*** (p<0.001) significantly different to all other groups). Representative images of cultures grown in M-CSF alone on day 3, 5 and 7 are shown (**B**).

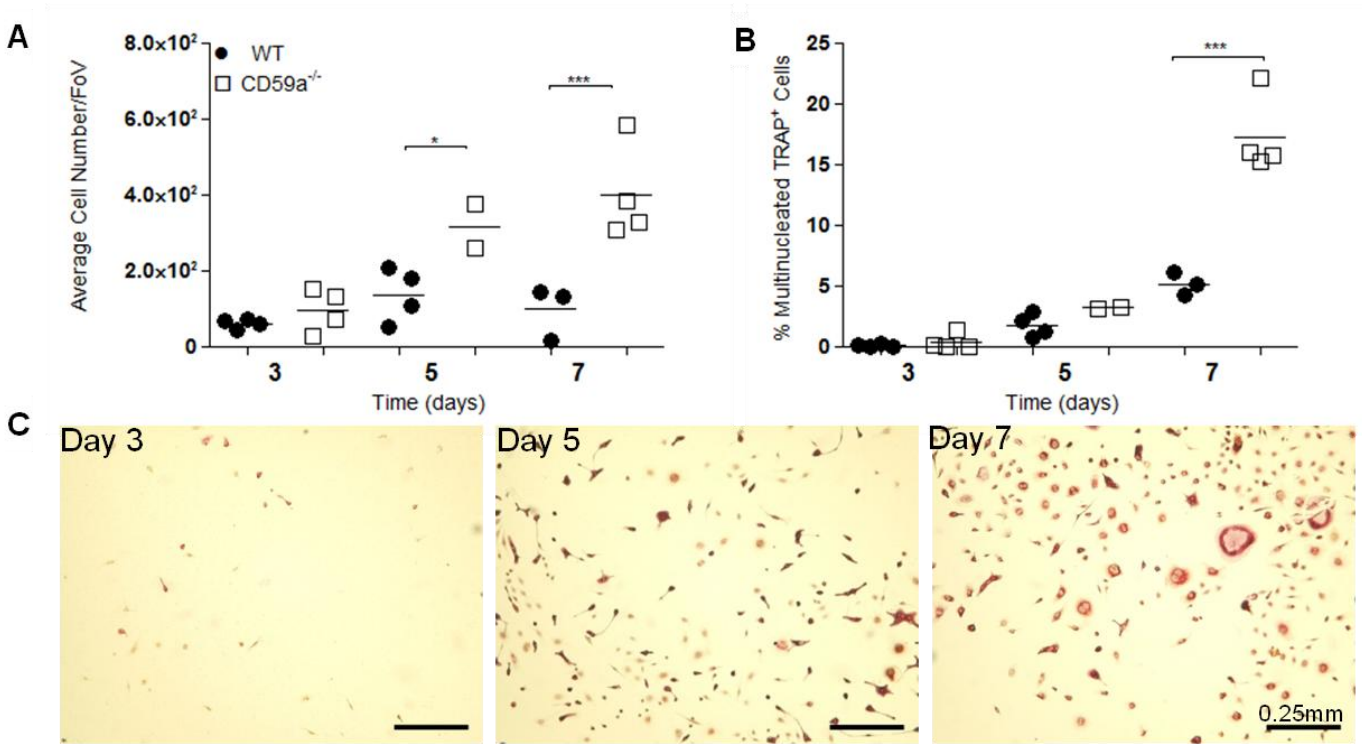

Figure 4.6 Time course testing to evaluate OC assay. Cells were harvested and plated as outlined in Fig. 4.5 (n=1 mouse per strain of which 4 wells containing 3 coverslips each were cultured). Cells were cultured in medium supplemented with M-CSF and RANKL. TRAP staining was performed after 3, 5 and 7 days. Total cells per FoV (**A**) and % multinucleated $TRAP^+$ cells (**B**) were determined for 5 FoV per coverslip. Two-way ANOVAs were performed for **A** (strain: p=0.0002, time: p=0.0013, interaction: p=0.0154) and **B** (strain: p<0.0001, time: p<0.0001, interaction: p<0.0001) and Bonferroni post-tests are indicated ((*p<0.05), ***(p<0.001). Representative images of cultures on day 3, 5 and 7 are shown (**C**).

4.3.4.1 Increasing Yield of OCs by Improving Efficacy of Adherence at Baseline

In the results described in section 4.3.3, 100 µl of bone marrow cells were dispensed onto each coverslip by flooding the well on day 0, the bone marrow cells looked broadly spread across the coverslip and only diminutive cell/cell contact was observed. At endpoint on day 7, the resultant patchy OCs were widely spread over the coverslip surface and OC yield was low. In order to improve the initial adherence of bone marrow cells and thereby improve OC yield, the bone marrow preparations were seeded at $6.4x10^4$ cells in 10 µl of culture medium per coverslip. This covered the surface area of the coverslip. The bone marrow preparations were cultured in differentiating medium containing M-CSF and RANKL. On day 3 the modified culture conditions revealed elevated cell counts in both $CD59a^{-/-}$ (266±113 cells/FoV) and WT (208±16 cells/FoV) samples (Fig. 4.7A). This was higher than the cell counts previously obtained with 100 µl seeded cells cultured under the same conditions; $CD59a^{-/-}$ (96±28 cells/FoV) and WT (62±6 cells/FoV). A reciprocal increase in OCG was also observed in $CD59a^{-/-}$ (28±0%) and WT (21±4%) samples. OC density was also higher at end point than in the previous method that used 100 µl of bone marrow cells (Fig. 4.7C). Assay optimisation was successful, and this was the final method employed for subsequent experiments.

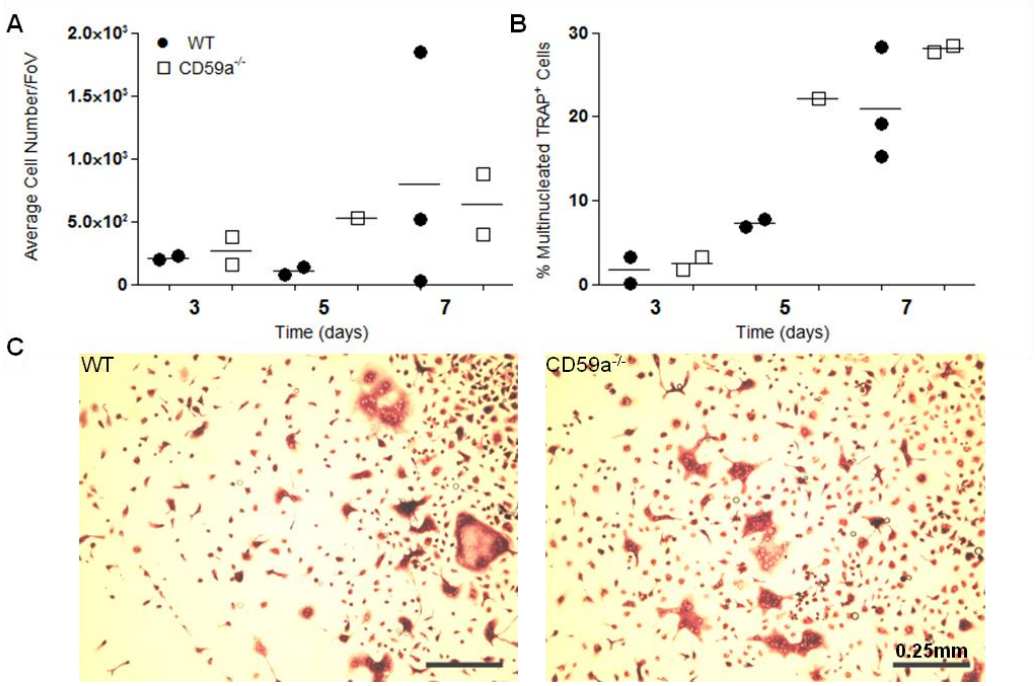

Figure 4.7 OC time course re-evaluation. Bone marrow cells obtained from 8-10 week old female WT (●) and CD59a$^{-/-}$ (□) were cultured on 6 mm glass coverslips. A pool of cells from 1 femur for each mouse was used (n=1 mouse per strain of which 1-3 coverslips were cultured per group at 5 FoV per time point). TRAP staining was performed on day 3, 5 and 7. Total cells counts were performed for samples stimulated with M-CSF and RANKL (**A**) and OCG was quantified as % multinucleated TRAP^{+} cells (**B**) on day 3, 5 and 7. Representative pictures at endpoint are shown (**C**).

4.3.5 Measuring CD59a Expression during OCG

CD59a expression was determined over the time course of the OCG assay in WT cells using qPCR (methodology in section 2.4.6). qPCR was performed using primers designed for CD59a and the housekeeping gene acid ribosomal phosphoprotein P0 (H36B4).

Primers were designed for CD59a and CD59b; both sets were tested for expression levels in murine testis and bone marrow. CD59a primers were found to be specific. qPCR data revealed expression of CD59a in adhered bone marrow samples on day 0. CD59a expression followed 5.6 cycles (C_T=31.1) after the house keeping gene that emerged at C_t=25.5 (Fig. 4.8A). CD59a expression in this sample was set as 1; it was used as the reference baseline value for all other samples (Fig. 4.8B).

On day 1, CD59a expression decreased in samples stimulated with M-CSF and RANKL (relative transcript level of 0.07) or M-CSF alone (relative transcript level of 0.08). However, from day 3 onwards expression increased to 0.32 for M-CSF and 0.26 for M-CSF plus RANKL. Transcription levels were further increased

on day 5 (M-CSF=0.71; M-CSF +RANKL=0.99). These levels did not increase any further to day 7 (relative transcript level = 0.73 for both conditions). This suggested that CD59a was expressed on the bone marrow preparation and the cell populations on day 3, day 5 and day 7, however it was unclear whether OCs specifically expressed CD59a.

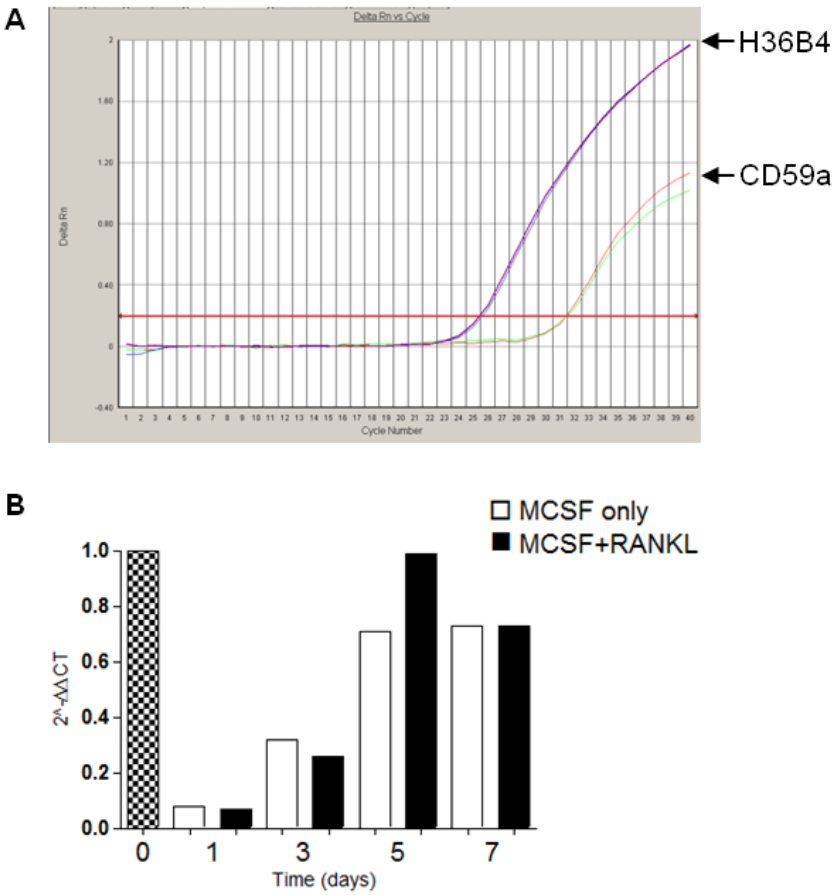

Figure 4.8 Determination of CD59a expression in OCG. Total RNA was isolated from cultures and analysed by qPCR for murine CD59a and H36B4 (n=1 mouse). At day 0 transcript levels for CD59a of adherent bone marrow cells was normalised to house keeping gene expression (**A**). This was utilised as baseline to monitor changes in mRNA expression of CD59a over time in cultures stimulated with M-CSF or M-CSF and RANKL (**B**).

4.3.6 Quantification of OCG from WT, CD59a$^{-/-}$ and C6$^{-/-}$ Bone Marrow Preparations

After the key set-up experiments described thus far were completed (section 2.4.4) and CD59a expression was confirmed (section 2.4.6); OC assays were performed using bone marrow preparations from male and female WT, CD59a$^{-/-}$ and C6$^{-/-}$ mice. 6.4x10^4 cells were plated onto 6 mm coverslips, they were left to adhere for 2 h and morphological assessments were performed. The remaining coverslips were run

through the optimised OCG assay described in section 4.3.4.1. Coverslips were sampled on day 3, 5 and 7 of the OCG assay, cells were stained with TRAP and differential cell counts were performed using a light microscope.

Morphological assessment of starting cell populations revealed no differences in cell number in female mice studied (Fig. 4.9A). In males, the cell number was significantly reduced ($p<0.05$) between WT and $C6^{-/-}$ mice but was comparable between all other groups (Fig. 4.9B). The majority of cells adhering to glass coverslips were identified as monocytes for WT, $CD59a^{-/-}$ and $C6^{-/-}$ in both female (36.0±3.2%, 44.1±4.1% and 48.9±3.8% respectively) and male (39.2±3.1%, 36.6±2.3% and 52.2±5.1% respectively) mice (Fig. 4.10A-D). Monocyte adherence was significantly higher in male $C6^{-/-}$ versus $CD59a^{-/-}$ cells ($p<0.05$).

Erythrocyte and lymphocyte numbers were comparable in cells from female and male mice (Fig. 4.10 E-H). Megakaryocyte numbers did not change in cells from female mice (Fig. 4.10I). Megakaryocyte numbers in male mice were 29.4±5.7% (WT), 36.8±3.1% ($CD59a^{-/-}$) and 16.8±2.4% ($C6^{-/-}$) respectively. $C6^{-/-}$ megakaryocyte numbers were significantly ($p<0.05$) lower than $CD59a^{-/-}$ samples (Fig. 4.10J).

On day 3, OC differentiation (percentage of total cells) in females was not significantly different in WT (1.65±0.7%), $CD59a^{-/-}$ (2.9±1.9%) and $C6^{-/-}$ (4.9±5.2%) samples (Fig. 4.11A). A similar observation was made in males where OCG was 1.8±1.1%, 4.28±2.2% and 0.82±0.3% in WT, $CD59a^{-/-}$ and $C6^{-/-}$ cells (Fig. 4.11B). A mixture of $TRAP^{+}$ and $TRAP^{-}$ cells was observed in WT, $CD59a^{-/-}$ and $C6^{-/-}$ as shown in Fig. 4.11C. On day 5, OC numbers in female and male samples were also not significantly different (Fig. 12A and B). The majority of cells were $TRAP^{+}$ (Fig. 4.12C). OCG significantly increased in both female ($p<0.001$) and male ($p<0.001$) WT, $CD59a^{-/-}$ and $C6^{-/-}$ mice cultures between day 3 and 7. After 7 days, OCG in females was 27±1.3% in WT, 29.8±2.4% in $CD59a^{-/-}$ and 28.1±3.4% in $C6^{-/-}$ samples (Fig. 4.13A). These values were not significantly different from one another. In male $CD59a^{-/-}$ samples (Fig. 4.13B) OCs were significantly raised to 34.2±1.9% in comparison to 26.6±1.7% in WT ($p<0.05$) and 24.6±1.5% in $C6^{-/-}$ samples ($p<0.01$).

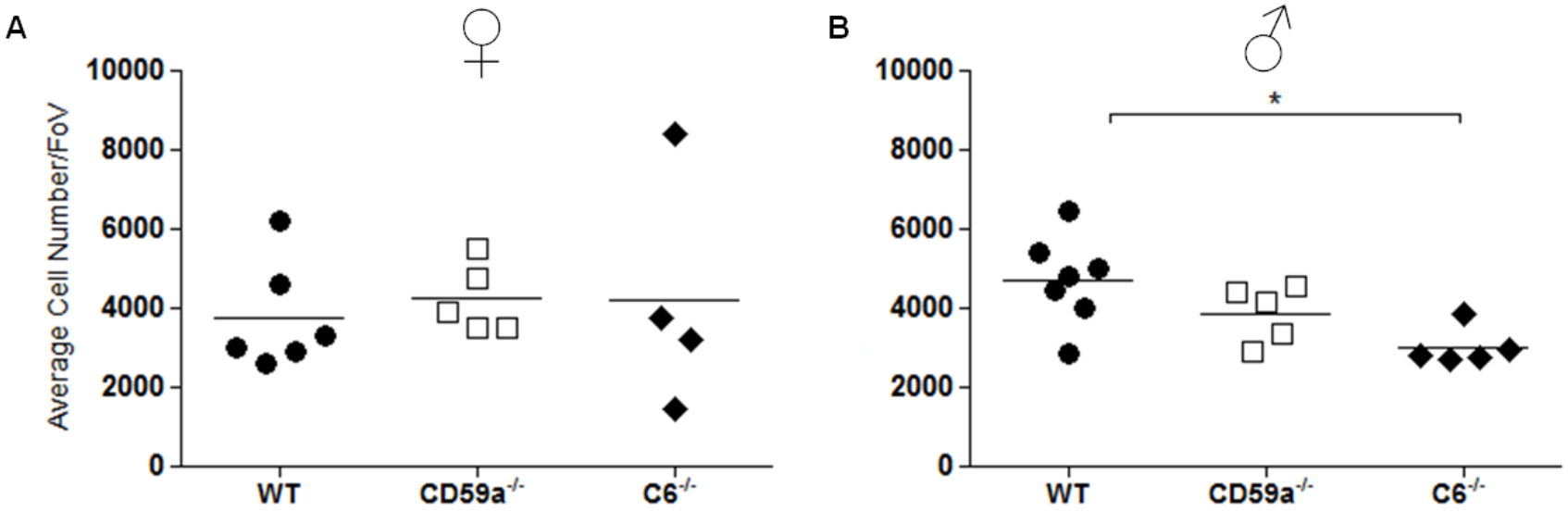

Figure 4.9 Evaluation of adherence ability of bone marrow preparations at day 0. 6.4x10^3 bone marrow cells from 8-10 week old WT (●), CD59a$^{-/-}$ (□) and C6$^{-/-}$ (♦) mice were plated onto 6 mm glass coverslips. A pool of cells from 1 femur for each mouse was used (n=5-7 mice per strain of which 3 coverslips were cultured per group). Cells were left to adhere for 2 h and washed before samples were taken for Giemsa/May-Grünwald staining. Average cell number per FoV was determined for female (**A**) and male (**B**) samples from 1:10 dilution by counting 5 FoV at x10 object magnification for 3 coverslips. One-way ANOVAs were performed for A ($p=0.8873$) and B ($p=0.0150$) and Bonferroni post-tests are indicated (*($p<0.05$)).

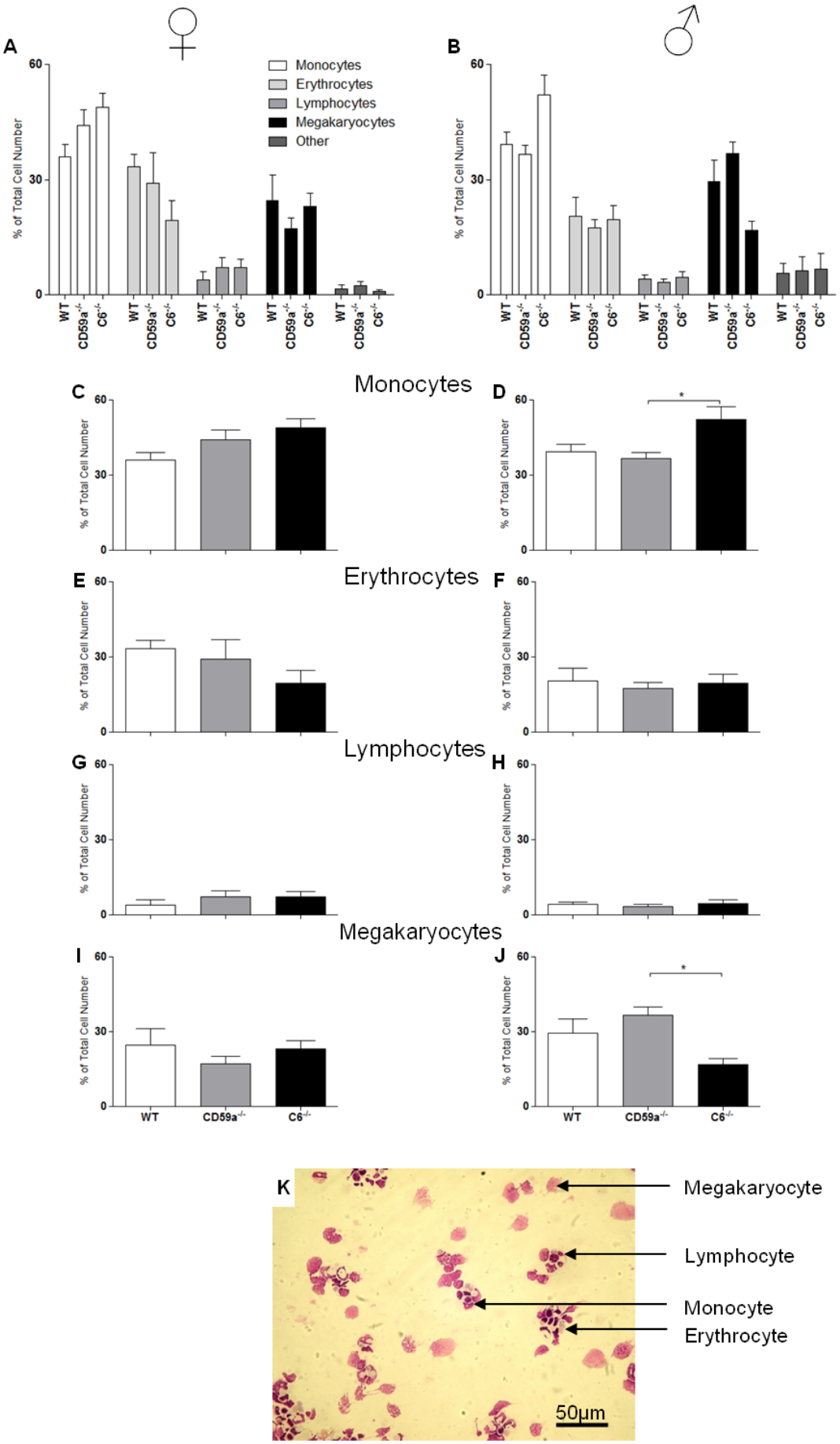
A
B
Monocytes
Erythrocytes
Lymphocytes
Megakaryocytes
Other
% of Total Cell Number
WT
CD59a-/-
C6-/-
C
D
E
F
G
H
I
J
K
Monocytes
Erythrocytes
Lymphocytes
Megakaryocytes
*
Megakaryocyte
Lymphocyte
Monocyte
Erythrocyte
50µm

Figure 4.10 Morphological assessment of bone marrow preparations at day 0. A pool of cells from 1 femur for each mouse was used at $6.4x10^4$ seeding density (n=5-7 mice per strain of which 3 coverslips were analysed at 5 random FoV). To determine differential cell counts coverslips at x40 object magnification were examined. Data is shown as percentage cell type of total cell counts for female (**A**) and male (**B**) samples. Two-way ANOVAs were performed for **A** (strain: p=0.9988, cell type: p<0.0001, interaction: p=0.0888) and **B** (strain: p=0.9925, cell type: p<0.0001, interaction: p=0.0058). A breakdown of this data is shown for monocytes (**C** and **D**), erythrocytes (**E** and **F**), lymphocytes (**G** and **H**) and megakaryocytes (**I** and **J**). Results of Bonferroni post-tests are indicated (*(p<0.05). A representative image illustrating the classification of cell types is presented (**K**).

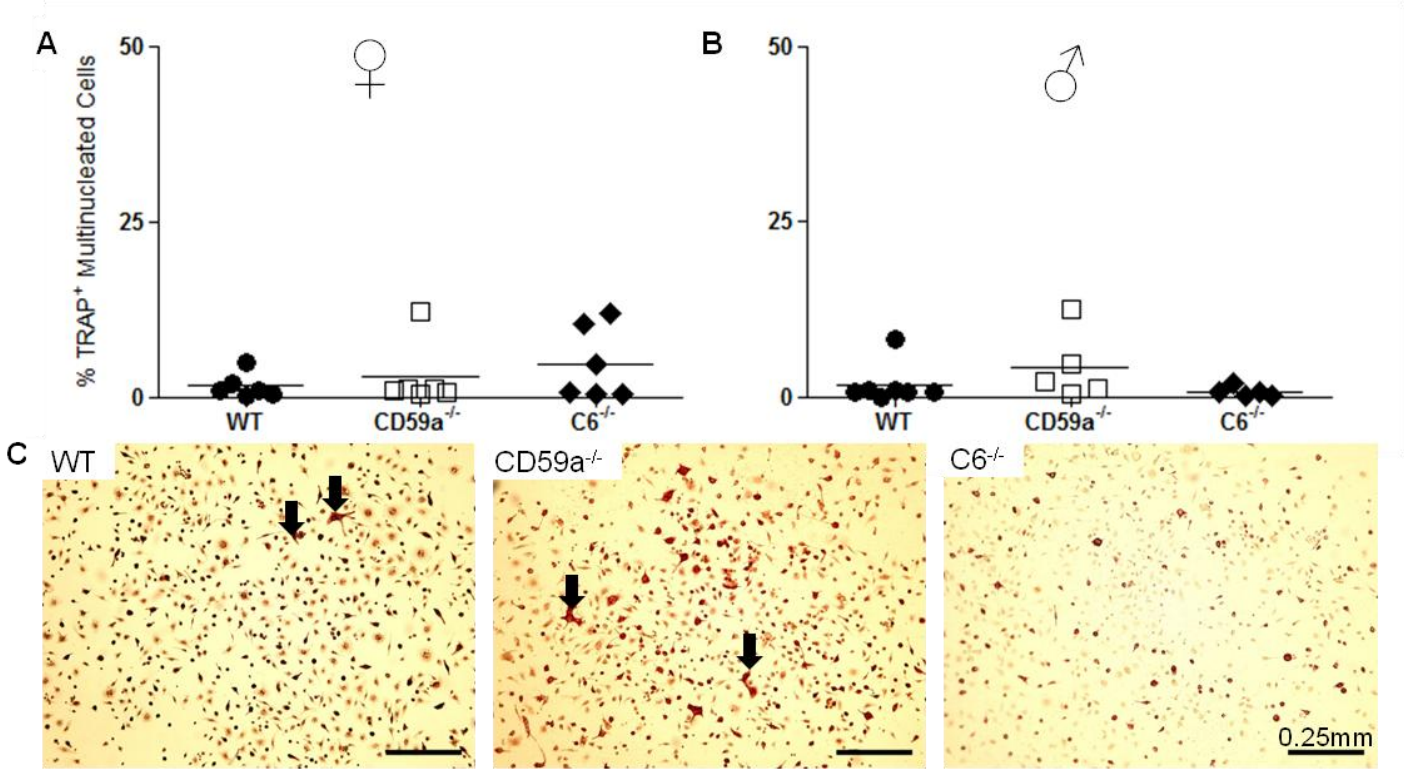

Figure 4.11 Cell differentiation at day 3. 6.4x10^4 bone marrow cells from 8-10 week old WT (●), CD59a$^{-/-}$ (□) and C6$^{-/-}$ (♦) mice were plated and adhered onto 6 mm glass coverslips. A pool of cells from 1 femur for each mouse was used (n=5-7 mice per strain of which 3 coverslips were prepared). Cells were cultured in M-CSF (25 ng/ml) and RANKL (2 ng/ml) for 3 days before TRAP staining was performed. Total cells and multinucleated TRAP$^+$ cells were counted on 15 FoVs. Data is displayed as percentage multinucleated TRAP$^+$ cells for females (**A**) and males (**B**). One-way ANOVAs were performed for A (p=0.4250) and B (p=0.2500). Representative images of OC cultures from male mice are displayed and arrows indicate examples of OCs (**C**).

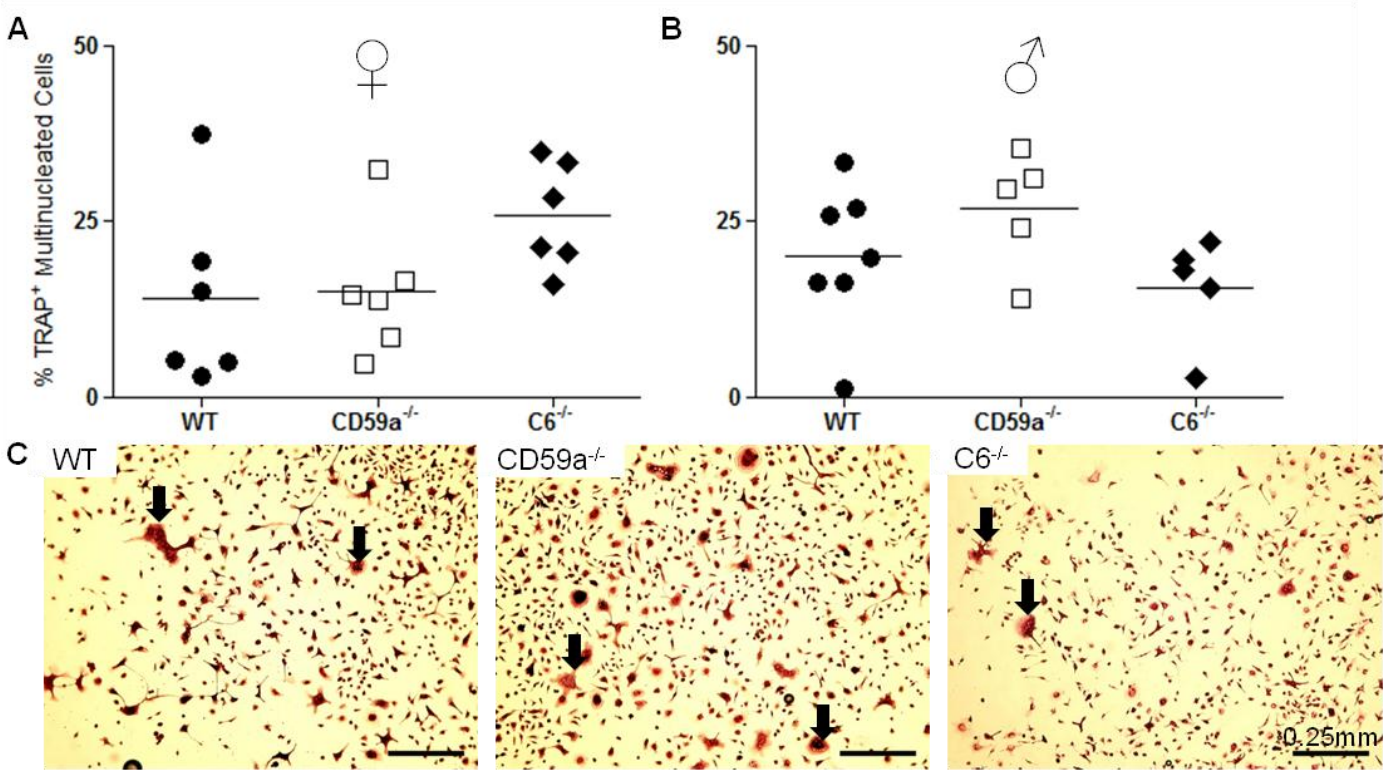

Figure 4.12 Cell differentiation at day 5. Bone marrow cells were seeded, cultured and stained as explained in Figure 4.11. A pool of cells from 1 femur for each mouse was used (n=5-7 mice per strain of which 3 coverslips were analysed at 5 FoV). Data is displayed as percentage multinucleated TRAP$^+$ cells for females (**A**) and males (**B**) on day 5. One-way ANOVAs were performed for A (p=0.1291) and B (p=0.1761). Representative images of OC cultures from male mice are displayed and arrows indicate examples of OCs (**C**).

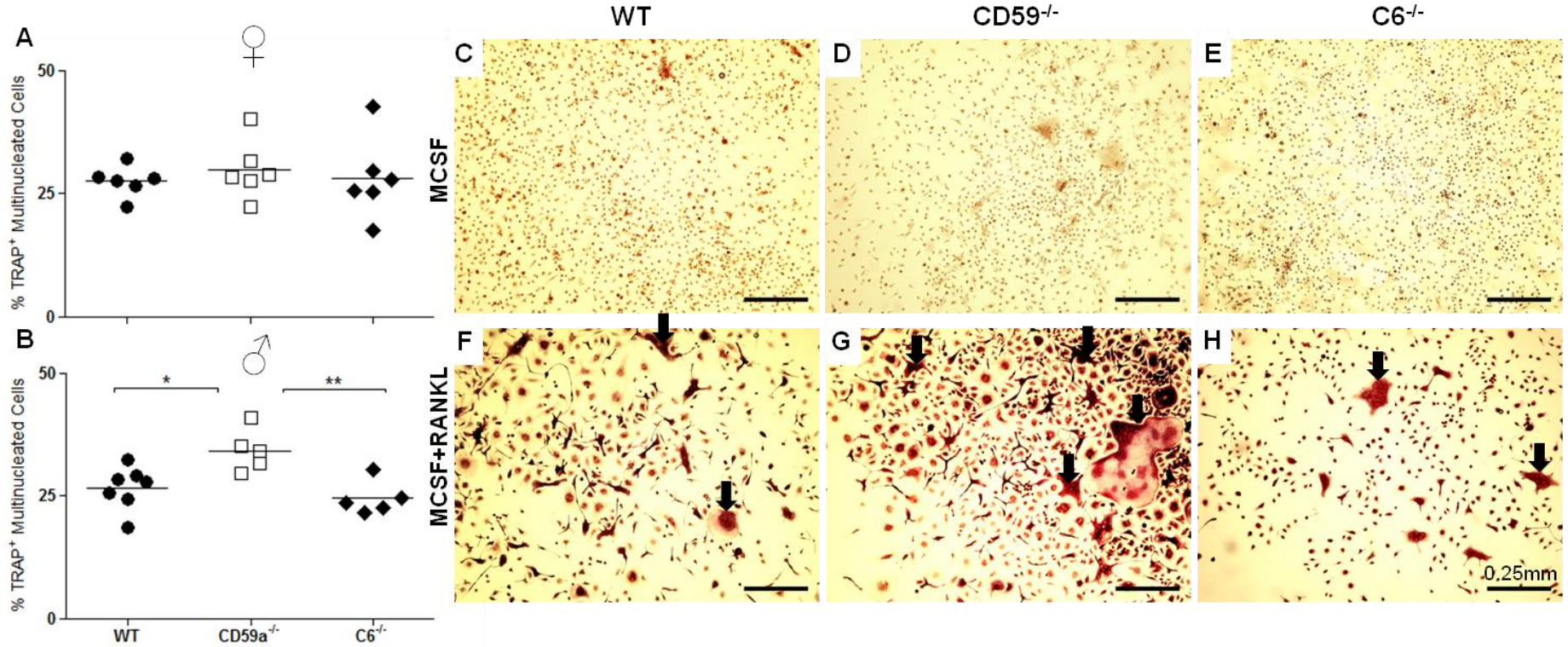

Figure 4.13 Cell differentiation at day 7. Bone marrow cells were plated as outlined in Fig. 4.13. A pool of cells from 1 femur for each mouse was used (n=5-7 mice per strain of which 3 coverslips were prepared). Cells were cultured in M-CSF (25 ng/ml) alone or in combination with RANKL (2 ng/ml) for 7 days before TRAP staining was performed. Total cells and multinucleated $TRAP^+$ cells were counted on 15 FoVs. Data is displayed as percentage multinucleated $TRAP^+$ cells for females (**A**) and males (**B**). One-way ANOVAs were performed for A (p=0.8015) and B (p=0.0052) and Bonferroni post-tests are indicated (*(p<0.05), **(p<0.01)). Representative images of OC cultures in M-CSF (**C**-**E**) and M-CSF plus RANKL (**F**-**H**) from male mice are shown.

4.3.7 Quantification of Cathepsin K

Cathepsin K (Cat K) is the major cysteine protease generated by OCs, and is essential for resorption of the organic bone matrix (Corisdeo *et al.* 2001). Cat K is produced as a zymogen. It means that Cat K contains an inactivating pro-domain when produced in the endoplasmic reticulum. After synthesis, Cat K is transported into lysosomal vesicles. Resorbing OCs release lysosomal vesicles at the ruffled border before Cat K is activated by other cathepsins, or by auto-activation at low pH (which may be dependent on presence of glycosaminoglycans). Once activated it cleaves fibrillar Col1 at numerous sites (Lecaille *et al.* 2008). ELISA, Col1 bioassay and zymography methodology were performed to confirm the activity of Cat K in OCs.

4.3.7.1 ELISA for Cat K Secretion

The only ELISA kit to measure protein levels available on the European market was a kit for human Cat K from Biomedica. However, the product advertised cross-species reactivity (Wada *et al.* 2005). The assay was carried out as described in section 2.4.7.1.

The data revealed that the positive Cat K control provided in the kit gave a strong signal for Cat K equivalent to 113.1±3.8 pmol/l (Fig. 4.14). The negative control used for the assay (medium containing 10% FCS) gave an average of 14.2±1.4 pmol/l (OD of 0.26 at 450 nm) and was significantly different ($p<0.001$) to the positive control. When WT and CD59a$^{-/-}$ supernatants were tested, the detectable signal was lower than the negative control. A commercially available source of human recombinant Cat K (Enzo Life Sciences) was tested as an additional positive control for the ELISA. Once again no signal was detected, and the assay was deemed not fit for purpose.

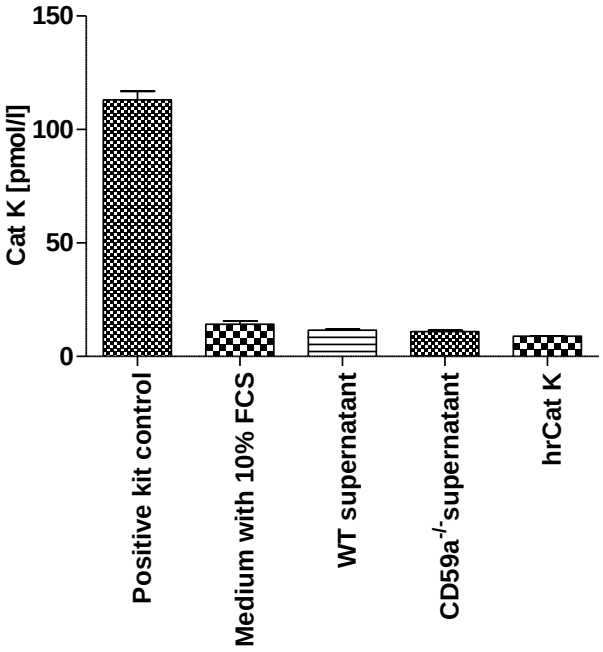

Figure 4.14 Cat K ELISA. Concentration of positive Cat K control (not further specified) was calculated from standard curve. Medium (containing 10% FCS) was used as negative control. WT and CD59a$^{-/-}$ samples were taken from OCG assays at day 5 and loaded neat (n=2 supernatants from 1 OCG assay per strain that were analysed in duplicates). Human recombinant (hr) Cat K was diluted to 300pmol/l (top standard concentration) with assay buffer (provided with kit). A One-way ANOVA was performed ($p<0.0001$) and Bonferroni post-tests are indicated (***($p<0.001$) significantly different to all other groups).

4.3.7.2 Cat K Bioassay

In order to examine functional activity of Cat K a type I collagen (Col1) bioassay was developed (section 2.4.7.2). Col1 was coated to a 96 well ELISA plate, the collagen was degraded using commercially available collagenase (Clostridiopeptidase A) as standards and collagenases within OCG assay supernatants. After washing, the remaining collagen bound to the plate was detected utilising a collagen-specific primary antibody and a biotinylated secondary antibody. The principles of ELISA were applied to measure the changes colorimetrically.

Antibodies bind the antigen of interest (specific binding), but when these binding sites are saturated, other antigens with lower affinity (non-specific binding) are targeted. The concentration range of primary and secondary antibodies was tested to detect Col1. The secondary antibody reached optimum concentration at 1:10,000 dilution (Fig. 4.15A). A dilution range of 1:1,000 to 1:16,000 of primary antibody was not sufficient to obtain specific binding and a further dilution to 1:128,000 did not show improvement (Fig. 4.15B). When comparing collagen

degradation curves, OD values drastically dropped from 2.0 to 0.3 within a 1:5 dilution of Clostridiopeptidase A. To avoid inaccuracy by over diluting, a 1:15,000 dilution of primary antibody was selected. Consequently a standard curve utilising Clostridiopeptidase A revealed a limited assay sensitivity of 3.2 to 400 ng collagenase per ml (Fig. 4.15C).

A blank consisting of buffer only (expressed as 100% collagen binding) was compared to recombinant human Cat K (active conformation) and matrix metalloproteinase 1 (MMP-1). These collagenases exhibited pH specificity; in buffer A (pH 7.4) MMP-1 significantly reduced ($p<0.001$) collagen binding to 12.3±0.3% at 5,000 ng/ml. Cat K only demonstrated 65±1.2% binding at 500 ng/ml which was significantly reduced ($p<0.001$) over the blank, but was less active ($p<0.001$) in comparison to MMP-1 at the same concentration (Fig. 4.15D). In buffer B (pH5.5) Cat K significantly degraded ($p<0.001$) collagen to a 15.0±0.6% binding capacity at 500 ng/ml which stayed constant when diluted further, demonstrating high enzyme activity (Fig. 4.15E). In comparison MMP-1 only slightly reduced collagen binding to 91±2.6% at 5,000 ng/ml. Therefore in succeeding experiments Cat K (diluted in buffer B) and MMP-1 (diluted in buffer A) were chosen as positive control at 500 ng/ml each to determine unknown collagenase specificity.

Supernatants of WT and CD59a$^{-/-}$ cultures diluted 1:2.5 in buffer A were compared to blank (buffer A) and MMP-1. 500ng/ml MMP-1 revealed 68.1±10.2% collagen binding relative to control, a significant reduction ($p<0.01$) and hence confirmed the assay's functionality (Fig. 4.16A). WT and CD59a$^{-/-}$ supernatants containing M-CSF did not show any collagenase activity at day 3 (WT=118.0±0.4%, CD59a$^{-/-}$=114.1±3.6%), 5 (WT=113.5±2.4%, CD59a$^{-/-}$=120±0.5%) or 7 (WT=113.7±4.7%, CD59a$^{-/-}$=116.3±0.1% binding). Instead, values were slightly raised in comparison to the blank. Interference from the FCS within the medium might have caused the recovery to exceeded 100%. In cultures supplemented with M-CSF and RANKL, collagen binding was significantly reduced ($p<0.001$) to 56±1.6% in WT and to 38.8±0.8% in CD59a$^{-/-}$ supernatants on day 5. The CD59$^{-/-}$ sample was also significantly reduced in comparison to the MMP-1 standard. On day 7 collagen digestion potential of WT (81.4±3.6%) and CD59a$^{-/-}$ (79.5±8.3%) supernatants was comparable; showing slight collagenase activity. Collagenase activity was highest on day 5 of OCG assays, but considering that FCS could have influenced the binding capacity; levels quantified may not be accurate.

At low pH (buffer B) Cat K degradation of Col1 resulted in 10.9±1.8% collagen binding in comparison to the blank (buffer B), again confirming the assays functionality (Fig. 4.16B). All WT and CD59a$^{-/-}$ samples diluted with buffer B showed

binding above 200%. The enhanced binding was probably caused by protein denaturation from the FCS. Hence the bioassays were terminated as accurate analyses were not possible and Cat K was not detectable.

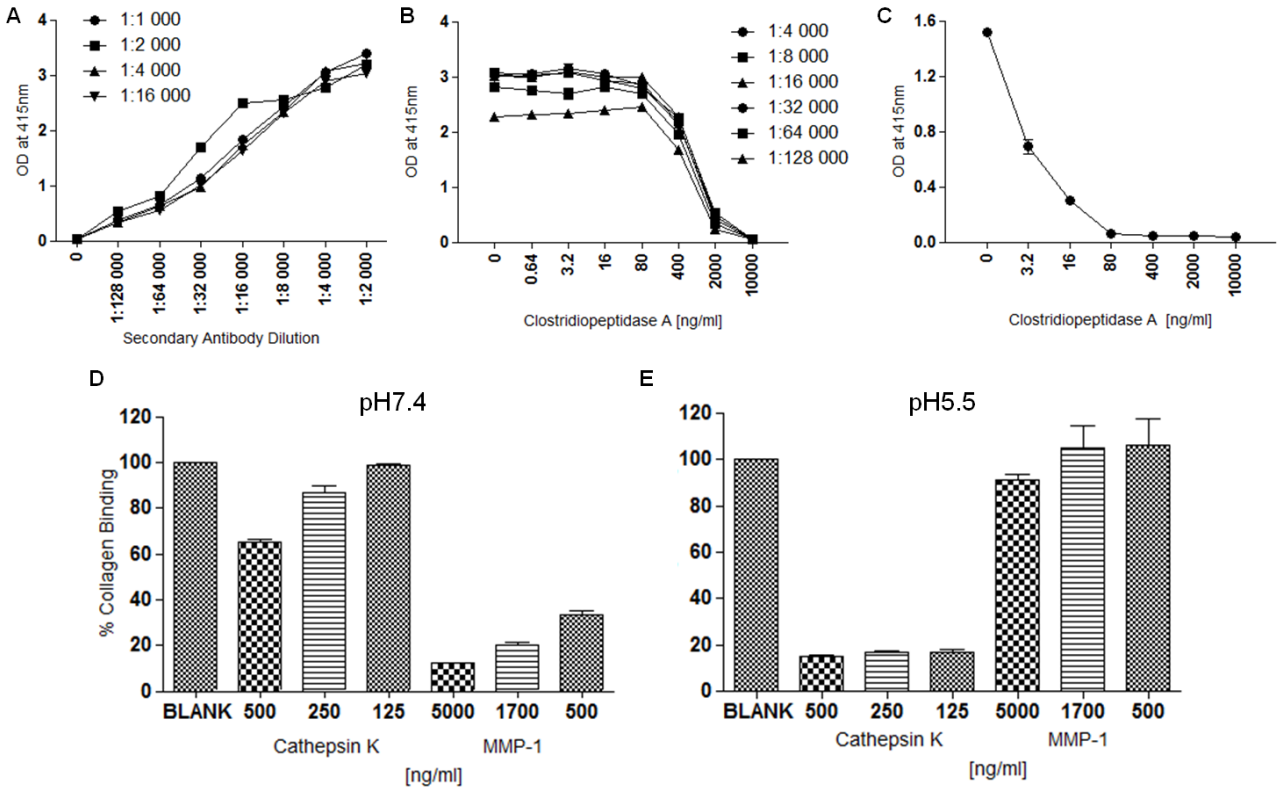

Figure 4.15 Testing of Cat K bioassay. 96 well plates were coated with Col1 (10 µg/ml). Initially different primary [mouse monoclonal anti-collagen type I] and secondary [anti-mouse IgG peroxidase conjugated] antibody concentrations were tested (**A**) to identify a gross dilution range. Clostridiopeptidase A was added at various concentrations to digest Col1 and primary antibody concentration (**B**) was further defined. A standard curve was generated with Clostridiopeptidase A (**C**). Further collagenase standards were tested on optimised protocol at pH 7.4 (**D**) and pH 5.5 (**E**). A two-way ANOVA of combined data (**D** and **E**, collagenase: $p<0.0001$, buffer: $p=0.0416$, interaction: $p<0.0001$) was performed.

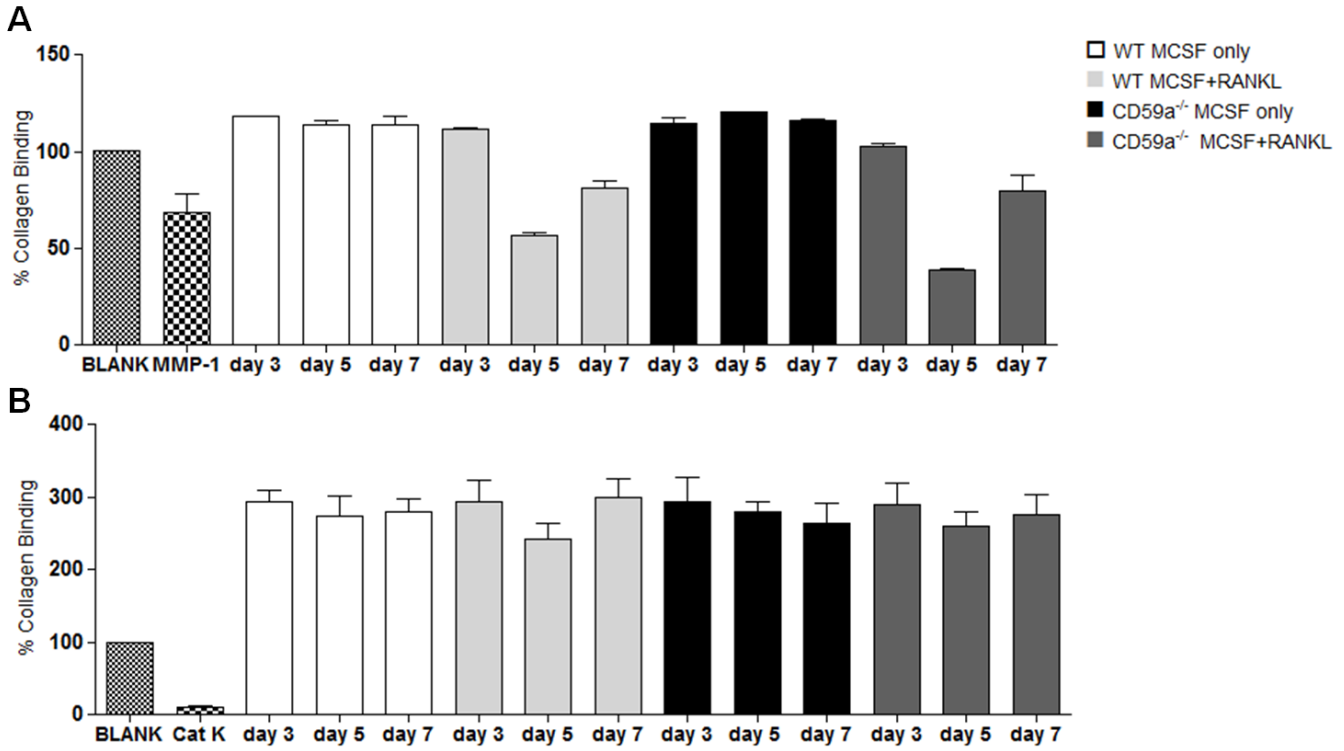

Figure 4.16 Quantification of Cat K on bioassay. Buffer A and buffer B are shown as blank. Samples (n=3 supernatants per group from 1 OCG assay per strain that were analysed in triplicates) were diluted 1:2.5 in buffer A (pH 7.4) and MMP-1 was applied as positive control at 500 ng/ml (**A**). Samples were diluted 1:2.5 in buffer B (pH 5.5) and Cat K was applied as positive control at 500 ng/ml (**B**). One-way ANOVAs were performed for **A** ($p<0.0001$) and **B** ($p<0.0001$). Bonferroni post-tests are stated in the text.

4.3.7.3 Type I Collagen Zymography

Zymography was utilised as an alternative method to identify functional Cat K and other potential collagenases according to their size (methodology in section 2.4.7.3). The SDS-PAGE gels were prepared with Col1 (0.2 mg/ml) as collagenase substrate. Once electrophoresis was performed, gels were incubated with zymography wash, refolding and digestion buffers to initiate collagen degradation (staining with Coomassie blue R leaves areas where collagen was digested as white bands). Zymograms incubated in wash and digestion buffer A (section 2.2., low pH) did not show any proteolytic activity (Fig. 4.17A). Instead dark bands were observed at 115kDa, 94kDa and 70kDa. As Cat K is functionally active at low pH I concluded it was not detectable.

When zymograms were treated with wash and digestion buffer B (neutral pH), bands of Col1 digestion emerged at the molecular weight (MW) of 115kDa, 54kDa and 29kDa indicating MMP-9, MMP-2 and MMP-1 activity according to Chau et al. (Chau *et al.* 2005) (Fig. 4.17B). No differences were observed between WT and CD59a$^{-/-}$ OCG samples. Additionally a white mark was visible at 70kDa in all samples which matched with a dark band in Fig. 4.18A. This is likely due to large amounts of bovine serum albumin (BSA) being present in the samples. BSA was pushing Col1 out of solution, therefore reducing the Coomassie blue stain at the 70kDa in Fig. 4.17B. As proteases were visible at neutral pH succeeding experiments focused on their optimised detection.

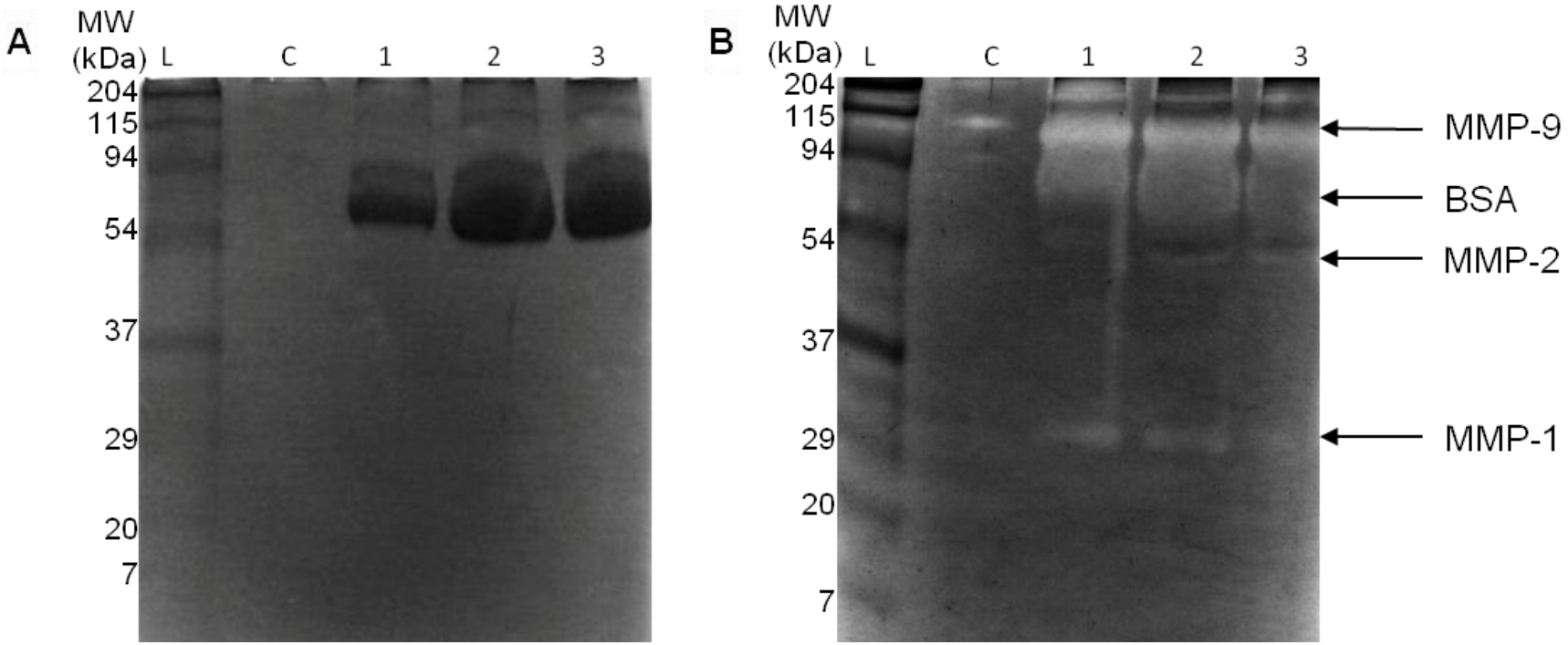

Figure 4.17 Col1 zymography. 12% non-reducing SDS-PAGE gels containing Col1 (0.2mg/ml) were prepared. Ladder (L), medium (C), day 7 OCG samples (n=1 OCG assay per strain) of WT 1:2 (1), 1:5 dilution (2) and CD59a$^{-/-}$ 1:5 dilution (3) were loaded. After electrophoresis gels were washed with either zymography wash buffer A (**A**) or zymography wash buffer B (**B**). Afterwards gels were incubated in zymography digestion buffer A (**A**) or zymography digestion buffer B (**B**) for 20 h. Gels were then stained with Coomassie blue R.

4.3.8 Quantification of MMP-9

MMP-9 is an extracellular matrix degrading protease. Amongst other cells it is highly expressed by OCs. It is also produced as zymogen and released in a similar manner to Cat K from lysosomal compartments. MMP-9 digests denatured collagen, such as gelatin, at different binding sites to Cat K (Lecaille *et al.* 2008). Herein its secretion was investigated via gelatin zymography and ELISA.

4.3.8.1 Gelatin Zymography

MMP-9 can be readily detected by the established method of gelatin zymography (Kleiner and Stetlerstevenson 1994). SDS-PAGE gels were prepared containing gelatin (0.2 mg/ml) as substrate for MMP-9 digestion (section 2.4.7.4). WT, CD59a$^{-/-}$ and C6$^{-/-}$ supernatants, obtained from cultures grown in M-CSF and RANKL for 7 days, were tested for proteolytic activity.

In Fig. 4.18A, a human neutrophil control sample demonstrated protease activity at 120kDa and 94kDa as well as 70kDa. These bands were known to be MMP-9 bound to NGAL (125kDa), ProMMP-9 (92kDa) as well as Pro-MMP-2 (72kDa) as described by Gupta et al (Gupta *et al.* 2007). OCG samples revealed a broad band around 115kDa followed by a thin band underneath. Murine ProMMP-9 is a larger protein than its human equivalent with a MW of 105kDa (Zeng *et al.* 1999; Hahn-Dantona *et al.* 2001). Once activated MMP-9 retains a MW of 92kDa. In OCG supernatants MMP-9 was predominantly present in its zymogen conformation. Another band was identified around 70kDa corresponding to ProMMP-2 which has a similar MW to the human protein. It demonstrated that OC precursor cells and OCs produce proteases that are functionally active. Expression of ProMMP-9, MMP-9 and ProMMP-2 was comparable between WT, CD59a$^{-/-}$ and C6$^{-/-}$ samples.

To confirm the identity of MMP-9, a zymograph was prepared with different dilutions of supernatant (Fig. 4.18B). An identical gelatin containing gel was blotted with polyclonal anti-MMP-9 antibody (section 2.4.7.5). The Western Blot revealed antibody binding at 105kDa in WT and CD59a$^{-/-}$ samples at 1:5 dilution as well as in medium containing heat-inactivated FCS (Fig. 4.18C). Additional bands appeared at higher MWs, likely representing inactive MMP-9 bound to other proteins.

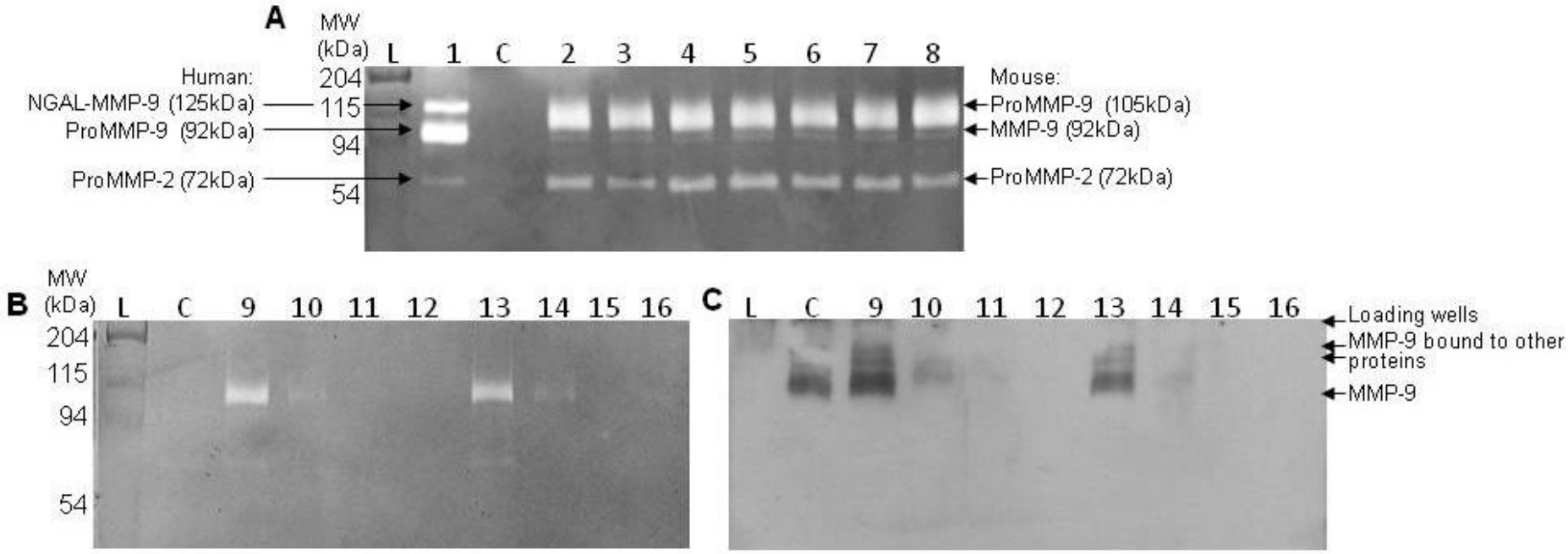

Figure 4.18 Gelatin zymography. 7.5% non-reducing SDS-PAGE gels containing gelatine (0.2 mg/ml) were prepared. Ladder (L), medium (C), supernatant of human neutrophils (1) and OCG samples from day 7 were loaded at 1:5 dilution (1-9, 13) for WT (2,4,6), CD59a$^{-/-}$ (3,5,7) (n=3 OGC assays per strain) and C6$^{-/-}$ (8, n=1 OGC assays per strain) samples. Serial 1:5 dilutions of WT (9) and CD59a$^{-/-}$ (13) samples were loaded (10-12 and 14-16). After electrophoresis gels were washed in zymography wash buffer C and incubated in zymography digestion buffer C (**A** and **B**) or blotted to detect MMP-9 (**C**).

4.3.8.2 ProMMP-9 ELISA

In order to determine specific ProMMP-9 concentrations in OCG supernatants an in-house ELISA was developed. Different buffers and incubation times were examined to obtain maximal specificity, while reducing background signal. The optimised protocol can be found in section 2.4.7.6. ProMMP-9 was detectable in samples cultured in M-CSF at day 3; concentrations averaged between 6 and 10 ng/ml ProMMP-9. The level of ProMMP-9 diminished below detection limit of the assay by day 5 and 7 (data not shown).

Samples grown in M-CSF and RANKL demonstrated comparable ProMMP-9 concentration in females (WT=24.8±4.6 ng/ml, CD59a$^{-/-}$=33.0±5.9 ng/ml, C6$^{-/-}$ =43.4±9.3 ng/ml) and males (WT=35.8±9.5 ng/ml, CD59a$^{-/-}$=50.9±18.9 ng/ml, C6$^{-/-}$ =26.8±5.1 ng/ml) on day 3 (Fig. 4.19A and B). By day 5 ProMMP-9 level increased, but this observation was not statistically significant as the variability between samples was high. On day 5, ProMMP-9 level was similar between WT, CD59a$^{-/-}$ and C6$^{-/-}$ in females and males (Fig. 4.19C and D). ProMMP-9 level remained constant between day 5 and day 7. On day 7 ProMMP-9 concentration in female samples; WT, CD59a$^{-/-}$ and C6$^{-/-}$ were not significantly different (Fig. 3.19E). Similarly, in males all data was comparable in WT, CD59a$^{-/-}$ and C6$^{-/-}$ samples. No correlation was identified between ProMMP-9 expression and OC or total cell number.

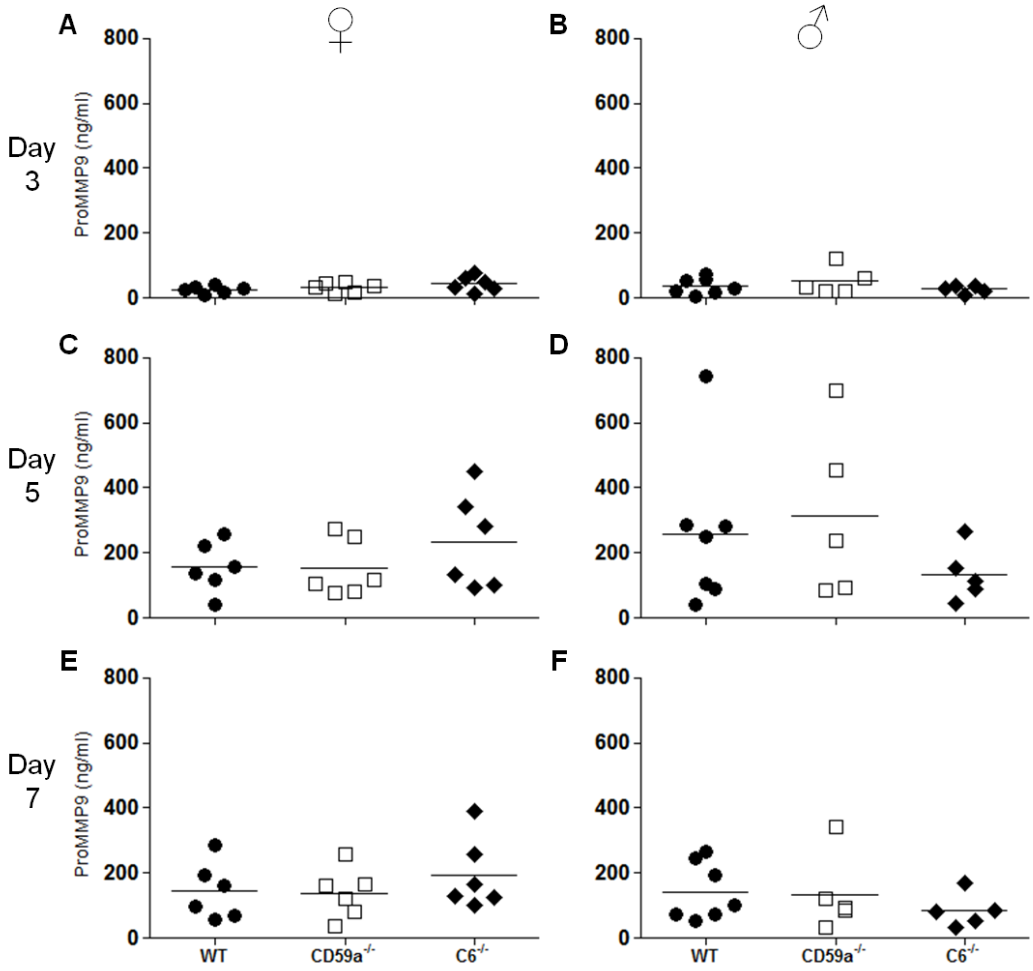

Figure 4.19 ProMMP-9 ELISA. ProMMP-9 concentrations were measured via ELISA and results for samples grown in M-CSF and RANKL are illustrated (n=5-7 OCG assays per strain of which 3 supernatants were analysed in duplicates). Concentrations were measured at day 3 (**A** and **B**), day 5 (**C** and **D**) and day 7 (**E** and **F**) for female (**A**, **C**, **E**) and male (**B**, **D**, **F**) WT (●), CD59a$^{-/-}$ (□) and C6$^{-/-}$ (♦) samples (n=5-7 mice per group). One-way ANOVAs were performed for **A** (p=0.1937), **B** (p=0.4265), **C** (p=0.3557), **D** (p=0.4119), **E** (p=0.5256) and **F** (p=0.5350).

4.3.9 Quantification of Cytokines/Chemokines

OC precursor cells rely heavily on cytokine and chemokine stimulation for differentiation and activity of OCs. RANKL is the most important cytokine and can be induced by various pro-inflammatory cytokines such as IL-1β, TNFα, IL-6. These cytokines support OCG via additional mechanisms; IL-1, for example, has been shown to enhance OC precursor cell interactions with bone matrix whereas TNFα stimulates pre-OCs to express c-Fms (Lorenzo *et al.* 2010). Chemokines, such as macrophage inflammatory protein-1α (MIP-1α) and IL8/mKc, also favour resorption

by inducing OC migration via chemotaxis (Fuller *et al.* 1995). Cytokines inhibiting OCG (IL-10, IL-12 and IFNγ) were found to prevent NFATc1 expression and nuclear translocation (Lorenzo *et al.* 2010). Many of these interactions have been shown to be aberrantly regulated leading to increased OCG in bone disease; these cytokines/chemokines were investigated here to uncover the mechanism of CD59a's involvement in OC up-regulation.

4.3.9.1 Murine Pro-Inflammatory Multiplex Assay

The multiplex assay, measuring IFNγ, IL-10, IL-12 p70, IL-1β, IL-6, mKc and TNFα in male WT and CD59a$^{-/-}$ samples at day 7, was utilised as described in section 2.4.7.7. The largest differences between WT and CD59a$^{-/-}$ samples were observed for IL-10 and mKc (Fig. 4.20). In cultures grown in M-CSF, IL-10 was 63.0pg/ml in WT samples which was slightly decreased to 35.8 pg/ml in CD59a$^{-/-}$ samples. IL-10 level was significantly reduced ($p<0.001$) to 17.5 pg/ml in WT and slightly diminished to 15.6 pg/ml in CD59a$^{-/-}$ samples when RANKL was added. No significant difference was observed between WT and CD59a$^{-/-}$ samples. mKc level was raised significantly ($p<0.05$) in CD59a$^{-/-}$ (47.9 pg/ml) over WT (9.9 pg/ml) samples when supplemented with M-CSF. In cultures grown in M-CSF and RANKL mKc level was slightly reduced to 4.7 pg/ml in WT and significantly reduced to 20.7 pg/ml in CD59a$^{-/-}$ samples over cultures grown in M-CSF. Hence a 4.5 fold difference was present in mKc level between WT and CD59$^{-/-}$ in absence and presence of RANKL in medium.

Other cytokines (IL-12 p70, IL-6, TNFα, IFNγ and IL-1β) did not show significantly different levels between CD59a$^{-/-}$ and WT samples. This data suggest that mKc is the most important target to investigate further as it was found to be up-regulated in CD59a$^{-/-}$ when compared to WT samples.

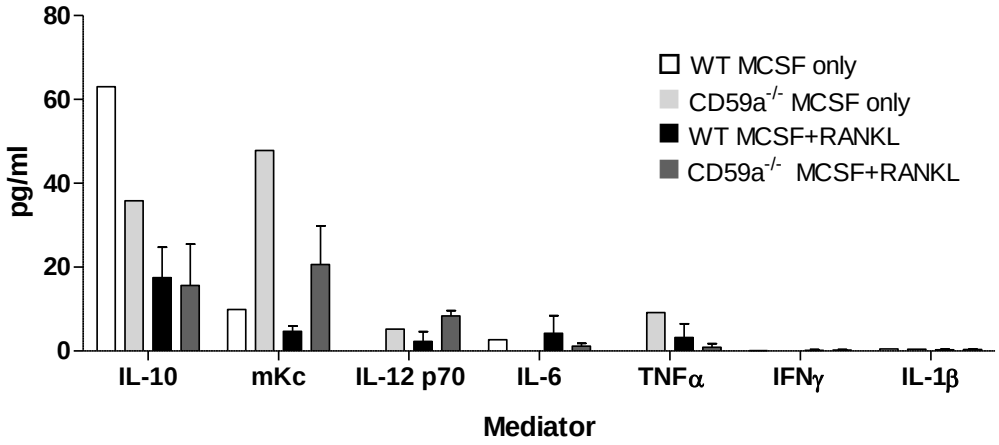

Figure 4.20 Pro-inflammatory multiplex assay. Mesoscale Multiplex assay kit for murine pro-inflammatory mediators was performed by Dr Bronwen Evans. Cytokine (IL-10, mKc, IL-12 p70, IL-6, TNFα, IFNγ and IL-1β) concentrations were determined in WT and CD59a$^{-/-}$ OCG supernatants grown in M-CSF and M-CSF plus RANKL on day 7 (n=1 OCG assay per strain of which 1-3 supernatants were analysed per sample in duplicates). A two-way ANOVA (condition: p=0.0368, cytokine: p<0.0001, interaction: p=0.0051) and Bonferroni post-tests were performed (see in text).

4.3.9.2 Quantification of mKc

To evaluate mKc concentration in all OCG supernatants, ELISAs were performed according to section 2.4.7.7. On day 3 baseline level of mKc was 6.3±1.4 pg/ml in female WT samples cultured in M-CSF alone (Fig. 4.21A). mKc level in CD59a$^{-/-}$ (7.0±1.1 pg/ml) and C6$^{-/-}$ (6.3±1.4 pg/ml) were significantly higher ($p<0.05$) than in WT samples. A similar trend was noted in males (Fig. 4.21B). This pattern continued on day 5 for both genders (Fig. 4.21C and D). By day 7 mKc level in female CD59a$^{-/-}$ (42.7±3.6 pg/ml ($p<0.001$)) samples was significantly increased over WT (10.2±2.6 pg/ml) (Fig. 4.21E). mKc level in C6$^{-/-}$ samples (26.5±6.6) was not significantly different from WT or CD59a$^{-/-}$ samples. In males mKc level of WT samples was significantly lower in comparison to CD59a$^{-/-}$ ($p<0.01$) and C6$^{-/-}$ samples ($p<0.01$) (Fig. 4.21F). Here, levels of CD59a$^{-/-}$ and C6$^{-/-}$ were comparable.

Upon the addition of RANKL to the medium the same pattern emerges for female WT, CD59a$^{-/-}$ and C6$^{-/-}$ samples on day 3 (Fig. 4.22A and B). By day 5 mKc level was comparable between WT (3.8±1.0 pg/ml), CD59a$^{-/-}$ (10.4±1.9 pg/ml) and C6$^{-/-}$ (11.6±3.7 pg/ml) samples (Fig. 4.22C). In contrast to day 5, mKc level in CD59a$^{-/-}$ was significantly increased ($p<0.01$) over WT samples on day 7 (Fig. 4.22E), C6$^{-/-}$ level was not different from WT and CD59a$^{-/-}$ samples. In males a constant pattern was observed. mKc levels in CD59a$^{-/-}$ and C6$^{-/-}$ were significantly raised over WT samples on day 3, 5 and 7 (Fig. 4.22B, D and F).

mKc (expressed by monocyte/macrophages) levels were normalised for total cell number to account for different proliferation rates. Interestingly, datasets differed upon this normalisation. In females, mKc level were not significantly different in WT, CD59a$^{-/-}$ and C6$^{-/-}$ samples on day 3 (WT=0.4±0.1, CD59a$^{-/-}$=1.2±0.1, C6$^{-/-}$= C6$^{-/-}$ =1.0±0.4 pg/ml/1000 cells) and 5 (Fig. 4.23A and C). mKc level in CD59a$^{-/-}$ was significantly ($p<0.01$) enhanced over WT samples on day 7 only. In males, mKc level of C6$^{-/-}$ was significantly raised compared to WT on day 3 (C6$^{-/-}$=1.6±0.3, WT=0.6±0.2 pg/ml/1000 cells), 5 and 7 (Fig. 4.23B, D and F). Additionally, mKc level of CD59a$^{-/-}$ was significantly different compared to WT ($p<0.05$) and C6$^{-/-}$ ($p<0.05$) samples on day 5.

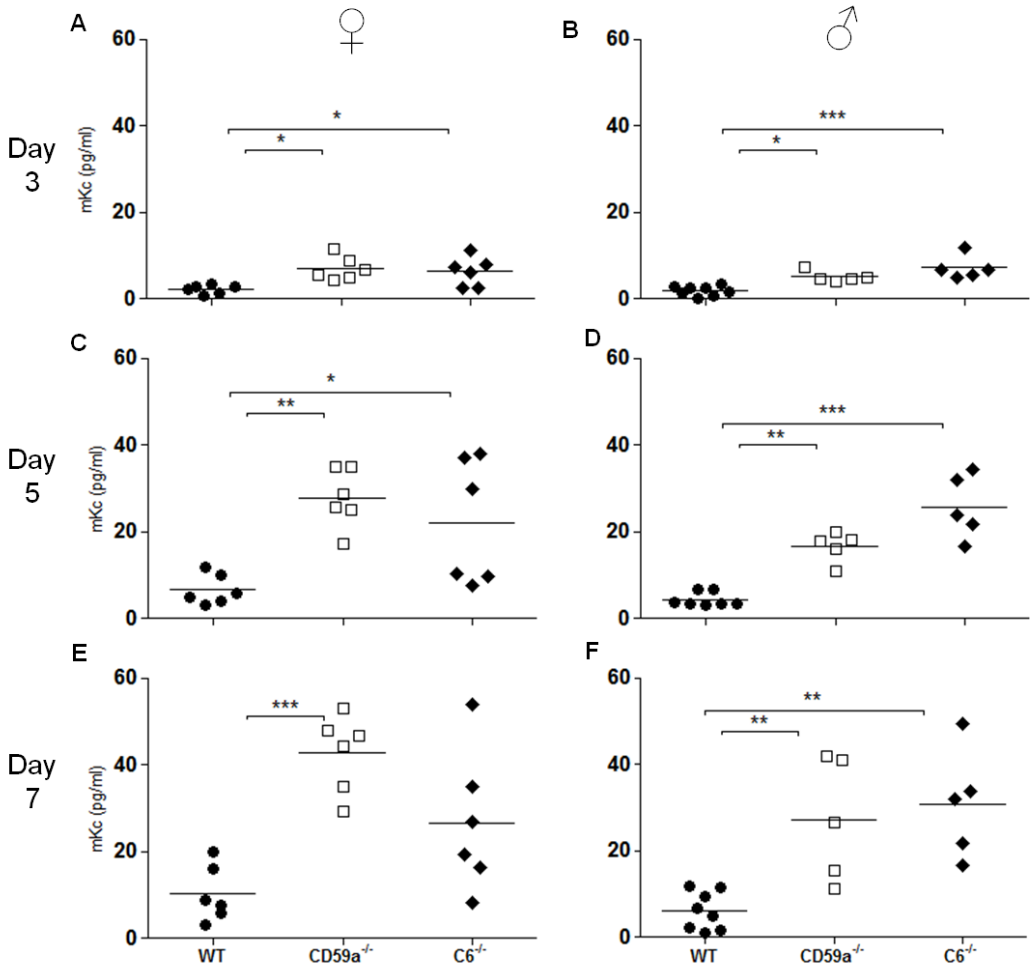

Figure 4.21 mKc ELISA of samples cultured in medium supplemented with M-CSF only. Concentrations were measured at day 3 (**A** and **B**), day 5 (**C** and **D**) and day 7 (**E** and **F**) for female (**A**, **C**, **E**) and male (**B**, **D**, **F**) WT (●), CD59a$^{-/-}$ (□) and C6$^{-/-}$ (♦) samples (n=5-7 OCG assays per strain of which 3 supernatants were analysed in duplicates). One-way ANOVAs were performed for **A** ($p=0.0123$) **B** ($p=0.0002$), **C** ($p=0.0041$), **D** ($p<0.0001$), **E** ($p=0.0007$) and **F** ($p=0.0011$) and Bonferroni post-tests are indicated (*($p<0.05$), **($p<0.01$), ***($p<0.001$)).

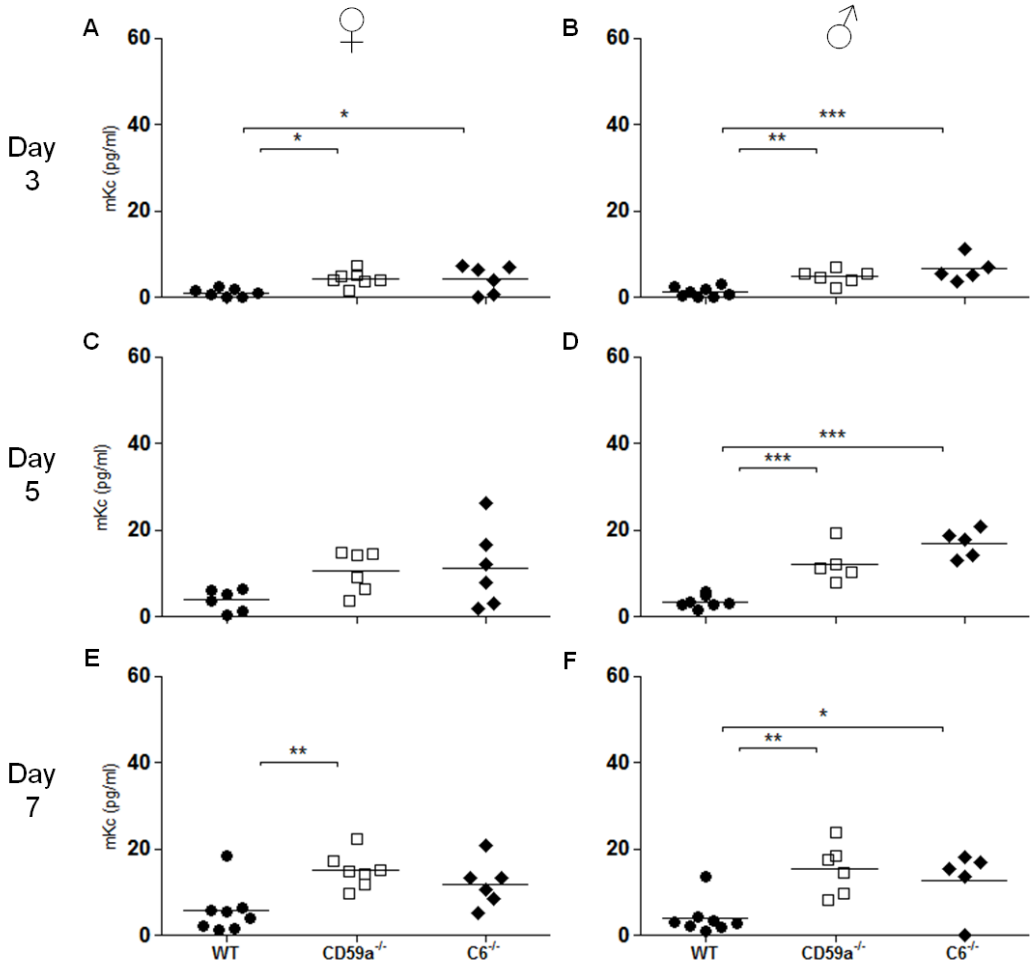

Figure 4.22 mKc ELISA of samples cultured in medium supplemented with M-CSF and RANKL. Concentrations were measured at day 3 (**A** and **B**), day 5 (**C** and **D**) and day 7 (**E** and **F**) for female (**A**, **C**, **E**) and male (**B**, **D**, **F**) WT (●), CD59a$^{-/-}$ (□) and C6$^{-/-}$ (♦) samples (n=5-7 OCG assays per strain of which 3 supernatants were analysed in duplicates). One-way ANOVAs were performed for **A** (p=0.0143) **B** (p=0.0003), **C** (p=0.1028), **D** (p<0.0001), **E** (p=0.0057) and **F** (p=0.0038) and Bonferroni post-tests are indicated (*(p<0.05), **(p<0.01), ***(p<0.001)).

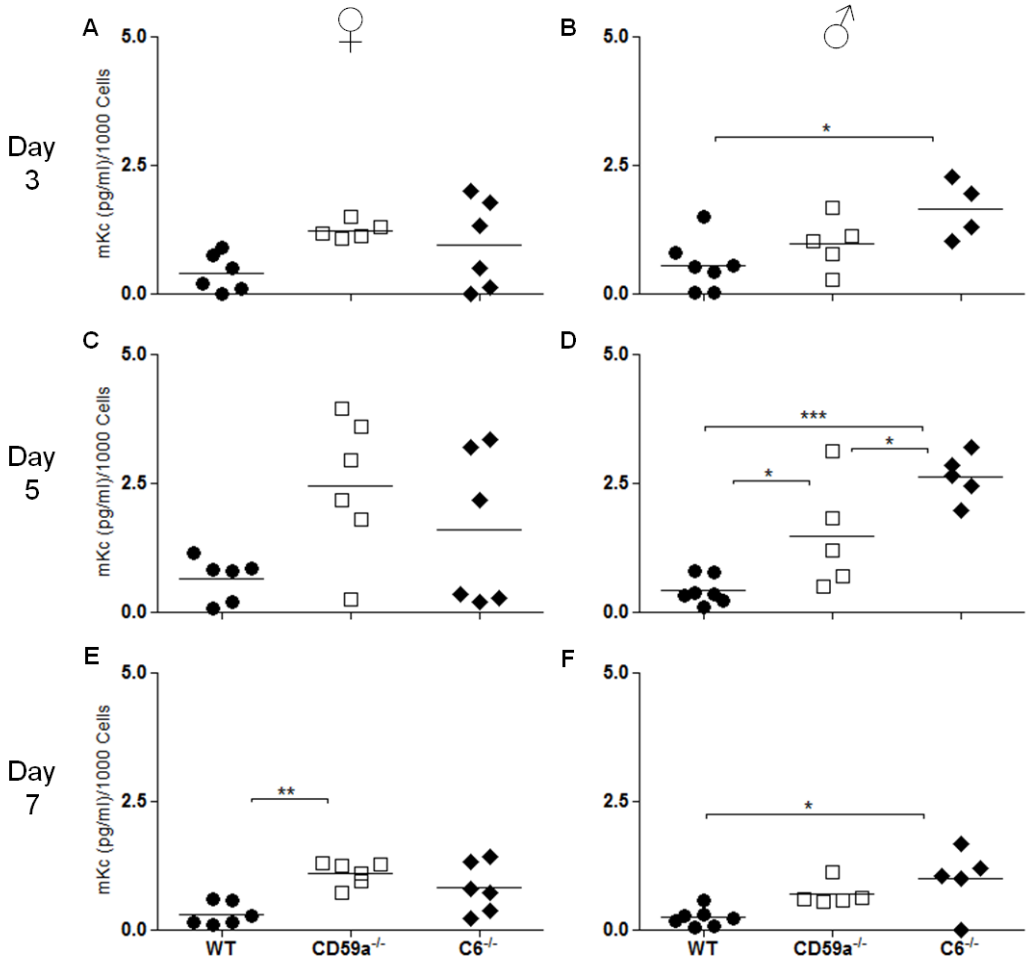

Figure 4.23 mKc ELISA of samples cultured in medium supplemented with M-CSF plus RANKL and normalised for total cell number. Concentrations were measured at day 3 (**A** and **B**), day 5 (**C** and **D**) and day 7 (**E** and **F**) for female (**A**, **C**, **E**) and male (**B**, **D**, **F**) WT (●), CD59a$^{-/-}$ (□) and C6$^{-/-}$ (♦) samples (n=5-7 OCG assays per strain of which 3 supernatants were analysed in duplicates). One-way ANOVAs were performed for **A** (p=0.0779) **B** (p=0.0183), **C** (p=0.0584), **D** (p<0.0002), **E** (p=0.0030) and **F** (p=0.0117) and Bonferroni post-tests are indicated (**(p<0.01), **(p<0.01), ***(p<0.001)).

4.4 Discussion

The development of a reliable OCG assay was essential in order to monitor cell differentiation from the stage of bone marrow precursor through to mature OC. This chapter provides a chronological description of the procedures employed to characterise and validate this OCG assay. Later in the chapter, the assay was adopted to study the impact of MAC and CD59a upon osteoclast function *in vitro*.

4.4.1 Morphological Assessment of Bone Marrow Preparations on Day 0

In the first instance differential cell counts were performed on WT bone marrow cell isolates; these were compared against cell data obtained from CD59a$^{-/-}$ and C6$^{-/-}$ mice. Surprisingly, phenotypic analysis of the starting bone marrow cell population is not routinely reported in the literature for OCG assays. A small number of studies applied a differential stain either to further define OC precursor cells (Arai *et al.* 1999) or identify OCs in starting cell populations (Ariffin *et al.* 2010). The nature of the bone marrow cell population at baseline was considered to be important for accurately delineating gene-dependent osteoclast responses in this study. Realistically, differences in the proportion of each individual cell type on day 0 (baseline) could affect the number and function of the osteoclasts generated in each assay at endpoint.

Consequently cell populations were positively selected according to their frequency. These were monocytes (OC precursor cells), lymphocytes (producer of RANKL) (Rodan and Martin 2000), erythrocytes and megakaryocytes (secrete OPG) (Kacena *et al.* 2006) whereas MSCs, stromal cells and granulocytes were grouped as other due to their low numbers. In the literature different monocytic cell populations determined as OC precursors were quantified after cell sorting as total of 0.2 to 1.99% of bone marrow mononuclear cells (Arai *et al.* 1999). Many studies do not quantify monocytes specifically. Craft et al. studied female dogs and found that 3.8% of bone marrow cells were premyelocytes and 4.7% were haemocytoblasts (Crafts 1948). However, when examining adherent human blood mononuclear cells, Takahashi et al. identified more than 95% as monocytes after incubation on plastic overnight (Takahashi *et al.* 1995). Therefore the concentration of monocytes and their precursor cells can vary. In my hands, about 40% of adherent cells isolated on glass constituted monocytes.

When comparing adhered cell populations, WT and CD59a$^{-/-}$ samples presented a similar pattern. This suggests that differences identified at a later stage did not result from variations in adherence ability so expression of molecules such as N-cadherin, β-catenin and VCAM which are important for the HSC homing and

OC precursor recruitment are likely to be regulated normally (Shin *et al.* 2005; Yin and Li 2006). Interestingly, when examining male CD59a$^{-/-}$ to C6$^{-/-}$ bone marrow cells a significant increase in monocyte numbers was observed in C6$^{-/-}$ samples. This suggested that more monocytes were present in the bone marrow or had adhered more readily. In the literature, the effects of MAC components on bone marrow monocytes had not been investigated. Kim et al. revealed that in bone marrow transplantation, deficiency in C5 resulted in impaired HSC engraftment probably because of less signalling through CR3 and CXCL12/stromal derived factor-1 (SDF-1) secretion (Kim *et al.* 2011). This demonstrated that complement and haematopoiesis are closely linked and a down-regulation of monocyte differentiation by background levels of MAC activation might be a possible mechanism.

4.4.2 Optimisation of OCG Assay

After bone marrow cell adherence, cells were cultured in M-CSF supplemented with and without RANKL; only cultures containing both mediators generated OCs. According to the literature, M-CSF stimulation is initially required to induce RANK expression and then provides for additional proliferation, differentiation and survival signals. RANKL is essential to induce OC generation and also guarantees resorption activity (Rosen 2008) as described in section 1.4.3.1.

There are ways of growing OCs using alternative supplementation without the addition of RANKL or M-CSF. When no recombinant M-CSF was added differentiation was supported by Flt3-ligand, IL-3, GM-CSF, VEGF or other growth factors (Galal *et al.* 2007; Karieb and Fox 2011; Kawamoto *et al.* 2011) whereas a lack of external recombinant RANKL was substituted by light stimulation, TNFα, IL-6 or other cytokines. OCs grown through these alternative routes have less nuclei and hence resorb bone less efficiently (Filgueira 2009; Knowles and Athanasou 2009) than with M-CSF and RANKL supplementation.

In addition to mediator supplementation, cell seeding concentrations were tested and $3x10^5$ cells/well resulted in an increased yield of OCG over $5x10^5$ cells/well. Ishida et al. identified that cells plated sparsely were not in optimal proximity to merge and therefore differentiation time was elongated; whereas cells that were plated too densely had a reduced ability for full differentiation (Ishida *et al.* 2002). Therefore this research confirms that initial cell density is crucial for successful generation of OCs.

OCs were plated onto glass coverslips in this study. In the literature OCs are commonly cultured directly onto tissue culture plates (Idris *et al.* 2010). Visualisation

of OCs by microscopy was challenging in the laboratory when the cells were adhered directly to plastic plates (data not reported). Glass coverslips have also been used extensively in the literature (Komarova *et al.* 2003; Calle *et al.* 2004) as myeloid cells have been reported to adhere to glass (Trinchieri *et al.* 1986). They provide an excellent support that enables cells to be observed microscopically at high magnification as illustrated by Chen et al. (Chen *et al.* 2008).

When culturing bone marrow cells on 13 mm glass coverslips, cells formed distinct colonies which left a large area of the coverslip untouched. Macrophages stimulated with M-CSF have been shown to form colonies *in vitro* (Hamilton 2008). Additionally, OCs grown sparsely on surfaces develop into colonies as illustrated by Barsony et al (Barsony *et al.* 2011). In order to achieve even distribution, the coverslip size was reduced to 6 mm giving cells less surface area for more contact between colonies.

On 6 mm glass coverslips, the differentiation was still a challenge. Initially bone marrow cells were plated in a volume of 100 µl as recommended by Flanagan and Massey (Flanagan and Massey 2003) . As known from the literature, monocytes readily adhere to plastic and are also able to migrate (Czepluch *et al.* 2007). Therefore adherence in 100 µl resulted in adherence to plastic as well as the glass coverslip. Cell migration of the glass coverslip towards the plastic might have been caused by cytokines produced in monocytes that induced chemotactic gradients (Gein *et al.* 2011). In order to increase the yield, cells were adhered for a short period of time to the glass coverslip in a minimal volume (10 µl). To selectively enrich myeloid cells, the cells were only in contact with the glass coverslip during adherence which might have reduced migration and finally resulted in increased OC density.

In order to track OC development, coverslips were stained with TRAP on day 3, 5 and 7. It revealed that cells grown in M-CSF were $TRAP^-$ throughout the assay and proliferated exponentially. Cells cultured in M-CSF and RANKL proliferated less readily, but became $TRAP^+$ and large OCs started to appear by day 5. Biskobing et al monitored the effect of M-CSF induced proliferation on OCs. For this cells were treated with anti-M-CSF antibody from day 3 to 7 of OCG. The authors identified that M-CSF stimulation is most effective on day 3 of a 7 day culture and RANKL induced cell fusion is more dominant from day 4 onwards (Biskobing *et al.* 1995), reducing further proliferation. Furthermore, Chen et al. confirmed that when analysing differentiation over time, mature OCs appeared on day 5 (Chen *et al.* 2008). Therefore my data is consistent with published research.

When quantifying OCs, the percentage of $TRAP^+$ multinucleated cells was reported in this thesis. The manner in which OC differentiation data is presented varies tremendously between research groups. OC data is commonly presented as the absolute number of $TRAP^+$ multinucleated cells in a particular culture condition (Chen *et al.* 2008; Kukita *et al.* 2011). Variations in total cell number can also influence the capacity of cells to differentiate into OCs, therefore OC numbers were normalised according to total cell counts. This format has already been published by our group (Bull *et al.* 2008).

4.4.3 Measuring CD59a Expression during OCG

After optimisation of the OCG assay, CD59a expression was investigated over the time course utilising qPCR. CD59a was identified in adhered bone marrow cultures on day 0 (Fig. 4.8A). Within the next 24 h expression levels of CD59a decreased in samples stimulated with M-CSF alone or M-CSF and RANKL (Fig. 4.8B). Additionally, by day 1 the cell density was reduced as only cells reacting to the stimulation with M-CSF survived (Takahashi *et al.* 2003). This indicates that CD59 expression levels on OC precursor cells, probably mixed with HSCs, was low and other cell types within the bone marrow population were the primary source of synthesis. Davies et al. identified CD59 expression using immunofluorescence from human blood cells (Davies *et al.* 1989). The authors revealed strong staining of lymphocytes and granulocytes whereas erythrocytes and platelets showed weak staining, but monocyte expression was not revealed. In mice, only total bone marrow expression of CD59a had been evaluated by Baalasubramanian et al. (Baalasubramanian *et al.* 2004). My data showed that lymphocytes adhered to coverslips (section 4.3.1) and presented 8-10% of the differential cell counts. Hence, if lymphocytes also have a strong expression profile in mice, they could have caused the expression levels seen on day 0.

Transcription levels started to recover on day 3 and further increased by day 5 in cultures grown in M-CSF plus RANKL and M-CSF alone. Takahashi et al. identified an M-CSF-dependent bone marrow macrophage phenotype after 3 days of M-CSF stimulation (100 ng/ml). The phenotype was acquired by most cells expressing macrophage specific antigens such as F4/80 (Takahashi *et al.* 2003). As M-CSF concentration in OCG assays was lower, the macrophage phenotype might have required 5 days to develop. Therefore qPCR data suggests that differentiation into macrophages could account for increased expression of CD59a.

On day 7 expression of CD59a was comparable to day 5. As OC assays produced a mixture of precursor cells and OCs, it implies that OCs did not up-

regulate CD59a expression. Expression levels were not different between M-CSF and M-CSF plus RANKL stimulated cultures, but as OCs result from merging precursor cells which express CD59a, it is likely that OCs express low levels of CD59a. This is supported by a recent study which demonstrated weak human CD59 expression using immunofluorescent staining on human OCs (Ignatius *et al.* 2011).

4.4.4 Quantification of OCG from WT, CD59a$^{-/-}$ and C6$^{-/-}$ Bone Marrow Preparations

When quantifying OC differentiation over time, male CD59a$^{-/-}$ samples showed significantly increased OCG over WT and C6$^{-/-}$ samples at day 7. This supported the findings of preliminary *in vivo* data by Dr Anwen Williams in which increased TRAP^{+} staining was observed in the epiphysis of femur and tibia at the knee joint in aging CD59a$^{-/-}$ mice. Additionally it was in agreement with findings of a human study in which CD59 and DAF deficiency was correlated to increased bone resorption markers found in plasma samples (Terpos *et al.* 2003). Taken together, it suggests that CD59a might down-regulate OCG directly via an unknown mechanism.

Increased OCG was not seen in female CD59a$^{-/-}$ mice. This gender specific effect is not restricted to OCs. PNH phenotype in CD59a$^{-/-}$ mice was also exclusively present in male mice which was caused by higher haemolytic complement activity as explained in section 1.3.3 (Holt *et al.* 2001). Many complement studies are performed in male mice as additional factors have been shown to be involved in gender specific effects (Bora *et al.* 2007; Mamane *et al.* 2009; Lewis *et al.* 2011). Baba et al., for example, identified a C5 dimorphism in male mice which were functionally identical, but the additional protein was controlled by testosterone (Baba *et al.* 1984). Furthermore sex-limited protein, a homologue of C4 with partial C4a functions, was also identified to be specific to males (DIJK 1999). Moreover, hormonal fluctuations were thought to be involved in gender specific effects of CD59a regulation in the brain during focal cerebral ischemia. In that study, progesterone was mentioned to exhibit protective effects in females (Harhausen *et al.* 2010). Another sex hormone, oestrogen had been found to influence the complement pathway in numerous ways. C3 expression was shown to be altered at the transcriptional level by oestrogen (Fan *et al.* 1996) and C5a-mediated calcium influx in neurones is modulated by estradiol (Farkas *et al.* 2012). Interestingly oestrogen was found to increase susceptibility of female mice to CIA by enhancing CR1 expression on B-cells and therefore linking the complement system to the hormonal response (Nilsson *et al.* 2009). Furthermore, bone diseases present different gender prevalence. Osteoporosis for example, results in fractures in 1:2

women and 1:5 men over the age of 50 years. Post-menopausal women are especially affected as oestrogen levels diminish dramatically (Rosen 2008). A large variety of studies have investigated the role of oestrogen in bone health and disease (Hughes *et al.* 1996; Bilezikian *et al.* 1998; Schiessl *et al.* 1998; Bone *et al.* 2000). Oestrogen acts directly on bone cells to favour OB formation over OCG as described in Tab. 1.10. Here it seems that the effect of sex hormones is stronger than the effect of CD59a, therefore sex hormones are likely to cause protection from increased OCG in female mice.

Finally, $C6^{-/-}$ had been included in the study to enable distinguishing between complement dependent or independent function. As initial cell populations from $C6^{-/-}$ behaved differently from $CD59a^{-/-}$ cultures a direct comparison was not possible and this should be investigated via an alternative method.

4.4.5 Quantification of Cathepsin K

Cat K is the major protease, produced by OCs, which degrades the organic component of the bone matrix (Corisdeo *et al.* 2001). In order to identify if OCs generated *in vitro* are functionally active, Cat K expression was investigated in OC assay supernatants.

A human Cat K ELISA kit was initially tested. Supernatants did not reveal Cat K levels above background readings of the medium. In a rat study by Wada et al., plasma Cat K levels of 2.5 to 10 pmol/l were quantified utilising the same kit. This illustrates the sensitivity of the assay (Wada *et al.* 2005). Sequence composition showed 85% amino acid identity between the human and mouse Cat K protein (Gelb *et al.* 1996). However, it is possible that the mouse isoform is not recognised by the antibodies raised against human Cat K.

Consequently, a bioassay was developed to evaluate Cat K activity. The bioassay had a limited sensitivity in the low ng/ml range for collagenase utilised. Many assays and ELISA kits commercially available can detect proteins in the picogram range. Zee et al., for example, developed a bioassay that allowed for sensitive collagenase activity detection. Radiolabelled [C^{14}] collagen was added to culture supernatants and left for digestion. Collagen that was not digested was centrifuged and radioactivity left in the supernatant was measured (Zee *et al.* 1998). My bioassay was unsuitable for measuring small quantities of Cat K and alternative techniques were considered.

A collagen type I zymography was set up to identify Cat K activity at low pH, but no proteolytic activity was revealed. Recently, Li et al. optimised a zymography methodology to quantify Cat K. Instead of using supernatants, cells were lysed and

protein extraction was concentrated before being subjected to zymography (Li *et al.* 2010). This suggests the possibility that small amounts of Cat K could be present within OCs which would not have been detected by my method.

In my bioassay and Col1 zymography collagenase activity was not identified at low pH. Cathepsin K is mainly present in its proform, but once activated by low pH is susceptible to denaturation which might have caused problems during my assays (Zhao *et al.* 2009).

Furthermore, bioassay and zymography were inhibited by FCS components at low pH. Kitami et al. cultured all OCG assays in serum free medium for the last 24 h to avoid interference (Kitami *et al.* 2010). This would have been a possibility to enhance signals of collagenase activity in this project.

Both methods confirmed collagenase activity at pH7.4 and MMP-1 was identified. MMP-1 is produced by OCs to initiate collagen degradation before the resorption pit has been established (Derenne *et al.* 1999), but it is not specific to this cell type (Kähäri and Saarialho-Kere 1997) and might have been secreted by monocytes/macrophages or stromal cells (Riikonen *et al.* 1995) that might have been present in the culture system.

After identifying that none of the methods were suitable to detect Cat K in OCG supernatants, there is a strong possibility that Cat K was not expressed in OCs on glass coverslips. Corisdeo et al. revealed that Cat K is only secreted by actively resorbing OCs. Therefore, it is likely that the absence of bone matrix was responsible for the lack of Cat K. The same study suggested that OPG is required to stimulate Cat K expression and as cultures in this study did not favour OBs, the microenvironment for resorption was not given (Corisdeo *et al.* 2001).

Furthermore, Wilson et al. showed that Cat K is essential for the initiation of resorption by uncovering Arginine-Glycine-Aspartic acid motifs for VNR to attach to (Wilson *et al.* 2009). RANKL induces Cat K expression in the early stages of resorption. The enzyme is then stored in lysosomal vesicles and should be released into the resorption pit (Zhao *et al.* 2009), again suggesting that the bone surface is required to induce Cat K.

In contrast to this, a study by Fuller et al. proved that a bone environment is not essential for resorption. In this study OC were grown in serum free medium and activity was tested on glass coverslips coated with vitronectin. Sole binding of the VNR induced a sealing zone and resorption like trail formation. When fibronectin coating was used instead of vitronectin, OC activity was not observed suggesting that VNR attachment to a substrate is required (Fuller *et al.* 2010). As VNR was not

used in my study, OCs did not anchor to the surface and therefore might not have received the correct signals to express or secrete Cat K.

A single paper described Cat K detection in culture supernatant by western blotting when growing Raw 264.7 on plastic (Kitami *et al.* 2010). This lack of studies looking at secreted protein suggests that Cat K release requires a trigger whether it is the bone surface or VNR.

4.4.6 Quantification of MMP-9

MMP-9 is another protease highly expressed by OCs (Ishibashi *et al.* 2006). After identification of MMP activity in Cathepsin K studies, the activity of MMPs was further investigated. A large band of ProMMP-9 as well as smaller bands of active MMP-9 and Pro-MMP-2 were identified by gelatin zymography. The literature confirms that multiple MMPs, such as MMP-2, -3, -7, -9, -10, 12 and -13, are expressed by OCs and MMP-9 is produced in the largest quantity (Ishibashi *et al.* 2006; Lynch 2011). Hence zymography proved that proteases are secreted by OCs and their precursor cells.

When comparing gelatin zymography results to zymography studies of other OCG assays, rat samples confirmed the presence of ProMMP-9 and ProMMP-2 (Oka *et al.* 2012). OC differentiation of Raw 264.7 cells and murine bone marrow precursor cells cultured on plastic produced a band for active MMP-9 at 92kDa, but no ProMMP-9 or MMP-2 (Sundaram *et al.* 2007; Franco *et al.* 2011; Ghayor *et al.* 2011). Interestingly, Samanna et al. reported Pro-MMP-9, active MMP-9 and MMP-14 secretion in WT OCG samples (Samanna *et al.* 2007). These findings revealed that the type of culture conditions and precursor cells used alters the MMP profile visible on gelatin zymography.

The high level of ProMMP-9 identified in my study suggested that ProMMP-9 activation is not triggered efficiently in the culture system in this study. ProMMP-9 is activated by MMP-1,-2, -3 and -7. MMP-2 in turn is activated by MMP-14 and plasmin (Baramova *et al.* 1997). Therefore, inactivity may result from a missing activation cascade.

Western blotting was utilised to confirm identity of MMP-9 on zymographs. Interestingly, the anti-MMP9 antibody did not only bind active MMP-9 and ProMMP-9, but it was identified in an inactive conformation in medium containing FCS. Clinical studies in humans have shown that serum from healthy participants contained 200 to 600µg/ml MMP-9 (Jung *et al.* 2001). Therefore it is likely high concentrations of ProMMP-9 were also present in FCS, but as these are inactive, they did not interfere with the detection of mouse ProMMP-9.

MMP-9 was also identified at higher MW in WT and CD59a$^{-/-}$ samples at 1:5 dilution. Tissue inhibitors of metalloproteases (TIMPs) have a molecular weight of 21 to 29kDa and are produced by MMP secreting cells to balance MMP activity. They can bind a wide range of MMPs (Reynolds 1996; Visse and Nagase 2003). As zymography is performed without reducing disulphide bonds, proteins bound together due to disulfide exchange can be identified at their combined MW. As TIMPs have a low MW it is likely that the additional bands identified are MMP-9 - TIMP complexes.

As ProMMP-9 was the major protease identified, concentrations were measured via ELISA. Cells stimulated with M-CSF alone, produced 6-10ng/ml ProMMP-9 on day 3 and levels diminished. Xie et al. identified that peripheral blood monocytes that did not receive any stimulation produced little ProMMP-9 whereas stimulation with M-CSF resulted in a 5 to 7-fold increase. ProMMP-9 levels were thought to be supporting cell adhesion, spreading and macrophage differentiation (Xie *et al.* 1998). Therefore if macrophage phenotype was reached by day 5 in cultures in this study as discussed in section 4.4.2, MMP-9 stimulation may have not been required anymore and therefore could have returned to basal levels.

Supplementation of cultures with RANKL resulted in a 5 fold increase in ProMMP-9 on day 3 which slightly increased by day 5 and then remained constant. The literature confirms that in OC precursor cells RANKL stimulation leads to MMP-9 up-regulation which in turn drives differentiation (Sundaram *et al.* 2007). Franco et al revealed that when inhibiting MMP-9 with doxycycline, cells were not able to express TRAP or Cat K (Franco *et al.* 2011). Additionally, Ishibashi et al. had discovered that MMP-9 is essential for pit formation, made possible by allowing OCs to migrate though matrixes containing proteoglycans (Ishibashi *et al.* 2006). This suggested that ProMMP-9 secretion in cultures of this study was likely related to OCG.

ProMMP-9 levels were comparable between WT, CD59a$^{-/-}$ and C6$^{-/-}$ suggesting that its concentration is not related to OCs specifically. Other markers of OCs, such as CTR, should be explored. This marker is also shared by macrophage precursor cells and OCs (Granholm *et al.* 2008). Therefore subtle differences between WT and CD59a$^{-/-}$ OC expression pattern might not be readily detectable.

4.4.7 Quantification of Cytokines/Chemokines

Cytokine screening revealed mKc up-regulation in CD59a$^{-/-}$ over WT samples in cultures containing M-CSF and RANKL (Fig. 4.20). mKc is the murine ortholog of human Groα and IL-8, and it signals through CXCR2 (Hol *et al.* 2010). mKc was

identified as one of the two major neutrophil chemoattractants expressed by resident tissue macrophages (De Filippo *et al.* 2008). Onan et al. identified mKc up-regulation in OB lineage cells after PTH or PTHrP stimulation. OB utilised mKc to attract OC precursor cells which possess CXCR2. It was demonstrated that CXCR2 knockout mice presented an underdeveloped phenotype with fragile jaw bones supporting the finding that mKc signalling might be involved in bone development. Therefore mKc was thought to play a role in OCG in this study.

When mKc levels were compared in WT, CD59a$^{-/-}$ and C6$^{-/-}$ samples utilising ELISAs, levels in CD59a$^{-/-}$ and C6$^{-/-}$ samples were significantly enhanced over WT samples, but when normalised to cell number the difference between WT and CD59a$^{-/-}$ samples in male samples disappeared on day 3 and 7. Onan et al. supplemented OCG assays with mKc and did not discover a difference in OC formation or function (Onan *et al.* 2009). This suggests that enhanced mKc expression was solely due to proliferation and not contributing to OCG. Proliferation rates should be investigated further to understand the function of CD59a in OCG.

More recently it has been shown that mKc is expressed by megakaryocytes in the bone marrow to induce neutrophil mobilisation into the blood stream (Köhler *et al.* 2011). As megakaryocytes were elevated in male CD59a$^{-/-}$ over C6$^{-/-}$ mice, mKc secretion by megakaryocytes might have stimulated bone marrow precursor cells, but this has not been investigated yet. Megakaryocytes and OC precursor cells originated from the common myeloid progenitor (Akashi *et al.* 2000) and it should be examined if numbers of these progenitors are up-regulated which could result in enhanced differentiation and maybe take forward the search for a mechanism of increased OCG in CD59a$^{-/-}$ mice.

In order to take forward this search, other chemokines should be analysed. CXCL12/SDF-1 has been shown to recruit OC precursor cells as well as support OC formation and activity. Moreover, MIP-γ is the main chemokine of OCs. It is up-regulated by RANKL directly and also responds to M-CSF in order to enhance OC formation. Finally, CCL2/monocyte chemotactic protein 1 (MCP-1) and CCL3/MIP-α are involved in precursor recruitment and OCG (Onan *et al.* 2009). Additionally, receptor expression on OCs, such as RANK, might be affected. Any of these might be a potential target of CD59a and should be investigated.

4.5 Conclusion

In summary, *in vitro* assessment of CD59a on OCG resulted in the following findings:

- An OCG assay was successfully developed with optimal yield of $TRAP^+$ multinucleated cells.
- Initial plating showed no difference in $CD59a^{-/-}$ and $C6^{-/-}$ in comparison to WT. However, male $CD59a^{-/-}$ samples showed increased formation of OCs after 7 days of culture.
- Mediator analysis (Cat K, ProMMP-9, mKc) did not reveal a mechanism for increased OCG in male $CD59a^{-/-}$ samples.

The main finding of significantly raised OCG in $CD59a^{-/-}$ in comparison to WT samples highlighted a role of CD59a in bone homeostasis and the investigation of CD59's effect in human OCG was performed subsequentially.

Chapter 5

Investigating the Role of Human CD59 in Bone Resorption

5.1 Introduction

The up-regulation of OCG in CD59a$^{-/-}$ mice revealed in chapter 4 provides a potential mechanism not only for increased bone pathology identified in murine inflammatory arthritis models, but also in human diseases. CD59 down-regulation has been shown in diseases with bone pathology, such as RA and PsA, as described in Tab.1.6. Additionally, a study in multiple myeloma patients revealed a correlation of CD59 and DAF deficiency with elevation of OC resorption (Terpos *et al.* 2003). In this chapter, the functional significance of the effect of CD59 on bone in humans was investigated, as this has not been addressed in previous studies.

5.2 Aim and Objectives

The aim of this chapter was to determine the effect of CD59 depletion on OCG in humans. In order to achieve this aim, three specific objectives were formulated, namely: -

1. To establish a human OC resorption assay from peripheral blood CD14^{+} monocytes from healthy donors.
2. To develop a stable knockdown system for CD59 in human CD14^{+} monocytes/macrophages.
3. To determine the effect of CD59 on human OCG and resorption from peripheral blood CD14^{+} monocytes from healthy donors.

5.3 Results

A resorption assay was set up to confirm CD59 induced down-regulation of OCG in humans. Peripheral blood CD14^{+} monocytes were used in these assays, as they are known to express CD59. To establish the efficacy of CD59 knockdown using shRNA, several specific issues needed to be addressed. Firstly, to achieve CD59 knockdown a suitable delivering system for the shRNA had to be tested. The next step was to identify the most effective shRNA sequence for the silencing of CD59. In addition the kinetics of achieving maximal knockdown of CD59 protein after infection were investigated. Finally, the viability of CD14^{+} monocytes after viral infection was examined. Data collected during these experiments are described below.

5.3.1 Establishment of a Resorption Assay for Human Cells

To reveal the involvement of CD59 in human OCG and OC function, a resorption assay was set up. Human CD14^{+} monocytes (6.4x10^{4} per ivory disc) were left to adhere to 6 mm ivory discs. Cells were cultured in M-CSF (5 ng/ml) alone or in combination with RANKL (2 ng/ml) for 14 days. TRAP staining was used to identify

OCs in the mixed cell population at endpoint, whilst subsequent staining of the disk with Toluidine blue revealed the OC-induced resorption pits (section 2.5.3 to 2.5.5).

$TRAP^+$ cells or resorption pits were rare in cultures grown in M-CSF alone (Fig. 5.1A and C). The addition of RANKL resulted in a higher density of mononucleated $TRAP^+$ and induced multinucleated $TRAP^+$ cells (Fig 5.1B). Cultures stimulated with M-CSF and RANKL generated a high density of resorption pits (Fig. 5.1D), confirming the functionality of the assay. These data validated the assay for subsequent tests.

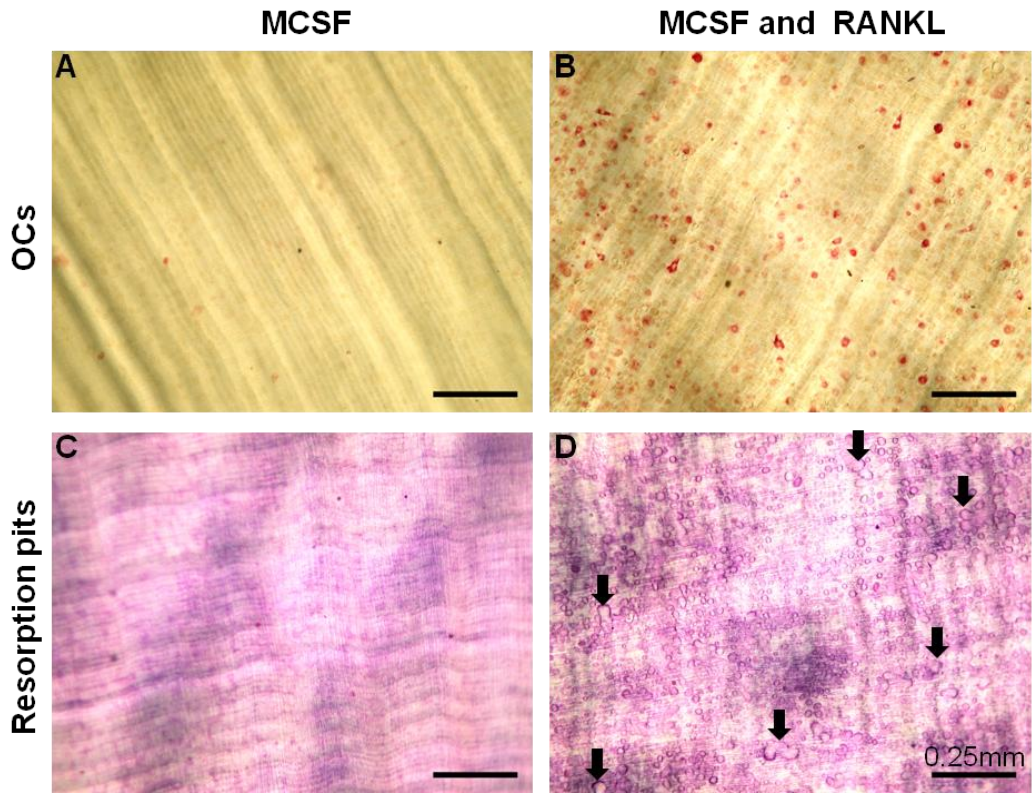

Figure 5.1 Testing of human OC for resorption activity. $CD14^+$ monocytes purified from peripheral blood were adhered to ivory discs and cultured in the presence of M-CSF (5 ng/ml) alone (**A** and **C**) or in combination with RANKL (2 ng/ml) (**B** and **D**) (n=1 donor of which 3 ivory discs were analysed at 5 FoV). After 14 days TRAP staining was performed to identify OCs (**A** and **B**) and cells were removed to stain for resorption pits utilising Toluidine blue (**C** and **D**). Examples of resorption pits are indicated (⬇).

5.3.2 Assessment of a Lentiviral Delivery System

Once the resorption assay was established, CD59 knockdown systems were tested in order to expose the role of CD59 in human OCG. Firstly the infection efficiency of a GFP-tagged lentivirus was investigated in Jurkat EB.1 cells (used as a positive control due to high levels of infectivity (Lombardo *et al.* 2007; Zhang *et al.* 2007; Yang *et al.* 2009)) and $CD14^+$ monocytes. Cells were cultured with the lentivirus for 2 days and then analysed by flow cytometry for GFP expression. Finally, CD59 shRNA containing virus was produced and its efficacy tested in Jurkat EB.1 cells (section 2.5.6).

Flow cytometry analysis of GFP-lentivirus infected Jurkat EB.1 cells demonstrated that 96% of the cells expressed GFP and the median fluorescent intensity shifted from 4 to 195, confirming that the virus had a high infection rate and the assay set up was correct (Fig. 5.2B). When infecting $CD14^+$ monocytes the median fluorescence of the population changed only slightly (from 3 to 5), indicating that either 1) the infection efficiency was low, 2) cells changed morphology causing autofluorescence to shift, 3) the cell viability was compromised or 4) the GFP expression and folding had slowed down (Fig. 5.3B). Jurkat EB.1 cells were therefore used to test the efficiency of the CD59 shRNA.

CD59 was consistently found to be expressed on the surface of Jurkat EB.1 as identified by antibody labelling and flow cytometry analysis (Fig. 5.4B). However, addition of control or indeed CD59 shRNA-containing lentivirus did not alter the expression level of CD59, indicating a poor knockdown, though other possible reasons for this are indicated below (Fig. 5.4C and D). In order to establish whether the lentivirus was able to infect cells, positive selection of the antibiotic puromycin was utilised. Only cells successfully infected with the lentivirus could grow in the presence of puromycin; therefore this would allow for the expansion of infected cells. Unfortunately, no infected cells could be enriched using this method.

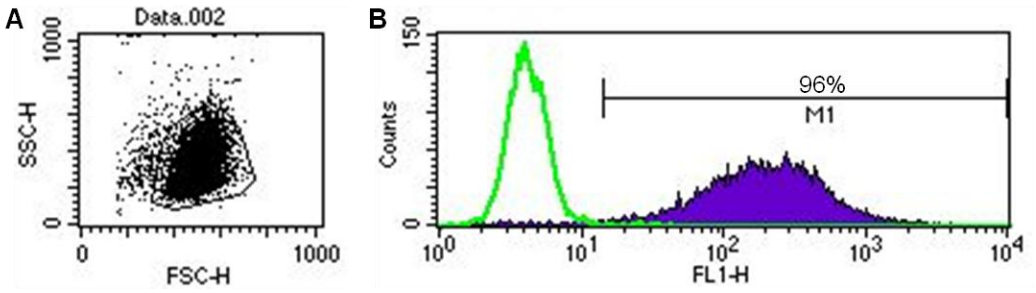

Figure 5.2 Flow Cytometry of GFP-lentivirus infected Jurkat EB.1 cells. $2x10^4$ Jurkat EB.1 cells were seeded and infected with GFP-lentivirus (MOI 8) for 2 days before analysis via flow cytometry (n=1 assay). The dot plot of cell size (FSC) versus granularity (SSC) identified a relatively homogenous population of cells which was gated (**A**). GFP was detected using FL1 (emission 525 nm). Cells without virus infection (green curve) were compared to infected cells (filled blue) and the percentage GFP positive cells (M1) as well as the median was determined (**B**).

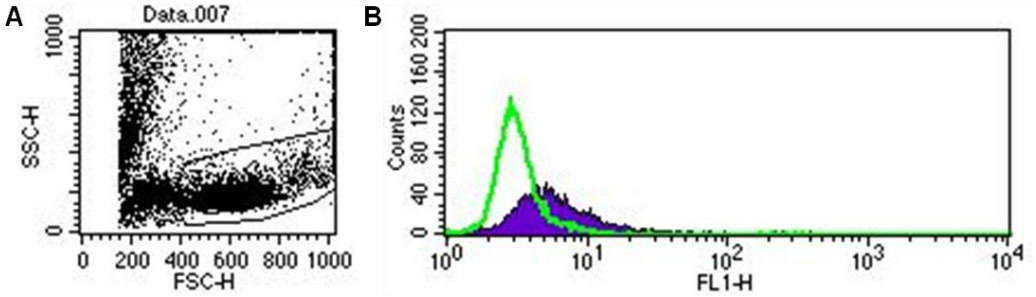

Figure 5.3 Flow cytometry of GFP-lentivirus infected human CD14$^+$ monocytes. $3.2x10^4$ monocytes were mixed with GFP-lentivirus (MOI 8) and Polybrene (6µg/ml), seeded and left to infect for 2 days before analysis via flow cytometry (n=1 assay from one donor). The dot plot of cell size (FSC) versus granularity (SSC) identified a relatively homogenous population of cells which was gated (**A**). GFP was detected in FL1 (emission 525 nm). Cells without virus infection (green curve) were compared to infected cells (filled blue) and the median was determined (**B**).

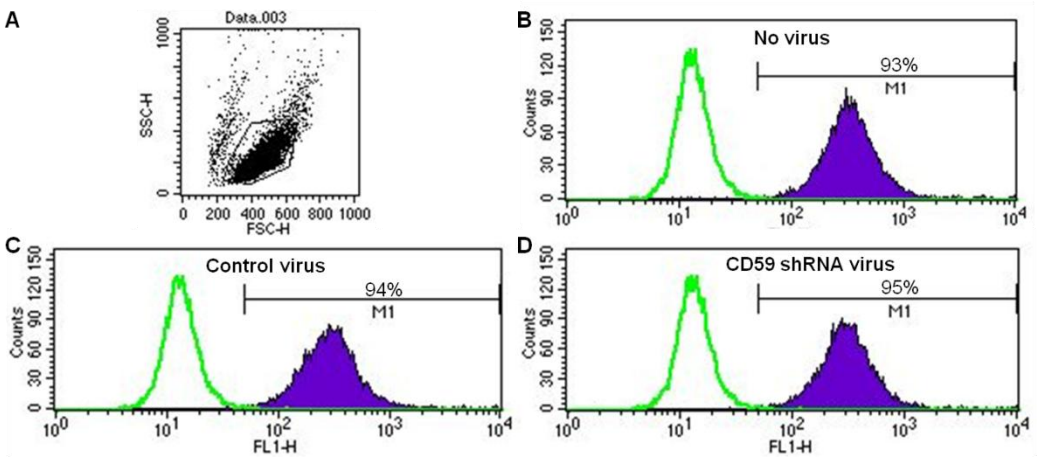

Figure 5.4 Flow cytometry of shRNA-lentivirus infected Jurkat EB.1 cells. $2x10^5$ cells were seeded and infected with virus (1:100 dilution) for 2 days (n=1 assay). Cells were stained for CD59 surface expression using an FITC conjugated secondary antibody. The dot plot of cell size (FSC) versus granularity (SSC) identified a relatively homogenous population of cells which was gated (**A**). FITC was detected in FL1 (emission 525nm). Isotype control (green curve) were compared to CD59 expression (filled blue) in cells that did not encounter viruses (**B**), cells infected with control virus without shRNA (**C**) and cells infected with CD59 shRNA expressing virus (**D**).

5.3.3 Development of an Adenoviral Delivery System

Adenoviruses only allow for a transient infection, but have the advantage of infecting monocytes readily (Mittal 2004; McLaren *et al.* 2010). Adenoviruses were therefore tested as an alternative delivery strategy for shRNA. GFP tagged, non-silencing shRNA control adenovirus and shRNA expressing adenoviruses were utilised to test infection efficiency and establish CD59 knockdown in $CD14^+$ monocytes/macrophages. Flow cytometry was performed to monitor cellular CD59 expression levels (section 2.5.7).

Initially, cells were transduced at different MOIs to test efficiency of infection. For this, viable cells were gated (Fig. 5.5A) and cell aggregates excluded (Fig. 5.5B). GFP expression at an MOI of 50 caused a clear shift in the histogram (median: 1,311,603) (Fig. 5.5C). Rising MOI resulted in higher median (MOI 500=7,167,817), even though the percentage of infected cells did not alter (Fig. 5.5D and E).

The knockdown potential of 3 different shRNA expressing adenoviruses was investigated. To select a virus, cells were gated as before and CD59 expression was confirmed in non-infected cells (Fig. 5.6A). All viruses tested knocked down CD59 expression (Fig. 5.6B). When comparing viruses, shRNA3 containing adenovirus down-regulated CD59 expression by 32% (median: 1,037,601) at an MOI of 50. With increasing MOI, the knockdown also improved; shRNA3 expressing adenovirus at an MOI of 500 caused the highest CD59 down-regulation by 56% (median: 674,944). TRAP staining of cultured $CD14^+$ monocytes/macrophages revealed declining cell density with increasing MOI (Fig. 5.7). Therefore higher MOIs were avoided in subsequent experiments.

As shRNA targets CD59 mRNA molecules, the translation into proteins and renewal of existing CD59 could be delayed. Therefore, protein expression was utilised as an indicator of knockdown efficiency. Cultures were incubated with virus for 2 or 4 days. Cell gating, CD14 and CD59 expression was carried out as before (Fig. 5.8A). Knockdown capacity was determined by comparing CD59 shRNA adenovirus to a control adenovirus at the same MOI. shRNA1 expressing adenovirus showed a 15% knockdown (median: 772,856) at an MOI of 200 in comparison to control virus, when cells were infected for 2 days after 5 day culturing in M-CSF (Fig. 5.8B). Similarly, when a combination of shRNA1 and 3 containing adenoviruses (an MOI of 100 each) were tested, a 12% reduction (median: 801,039) in CD59 expression was achieved at the same time point. When incubating cells with shRNA adenovirus for 4 days after 5 day culturing in M-CSF, a 48% knockdown (median: 679,767) of CD59 was achieved in cultures infected with shRNA1

expressing adenovirus at an MOI of 100. An MOI of 200 or combination of 2 viruses did not reach the same level of knockdown (42% and 35% respectively). After 7 days of pre-culturing in M-CSF, 7% knockdown was achieved when infecting $CD14^+$ monocytes with either shRNA1 containing adenovirus alone or a combination of shRNA1 and 3 expressing adenoviruses (total MOI of 200). shRNA1 containing adenovirus at an MOI of 100 therefore produced the most effective knockdown and was utilised in subsequent experiments.

To improve the cell viability, monocytes at different cell densities were infected after 1 day in culture. This time 7AAD was utilised to gate dead cells after aggregate exclusion (Fig. 5.9A-C). Viable cells were negative for 7AAD. CD59 expression was confirmed on uninfected cells (Fig. 5.9D), 20% knockdown (median: 358,278) was achieved when transducing $1x10^5$ cells with shRNA containing virus at an MOI of 100 whereas a 40% knockdown was obtained when $3x10^5$ cells were infected (Fig. 5.9E and F). TRAP staining uncovered a comparable cell density in both conditions after infection (Fig. 5.10). When cultured, these cells died instead of proliferating and therefore experiments were terminated. Unfortunately the limited time frame of the project did not allow further experimentation in this area.

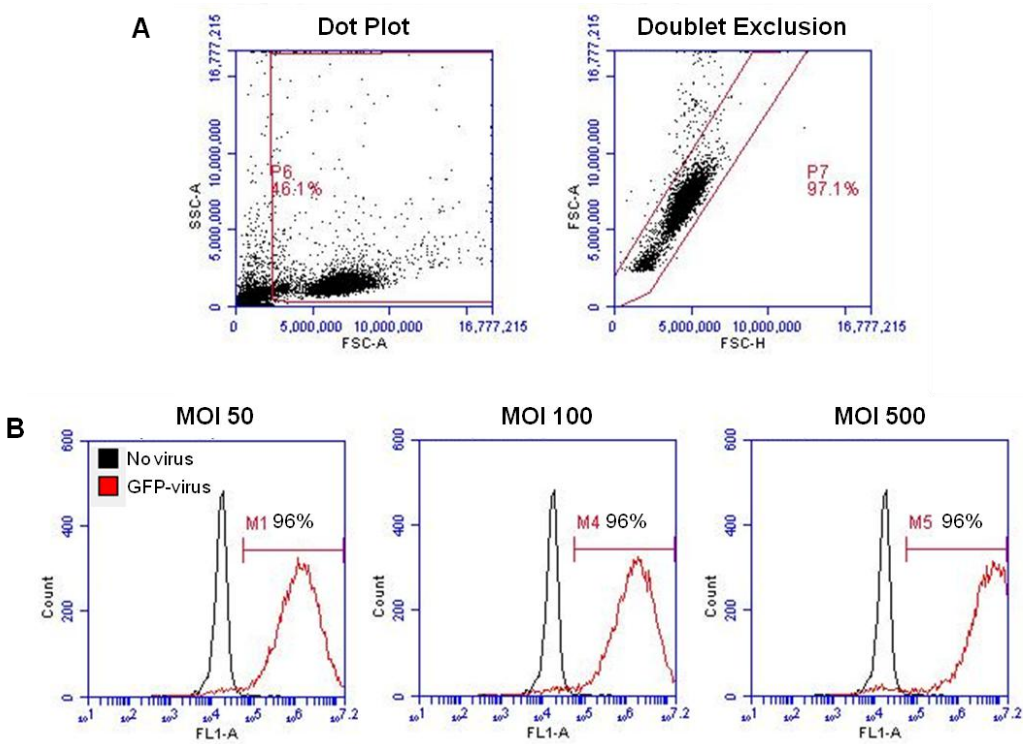

Figure 5.5 Flow cytometry to establish infection efficiency. 1x10^5 $CD14^+$ monocytes were seeded and cultured in medium supplemented with 5 ng/ml M-CSF for 5 days (n=1 assay from 1 donor). Cells were infected with GFP expressing adenovirus at MOI 50, 100 and 500 for 2 days. The dot plot of cell size (FSC) versus granularity (SSC) identified a relatively homogenous population of cells which was gated. To remove cell aggregates FCS-H (height) was plotted against FCS-A (area) and cells that did not follow the linear correlation were excluded (**A**). GFP was detected in FL1 (emission 530 nm). Unstained cells were compared to GFP expression and the percentage GFP positive cells (M1) as well as the median were determined (**B**).

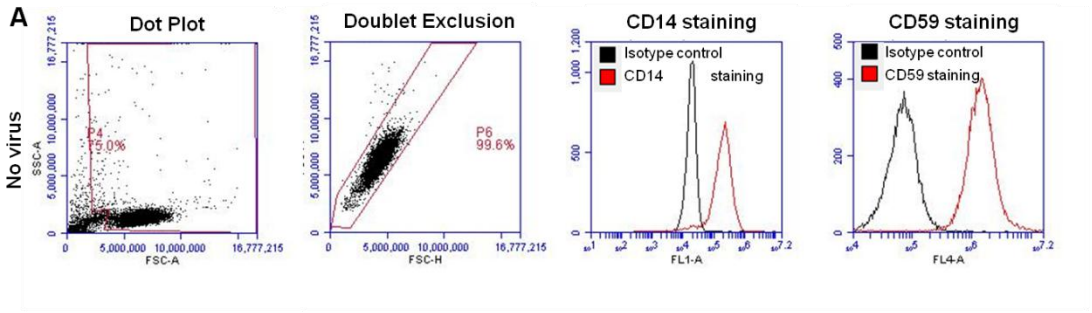

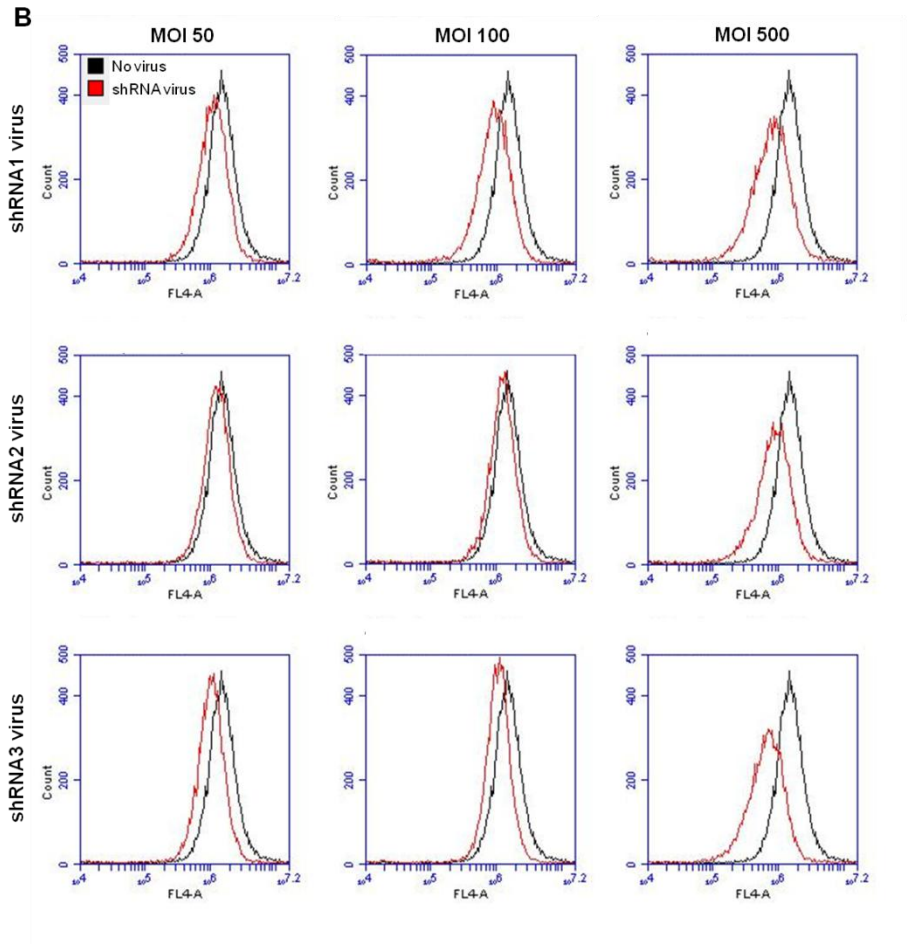

Figure 5.6 Flow cytometry to select the best CD59 shRNA containing adenovirus. 1x10^5 CD14$^+$ monocytes were seeded and cultured in medium supplemented with 5 ng/ml M-CSF for 5 days (n=1 assay from 1 donor). Cells were infected with shRNA1, 2 and 3 expressing adenovirus at MOI 50, 100 and 500 for 2 days. CD14 and CD59 staining was compared to isotype staining. FITC and Alexa Fluor 647 were detected in FL1 and FL4 respectively (emission 530 nm and 675/25 nm) (**A**). CD59 expression of cells that did not encounter virus was compared to shRNA containing viruses and the median was determined (**B**).

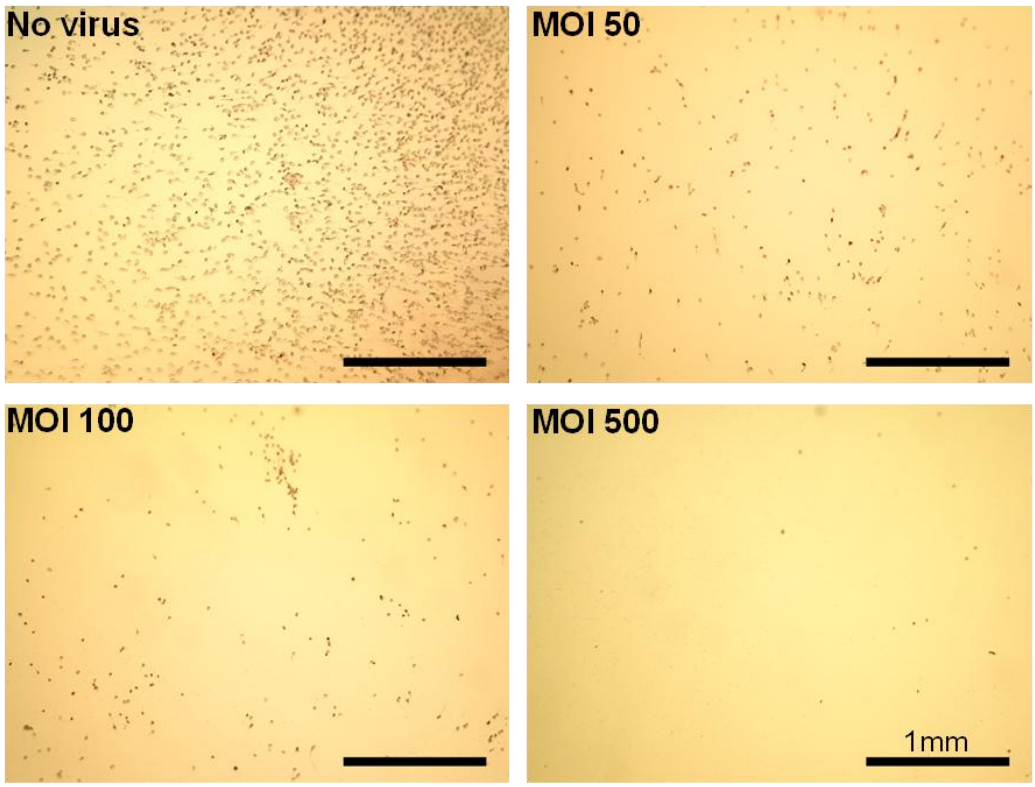

Figure 5.7 Representative images of cultured CD14$^+$ monocytes/macrophages. Cells were cultured and infected as outlined in Fig. 5.6. TRAP staining was performed to monitor cell phenotype of non-infected cells to cells with different virus load. Cells infected with shRNA 1 expression adenovirus are shown.

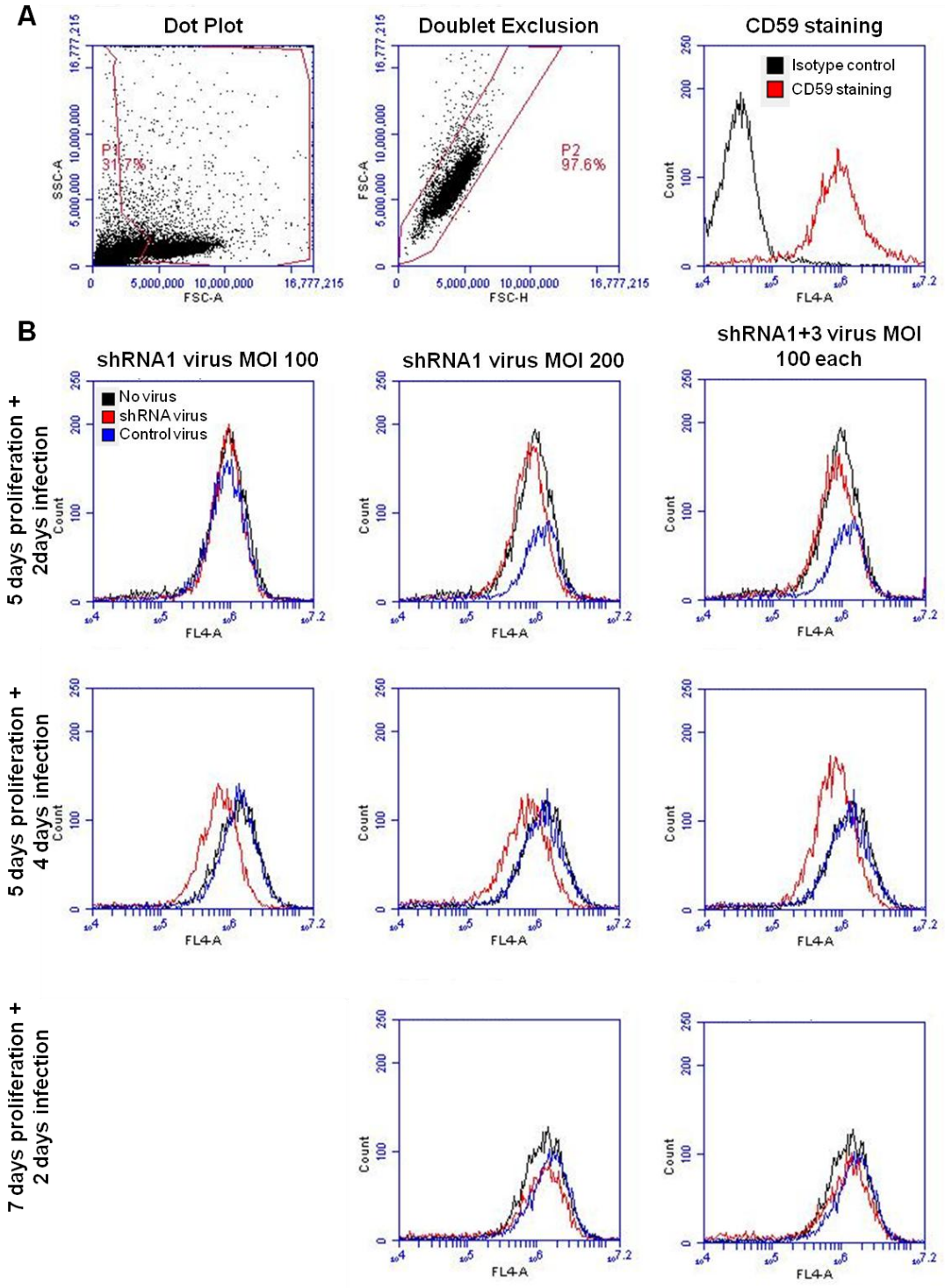

Figure 5.8 Flow cytometry to establish efficiency of knockdown at different time points of infection. 1x10^5 monocytes were seeded and cultured in medium supplemented with 5 ng/ml M-CSF for 5 or 7 days (n=1 assay from 1 donor). Cells were infected with shRNA1 alone or in combination with shRNA3 expressing adenovirus at MOI 100 and 200 for 2 to 4 days. Dot plot and aggregate exclusion was performed as described in Fig. 5.5A. CD59 staining was compared to isotype staining. Alexa Fluor 647 was detected in FL4 (emission 675/25 nm) (**A**). CD59 expression of cells that did not encounter virus and control virus were compared to shRNA viruses and the median was determined (**B**).

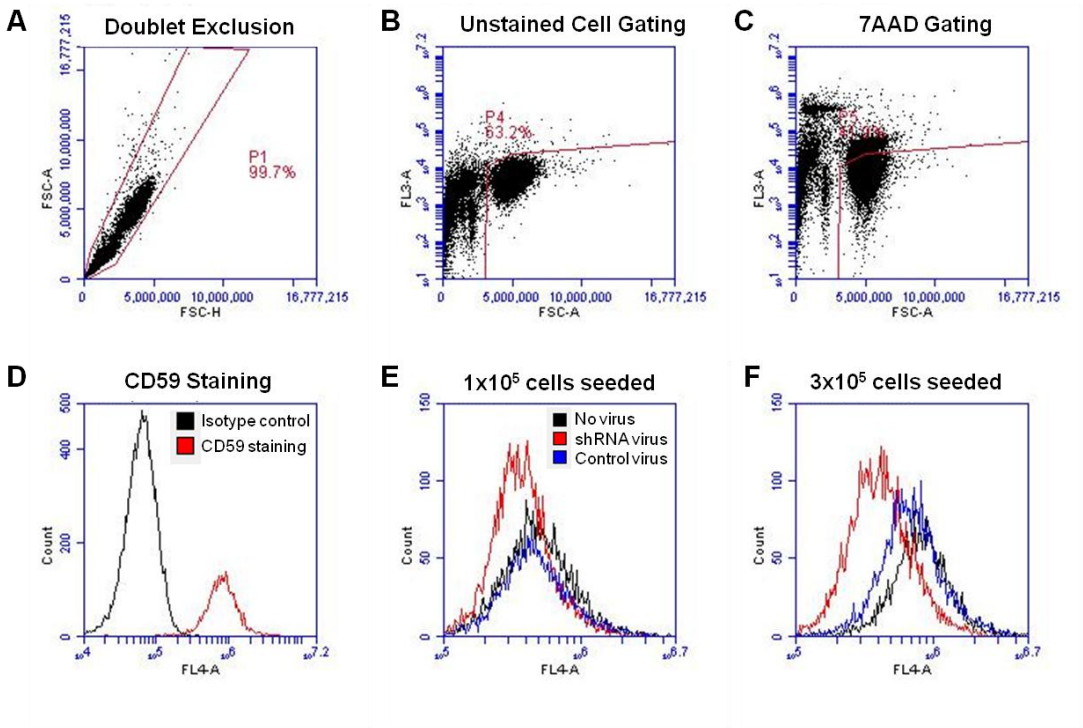

Figure 5.9 Flow cytometry to determine cell density. 1x10^5 or 3x10^5 CD14$^+$ monocytes were seeded and cultured in medium supplemented with 5 ng/ml M-CSF overnight (n=1 assay from 1 donor). Cells were infected with shRNA1 expressing adenovirus at MOI 100 for 2 days. To remove cell aggregates FCS-H (height) was plotted against FCS-A (area) and cells that did not follow the linear correlation were excluded (**A**). 7AAD was detected in FL-3 (580/40 nm) in unstained cells and were plotted against FSC (size) (**B**). A gate was determined for low FL-3 expressing cells and to also exclude cell debris. This gate was applied to stained cells to exclude non-viable cells utilising 7AAD staining (**C**). CD59 staining was compared to isotype staining. Alexa Fluor 647 was detected at FL4 (emission 675/25 nm) (**D**). CD59 expression of cells that did not encounter virus, transfected with control virus or with shRNA1 containing virus, were compared (**E** and **F**) and the median was determined.

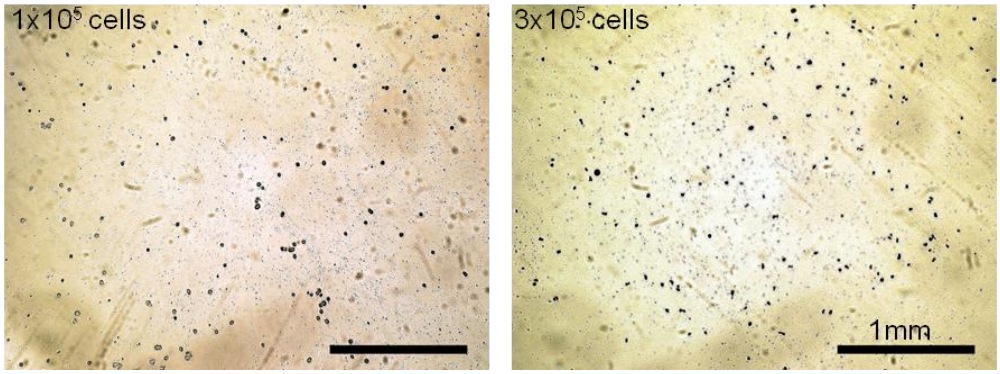

Figure 5.10 Representative images CD14$^+$ monocytes infected at different cell densities. Cells were cultured and infected as described in Fig. 5.9. TRAP staining was performed to monitor monocytic cell phenotype.

5.4 Discussion

A human OCG and resorption assay was set up to build a basis for introducing a CD59 knockdown system. The latter was crucial to depict the involvement of CD59 in OCG. In this 5th chapter, a number of viral delivery systems were developed and explored, with the eventual aim of achieving successful CD59 knockdown in target cells.

5.4.1 Establishment of a Resorption Assay for Human Cells

A resorption assay of human OCs was initiated on ivory discs. In the literature it was determined that these are the better source of bone supplement compared to calcium phosphate-coated plates (also called Osteologic discs). Beeton et al. confirmed functionality of both methods, but identified greater reproducibility when using Osteologic discs. In contrast, Contractor et al. highlighted that Osteologic discs were missing essential bone proteins, including collagen which builds a network that contains minerals (Contractor *et al.* 2005). As the structure of bone was mimicked closely by the ivory discs, they represented the best substrate for the assessment of the function of CD59 in the regulation of bone resorption.

Once monocytes were cultured on ivory, differentiation into TRAP$^+$ cells and some multinucleated TRAP$^+$ cells were observed in cultures supplemented with 5 ng/ml M-CSF and 2 ng/ml RANKL. These cells were functionally active and able to resorb bone, evidenced by pitting on the ivory discs. In the literature OCG and resorption on ivory discs were commonly induced by 25 ng/ml M-CSF and 20-50 ng/ml RANKL and stimulation was supplemented by other mediators (Kudo *et al.* 2002; Kim *et al.* 2005; Beeton *et al.* 2006). Here resorption was achieved with a lower concentration of M-CSF and RANKL compared to published data. As recombinant proteins from different suppliers might have varying activity, this suggested that R&D Systems reagents are suitable for supplementation at low concentrations.

5.4.2 Assessment of a Lentiviral Delivery System

Lentiviral infection of mammalian cells for research use and gene therapy were initially developed by Naldini et al. (Naldini *et al.* 1996). These recombinant lentiviruses were derived from human immunodeficiency virus type I (HIV-1) and other lenti- or retroviruses such as Venezuelan equine encephalitis to allow infection of non-dividing cells and genome integration (Paessler *et al.* 2003; Schambach *et al.* 2006; Picanço-C *et al.* 2012). To obtain a stable down-regulation of CD59 on human

$CD14^+$ monocytes/macrophages, a lentiviral knockdown system was desired for this project.

When infecting $CD14^+$ monocytes/macrophages with lentivirus, substantially less GFP signal was detected than in Jurkat EB.1 cells, suggesting higher infectivity in the latter (Lombardo *et al.* 2007; Zhang *et al.* 2007; Yang *et al.* 2009)). In monocytes the shift of fluorescent intensity was small but the fluorescent signature of the whole cell population was altered. Therefore cells might have been GFP positive but level of expression of the vector was low as not only transfection efficiency but also expression can differ between cell types (Zhang *et al.* 2004), but this was not confirmed here.

Studies utilising lentiviral infection of $CD14^+$ monocytes are mainly concerned with dendritic cell generation, achieved by stimulation with granulocyte colony stimulating factor (Rouas *et al.* 2002; Koya *et al.* 2003; Breckpot *et al.* 2004; Schmid *et al.* 2007). Only a small number of studies have infected monocytes with lentivirus for the purpose of OCG. Hamaza et al. generated a lentivirus containing shRNA against $P2X_7$ the pLKO.1-puro vector. This virus was successfully introduced into human $CD14^+$ monocytes and caused significant down-regulation of $P2X_7$ (Hazama *et al.* 2009). Additionally, Park-Min et al. reported a 90% infection efficiency in pre-OCs utilising a lentivirus (Park-Min *et al.* 2009). These previous reports showed that it is possible to infect $CD14^+$ monocytes with lentivirus under certain conditions; unfortunately this success could not be replicated in this study.

Furthermore, the findings of this chapter showed that addition of CD59 shRNA-lentivirus did not alter the cell surface expression level of CD59 on Jurkat EB.1 cells. This indicated that no knockdown of CD59 was achieved. The principle aim of this study was to prepare viral titres from the degree of knockdown at different lentiviral concentrations tested and the Poisson distribution, which was inconclusive. To further examine if the infection rate was disturbed by a viral defect or concentration problem, viral titres could also be established with the use of an ELISA to detect the HIV p24 gag antigen (Marr *et al.* 2003). Additionally genomic viral RNA qPCR could have been used to scan for integrated virus and quantify infection rate (Perez *et al.* 2010).

Further reasons for malfunction of virus production need to be considered. Plasmid transfection to generate recombinant lentivirus was performed with Effectene transfection reagents. The lipid formation relies on a optimal ratio of plasmids and Effectene, incubation time and vector size (Qiagen 2002). Unfortunately due to time and cost constraints this optimisation could not be performed.

When considering the density of lentivirus, it has to be noted that the virus was concentrated by ultracentrifugation. However, as the MOI was unknown, the virus concentration could have still been low, which could have resulted in a low infectivity. Interestingly, Rouas et al. reported that upon infection with 2 lentivirus solutions of the same virus and MOI, of which one was diluted 1:2, the more concentrated virus infected cells at a higher rate (Rouas *et al.* 2002). Therefore, highly concentrated lentivirus would have been desirable in this study.

Finally, not only are optimised viral preparation and high concentration essential for a high infection rate, but the surface interaction of the cell of interest with the viral envelope is also thought to be critical. In this study, the vesicular stomatitis virus glycoprotein (VSV-g) was utilised. VSV-g associates with phospholipids rather than by specific receptor interaction and therefore viruses expressing VSV-g should potentially be able to infect any cell type. Due to this lack of specificity, certain cell types such as airway epithelial cells have proven difficult to infect with VSV-g. A range of pseudotyped envelope vectors have been developed to overcome this problem (Burns *et al.* 1993; Engelke and Rossi 2005; Schambach *et al.* 2006). In a recent study the Aura virus derived pseudotyped Aura-G, which uses lectins to enter dendritic cells, was engineered (Froelich *et al.* 2011) and hence provides a more effective mechanism of cell entry for myeloid lineage cells.

Each of the factors outlined might have influenced the infection efficiency. Better checkpoints in virus development such as the p24 ELISA should be considered in the future to improve the quality of virus preparations before attempting infection.

5.4.3 Development of an Adenoviral Delivery System

Adenoviruses are an effective transient RNAi delivering system, producing large quantities of double-stranded RNA that is cleaved into miRNA within the cell allowing for effective knockdown. High infection efficiency was obtained when infecting human $CD14^+$ monocytes with GFP-tagged adenovirus. CD59 knockdown (up to 56%) was observed when cells were treated with shRNA containing adenovirus. McLaren et al., who also utilised this adenovirus system, achieved successful knockdown of death receptor 3 in human monocytic leukaemia THP-1 cells and human primary macrophages (McLaren *et al.* 2010). Adenoviruses do not naturally target human monocytes/macrophages, but have been found to be easily adaptable (Foxwell *et al.* 1998) and are generally known to infect at a high rate (Leyva *et al.* 2011). Hence the adenoviral system was more suitable for this study, as the infection efficiency of human monocyte/macrophages was already

established. Interestingly, adenoviruses have been shown to infect terminally differentiated cells including OCs (Tanaka *et al.* 1998). Therefore to study resorption, differentiated OCs could have been infected in this study, instead of $CD14^+$ monocytes/macrophages.

The knockdown system was not only dependent on the infection efficiency of the viral delivery, but also on a shRNA that was able to mediate the degradation of a substantial amount of CD59 mRNA. shRNA1 adenovirus showed the highest level of knockdown at MOI of 50 and 500. In the literature, MOI of 1 to 1,000 have been utilised for sufficient infection (Craig 2009; Borniquel *et al.* 2010; Minamitani *et al.* 2011). This suggests a wide range of potential viral load on the cells; however when TRAP staining on cultured $CD14^+$ monocytes was performed declining cell densities were observed with increasing MOI. The literature shows that adenoviruses can induce cell lysis via autophagy (Jiang *et al.* 2011). Therefore, in the current study, it is possible that cell death may have occurred via this mechanism.

To avoid this, a moderate MOI of 100 was selected for shRNA1 infection. shRNA1 reduced CD59 expression by 48% when incubated for 4 days with virus before analysis. Knockdown efficiency depends on the half-life of the target protein. Kolodekic et al. analysed vascular ATPase knockdown with siRNA after 2.5 h (Kolodecik *et al.* 2009). In contrast, CD59 is a GPI-anchored protein which, turns over at the cell surface within 4 h (Bojkowska *et al.* 2011); suggesting a different mechanism involved. As part of membrane traffic some proteins internalised from the cell membrane can be recycled. Cell surface proteins are captured in early endosomes which merge with trans-Golgi network vesicles. Here undamaged proteins are selected to be transported back to the cell membranes (Peer 2011). CD59 is likely to be a protein that was selected for recycling as it is essential for cell viability. Therefore mRNA levels might not be reflected in surface CD59 expression after a short time period. Alternatively, the down-regulation of CD59 expression identified using flow cytometry could have resulted from cell apoptosis. Cell death was shown to result in decreased expression of CD59 (Jones and Morgan 1995) and viability should be monitored more closely. Before any of these theories can be tested, knockdown of total CD59 expression should be visualised by qPCR/RT-PCR or western blotting of lysed cells (Szulc *et al.* 2006; Perez *et al.* 2010) to confirm and validate data obtained by flow cytometry.

Viral delivering systems were desirable in this study to obtain sustained knockdown of CD59, but siRNA or anti-sense mediated silencing can be achieved by direct delivery or utilising cyclodextrin-containing polycations, lipids or polymers

as coating molecules (Bartlett and Davis 2006). These systems could be tested to improve infectivity with reduced toxicity.

5.5 Conclusion

In attempting to determine the role of CD59 in human precursor cell differentiation and subsequent OC function *in vitro*, the following key results were obtained:

- Human $CD14^+$ monocytes generated functional OCs in the presence of M-CSF and RANKL.
- The lentiviral delivery of CD59 shRNA was unable to knockdown CD59 expression, however, adenoviral delivery of CD59 shRNA showed up to 48% CD59 knockdown, but cell viability was compromised.
- The role of CD59 in human OCG and OC function could not be determined within the given time scale, but this builds the basis for future investigations.

To further investigate findings from chapter 4, morphologic and mechanistic studies of CD59a's effect *in vivo* were carried out in WT and $CD59a^{-/-}$ mice.

Chapter 6

Phenotypic Analysis of Bone Structure in CD59a$^{-/-}$ Mice

6.1 Introduction

Murine OB and OC cultures *in vitro* highlighted CD59a's regulatory function of cell differentiation *in vitro*. *In vivo* their differentiation and function is influenced by numerous cell types, such as OTs, stromal cells, bone lining cells and OBs, OCs, monocytes and other haematopoietic progeny (section 1.5) (Rosen 2008). These function through membrane bound and secreted mediators, such as RANKL, OPG, cytokines, M-CSF and other growth factors. Furthermore hormones (eg. PTH), and environmental factors are able to direct bone homeostasis as summarised in Tab 1.10 (Rosen 2008). The role of CD59a in this regulatory environment *in vivo* has not been established.

6.2 Aim and Objectives

The aim of this chapter was to compare histomorphometry of bone in WT and CD59a$^{-/-}$ mice over a 50 week time course. To address this aim the subsequent key objectives were derived:

- To identify architectural changes in femora of WT and CD59a$^{-/-}$ mice at 8-10, 20 and 50 weeks.
- To measure bone mineral density (BMD) in cortical and trabecular bone of WT and CD59a$^{-/-}$ mice at 8-10, 20 and 50 weeks.
- To determine if CD59's function is gender specific.
- To establish if bone phenotype in CD59a$^{-/-}$ mice is localised to long bones or extends to other areas of the body.
- To quantify *in vivo* OB function by measuring osteoids and mineral apposition rate (MAR) in trabecular bone of WT and CD59a$^{-/-}$ mice.
- To measure OCs via TRAP staining in trabecular bone of WT and CD59a$^{-/-}$ mice.

6.3 Results

Femoral length and shaft diameter were determined for 8-10, 20 and 50 week old female and male WT and CD59a$^{-/-}$ mice to reveal morphological changes in CD59a$^{-/-}$ mice. These were determined utilising X-ray projections and a digital caliper. Once differences were identified, architectural parameters of cortical and trabecular bone were determined in specific areas of femora and spines using MicroCT. Femoral samples of 8-10 and 20 week old male WT and CD59a$^{-/-}$ samples were then processed for histological quantification of osteoids and OC. To further evaluate bone formation calcein was injected into a new cohort of 8-10 week old WT and

CD59a$^{-/-}$ mice to determine bone mineral apposition rate histologically. The results obtained from these studies are explained in detail below.

6.3.1 Quantification of Femoral Length and Shaft Diameter

Hindlimbs fixed in 70% ethanol were subjected to X-ray scanning in order to accurately measure femoral length as described in section 2.6.2. In females, values were comparable at 17.6±0.2 mm and 17.7±0.1 mm (results in this format: Mean±SEM unless stated otherwise) for CD59a$^{-/-}$ and WT samples respectively at 8-10 weeks of age (Fig. 6.1A and 6.2A). Femoral length rose significantly ($p<0.0001$) over time and was still comparable at 50 weeks (CD59a $^{-/-}$=19.8±0.5, WT= 19.7±0.2 mm).

In males, femoral length was significantly increased in CD59a$^{-/-}$ over WT mice at 8-10 (CD59a$^{-/-}$=18.4±0.1, WT=17.7±0.2 mm, $p<0.01$), 20 (CD59a$^{-/-}$ =19.2±0.2, WT=18.8±0.1 mm, $p<0.01$) and 50 weeks (CD59a$^{-/-}$=20.0±0.2, WT=19.3±0.2 mm, $p<0.05$) of age (Fig. 6.1B and 6.2B). Femoral length significantly increased ($p<0.0001$) over time in male CD59a$^{-/-}$ and WT samples.

When determining mid-shaft diameter, there was no difference in posterior-anterior direction in females at 8-10 (CD59a$^{-/-}$=1.29±0.01, WT=1.28±0.01 mm), 20 (CD59a$^{-/-}$=1.30±0.01, WT=1.32±0.01 mm) or 50 weeks (CD59a$^{-/-}$=1.53±0.05, WT=1.49±0.02 mm) (Fig. 6.3A). However in males, posterior-anterior diameter was significantly raised ($p<0.001$) in CD59a$^{-/-}$ (1.39±0.03 mm) over WT (1.22±0.02 mm) samples at 8-10 weeks (Fig. 6.3B). By 20 ($p<0.05$) and 50 weeks ($p<0.001$), diameter in WT samples were significantly increased in comparison to 8-10 weeks. In CD59a$^{-/-}$ samples the diameter did not change over time. This resulted in comparable diameters in WT and CD59a$^{-/-}$ samples at 20 and 50 weeks of age.

Similarly, female CD59a$^{-/-}$ and WT samples had a comparable medial-lateral diameter at 8-10, 20 and 50 weeks of age (Fig. 6.3C). However in males, the diameter in CD59a$^{-/-}$ was significantly enhanced ($p<0.01$) over WT samples at 8-10 weeks (Fig.6.3D). Again, the diameter only significantly increased in WT sample over time ($p<0.001$), resulting in no difference between CD59a$^{-/-}$ and WT samples at 20 and 50 weeks of age.

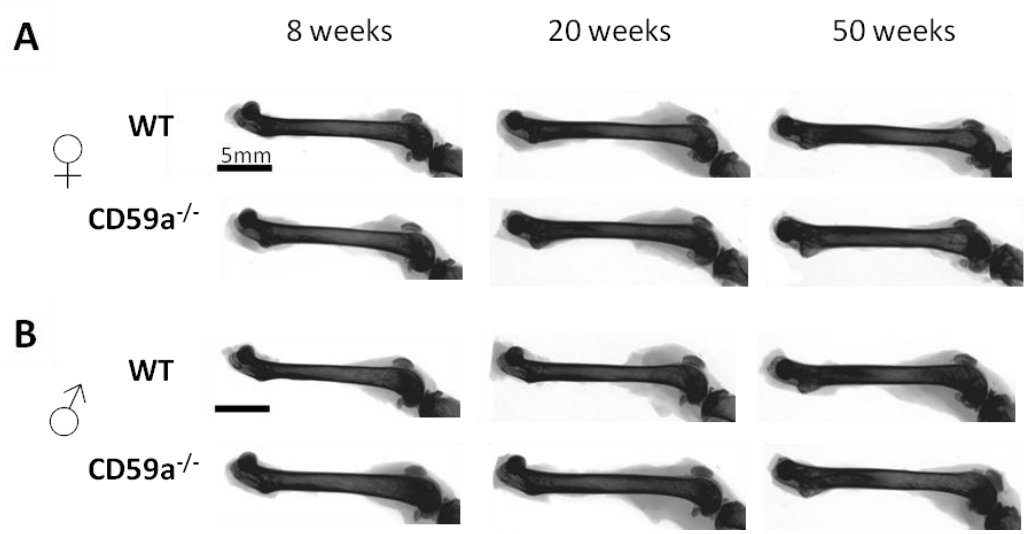

Figure 6.1 Representative X-ray projections of femora. Hindlimbs from female (**A**) and male (**B**) WT and CD59a$^{-/-}$ mice were submitted to X-rayed imaging at 8-10, 20 and 50 week of age utilising the Kodak In-vivo Imaging System FX Pro and representative images are shown.

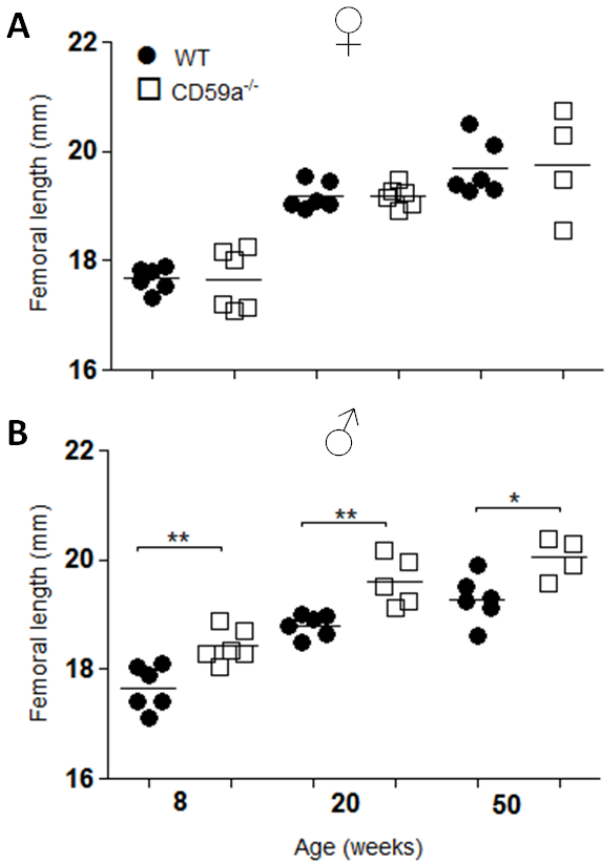

Figure 6.2 Quantification of femoral length. X-ray projections of female (**A**) and male (**B**) WT and CD59a$^{-/-}$ femora at 8-10, 20 and 50 weeks of age were assessed (n=6 mice per group). Femoral length was quantified utilising the Kodak MI SE software. Two-way ANOVAs were performed for **A** (strain: p=0.8983, age: p<0.0001, interaction: p=0.9643) and **B** (strain: p<0.0001, age: p<0.0001, interaction: p=0.9922). Bonferroni post-tests are indicated (*(p<0.05), **(p<0.01)).

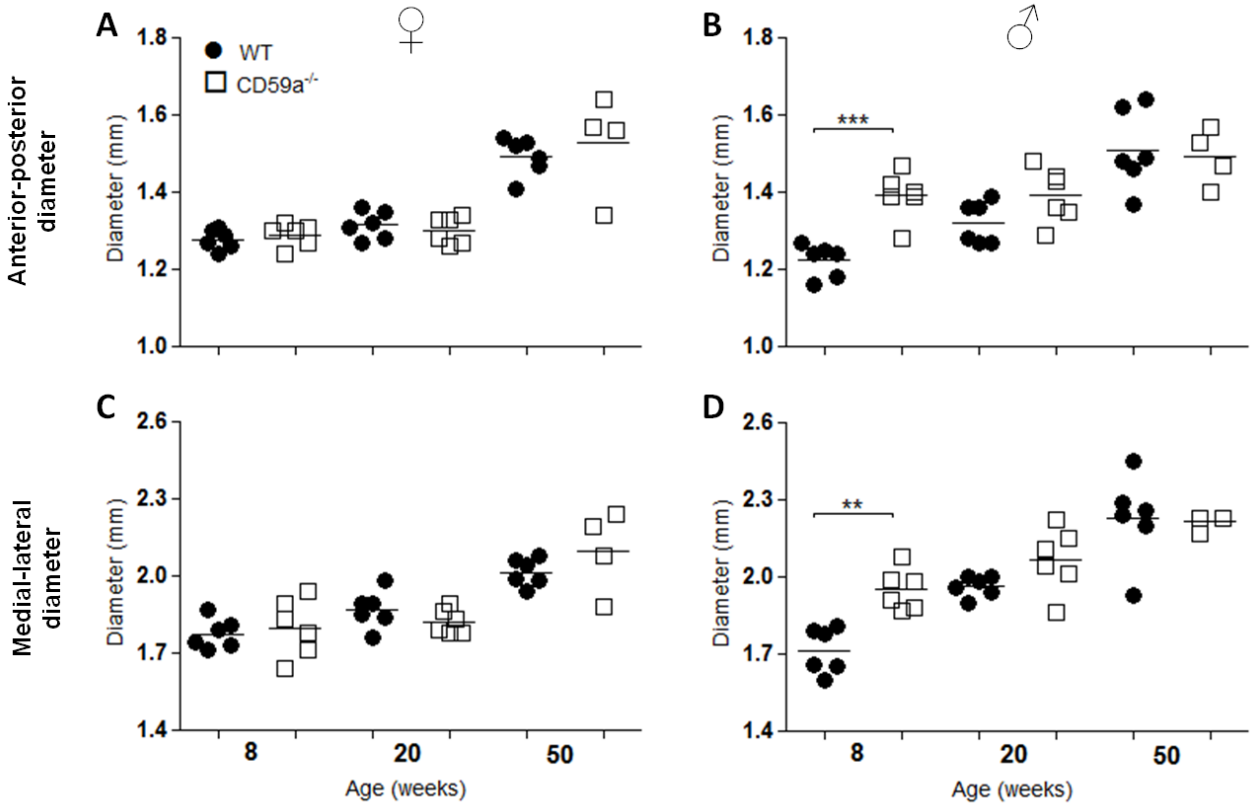

Figure 6.3 Measurement of shaft diameter. Diameter was determined with a digital caliper for female (**A** and **C**) and male (**B** and **D**) WT and CD59a$^{-/-}$ femora at 8-10, 20 and 50 weeks of age (n=6 mice per group). Measurements were performed for anterior-posterior (**A** and **B**) and medial-lateral (**C** and **D**) direction. Two-way ANOVAs were performed for **A** (strain: p=0.5712, age: p<0.0001, interaction: p=0.6050), **B** (strain: p=0.0052, age: p<0.0001, interaction: p=0.0167), **C** (strain: p=0.5154, age: p<0.0001, interaction: p=0.2373) and **D** (strain: p=0.0057, age: p<0.0001, interaction: p=0.0326). Bonferroni post-tests are indicated (**(p<0.01), ***(p<0.001)).

6.3.2 3D Assessment of Cortical Bone in Femora

After identification of differences in bone length and diameter between CD59a$^{-/-}$ and WT samples (section 6.3.1), phenotypical analysis of structural parameters was performed utilising MicroCT (methodology in section 2.6.3.3). Initially cortical bone in the femoral shaft was evaluated.

In females, cortical bone volume (cBV) was comparable in CD59a$^{-/-}$ and WT samples at 8-10 and 20 weeks (Fig. 6.4A). Interestingly at 50 weeks, cBV is significantly reduced ($p<0.05$) in CD59a$^{-/-}$ (0.89±0.05 mm^3) over WT (0.98±0.01 mm^3) samples. cBV significantly grew ($p<0.001$) between 8-10 and 20 weeks for CD59a$^{-/-}$ and WT samples, but no significant difference was identified between 20 and 50 weeks for either sample group.

In males, significantly more cBV was present in CD59a$^{-/-}$ than in WT samples at 8-10 (CD59a$^{-/-}$=0.86±0.03, WT=0.68±0.03 mm^3, $p<0.001$) and 20 (CD59a$^{-/-}$ =0.93±0.03, WT=0.83±0.02 mm^3, $p<0.05$) weeks (Fig. 6.4B). At 50 weeks, cBV was slightly decreased in CD59a$^{-/-}$ over WT samples. This was due to a significant increase ($p<0.001$) in cBV in WT, but constant cBV in CD59a$^{-/-}$ samples between 8-10 and 50 weeks.

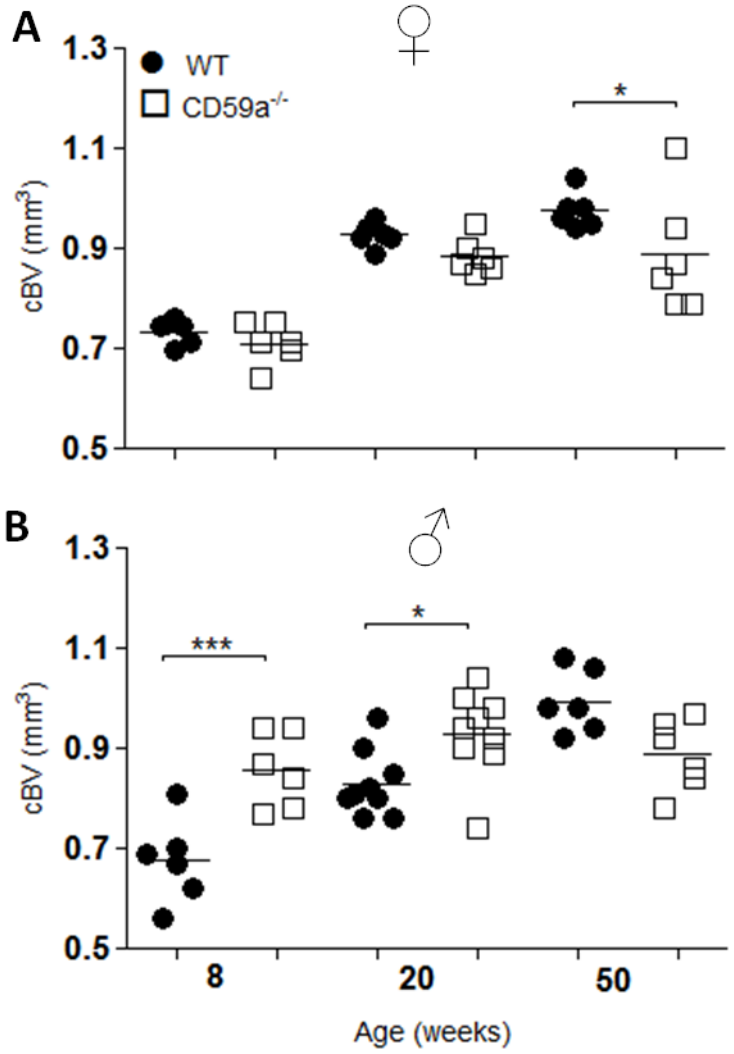

Figure 6.4 cBV evaluation in the femoral shaft. Femora of 8-10, 20 and 50 week old WT and CD59a$^{-/-}$ mice were analysed utilising MicroCT. A (1 mm) segment of bone shaft was analysed in female (n=6 mice per group) (**A**) and males (n=6 mice per group) (**B**). cBV was determined and shown. Two-way ANOVAs were performed for **A** (strain: p=0.0118, age: p<0.0001, interaction: p=0.3863) and **B** (strain: p=0.0177, age: p<0.0001, interaction: p=0.0001). Bonferroni post-tests are indicated (*(p<0.05), ***(p<0.001)).

6.3.2.1 Examination of Crossectional Thickness

Crossectional Thickness (CsTh) is a measure of cortical bone thickness and was determined to reveal if size and cBV differences translate to a stronger cortical structure. In females, CsTh was comparable between CD59a$^{-/-}$ (0.128±0.002 mm) and WT (0.132±0.002 mm) samples at 8-10 weeks (Fig. 6.5A). CsTh significantly increases (p<0.001) in CD59a$^{-/-}$ (0.172±0.002 mm) and WT (0.177±0.002 mm) samples between 8-10 and 20 weeks and samples groups were still comparable at

20 weeks. By 50 weeks CsTh did not change in WT samples, but showed a trend of reduced CsTh in CD59a$^{-/-}$ samples.

In males, no significant differences were identified between CD59a$^{-/-}$ and WT samples at 8-10, 20 or 50 weeks (Fig. 6.5B), but a trend to enhanced CsTh was visible in CD59a$^{-/-}$ over WT samples at 8-10 weeks. By week 20, CsTh had significantly increased ($p<0.001$) in CD59a$^{-/-}$ and WT samples in comparison to 8-10 weeks as also seen in female samples. At 50 weeks again, a trend to reduced CsTh was present in CD59a$^{-/-}$ over WT samples.

To relate changes in cBV and CsTh to each other, crossections of all samples were compared. These crossectional views confirm that cBV was comparable in females at week 8-10 and 20 (Fig. 6.6A, B, D and E). At 50 weeks CD59a$^{-/-}$ samples exhibit slightly thinner cortical rings (cBV) than in WT samples confirming the trend seen in CsTh (Fig. 6.6C and F). In males, CD59a$^{-/-}$ samples revealed larger and thicker rings of cortical bone than WT samples at 8-10 weeks which was also seen as a trend in the CsTh (Fig. 6.6G, H, J and K). At 50 weeks CD59a$^{-/-}$ samples present smaller and slightly thinner cortical bone rings than WT samples (Fig 6.6I and L).

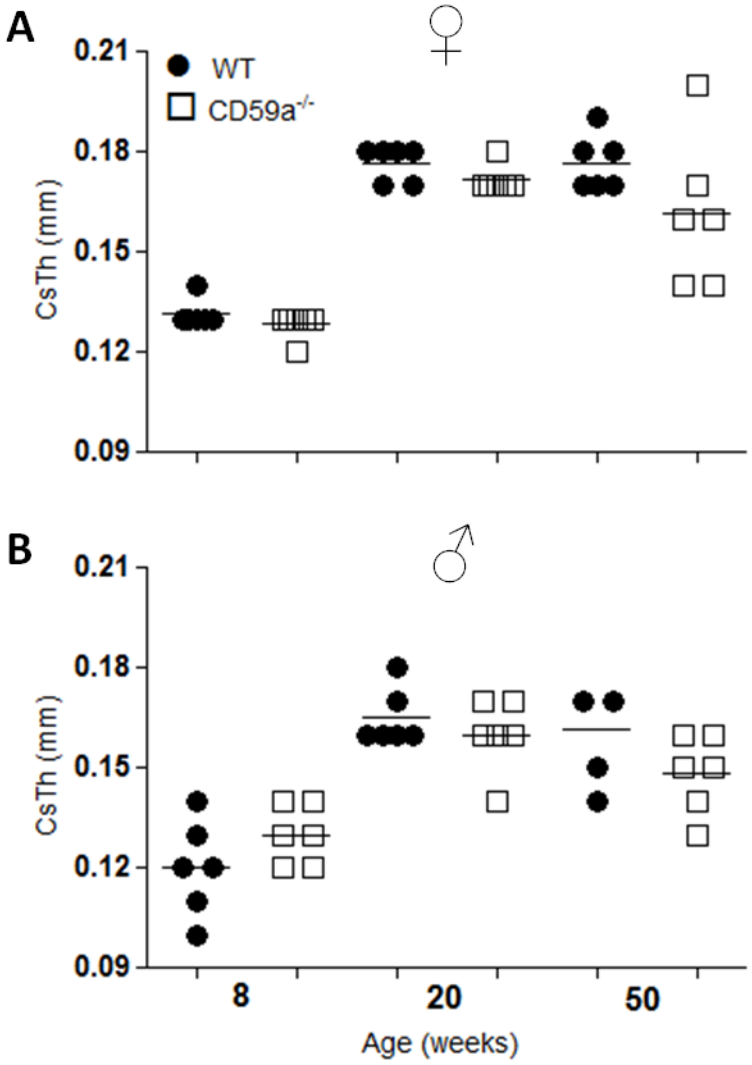

Figure 6.5 Assessment of CsTh. Column scatter plots showing a comparison of CsTh in WT and CD59a$^{-/-}$ mice. A (1 mm) segment of bone shaft was analysed in female (n=6 mice per group) (**A**) and males (n=6-9 mice per group) (**B**). Two-way ANOVAs were performed for **A** (strain: p=0.0313, age: p<0.0001, interaction: p=0.3396) and **B** (strain: p=0.4715, age: p<0.0001, interaction: p=0.0544).

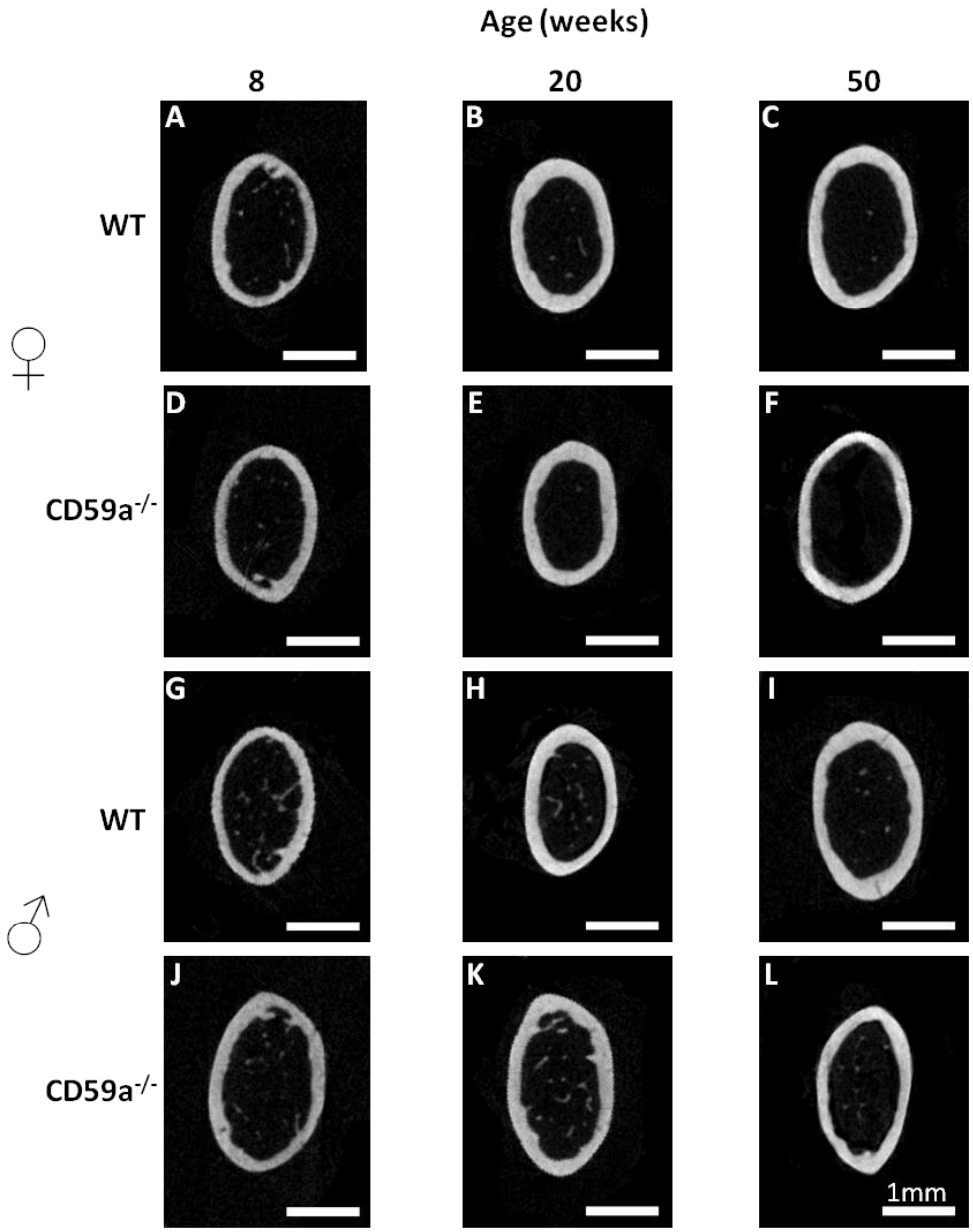

Figure 6.6 Representative images of cortical bone. Crossectional view is displayed of cortical bone within the femoral shaft. Images were obtained from the mid slice (0.5 mm) of quantified 1 mm area for female (**A** to **F**) and male (**G** to **L**) WT (**A** to **C** and **G** to **I**) and CD59a$^{-/-}$ (**D** to **F** and **J** to **L**) samples at 8-10 (**A**, **D**, **G**, **J**), 20 (**B**, **E**, **H**, **K**) and 50 (**C**, **F**, **I**, **L**) week of age (n=6-9 per group).

6.3.2.2 Quantification of BMD of Cortical Bone in Femora

Additionally to the shape of bone, the BMD is a characteristic parameter of bone and was measured in cortical bone as described in section 2.6.3.4. In females, BMD was significantly lower ($p<0.05$) in CD59a$^{-/-}$ samples at 1.23±0.02 g/cm^3 in comparison to WT samples at 1.29±0.01 g/cm^3 at 8-10 weeks (Fig. 6.7A). Between 8-10 and 20 weeks BMD significantly rose ($p<0.001$) to 1.38±0.01 g/cm^3 and 1.37±0.01 g/cm^3 in CD59$^{-/-}$ and WT samples resulting in comparable values between strains. Between 20 and 50 weeks a further significant increase ($p<0.001$) in CD59a$^{-/-}$ and WT samples was identified. At 50 weeks BMD was significantly raised ($p<0.05$) in CD59a$^{-/-}$ samples over WT samples. Therefore the genotypes showed a different effect over time.

In males, BMD was significantly lower in CD59a$^{-/-}$ in comparison to WT samples at 8-10 and 20 weeks (Fig. 6.7B). Between 20 and 50 weeks BMD in CD59a$^{-/-}$ samples (1.48±0.02 g/cm^3) rose significantly ($p<0.001$) whereas BMD in WT samples (1.40±0.02 g/cm^3) did not change, again the different strains changed their phenotype over time. This caused a significantly increased ($p<0.05$) BMD in CD59a$^{-/-}$ over WT samples at 50 weeks. When comparing 3D images of 8-10 week old male samples, CD59a$^{-/-}$ shafts presented a more porous bone structure than WT shafts as illustrated in Figure 6.7C.

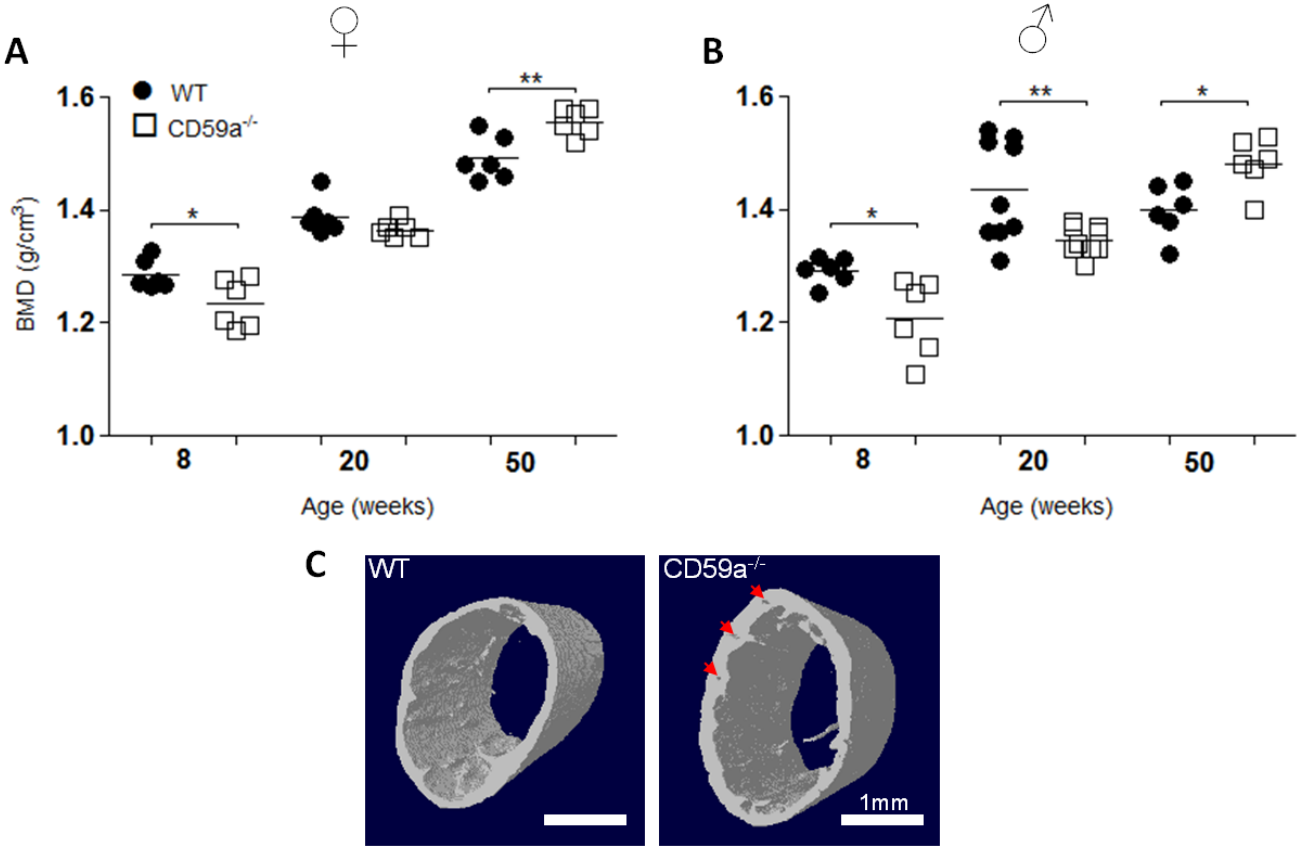

Figure 6.7 Cortical BMD assessment in the femoral shaft. Column scatter plots showing a comparison of mean BMD in WT and CD59a$^{-/-}$ mice. A (1 mm) segment of bone shaft was analysed in female (n=6 mice per group) (**A**) and males (n=6-9 mice per group) (**B**). Two-way ANOVAs were performed for **A** (strain: p=0.7530, age: p<0.0001, interaction: p=0.0002) and **B** (strain: p=0.1032, age: p<0.0001, interaction: p=0.0005). Bonferroni post-tests are indicated (*(p<0.05), **(p<0.01)). Representative 3D images of cortical bone from 8-10 week old male mice are shown and porosity is highlighted by red arrows (**C**).

6.3.2.3 Cortical Bone at a Glance

When summarising analysed parameters, alterations of cortical bone between CD59a$^{-/-}$ and WT were compared between genders and over time (Tab. 6.1). Whereas cBV did not change in femora from 8-10 and 20 week old female mice, it was increased in males. Interestingly at 50 weeks, cBV significantly decreased in females whereas no significant difference was identified in males. CsTh did not significantly alter in any group at 8-10, 20 or 50 weeks. Similarly in crossections, alterations did not present before the age of 50 weeks in females, whereas slightly larger cortical rings were present at 8-10 and 20 weeks in males. Thinner cortical rings were present in both genders at the age of 50 weeks. Finally, BMD alterations were comparable between females and males at 8-10 weeks, where a decreased BMD was monitored, and 50 weeks, where an increase was shown. Therefore, cortical bone from CD59a$^{-/-}$ femora differed between genders.

Parameter	Age in weeks	♀	♂
cBV	8-10	-	↑
	20	-	↑
	50	↓	-
CsTh	8-10	-	-
	20	-	-
	50	-	-
Cross-section	8-10	-	Larger, thicker cortical ring
	20	-	Larger, thicker cortical ring
	50	Thinner cortical ring	Smaller, thinner cortical ring
BMD	8-10	↓	↓
	20	-	↓
	50	↑	↑

Table 6.1 Summary of cortical bone parameters. Alterations in CD59a$^{-/-}$ compared to WT samples are presented for cBV, CsTh, crossections and BMD. Significant increase (↑), decrease (↓) and no significant changes (-) are indicated for female and male samples at 8-10, 20 and 50 weeks of age.

6.3.3 3D Assessment of Trabecular Bone in Femora

Datasets obtained for cortical bone assessment utilising MicroCT were also analysed for trabecular bone (methodology in section 2.6.3.6) which is predominantly present in the metaphysis. As trabecular bone consists of a meshwork of thin rod and plate structures (trabeculae) different parameters had to be considered than in the analysis of cortical bone.

Initially percentage bone volume over tissue volume (BV/TV) was determined. In females, BV/TV was comparable in CD59a$^{-/-}$ and WT samples at 8-10 (CD59a$^{-/-}$=12.5±0.7, WT=13.0±0.6%), 20 and 50 weeks of age (Fig. 6.8A). BV/TV significantly decreased ($p<0.0001$) in CD59a$^{-/-}$ and WT samples over time.

This contrasted in males, BV/TV was significantly higher ($p<0.01$) in CD59a$^{-/-}$ (22.0±1.6%) in comparison to WT (11.6±0.3%) samples at 8-10 weeks and a similar trend was present at 20 weeks (Fig. 6.8B). Whereas BV/TV in WT samples did not alter over the timecourse, it significantly decreased ($p<0.001$) in CD59a$^{-/-}$ samples; this resulted in comparable values at 50 weeks.

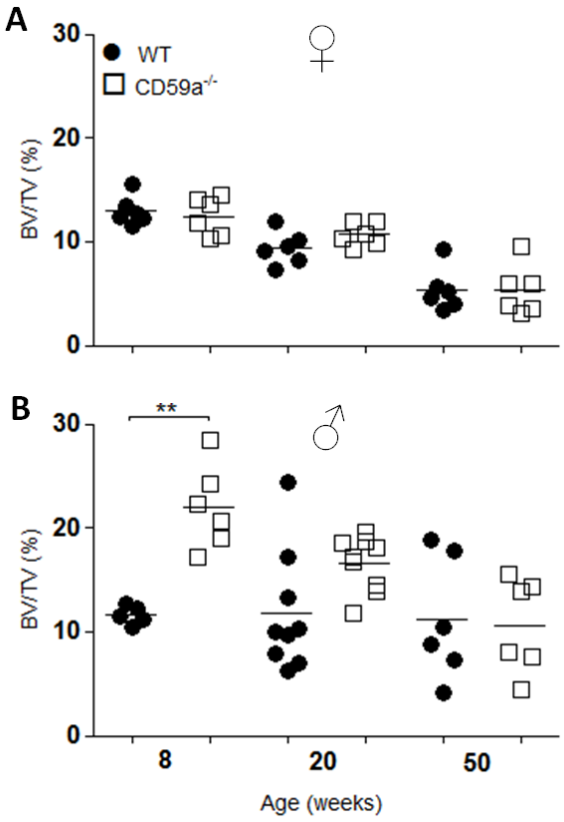

Figure 6.8 BV/TV examination of trabecular bone in the metaphysis. Column scatter plots showing a comparison of BV/TV in WT and CD59a$^{-/-}$ mice. A (1 mm) segment of the metaphysis was analysed in female (n=6 mice per group) (**A**) and males (n=6-9 mice per group) (**B**). Two-way ANOVAs were performed for **A** (strain: p=0.6708, age: p<0.0001, interaction: p=0.4196) and **B** (strain: p=0.0015, age: p=0.0117, interaction: p=0.0199). Bonferroni post-tests are indicated (**(p<0.01)).

6.3.3.1 Examination of Trabecular Number in the Metaphysis of Femora

When examining trabecular number (TbN) the result was similar to BV/TV. In females, there was no significant difference between CD59a$^{-/-}$ and WT at 8-10 (CD59a$^{-/-}$=2.1±0.1, WT=2.1±0.1 mm^{-1}), 20 (CD59a$^{-/-}$=1.5±0.1, WT=1.3±0.1 mm^{-1}) or 50 (CD59a$^{-/-}$=0.8±0.1, WT=0.7±0.1 mm^{-1}) weeks and the TbN decreased significantly ($p<0.0001$) in both strains over time (Fig 6.9A).

In males, TbN in CD59a$^{-/-}$ samples was 3.2±0.2 mm^{-1}, this was significantly higher ($p<0.01$) than WT samples, which was 2.0±0.04 mm^{-1} at 8-10 weeks of age (Fig. 6.9B). This was followed by a trend of increased TbN in CD59a$^{-/-}$ over WT at 20 weeks. CD59a$^{-/-}$ and WT samples were comparable at 50 weeks.

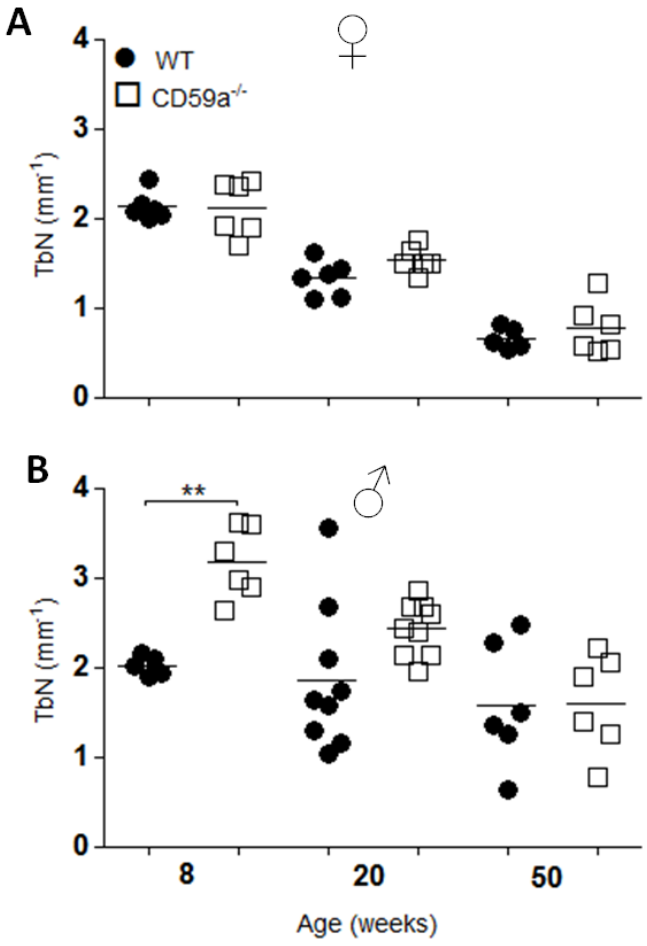

Figure 6.9 TbN evaluation in the metaphysis. Column scatter plots showing a comparison of TbN in WT and CD59a$^{-/-}$ mice. A (1 mm) segment of the metaphysis was analysed in female (n=6 mice per group) (**A**) and males (n=6-9 mice per group) (**B**). Two-way ANOVAs were performed for **A** (strain: $p=0.1992$, age: $p<0.0001$, interaction: $p=0.4391$) and **B** (strain: $p=0.0024$, age: $p=0.0005$, interaction: $p=0.0627$). Bonferroni post-tests are indicated (**($p<0.01$)).

6.3.3.2 Evaluation of Trabecular Thickness in the Metaphysis of Femora

Additionally, trabecular thickness (TbTh), another important parameter of trabecular architecture, was analysed. In females, values were comparable between CD59a$^{-/-}$ and WT at 8-10 (CD59a$^{-/-}$=0.059±0.001, WT=0.061±0.001 mm), 20 (CD59a$^{-/-}$ =0.070±0.002, WT=0.070±0.002 mm) and 50 (CD59a$^{-/-}$=0.068±0.002, WT=0.069±0.002 mm) weeks as seen for all other trabecular parameters so far (Fig. 6.10A). In comparison to TbN, TbTh significantly increased ($p<0.0001$) over time in CD59a$^{-/-}$ and WT samples.

In males, TbTh was also significantly higher ($p<0.01$) at 8-10 weeks and slightly increased at 20 weeks in CD59a$^{-/-}$ over WT samples (Fig. 6.10B). Between 8-10 and 50 weeks TbTh in WT (0.069±0.003 mm) samples significantly rose ($p<0.01$) whereas in CD59a$^{-/-}$ samples (0.065±0.002 mm) no significant difference was observed. Hence, at 50 weeks TbTh was comparable in WT and CD59a$^{-/-}$ samples.

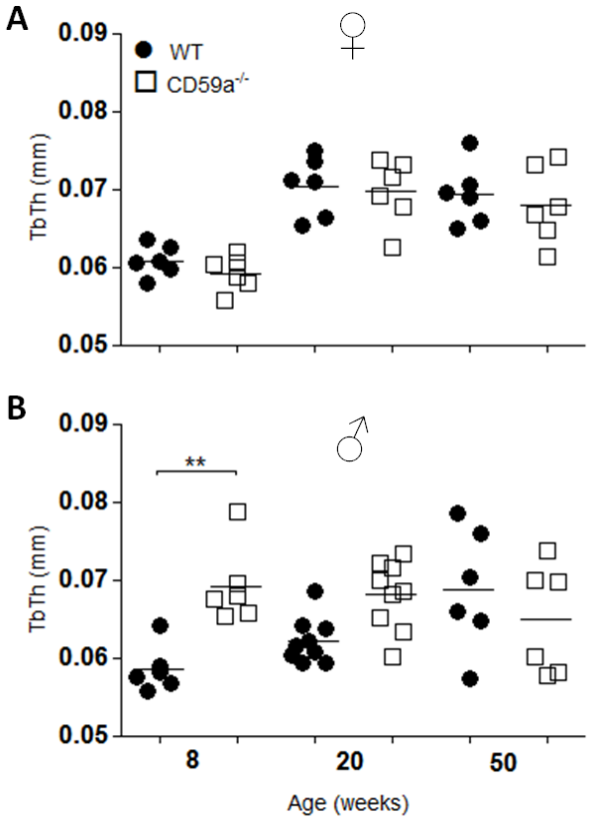

Figure 6.10 TbTh assessment in the metaphysis. Column scatter plots showing a comparison of TbTh in WT and CD59a$^{-/-}$ mice. A (1 mm) segment of the metaphysis was analysed in female (n=6 mice per group) (**A**) and males (n=6-9 mice per group) (**B**). Two-way ANOVAs were performed for **A** (strain: p=0.3294, age: p<0.0001, interaction: p=0.9463) and **B** (strain: p=0.0126, age: p= 0.3618, interaction: p=0.0042). Bonferroni post-tests are indicated (**(p<0.01)).

6.3.3.3 Investigation of Trabecular Separation in the Metaphysis of Femora

Trabecular separation (TbSp) is the width of the spaces between bone structures in the metaphysis (Skyscan 2009). In females, TbSp was comparable between CD59a$^{-/-}$ and WT samples at 8-10 and 20 weeks (Fig. 6.11A). Over the timecourse, TbSp significantly increased ($p<0.001$) in different strains (CD59a$^{-/-}$=0.65±0.05 mm and WT=0.47±0.04 mm). This increase was elevated in CD59a$^{-/-}$ samples and resulted in a significant difference ($p<0.001$) between CD59a$^{-/-}$ and WT samples at 50 weeks. In males, TbSp did not change between CD59a$^{-/-}$ and WT samples at 8-10 (CD59a$^{-/-}$ =0.19±0.01, WT=0.22±0.01 mm), 20 or 50 weeks (Fig. 6.11B). TbSp significantly rose ($p<0.001$) in CD59a$^{-/-}$ and WT samples between 8-10 and 50 weeks, but was significantly less (CD59a$^{-/-}$=$p<0.001$, WT=$p<0.05$) than in females at end point.

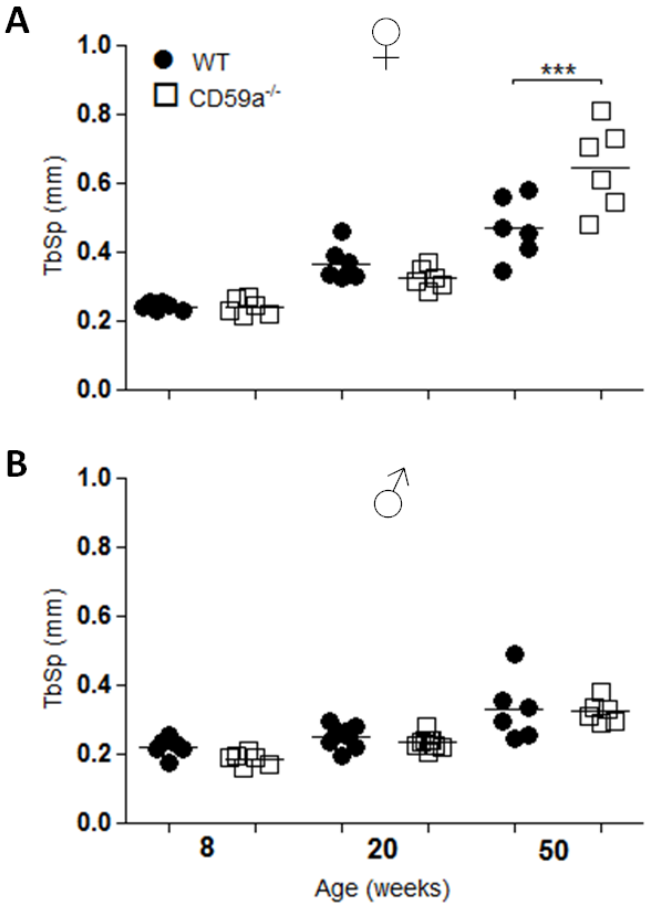

Figure 6.11 Examination of TbSp in the metaphysis. Column scatter plots showing a comparison of TbSp in WT and CD59a$^{-/-}$ mice. A (1 mm) segment of the metaphysis was analysed in female (n=6 mice per group) (**A**) and males (n=6-9 mice per group) (**B**). Two-way ANOVAs were performed for **A** (strain: p=0.0558, age: p<0.0001, interaction: p=0.0009) and **B** (strain: p=0.1511, age: p<0.0001, interaction: p=0.6895). Bonferroni post-tests are indicated (***(p<0.001)).

6.3.3.4 Assessment of Trabecular Pattern Factor in the Metaphysis of Femora

When examining trabecular pattern factor (TbPf), which is a measure of how well the trabeculae are connected. Lower TbPf resulted from better connected trabeculae (Skyscan 2009). In females, TbPf of CD59a$^{-/-}$ and WT samples did not differ at 8-10 and 20 weeks (Fig. 6.12A). In WT samples connectivity was significantly reduced (higher TbPf) ($p<0.001$) by 50 weeks causing a significant difference between CD59a$^{-/-}$ (20.3±1.3 mm^{-1}) and WT (26.9±1.25 mm^{-1}) samples. Interestingly in males, CD59a$^{-/-}$ samples presented with significantly reduced ($p<0.05$) TbPf and hence better connectivity at 8-10 and 20 weeks and no difference was observed at 50 weeks (Fig. 6.12B).

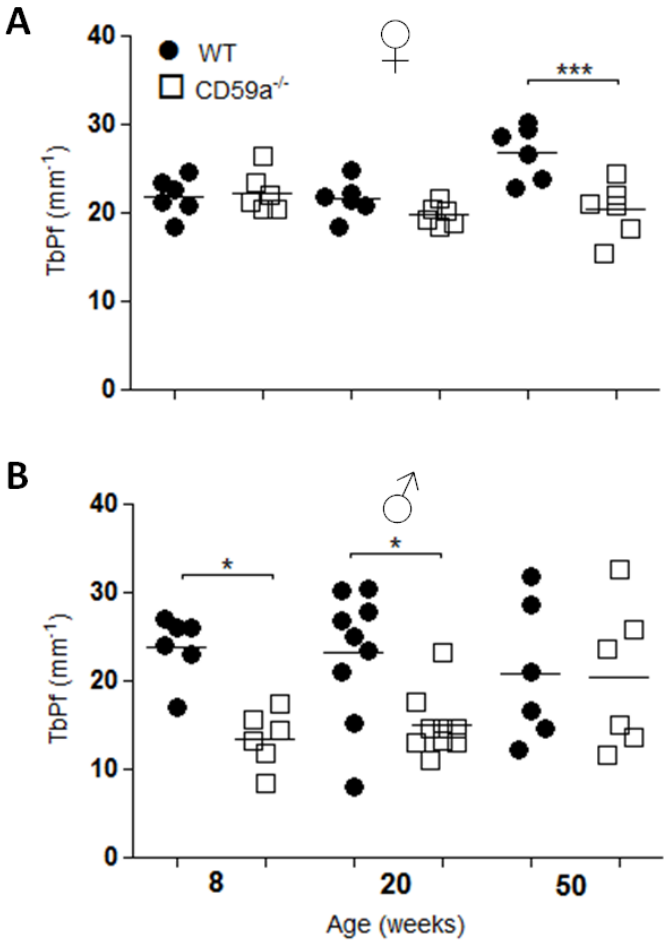

Figure 6.12 Evaluation of TbPf in the metaphysis. Column scatter plots showing a comparison of TbPf in WT and CD59a$^{-/-}$ mice. A (1 mm) segment of the metaphysis was analysed in female (n=6 mice per group) (**A**) and males (n=6-9 mice per group) (**B**). Two-way ANOVAs were performed for **A** (strain: p=0.0030, age: p=0.0217, interaction: p=0.0042) and **B** (strain: p=0.0019, age: p=0.6982, interaction: p=0.1146). Bonferroni post-tests are indicated (*($p<0.05$), ***($p<0.001$)).

6.3.3.5 Examination of Structure Model Index in the Metaphysis of Femora

SMI is a measure of rod (0) or plate (3) like shape of trabeculae. The lower the SMI the better is the quality of the trabeculae structure (Skyscan 2009). SMI changed in a similar pattern as TbPf (Fig. 6.13A and B). In females, only WT samples developed a more rod-like structure over time. However, SMI was significantly different ($p<0.001$) at 50 weeks between CD59a$^{-/-}$ (2.1±0.04) and WT (2.5±0.03) samples. In males, there was a trend to more plate-like structure in CD59a$^{-/-}$ over WT samples at 8-10 weeks. By 20 weeks this trend was significant ($p<0.05$). At 50 weeks SMI was comparable between CD59a$^{-/-}$ and WT samples.

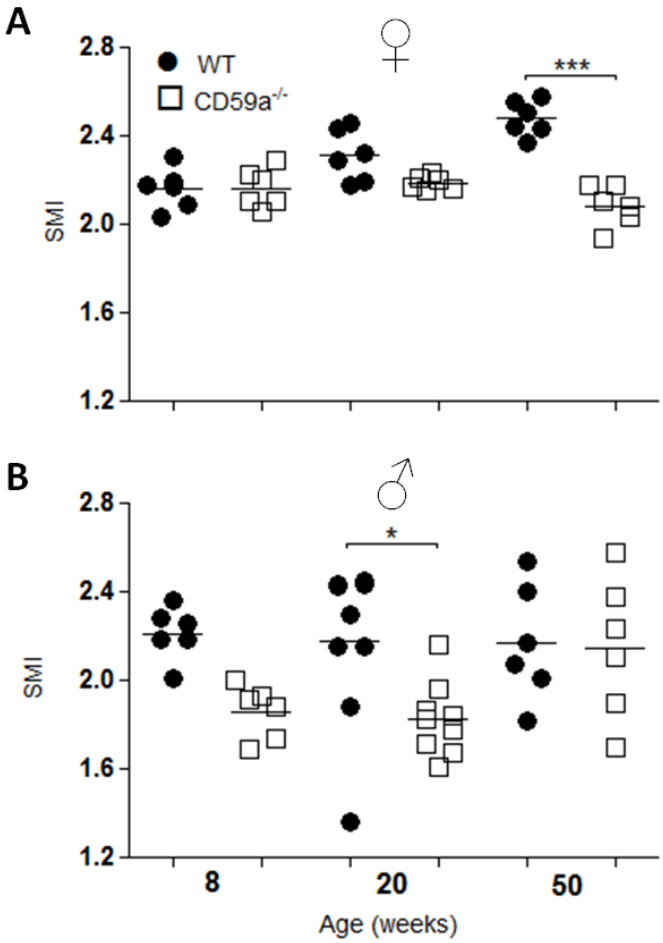

Figure 6.13 Assessment of SMI in the metaphysis. Column scatter plots showing a comparison of SMI in WT and CD59a$^{-/-}$ mice. A (1 mm) segment of the metaphysis was analysed in female (n=6 mice per group) (**A**) and males (n=6-9 mice per group) (**B**). Two-way ANOVAs were performed for **A** (strain: $p<0.0001$, age: $p=0.0061$, interaction: $p<0.0001$) and **B** (strain: $p=0.0041$, age: $p=0.2429$, interaction: $p=0.1642$). Bonferroni post-tests are indicated (***($p<0.001$)).

6.3.3.6 Evaluation of Vertical Crossections in the Metaphysis of Femora

When comparing trabecular bone meshwork of the metaphysis (cut vertically), female and male WT and CD59a$^{-/-}$ samples showed diminished trabecular meshwork over time (Fig. 6.14). Additionally, more trabecular bone was present in male than female samples. Females had comparable amounts of trabecular bone in WT and CD59a$^{-/-}$ samples at 8-10, 20 and 50 week of age (Fig. 6.14A-F). In males, the difference of trabecular bone between WT and CD59a$^{-/-}$ samples at 8-10 weeks was striking (Fig. 6.14G and J); an increased amount of TbN and connectivity was present and the increased TbTh was also clearly visible in CD59a$^{-/-}$ samples. At 20 weeks the denser trabecular meshwork was still identifiable in CD59a$^{-/-}$ samples, but less pronounced than at 8-10 weeks of age (Fig. 14H and K). By 50 weeks trabecular bone was comparable between WT and CD59a$^{-/-}$ samples (Fig. 14I and L).

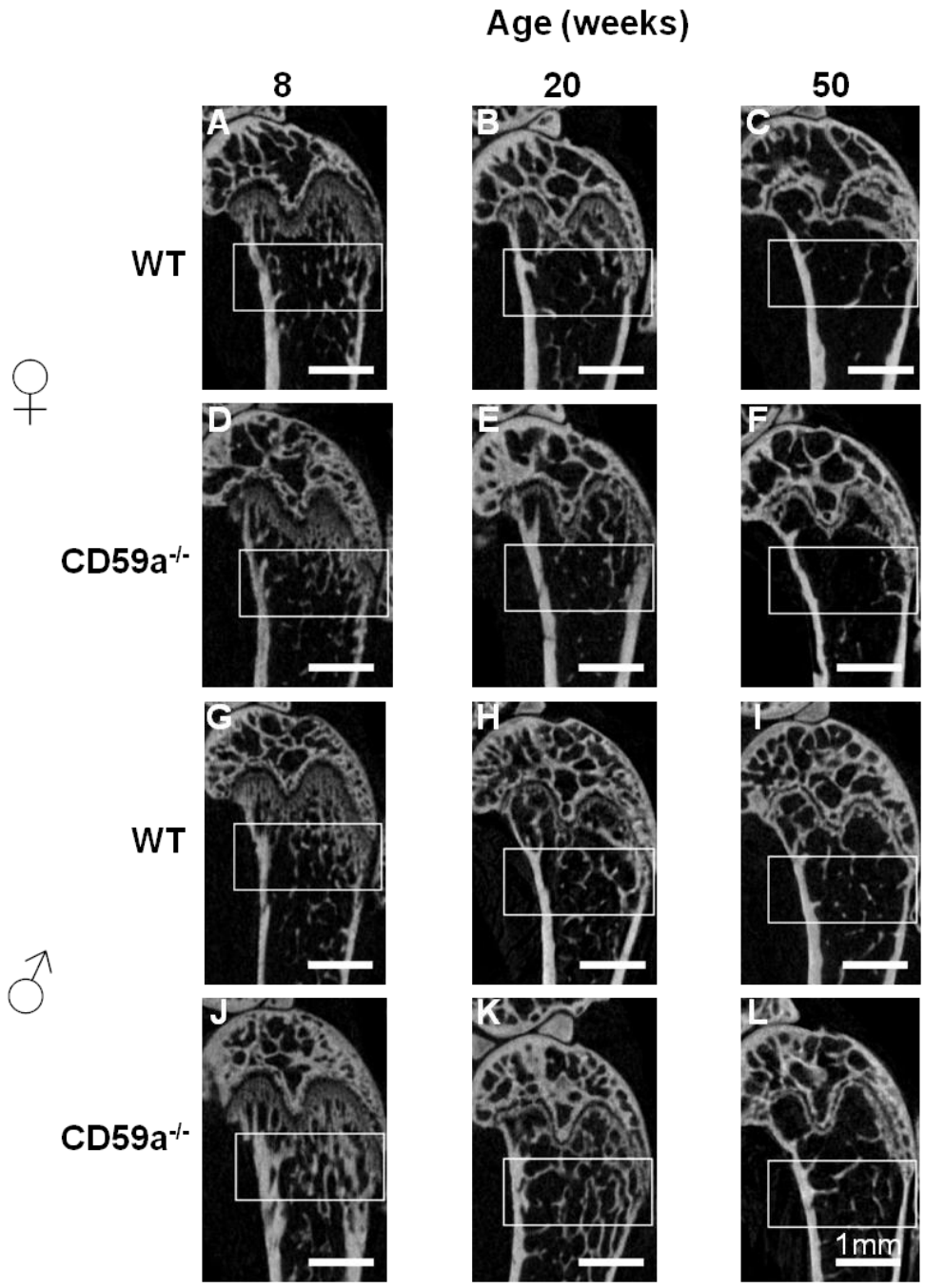

Figure 6.14 Representative images of trabecular bone in the metaphysis. The vertical view of distal femora is displayed. The area of metaphysis analysed is marked in a rectangular shape. Images were obtained by cutting across growth plate rings within the reference slice. Representative images of female (**A** to **F**) and male (**G** to **L**) WT (**A** to **C** and **G** to **I**) and CD59a$^{-/-}$ (**D** to **F** and **J** to **L**) samples at 8-10 (**A**, **D**, **G**, **J**), 20 (**B**, **E**, **H**, **K**) and 50 (**C**, **F**, **I**, **L**) week of age (n=6-9 per group) are illustrated.

6.3.3.7 Quantification of BMD within the Metaphysis of Femora

Finally, total BMD was quantified to determine the mineral content within the TV of the metaphysis. In females, the total BMD showed no significant differences between WT and CD59a$^{-/-}$ samples at 8-10 (WT=0.21±0.01, CD59a$^{-/-}$=0.20±0.01 g/cm^3), 20 (WT=0.16±0.01, CD59a$^{-/-}$=0.18±0.01 g/cm^3) or 50 (WT=0.07±0.01, CD59a$^{-/-}$=0.06±0.02 g/cm^3) weeks of age (Fig. 15A) which was comparable to other trabecular parameters established. Over the timecourse total BMD significantly decreased ($p<0.0001$) in WT and CD59a$^{-/-}$ samples.

In males, total BMD was significantly higher ($p<0.05$) in CD59a$^{-/-}$ over WT samples at 8-10 and 20 weeks (Fig. 15B), again mirroring BV/TV, TbN and TbTh data, but contrasting with the reduced total BMD identified in CD59a$^{-/-}$ samples of cortical bone at earlier time points. Between 8-10 and 50 weeks, total BMD of CD59a$^{-/-}$ samples (0.15±0.02 g/cm^3) significantly decreased ($p<0.001$) whereas WT samples (0.18±0.03 g/cm^3) only showed a slight reduction in total BMD. Consequently, a slightly lower total BMD was observed in CD59a$^{-/-}$ over WT samples at 50 weeks. 3D models of 8-10 week old samples (displayed in Fig. 15C) demonstrated a complex meshwork of trabeculae in CD59a$^{-/-}$ samples, which was denser than in WT samples.

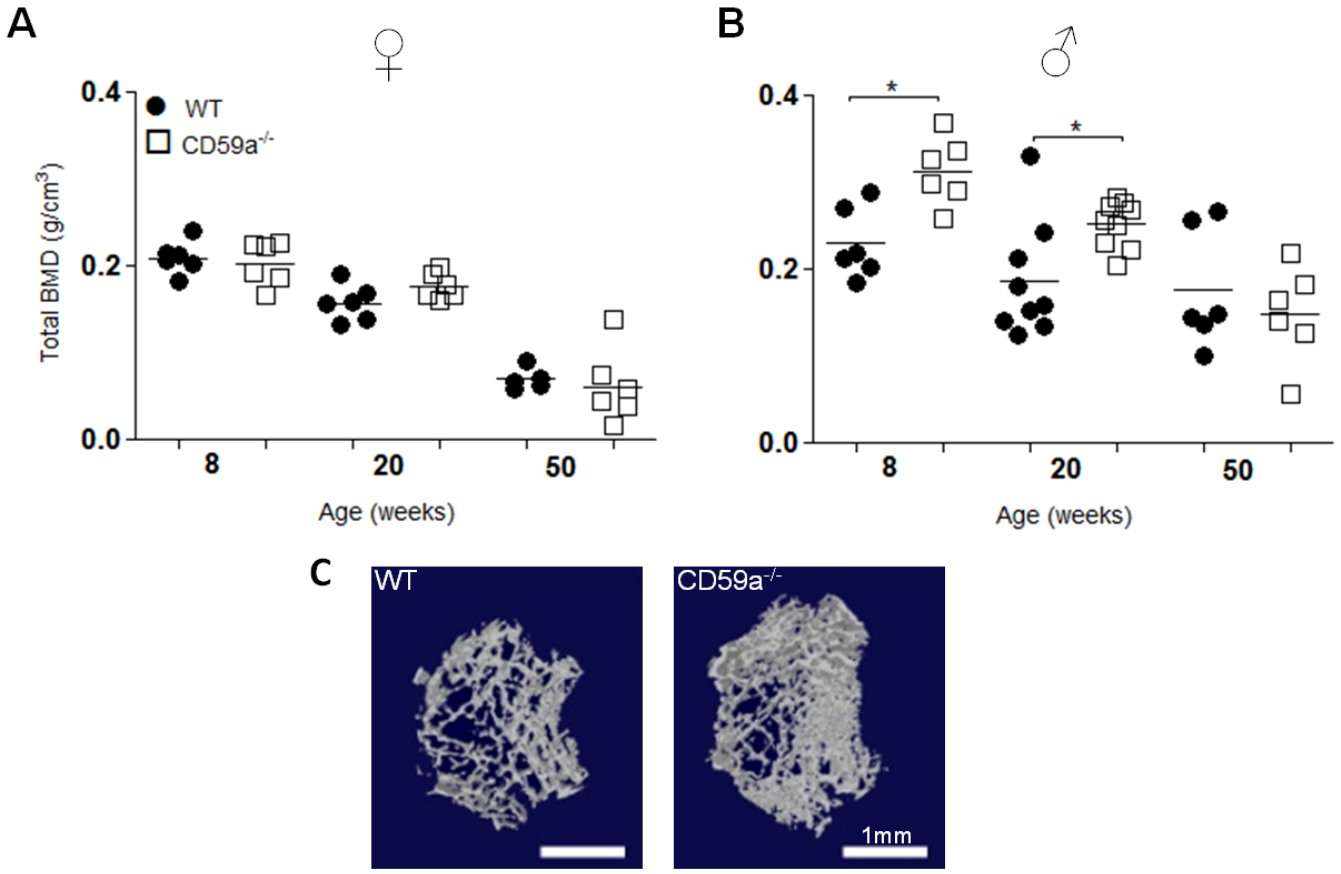

Figure 6.15 BMD evaluation of trabecular bone in the metaphysis. Column scatter plots showing a comparison of total BMD (including TV that is occupied by trabeculae) in WT and CD59a$^{-/-}$ mice. A (1 mm) segment of the metaphysis was analysed in female (n=6 mice per group) (**A**) and males (n=6-9 mice per group) (**B**). Two-way ANOVAs were performed for **A** (strain: p=0.8442, age: p<0.0001, interaction: p=0.3179) and **B** (strain: p=0.0169, age: p<0.0001, interaction: p=0.0240). Bonferroni post-tests are indicated (*(p<0.05)). Representative 3D images of trabecular bone from 8-10 week old male mice are shown (**C**).

6.3.3.8 Trabecular Bone in the Metaphysis at a Glance

Once data of trabecular architecture was collected, alterations of trabecular bone between WT and CD59a$^{-/-}$ were compared between genders and over time (Tab. 6.2). In females trabecular bone was comparable between WT and CD59a$^{-/-}$ samples in BV/TV, TbN and TbTh. TbSp and connectivity was increased and trabeculae were more plate-like in CD59a$^{-/-}$ over WT samples at 50 weeks respectively. In males, architectural changes were present in young adult mice only. BV/TV, TbN and TbTh were up-regulated at 8-10 weeks. The connectivity of these structures was increased at 8-10 and 20 weeks and also more plate-like at 20 weeks in CD59a$^{-/-}$ over WT samples. Meshwork and total BMD were increased at 8-10 and 20 weeks of age. These data again present a gender specific phenotype.

Parameter	Age in weeks	♀	♂
BV/TV	8-10	-	↑
	20	-	-
	50	-	-
TbN	8-10	-	↑
	20	-	-
	50	-	-
TbTh	8-10	-	↑
	20	-	-
	50	-	-
TbSp	8-10	-	-
	20	-	-
	50	↑	-
TbPf	8-10	-	↓
	20	-	↓
	50	↓	-
SMI	8-10	-	-
	20	-	↓
	50	↓	-
Cross-section	8-10	-	Denser meshwork
	20	-	Denser meshwork
	50	-	-
Total BMD	8-10	-	↑
	20	-	↑
	50	-	-

Table 6.2 Summary of trabecular bone parameters. Alterations in CD59a$^{-/-}$ over WT samples are presented for BV/TV, TbN, TbTh, TbSp, TbPf, SMI, crossections and total BMD. Significant increase (↑) and no significant changes (-) are indicated.

6.3.4 3D Evaluation of Trabecular Bone in Vertebra L6

As all previous analysis was carried out in a femur from each mouse, it was crucial to identify if changes applied to other bones. Due to the consistent phenotype identified in young male mice, vertebra L6 of male mice at 8-10 and 20 weeks of age were scanned using MicroCT and trabecular parameters were determined as described in section 2.6.4.

When BV/TV was determined, CD59a$^{-/-}$ samples were significantly higher than WT samples at 8-10 (CD59a$^{-/-}$=27.8±0.7, WT=23.1±0.9%, $p<0.01$) and 20 ($p<0.001$) weeks (Fig. 6.16A). Similarly, TbN was increased significantly in CD59a$^{-/-}$ over WT samples at 8-10 (CD59a$^{-/-}$=4.8±0.1, WT=4.4±0.1 mm^{-1}, $p<0.05$) and 20 ($p<0.001$) weeks (Fig. 16B). TbN of WT samples significantly decreased ($p<0.05$) between 8-10 and 20 weeks of age, whereas TbN of CD59a$^{-/-}$ stayed constant. Furthermore, TbTh in CD59a$^{-/-}$ (0.058±0.001 mm) significantly differed ($p<0.05$) from WT samples (0.053±0.001 mm) at 8-10 weeks (Fig. 16C). By 20 weeks, this significant increase ($p<0.05$) was retained. TbSp and TbPf were significantly reduced in CD59a$^{-/-}$ over WT samples at 8-10 (TbSp=$p<0.05$, TbPf=$p<0.01$) and 20 (TbSp=$p<0.001$, TbPf=$p<0.001$) weeks, again revealing increased connectivity and more plate-like structure (Fig. 16D and E). Similar to trabecular bone in the metaphysis, SMI revealed a significantly more ($p<0.001$) plate-like structure in CD59a$^{-/-}$ samples over WT samples at 20 weeks of age (Fig. 16F).

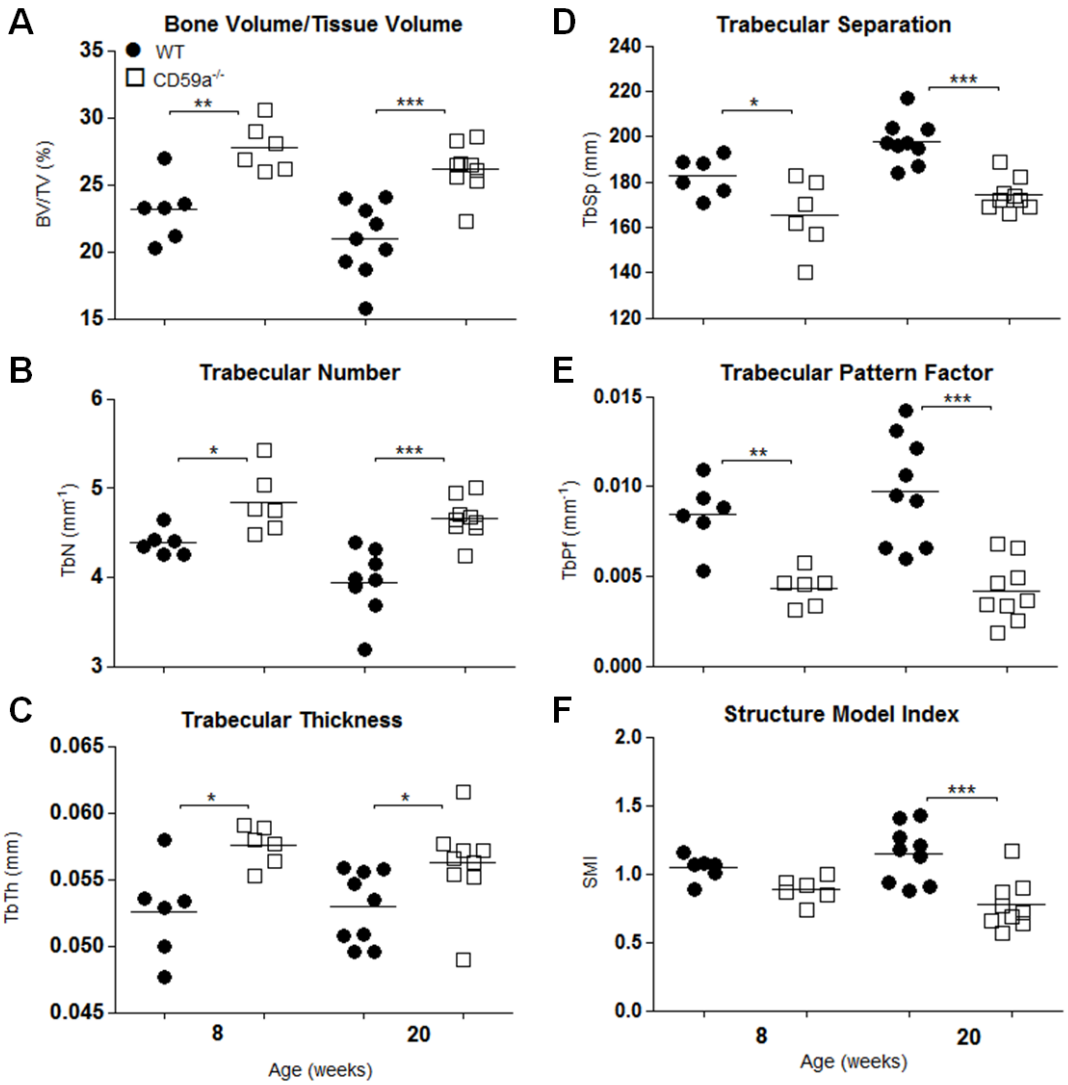

Figure 6.16 Trabecular bone parameters were determined in the vertebra L6. Vertebra L6 of 8-10 and 20 week old male WT and CD59a$^{-/-}$ mice were analysed with MicroCT. Trabecular bone was selected in the main body of the vertebrae between the cartilage surfaces on either side (n=6-9 mice per group). Percentage BV/TV (**A**), TbN (**B**), TbTh (**C**), TbSp (**D**), TbPf (**E**) and SMI (**F**) were determined. Two-way ANOVAs were performed **A** (strain: p<0.0001, age: p=0.0312, interaction: p=0.7241), **B** (strain: p<0.0001, age: p=0.0081, interaction: p=0.2170), **C** (strain: p=0.0007, age: p=0.6506, interaction: p=0.4500), **D** (strain: p<0.0001, age: p=0.0048, interaction: p=0.4407), **E** (strain: p<0.0001, age: p=0.4721, interaction: p=0.3695) and **F** (strain: p=0.0002, age: p=0.9647, interaction: p=0.0923). Bonferroni post-tests are indicated (*(p<0.05), **(p<0.01), ***(p<0.001)).

6.3.4.1 Evaluation of Vertical Crossections in Vertebra L6

When examining crossections of vertebra L6, a size difference was observed between 8-10 and 20 weeks in WT and CD59a$^{-/-}$ samples (Fig. 17). Additionally, the vertebra L6 was larger in CD59a$^{-/-}$ than in WT samples at 8-10 and 20 weeks.

Furthermore, the trabecular meshwork was more complex and trabeculae were thicker in CD59a$^{-/-}$ over WT samples at 8-10 and 20 weeks.

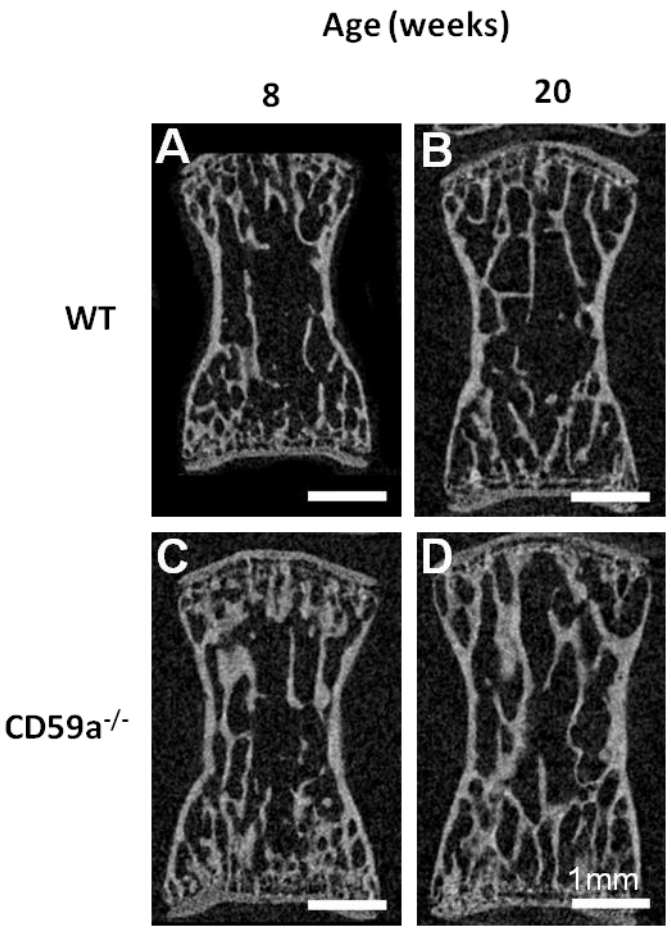

Figure 6.17 Representative images of trabecular bone in the vertebra L6. The vertical view of the main body of L6 is displayed. Images were obtained by selecting the mid-section within the dataset and cutting across the man body of the vertebra. Representative images of male WT (**A** and **B**) and CD59a$^{-/-}$ (**C** and **D**) samples at 8-10 (**A** and **C**) and 20 (**B** and **D**) weeks of age are illustrated.

6.3.4.2 Quantification of BMD within the Vertebra L6

Finally, total BMD was determined at 8-10 and 20 weeks (Fig. 18A). Again, total BMD in CD59a$^{-/-}$ samples (8-10 weeks=0.27±0.01, 20 weeks=0.25±0.01 g/cm^3) was significantly raised over WT samples (8-10 weeks=0.23±0.01, 20 weeks=0.20±0.01 g/cm^3). 3D models of trabecular bone at 8-10 weeks confirmed the size difference of the vertebrae and highlighted the more tightly connected meshwork of trabeculae in CD59a$^{-/-}$ over WT samples (Fig. 18B). The data obtained from the vertebra L6 were comparable to findings acquired for the same trabecular parameters in the femur.

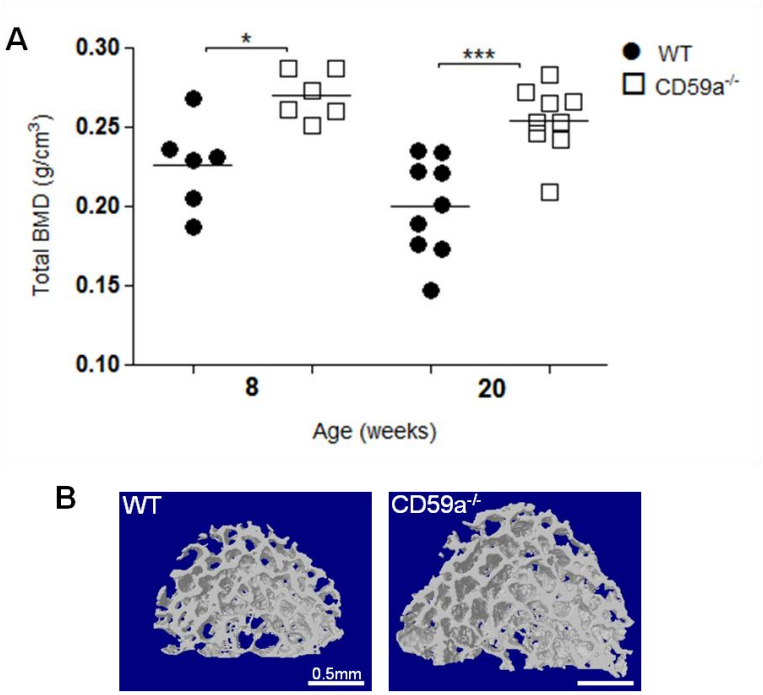

Figure 6.18 BMD evaluation of trabecular bone in the vertebra L6. Trabecular bone was selected in the main body of the vertebrae between the cartilage surfaces on either side (n=6-9 mice per group) (**A**). Total BMD was determined. A two-way ANOVA was performed (strain: p<0.0001, age: p=0.0346, interaction: p=0.5680) and Bonferroni post-tests are indicated (*(p<0.05), ***(p<0.001)). Representative 3D images of trabecular bone from 8-10 week old mice are shown (**B**).

6.3.5 *In Vivo* OB Activity in the Trabecular Bone of Femora

After the MicroCT assessment, femora of 8-10 and 20 week old male WT and CD59a$^{-/-}$ samples were methylmethacrylate (MMA)-embedded and von Kossa/van Gieson staining was performed on bone sections as described in section 2.6.5.

Firstly, the osteoid surface was normalised for the trabecular bone surface (OSS/BS) (Fig. 6.19A). Interestingly, the OSS/BS was significantly reduced (p<0.001) in CD59a$^{-/-}$ (8.5±1.6%) over WT (22.9±1.4%) samples at 8-10 weeks. By 20 weeks, the OSS/BS in WT samples was significantly reduced (p<0.001) compared to 8-10 weeks, and therefore was comparable to the stagnated OSS/BS in CD59a$^{-/-}$ samples.

When normalising the osteoid surface for TV (OSS/TV) the results were comparable (Fig. 6.19B). OSS/TV in CD59a$^{-/-}$ samples (0.15±0.03%) was significantly lower (p<0.001) than in WT samples (0.37±0.04%) at 8-10 weeks, as illustrated in Fig. 6.19C. Over time OSS/TV in WT samples was significantly reduced (p<0.001); hence OSS/TV was slightly lower in WT over CD59a$^{-/-}$ samples at 20 weeks of age.

As this did not account for the increased bone length and BV observed utilising X-ray and MicroCT, a new cohort of 8-10 week old mice was treated with calcein to measure mineral apposition by OBs (methodology in section 2.6.5.7).

CD59a$^{-/-}$ samples (2.2±0.1 µm) showed a significantly higher ($p<0.05$) MAR than WT samples (1.7±0.1 µm) (Fig. 20A). Bone formation rate (BFR/BS) showed the same pattern (Fig. 20B), opposing the results obtained utilising von Kossa/van Gieson staining.

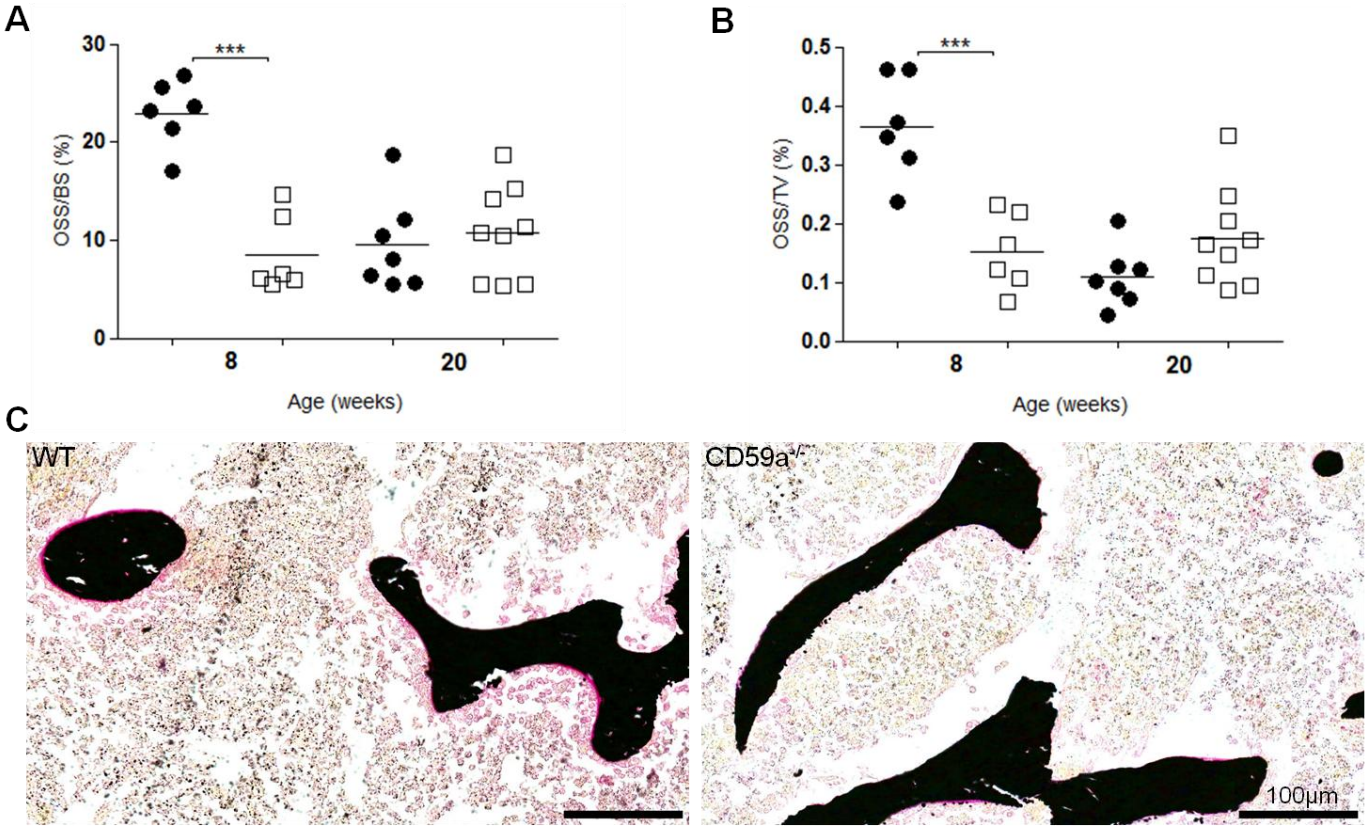

Figure 6.19 Osteoid quantification of trabecular bone in the metaphysis of femora. Femora of 8-10 and 20 week old male WT and CD59a$^{-/-}$ mice were analysed utilising von Kossa/van Gieson staining on sections. TV, Trabecular bone (black) and collagen-rich osteoids (pink) were quantified (n=6-9 mice per group). OSS was calculated and normalised for BS (**A**) and TV (**B**). Two-way ANOVAs were performed for **A** (strain: p=0.0006, age: p=0.0026, interaction: p<0.0001) and **B** (strain: p=0.0163, age: p=0.0004, interaction: p<0.0001). Bonferroni post-tests are indicated (***(p<0.001)). Representative images of trabecular bone from 8-10 week old mice are shown (**C**).

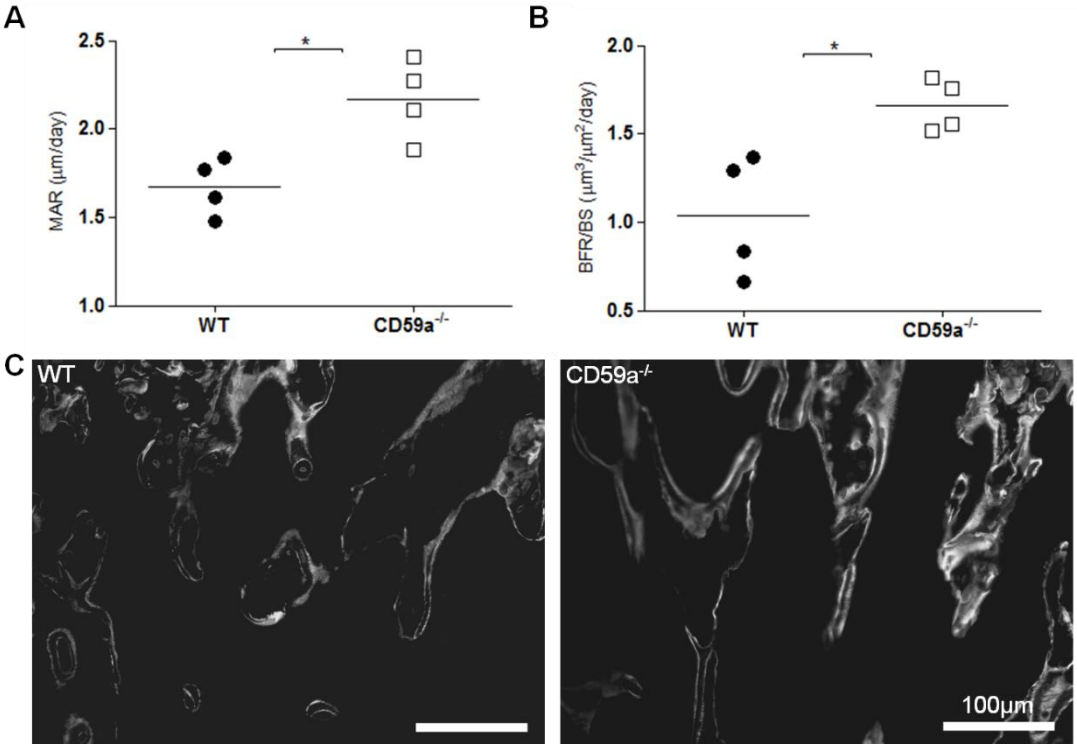

Figure 6.20 Calcein assessment of trabecular bone in the metaphysis of femora. 8-10 week old male WT and CD59a$^{-/-}$ mice (n=4 mice per group) were injected with calcein 4 and 1 day before sacrifice. Femoral sections were counterstained with Aniline blue to identify bone surfaces. Calcein was captured at 515 nm and analysed for double (calcein deposition at both time points) and single (calcein deposition on a single time point) staining. MAR (**A**) and BFR/BS (**B**) were calculated. Unpaired student T-tests were performed and indicated (*($p<0.05$)). Representative images are shown (**C**).

6.3.6 Resorption Area in the Trabecular Bone of Femora

Femoral sections obtained in methodology section 2.6.5 were also stained for TRAP (OCs) to reveal active resorption surfaces (2.6.6). The OC surface normalised for BS (OCS/BS) was significantly higher in CD59a$^{-/-}$ over WT samples at 8-10 (CD59a$^{-/-}$=18.3±2.4, WT=10.7±1.0%) and 20 (CD59a$^{-/-}$=23.0±2.0, WT=13.7±2.0%) weeks (Fig. 6.21A).

When normalising OC number for BS (OCNr/BS), CD59a$^{-/-}$ samples were significantly raised over WT samples at 8-10 (CD59a$^{-/-}$=1.16±0.16, WT=0.65±0.05%, $p<0.05$) and 20 (CD59a$^{-/-}$=1.5±0.13, WT=0.92±0.14%, $p<0.01$) weeks (Fig. 21B).

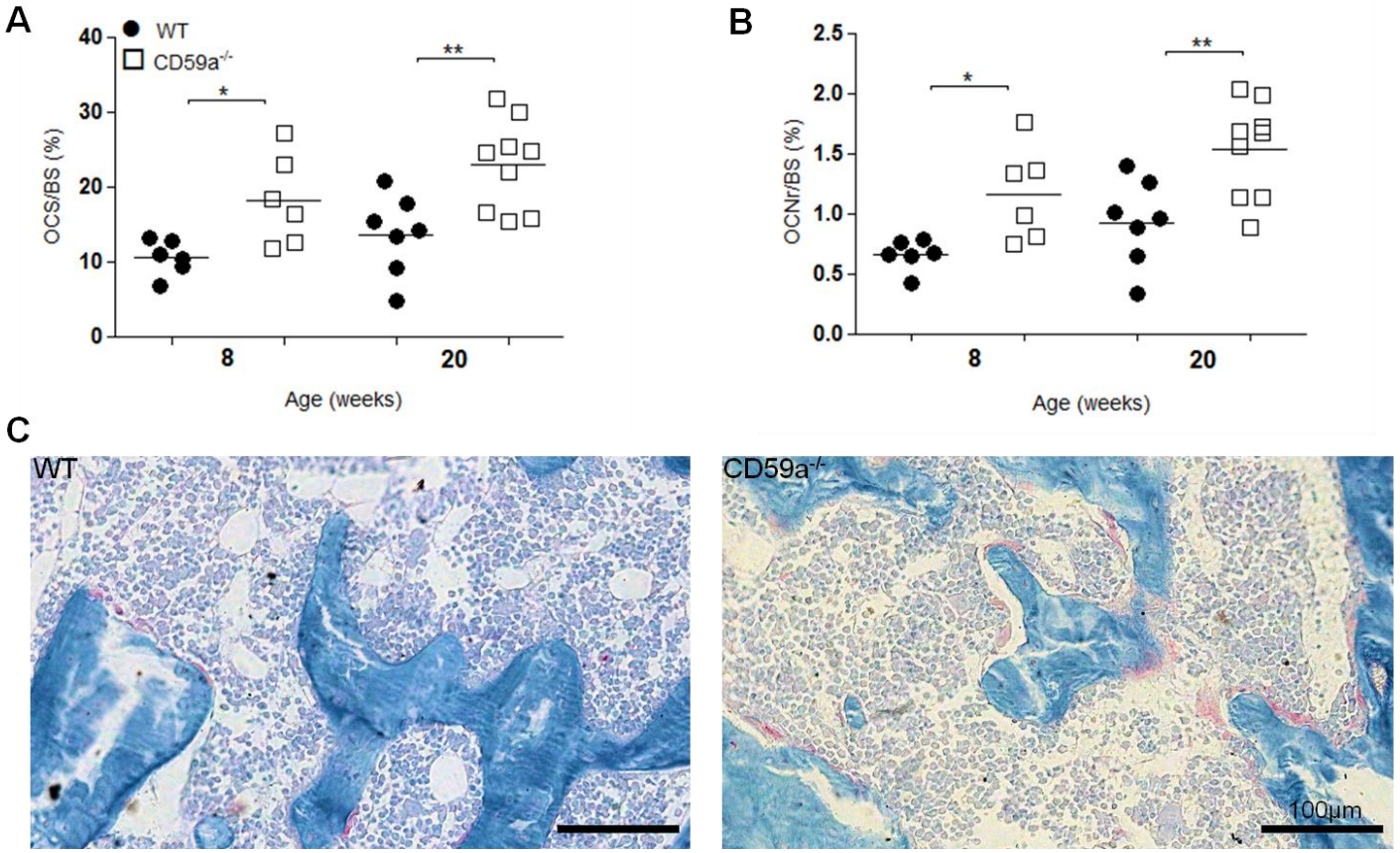

Figure 6.21 OC analysis of trabecular bone in the metaphysis of femora. Femora of 8-10 and 20 week old male WT and CD59a$^{-/-}$ mice were analysed utilising TRAP/Aniline blue staining on sections. Trabecular bone (blue) and OC (maroon) were quantified (n=6-9 mice per group). OCS (**A**) and OCNr (**B**) were calculated and normalised for BS. Two-way ANOVAs were performed for **A** (strain: p=0.0003, age: p=0.0668, interaction: p=0.6882) and **B** (strain: p=0.0003, age: p=0.0236, interaction: p=0.7082). Bonferroni post-tests are indicated (*(p<0.05), **(p<0.01)). Representative images of trabecular bone from 8-10 week old mice are shown (**C**).

6.4 Discussion

This study utilised a variety of imaging techniques to characterise the bone phenotype of CD59a$^{-/-}$ mice. The main focus was on weight-bearing bones such as femora, but vertebrae L6 were also analysed (Högler *et al.* 2003).

6.4.1 Quantification of Femoral Length and Shaft Diameter

Morphological assessment of femora was carried out utilising X-ray projections (radiographs). Zhang et al. demonstrated that radiographs are a valuable method to determine bone changes. The authors studied a BMP receptor type IA mutant mouse that had abnormal trabecular bone like structures which developed within the femoral shaft. These structures were clearly visible on X-ray projections. Zhang et al. were therefore able to localise aberrant features to direct histological analysis (Zhang *et al.* 2003) which was aimed for in this study also.

When evaluating the femoral length of WT samples on C57/BL6J background, the length in male mice was recorded between 17.7 mm at 8-10 weeks and 19.3 mm at 50 weeks of age. Other studies reported shorter bone length (Rowling *et al.* 2007; Philip *et al.* 2010; Yao *et al.* 2010). Rowling et al. for example, identified 16.5 mm long femora in 12 week old male mice with C57/BL6 background (Rowling *et al.* 2007). These measurements were mostly acquired via a digital calliper and not from X-ray projections which might account for some of the variation. Variability may have also arisen from diet and other housing conditions (Graham 1972; Borer *et al.* 1988; Sarma 2009). These mice were an established colony and were healthy (monthly screening by Debora Adams), therefore this increased femoral length in WT mice was not viewed as an adverse effect.

In this study, radiographs revealed comparable morphology in female WT and CD59a$^{-/-}$ mice at 8-10, 20 and 50 weeks. In males only, significantly increased (2-4%) femoral length was observed in CD59a$^{-/-}$ mice over WT mice at 8-10, 20 and 50 week of age. Larsson et al. for example, identified a 24% reduction in femoral length in the human FGF-23 transgenic mice on CBA X C57/BL6 background (Larsson *et al.* 2004) whereas Mohan et al. revealed a 40% reduction in femoral length when IGF-1 was deleted (Mohan *et al.* 2003). In contrast oestrogen receptor knockout mice showed a 4-14% change in femoral length in comparison to WT mice (Lindberg *et al.* 2001). Small differences obtained here were significant due to low variability between samples and suggested a subtle effect of CD59a. Studies characterising long bones, reported that enhanced femoral or tibial length was not accompanied by an increased cortical area. Additionally, the BMD was increased in these long bones, but the 4 point bending test revealed that femora and tibiae were

more brittle (Tommasini *et al.* 2005; Miller *et al.* 2007). This suggested a possible reduction in bone quality in the femora of male CD59a$^{-/-}$ mice.

This interpretation was further supported by the shaft diameter measurements. In males, CD59a$^{-/-}$ had significantly higher anterior-posterior and medial-lateral diameter compared to WT samples at 8-10 weeks, but were not significantly different at 20 and 50 weeks of age. Tommasini et al. also revealed a reduced shaft diameter when characterising more fragile tibiae (Tommasini *et al.* 2005). Therefore at 20 and 50 weeks in my study femora were slender and therefore more likely to be brittle.

When studying the X-rays further no other gross architectural changes were observed, but evaluation for clinical bone pathology such as: osteophytes, subchondral sclerosis or joint space narrowing; features that are characteristic for OA (Gale *et al.* 1999; Abramson and Attur 2009) was not performed. Furthermore, for identification of an osteopenic phenotype (murine model of osteoporosis) DXA analysis is commonly carried out to obtain BMD. This method has proved useful for whole animal studies, but accuracy is lost upon selection of a region of interest on particular bone areas (Rosen 2008) and was not available for this study. As radiographs were limited to 2D assessment (Rosen 2008) and did not allow for establishment of BMD, 3D evaluation was conducted.

6.4.2 3D Assessment of Cortical Bone in Femora

MicroCT was utilised for characterising bone pathology in CD59a$^{-/-}$ mice. MicroCT is the preferred method of many researchers when studying micro-architecture of murine bone samples. High resolution (6-10 µm) analysis of small trabeculae is possible by utilising images taken from bone acquisition obtained from multiple projections at different angles (3D). MicroCT enables evaluation of specific regions of interest, but at the same time allows for analysis of a larger volume of bone than is possible by histology (Rosen 2008).

Initially, cortical bone in the femoral shaft was analysed. cBV was comparable in females at 8-10 (WT=0.73±0.01, CD59a$^{-/-}$= 0.71±0.02 mm^3) and 20 weeks. cBV in the shaft (1 mm) was also analysed by Zhang et al. At 6 weeks of age, female WT mice on FVB-N background had a cBV of 0.537±0.025 mm^3 (Zhang *et al.* 2002). These values were comparable to data obtained in this study if the growth phase is considered (Efstratiadis 1998). Lloyd et al. determined a cBV of 5.5-6.5 mm^3 per 3 mm shaft area measured in female C57/BL6J mice at 10 weeks of age (Lloyd *et al.* 2008). When correcting for the ROI as measured here, 1.8-2.1 mm^3 cBV were calculated which is hugely raised over the values obtained in this study.

Interestingly femora were air-dried and MicroCT was performed with different equipment (µCT20 scanner, SCANCO Medical AG, Switzerland) (Lloyd *et al.* 2008) which might have caused higher readings. Hoenderop et al. also measured cBV in mm^3, but did not provide a size for the ROI (Hoenderop *et al.* 2003), therefore not allowing for comparison. Consequently, to avoid these problems cBV in the literature is often normalised for TV, but alterations in cBV/TV were not identified in this study. cBV was presented here, because male CD59a$^{-/-}$ mice demonstrated an increased cBV over WT at 8-10 (21%) and 20 (11%) weeks. When comparing these data to changes obtained in the literature, for example in ovariectomy or RANKL supplementation (0.4 mg/kg/day) of mice, a 6-11% alteration in cBV was observed (Potts *et al.* 2004; Lloyd *et al.* 2008); whereas knockout models that affected Ca^{2+} channels or were related to IGF-1 produced a 14-36% alteration. Hence changes revealed within the CD59a$^{-/-}$ model was comparable to published data and revealed that more cortical bone was formed in young male CD59a$^{-/-}$ mice.

Over time cBV significantly increased in female (WT and CD59a$^{-/-}$) samples and male WT samples whereas cBV stagnated in male CD59a$^{-/-}$ samples. At 50 weeks a significantly lower (9%) cBV in female CD59a$^{-/-}$ over WT mice was seen. A similar trend (not significant) was present in male mice. In the literature cortical area in femora of C57/BL6 mice was identified to increase until the age of 52 weeks (Price *et al.* 2005), but Halloran et al. revealed that in male C57/BL6J mice cortical thickness only grew for the first 24 weeks of age and then decreased continuously with aging (Halloran *et al.* 2002). This suggested that bone growth slowed in CD59a$^{-/-}$ mice before WT mice and that bone loss was initiated earlier.

6.4.2.1 Examination of Crossectional Thickness

An additional parameter that reveals the bone quality is cortical thickness. This was measured by CsTh and did not differ between WT and CD59a$^{-/-}$ at 8-10, 20 or 50 weeks. In 8-10 week old, male WT mice CsTh was 0.12±0.006 mm. Zhong et al. reported a CsTh of 0.125 mm in 7 week old WT mice (Zhong *et al.* 2012). Hence my data is in agreement with published work. Thicker cortical bone should accompany an increase in cortical diameter/area to retain bone quality as discussed by Watkins et al. (Watkins *et al.* 2012). In my study cortical thickness was unchanged, but shaft diameter was increased at 8-10 weeks as well as tissue area at 8-10 and 20 weeks (data not shown), suggesting that bone strength was compromised in young adult mice. Watkins et al. further reported that mice lacking the gap junction protein annexin 43, present with increased cortical tissue area and slender cortical thickness. This was due to increased resorption at the endosteum as well as up-

regulated periosteal formation of bone (Watkins *et al.* 2012). To identify whether cortical bone changes were caused by alterations in remodelling at endo- and periosteum in my study, OB and OC should be quantified on cortical bone.

6.4.2.2 Quantification of BMD of Cortical Bone in Femora

Another indicator of bone quality is BMD. At 8-10 weeks CD59$^{-/-}$ samples were shown to have decreased BMD (female (4%) and male (7%)) over WT samples in my study. Uveges et al. identified 3-4% cortical BMD change between Brtl (osteogenesis imperfecta mouse model) and WT mice. Cortical BMD (1.5-1.6 g/cm^3) was measured in SV129/CD-1/C57BL/6S mice at 6 and 12 weeks of age (Uveges *et al.* 2009). In my study BMD values between 1.2 and 1.3 g/cm^3 were identified which is lower than published data. When comparing changes in cortical BMD, Högler et al. identified a rise in cortical BMD between puberty and young adulthood. BMD alterations were comparable between sexes (Högler *et al.* 2003), suggesting that BMD during growth is less dependent on sex hormones than other cortical bone parameters. When examining the effect of calcium supplementation on BMD in a human study in 6-14 year old children, Slemenda et al. revealed that the treatment resulted in enhanced BMD and a 15% decrease in osteocalcein. The authors concluded that the rise in BMD was accompanied by a reduced rate in bone remodelling (Slemenda *et al.* 1997). Therefore the reduced BMD, identified in my study at 8-10 weeks, could have resulted from increased bone remodelling. By 50 weeks BMD was enhanced in female and male CD59a$^{-/-}$ over WT samples in my study. This suggested that the rate of remodelling was reduced and resorption markers should be analysed in serum samples of CD59a$^{-/-}$ and WT mice to investigate this theory.

Bone stiffness and flexibility are not only determined by BMD, but other component of the bone matrix. The analysis of Col1 or it's cross-linking was not considered in this project and might have helped to predict bone quality and fracture risks (Seeman 2007). Structural changes seen in the skeleton of CD59a$^{-/-}$ mice may have resulted from adaptations to different loads caused by the deficiency. In disease models such as the brittle IV mouse (another model of osteogenesis imperfecta) an altered ratio of collagen and minerals to counteract the collagen mutations was observed (Seeman and Delmas 2006). Therefore longer bones in CD59a$^{-/-}$ mice might have been sufficiently supported by their BMD if other matrix components were up-regulated. Structure and flexibility of bone is also controlled by trabecular bone, which was also investigated.

6.4.3 3D Assessment of Trabecular Bone in Femora

Trabecular bone is most commonly analysed in the metaphysis of femora or tibiae. Bone diseases, such as OA, usually affect the epiphysis which contains complex trabecular architecture known as the subchondral bone. Imaging techniques, such as MicroCT, do not always support analysis of joint damage as similarities are quantified and pathological features that differ are difficult to measure. Therefore joint analysis was not included in this study and trabecular bone of the metaphysis was a major focus.

In females, BV/TV, TbN, TbTh and total BMD were comparable at 8-10, 20 and 50 weeks. TbSp and trabeculae connectivity were increased with a more plate-like structure at 50 weeks. Whereas TbSp points toward reduced bone quality, the more plate-like structure of trabeculae suggested a stronger trabecular bone architecture (Recker *et al.* 2009; Skyscan 2009). As the cortical bone volume was also reduced in CD59a$^{-/-}$ mice at 50 weeks, more plate-like structure might have developed to counteract weaknesses in bone strength.

In males, BV/TV, TbN, TbTh, trabecular connectivity and total BMD were significantly raised in CD59a$^{-/-}$ over WT samples at 8-10 weeks of age. By 20 weeks, trabeculae were still better connected and had an increased total BMD in CD59a$^{-/-}$ over WT mice. Additionally, trabeculae presented a more plate-like structure in CD59a$^{-/-}$ samples. At 50 weeks, trabecular bone was comparable in all parameters between CD59a$^{-/-}$ and WT mice.

Male WT samples had a BV/TV of 11.6±0.3%, TbN of 2.0±0.04 mm^{-1}, TbTh of 0.059±0.001 mm, TbSp of 0.2±0.01 mm, SMI of 2.2±0.05 and total BMD of 0.23±0.02 g/cm^3 at 8-10 weeks. Halloran et al. characterised the trabecular parameters of male WT C57/BL6 tibiae over time. At 8 weeks, the BV/TV was 14%, TbN 5.5 mm^{-1}, TbTh 0.043 mm, TbSp 0.26 mm and SMI 2.8 (Halloran *et al.* 2002). Similar data were published for trabecular bone in the femur by Gowen et al. (Gowen *et al.* 2003). Therefore values in my study were slightly lower than in published data which again might be due to different equipment or sample preparation. A total BMD of 0.29±0.03 g/cm^3 of WT femora was obtained by Larsson et al. (Larsson *et al.* 2004) and this was also in agreement with data of this study.

To reveal the effect of CD59a, differences between CD59a$^{-/-}$ and WT samples need to be interpreted. All parameters pointed towards increased trabecular bone that is thicker, denser and more connected meshwork in young adult male mice. In humans it was shown that people from different ethnicities have different structural features. African Americans were reported to have shorter vertebrae with higher trabecular volume which was suggested to have protective

affects for age related bone loss (Seeman and Delmas 2006). Hence, alterations of trabecular bone in CD59a$^{-/-}$ mice might have been required to counteract reduced BMD in cortical bone at 8-10 and 20 weeks.

Interestingly, micro-architectural variations between inbred strains have been shown to be significant (Beamer *et al.* 1996). As WT and CD59a$^{-/-}$ mice were not obtained from a heterozygous colony, variations might have arisen from genetic alterations of these in-house colonies, therefore experiments should be performed with WT control animals from different sources to confirm these findings.

6.4.4 3D Evaluation of Trabecular Bone in Vertebra L6

It was essential to perform trabecular analysis on several parts of the skeleton to determine if the effect of CD59a was localised to the femur or not. Hildebrand et al. examined CT parameters in human spine, femur, iliac crest and calcaneus biopsies. The authors identified the largest amount of bone in femora and the lowest in the lumbar spine. Additionally, lumbar spines consisted of thin rod-like structures whereas femoral trabeculae were thick and appeared plate-like (Hildebrand *et al.* 1999). Interestingly, my data presented comparable trabecular architecture in femur and spine at 8-10 weeks of age whereas at 20 weeks the modifications in CD59a$^{-/-}$ samples were more pronounced in spine samples. This implied not only that femora and vertebrae are differentially regulated, but that control of CD59a is not restricted to femora.

6.4.5 *In Vivo* OB Activity in the Trabecular Bone of Femora

As MicroCT does not support analysis of cellular composition, histology was carried out (Rosen 2008). This 2D analysis is an established method that allows for *in situ* hybridization, RT-PCR, immunohistochemistry, bone histomorphometry and electron microscopy (Helfrich and Ralston 2003). To distinguish between osteoids and mineralised bone, von Kossa/van Gieson staining was utilised in my study. The quantification of osteoids can be difficult, because they appear as thin structures which require strong staining and high magnification analysis to be identified correctly. Vedi and Compston suggested to exclude structures of less than 3 µm for precise determination of osteoid surfaces (Helfrich and Ralston 2003). Von Kossa staining was consistent in this study and no readjustment was required.

An alternative method for monitoring OB activity is the application of near infrared imaging reagents which allow for *in vivo* monitoring of bone apposition. Examples are reagents such as Osteosense (Perkins Elmer) and BoneTag (Licor). Imaging with these reagents can be performed on live animals and therefore can be

repeated over time. The resolution is limited to 50 µm when utilising, for example the Ivis system (Caliper Life Sciences 2009). These methods should be considered as a less time consuming technique in future studies.

Von Kossa staining of trabecular bone within the metaphysis revealed, decreased OSS/BS in CD59a$^{-/-}$ mice at 8-10 weeks of age in this study. By 20 weeks, OSS/BS in WT samples decreased to the level (approx. 10%) of the unchanged CD59a$^{-/-}$ sample. Luo et al. identified 20% OSS/BS at the first two days after birth (Luo *et al.* 2009) whereas Potts et al. quantified OSS/BS at 3 month of age with 10.186±3.17% (Potts *et al.* 2004). This was in agreement with my theory that the osteoid levels were higher during initial growth and that the number reduced once the growth rate had slowed down. As CD59a$^{-/-}$ mice contained larger bones, the growth rate had reached the peak of osteoid formation earlier than WT mice.

To obtain readout for OB activity, MAR was determined at 8-10 weeks of age. MAR was significantly up-regulated in CD59a$^{-/-}$ (2.2±0.1 µm/day) over WT samples (1.7±0.1 µm/day). This pattern also emerged for BFR/BS. MAR rate was relatively low compared to published data which averaged around 2.5-2.9 µm/day (Ferguson *et al.* 2003; Rubin *et al.* 2007; Luo *et al.* 2009); this variability was likely dependent on the type of analysis performed. Microscope, camera and software packages utilised would have influenced the outcome. Increased MAR in CD59a$^{-/-}$ samples confirmed that OB activity was increased and therefore resulted in faster bone growth (Erlebacher *et al.* 1998) and turnover (Shih and Norrdin 1986) as observed during X-ray and MicroCT analysis.

6.4.6 Resorption Area in the Trabecular Bone of Femora

TRAP staining was used to highlight OC activity histologically. This method should be complemented by investigation of resorption cavities which can be performed by polarised light microscopy to highlight the structure of lamellae. When lamellae are disturbed at an angle, resorption pits are formed. Additionally, lamellae filled with an osteoid can be noted as a complete resorption cavity (Helfrich and Ralston 2003), therefore allowing for an accurate account of remodelling surfaces. This was not performed in this study.

When evaluating OCs *in vivo*, TRAP staining was performed to determine OCS/BS. This surface was significantly raised in CD59a$^{-/-}$ over WT (18.3±2.4% vs 10.7±1.0%) samples at 8-10 weeks of age. Hoenderop et al. obtained a similar OSC/BS (10.5±1.37%) for WT controls samples (Hoenderop *et al.* 2003). As data is in agreement, it is most likely that enhanced OC, stimulate increased bone

remodelling and therefore growth, but this has to be further investigated because bone development is dependent on chondrocyte action (Rauch 2005).

To complete the characterisation of bone pathology, mechanical loading should have been tested. Bone gives strength to the body and guards organs, so it should be rigid and withstand impact at the same time. In rodents the most commonly used tests are 3 and 4 point bending. In the 3 point test, force is applied to the middle of the bone shaft whereas in the 4 point method the force is distributed evenly over the shaft (Helfrich and Ralston 2003). Breaking or bending of bone, aberrant from WT controls would have supported characterisation of bone phenotypes. Mechanical testing could have therefore helped in estimating bone quality of CD59a$^{-/-}$ samples.

6.5 Conclusion

In vivo examination of the effect of CD59a on bone architecture uncovered the following points:

- Femoral architecture was altered in CD59a$^{-/-}$ when compared to WT mice at 8-10, 20 and 50 weeks. This was apparent from increased femoral length, and increased bone volume in cortical and trabecular bone.
- The balance of BMD was shifted from cortical to trabecular bone in young CD59a$^{-/-}$ mice.
- Male CD59a$^{-/-}$ mice showed a defect over more parameters of bone growth and remodelling than females, indicating gender specificity.
- The trabecular bone phenotype in male CD59a$^{-/-}$ mice was also present in vertebra L6 and hence not restricted to the femur.
- OC numbers and OB function were enhanced in young CD59a$^{-/-}$ male mice indicating an accelerated rate of bone remodelling.

Therefore CD59a influences bone growth and homeostasis *in vivo.* This was the first time that the detailed histomorphometry was performed on, not only CD59a$^{-/-}$ mice, but also complement deficient mice, as arthritis studies were restricted to scoring systems of bone erosion (section 1.3.3.1.3).

Chapter 7

General Discussion

The role of CD59a in inflammatory arthritis models has been previously established in the literature. During an experimental model of RA enhanced bone erosion was identified, whereas during a trauma induced osteoarthritis model osteophyte formation was revealed in CD59a$^{-/-}$ mice in comparison to WT mice (Williams *et al.* 2004; Wang *et al.* 2011). Opposing bone pathologies were reportedly due to inflammatory response by two independent disease triggers (immune complex and injury). In the immune complex-driven antigen-induced arthritis model a degenerative bone phenotype was revealed, whilst in the medial meniscectomy model excess bone formation was observed in the knee joint. As inflammatory arthritis and bone were shown to be regulated through shared myeloid progenitors and cytokines (such as RANKL, IL-1, TNF and IL-6), the complexity of signalling did not allow for the extraction of CD59a function in bone homeostasis (Lorenzo *et al.* 2010). Hence CD59a was studied in a non-inflammatory context here. This homeostatic effect of CD59a on bone was not investigated and had not been reported in the literature in advance of the initiation of this project.

Revealing a role of CD59a in bone homeostasis could support research of bone pathology upon aging. The aging population was shown to develop alterations in extracellular matrix proteins, cell apoptosis and regeneration, joint loading and capacity to resolve inflammation which often results in osteoarthritis (Geurts and Valderrabano 2012). A study of 90 year olds in Leiden, Netherlands, identified that only 16% of participants did not present with osteoarthritic symptoms on radiographs when scored for sclerosis, osteophytes, ossicles, pseudocystic areas, joint space narrowing and shape of bone ends. This highlighted the association between age and osteoarthritis (Kellgren and Lawrence 1957; Goekoop *et al.* 2011; Loeser 2011). As the aging population was predicted to rise to 25% of over 65 year old by 2033 in the UK and the increased burden on the health system as well as contradictory evidence for current pharmaceutical interventions was reported, new therapeutic approaches are needed (Birrell and Felson 2009; Box *et al.* 2010). These can only be taken forward by understanding bone homeostasis in detail.

During the course of the research that embodies this thesis; the role of CD59a in regulating bone homeostasis was examined. Key findings emerged with regard to CD59a's contribution to osteoblast-driven mineralisation, osteoclastogenesis and defining the micro-architecture of bone *in vivo*. These are discussed in relation to the current literature below.

7.1 Determining the Role of CD59a in Osteoblast Differentiation and Maturation

In chapter 3, the effect of CD59a upon osteoblast differentiation (measured by alkaline phosphatase staining) and osteoblast function (measured in mineralisation assays) was reported. *In vitro* bone marrow cultures were established with precursor cells derived from age matched (7 to 20 weeks) wild-type and CD59a-deficient mice. In the absence of CD59a, the surface area of alkaline phosphatase positive colony forming units showed reduced staining when compared against wild-type cultures in a single experiment. This experiment needs to be repeated before drawing conclusion and the investigation could also be advanced by studying Runx2, β-catenin and osterix, the main transcription factors that regulate osteoblast differentiation. qPCR could to be utilised to observe their expression levels to determine if cells from CD59a$^{-/-}$ samples are aberrantly regulated (Otto *et al.* 1997; Nakashima *et al.* 2002; Haÿ *et al.* 2009; Cawthorn *et al.* 2011).

Although CD59a insufficiency reduced colony forming units (n=1 only) there was no significant effect upon osteoblast function assessed by mineralisation assays. In order to demonstrate formation of osteoblasts in mineralisation cultures, secondary markers such as osteocalcin, osteopontin, bone sialic protein and type I collagen should be analysed utilising qPCR (Haÿ *et al.* 2009; Teplyuk *et al.* 2009; Cawthorn *et al.* 2011; Zhang *et al.* 2011a) (Fig. 7.1). To confirm protein levels of these markers, culture supernatants should also be examined. Ferron et al. for example, developed an ELISA method to detect osteocalcin allowing for distinguishing between active (undercarboxylated) and total osteocalcein (Ferron *et al.* 2010). Alternatively, flow cytometry of markers such as RANKL or immunohistochemistry of osteopontin, should be performed to identify osteoblasts in culture (Atkins *et al.* 2003; Uaesoontrachoon *et al.* 2008).

Published literature revealed an inverse association between osteoblast differentiation and adipogenesis (Duque 2008). This was identified during *in vitro* and *in vivo* studies with Runx2 and PPARγ which are controlled by the common transcriptional co-activator with PDZ binding motif (TAZ) (Hong *et al.* 2005). Therefore the same bone marrow cell population was stimulated towards adipocytes in this study and an increase in adipocyte numbers (measured by Oil red O) was expected. Interestingly, data analysis pointed once again towards less adipocyte maturation in CD59a$^{-/-}$ over WT bone marrow (n=1) which was an unexpected finding. Other differentiation pathways of mesenchymal stem cells were not investigated here, but the literature describes that mesenchymal stem cell activity can be altered. During aging, for example, mesenchymal stem cells were shown to

undergo less cell division and be prone to oxidative stress resulting in declining cell density (Stolzing *et al.* 2008). A sensitivity or damage to mesenchymal stem cells in a CD59a$^{-/-}$ environment could possibly have caused a decreased differentiation.

CD59 expression has been revealed on mesenchymal stem cells and used as a surrogate marker in many studies to identify mesenchymal stem cells from primary cell sources and long term cultures (Izadpanah *et al.* 2006; Lange *et al.* 2007; Watson *et al.* 2010). Furthermore, Moll et al. reported that mesenchymal stem cells within the blood express CD59 as the sole complement regulator (Moll *et al.* 2011). The effect of the membrane attack complex on mesenchymal stem cells has not yet been identified, but lack of CD59 might affect mesenchymal stem cell survival and subsequently differentiation potential. Furthermore, Ignatius et al. revealed its presence on human osteoblasts and Festy et al. identified expression of CD59 on mature adipocytes (Festy *et al.* 2005; Ignatius *et al.* 2011). This evidence highlighted not only the continued expression of CD59 once differentiated, but also possible involvement in different tissue mechanisms.

In order to assess the impact of CD59a upon OB function one must look *in vivo* where all mediators and cells that regulate the bone balance are present. The *in vitro* study did not take into account environmental changes encountered by the mice during the ageing process. The *in vivo* effect of CD59a$^{-/-}$ in OB is reported in chapter 6 and discussed further in section 7.4 of the general discussion.

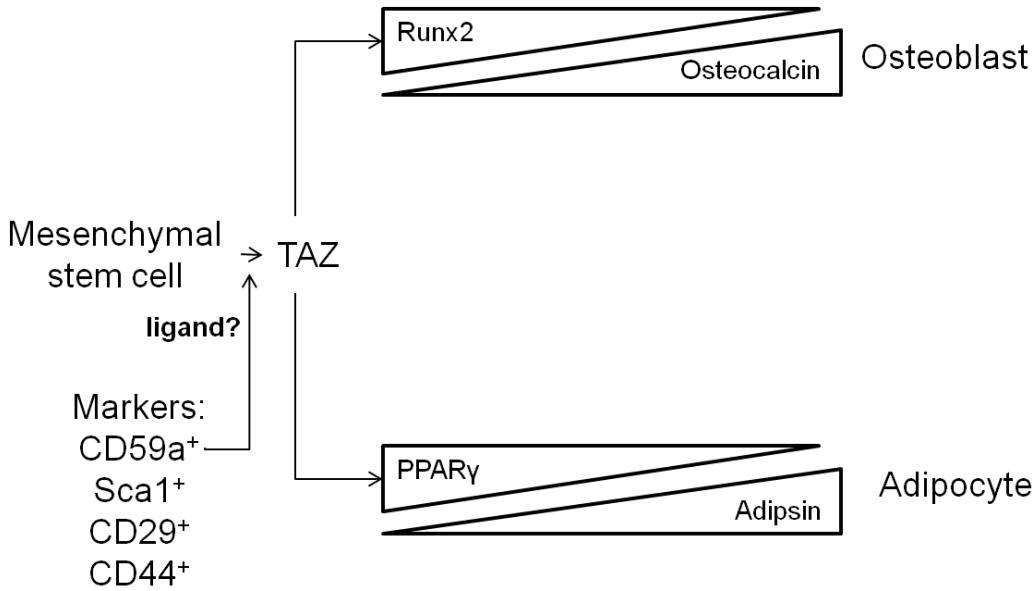

Figure 7.1 Schematic illustrating potential experimental plans to identify a mechanism for CD59a regulation of osteoblast differentiation. Mesenchymal stem cells should be characterised from WT and CD59a$^{-/-}$ bone marrow. Upon differentiation of mesenchymal stem cells towards osteoblast or adipocytes,

transcription factor and protein expression (examples given) should be monitored to identify regulatory role of CD59a and reveal its potential ligand (Tropel *et al.* 2004; Kumar *et al.* 2005).

7.2 Assessing the Impact of CD59a on Osteoclastogenesis

The impact of CD59a on osteoclastogenesis was assessed in chapter 4. Mouse bone marrow preparations from 8-10 week old mice were utilised; osteoclastogenesis assays were performed in $C6^{-/-}$ and $CD59a^{-/-}$ and all outcome measures (Cathepsin K, MMP-9, mKc) compared against WT data.

Once bone marrow cells were plated, the majority of cells adhering to glass coverslips were identified as monocytes for WT, $CD59a^{-/-}$ and $C6^{-/-}$ in both female and male mice. This revealed an enrichment of precursor cells, but populations should be further characterised by flow cytometry to obtain an accurate breakdown of cell populations and identify small differences. Qui et al. for example, developed software called spanning-tree progression analysis of density normalised events which allowed for distinguishing between different cell types according to their levels of marker expression. These markers should include ckit/Sca1 for haematopoietic, CD11b for myeloid, B220 for B-cells and TCR-β/CD4/CD8 for T-cell populations (Qiu *et al.* 2011) and should be considered for further characterisation of adherent cells, which were not readily distinguishable during differential cell counts.

CD59a expression was gauged by qPCR in adhered murine bone marrow cells. Although CD59a expression was detected the assay did not discriminate which cells expressed this regulator of the terminal complement pathway. In order to overcome this problem flow cytometry analysis was employed. Flow cytometry using the murine antibodies such as MEL-4 or anti-mCD59a.1 have been reported (Harris *et al.* 2003; Lin *et al.* 2004), a number of in-house antibodies were tested, but a specific antibody having satisfactory background staining was not identified. Therefore, phenotypic analysis of the cell localisation of CD59a in mouse was not pursued further. To reveal CD59a expression on different cell types qPCR analysis should be performed on the individual time points to identify markers essential for myeloid cells and their progeny such as bone marrow precursor ($CD11b^{+}/Gro^{-/low}$), macrophage precursor (F4/80) and osteoclast (Cathepsin K, CTR, integrin receptors) (Takahashi *et al.* 2003; Yao *et al.* 2006; Otero *et al.* 2010). Although the current research did not definitively show CD59a expression on murine osteoclasts, a study identified CD59 on human osteoclasts (Ignatius *et al.* 2011). It is therefore likely that mouse OC also express CD59a; however this was not conclusively demonstrated.

Once assays were performed, data demonstrated that insufficiency of CD59a *in vitro* resulted in enhanced osteoclastogenesis in male mice (Fig. 7.2). This anti-osteoclastogenic functionality of CD59a has not been reported previously in mice. However, in a human study where both CD59 and DAF deficiency was recorded on erythrocytes. Researchers found an inverse correlation between these complement regulatory proteins and plasma levels of bone resorption markers: tartrate resistant acid phosphatase, RANKL, IL-6 and N-terminal cross-linking telopeptide of type-I collagen (Terpos *et al.* 2003). This study did not identify whether one or both mediators were involved, nor did conclusively explore the effect of each regulator on osteoclastogenesis. In my study increased differentiation was identified at the late stage of osteoclast formation. This might have resulted from variations in precursor cell merging or because of increased proliferation in CD59a$^{-/-}$ samples. Hence, proliferation assays and expression of fusion proteins (MITF, DC-STAMP and CD47) should be performed to demonstrate if mediators or receptors of these pathways are affected by CD59a (Battaglino *et al.* 2004; Lorenzo *et al.* 2010). In the literature, conditional knockouts of NOTCH1-3 have shown to enhance bone marrow macrophage proliferation by increased sensitisation of the M-CSF receptor c-Fms (Bai *et al.* 2008). Moreover, PU.1 which induces c-Fms expression as well as down-stream targets of M-CSF, such as MITF and Bcl-2, have been associated with proliferation (Negishi-Koga and Takayanagi 2009). These proliferation and fusion factors should be analysed via qPCR to uncover a possible mechanism of enhanced osteoclastogenesis.

From collected osteoclastogenesis supernatants, quantification of Cathepsin K was attempted utilising a Cat K ELISA kit, a developed bioassay and type I collagen zymography, but it could not be detected. A single paper described Cathepsin K detection in culture supernatant by western blotting when growing the murine macrophage cell line Raw 264.7 cells on plastic dishes (Kitami *et al.* 2010). However this Cathepsin K is difficult to detect from primary cell cultures. The expression of mRNA or internal Cathepsin K has been reported frequently and should be utilised in future to confirm osteoclast formation (Chen *et al.* 2008; Song *et al.* 2009; Li *et al.* 2010).

After Cathepsin K, other proteases were analysed. Gelatin zymography presented ProMMP-9, MMP-9 and ProMMP-2 activity and quantification of ProMMP-9 by ELISA revealed comparable levels in WT and CD59a$^{-/-}$ samples. This suggested that either protease secretion was not altered by CD59a or that differences in osteoclasts cannot be identified by measuring secreted ProMMP-9 as it is not a functional output. Therefore mRNA expression or concentrations in cell

extracts of total MMP-9 in osteoclast should be determined instead to identify potential aberrant MMP-9 expression (Chen *et al.* 2011; de Vrieze *et al.* 2011). If differences could be identified in MMP-9 expression, then pathways including AP-1, STAT3 and Runx2, which regulate MMP-9 expression, might be included in the search for a CD59a signalling pathway in bone homeostasis (Fanjul-Fernández *et al.* 2010).

Not only proteases, but cytokines and chemokines are important for osteoclastogenesis and osteoclast resorption. The level of the chemokine mKc (measured by ELISA) was not significantly different between male WT and CD59a$^{-/-}$ samples when normalised for cell density. In order to identify a mechanism for CD59a's regulation of osteoclastogenesis, other chemokines should also be considered. CXCL12/SDF-1 has been shown to recruit osteoclast precursor cells as well as support osteoclast formation and activity. Moreover, MIP-γ was identified as the main chemokine produced by osteoclasts and has been shown to be up-regulated by RANKL directly; it also responded to M-CSF in order to enhance osteoclast formation. Finally, MCP-1 and CCL3/MIP-α were reported to be involved in precursor recruitment and osteoclastogenesis (Onan *et al.* 2009). Any of these might be a potential target of CD59a and should be measured utilising qPCR or ELISA (Zhang *et al.* 2011c; Schüler *et al.* 2012).

In vitro findings of osteoclastogenesis should also be considered in relation to the *in vivo* environment to examine the function of CD59a as described and discussed in chapter 6 and section 7.4.

7.3 Investigating the Role of Human CD59 in Resorption

To investigate the role of human CD59 in resorption assays, peripheral blood CD14^{+} monocytes were utilised to grow functional osteoclasts on ivory discs in the presence of M-CSF and RANKL (chapter 5). To improve the characterisation of human osteoclasts, qPCR and immunohistochemistry should be performed to identify markers such as Cat K as suggested in section 7.2 (Cenni *et al.* 2010; Grigoriadis *et al.* 2010).

As CD14^{+} monocytes also express CD59, a CD59 knockdown system using shRNA was established. The lentiviral CD59-containing shRNA was unable to knockdown CD59 expression. A small number of studies have infected monocytes with lentivirus for the purpose of osteoclastogenesis. Hamaza et al. generated a lentivirus containing shRNA against P2X$_7$ in the pLKO.1-puro vector which was also used in my study. This virus generated by Hamza et al. was successfully introduced into human CD14^{+} monocytes and caused significant down-regulation of P2X$_7$

(Hazama *et al.* 2009). Additionally, Park-Min et al. mentioned a 90% infection efficiency in human osteoclast precursor cells utilising a lentivirus against TREM-2 cDNA followed by enhanced green fluorescent protein (Park-Min *et al.* 2009). In my project, infectivity should be enhanced by monitoring viral titres via ELISA to detect the HIV p24 gag antigen (Marr *et al.* 2003) or genomic viral RNA qPCR (Perez *et al.* 2010). Additionally, a different viral envelope should be tested to improve infectivity. In a recent study the Aura virus derived pseudotyped Aura-G which uses lectins to enter dendritic cells, was engineered (Froelich *et al.* 2011). Different coating proteins should be utilised to enhance transfection efficiency of $CD14^+$ monocytes/macrophages here.

In my study an adenoviral CD59 shRNA delivery system was consequently developed and showed up to 48% CD59 knockdown, but unfortunately cell viability was low. McLaren et al., who also utilised the adenovirus type 5 vector developed by Dr Stanton, achieved successful knockdown of death receptor 3 in THP-1 cells and human monocyte-derived macrophages obtained from peripheral blood (McLaren *et al.* 2010). Therefore experimental design required further optimisation in my study. Interestingly, adenoviruses have been shown to infect terminally differentiated cells including osteoclasts (Tanaka *et al.* 1998). Therefore to examine resorption, differentiated osteoclasts should be infected in subsequent experiments of my study, instead of $CD14^+$ monocytes/macrophages; this might supply functional data before apoptosis is triggered. The literature shows that adenoviruses induce cell lysis via autophagy, a mechanism utilised in cancer therapy (Jiang *et al.* 2011). It was likely that this pathway caused cell death within my study. Viral delivery systems were desirable in this study to obtain stable knockdown of CD59, but siRNA or anti-sense mediated silencing could be achieved by direct delivery or utilising cyclodextrin-containing polycations, lipids or polymers as coating molecules (Bartlett and Davis 2006). These systems should be tested to improve infectivity with the reduced toxicity and therefore allow osteoclastogenesis after infection.

7.4 Phenotypic Analysis of Bone Structure in $CD59a^{-/-}$ Mice

In chapter 6, phenotypic analysis of bone structure was studied in $CD59a^{-/-}$ mice at 8-10, 20 and 50 weeks of age. Femoral length was determined via X-ray and femoral diameters established utilising a digital caliper. Micro-architectural parameters of cortical and trabecular bone were examined in specific areas of femora and spines utilising microcomputed tomography. Femoral samples of young adult male WT and $CD59a^{-/-}$ samples were then processed for histological

quantification of osteoids (von Kossa/van Gieson staining), mineral apposition rate (calcein labelling) and osteoclasts (tartrate resistant acid phosphatase staining).

Femoral architecture was studied first and found to be altered in male CD59a$^{-/-}$ over WT mice at 8-10, 20 and 50 weeks. This was apparent from increased femoral length, diameter and increased bone volume in cortical and trabecular bone (Fig. 7.2). In the literature increased length was correlated with reduced cortical area of tibiae of male human donors (17-46 years of age). Furthermore, femora of C57BL/6J mice treated with a low dose of xenoestrogen (10-23 weeks of age) showed the same phenomenon. Murine bone samples also revealed enhanced bone mineral density suggesting that this increase compensated for lost bone strength upon architectural changes. When performing the 4 point bending test on human tibia and murine femora, long and slender bones were more brittle than shorter/untreated bones, suggesting that increased stiffness reduced overall bone quality (Tommasini *et al.* 2005; Pelch *et al.* 2011). This could be translated to the CD59a$^{-/-}$ mice model where cortical bone volume and cortical thickness was comparable to WT samples at 50 weeks of age, whereas femoral length was increased and therefore lower bone quality was likely and mechanical studies should be performed. According to the literature, to retain bone strength, variations in length also have to be accompanied by changes in shaft diameters (Rauch 2005), which was the case in this study at 8-10 weeks only; this again suggested reduced bone quality. Trabecular bone was reported to be an additional indicator of bone structure and flexibility. It was shown that people from different ethnicities have different structural features. African Americans were reported to have shorter vertebrae with higher trabecular volume which was suggested to have protective effects for age related bone loss (Seeman and Delmas 2006). Hence, increased trabecular bone in CD59a$^{-/-}$ mice was maybe increasing bone quality, possibly to compensate for the reduced cortical thickness. In order to draw conclusions, structural and micro-architectural variations between inbred strains should be considered as they have been shown to be significant (Beamer *et al.* 1996). As WT and CD59a$^{-/-}$ mice were not obtained from a het/het colony, variations might have partly arisen from genetic alterations of these in-house colonies and experiments should be performed with WT control animals from different sources to confirm obtained findings.

Not only bone volume, but also bone mineral density is an essential parameter of bone quality. Bone mineral density was down-regulated in cortical and up-regulated in trabecular bone of CD59a$^{-/-}$ over WT mice at 8-10 weeks. By 50 weeks of age, cortical bone mineral density was enhanced in CD59a$^{-/-}$ mice, but no

significant difference was identified in trabecular bone. Fritton et al. reported site specific bone mineral content alterations after 2-6 weeks of mechanical loading of 10 week old, male C57BL/6 mice. The authors identified 14% change in the metaphysis (mainly trabecular bone) and only 4% change in the cortical bone of the shaft (Fritton *et al.* 2005). Additionally, Hamann et al. reported that 6 week old female Sprague-Dawley rats subjected to downhill running for 1 week presented significantly enhanced trabecular bone mineral density, whereas no difference was identified in cortical bone mineral density. They concluded that changes were visible earlier in trabecular bone because of its higher bone remodelling rate (Hamann *et al.* 2012). Hence a phenotype of enhanced bone mineral density which was visible at an earlier stage in trabecular bone than cortical bone was present in CD59a$^{-/-}$ samples in this study. Alternatively, trabecular bone mineral density in CD59a$^{-/-}$ samples might have compensated for the reduced bone mineral density in cortical bone to enhance bone strength at a young age, which was not required at an older age due to the increased cortical thickness, but no published research was identified to support this notion. Additionally, bone quality is determined by a balance of stiffness and flexibility, which relies not only on the mineralisation, but on the type I collagen structure and cross-linking (Seeman and Delmas 2006). The analysis of type I collagen should be performed by scanning and transmission electron microscopy to support bone mineral density findings in predicting bone quality (Seeman and Delmas 2006; Seeman 2007).

All parameters so far were generated from femora. When looking at the vertebra L6, the trabecular bone phenotype of enhanced bone volume, trabecular thickness and bone mineral density, seen in femora of CD59a$^{-/-}$ mice, was also present here. Hildebrand et al. analysed trabecular bone architecture in the femora, spine and other sites in the human body and identified site specific variations in trabecular bone volume as well as in the structure of trabeculae (Hildebrand *et al.* 1999). In my study trabecular architecture in femur and spine at 8-10 weeks of age were comparable whereas at 20 weeks the modifications in CD59a$^{-/-}$ samples were more pronounced in spine samples indicating that the effect of CD59a is not restricted to long bones.

When evaluating histological samples, *in vivo* quantification of osteoblast function in trabecular bone revealed less osteoids and an enhanced mineral apposition rate in CD59a$^{-/-}$ over WT mice at 8-10 weeks. Luo et al. identified 20% osteoid surface over bone surface in mice 1 or 2 days after birth (Luo *et al.* 2009) whereas Potts et al. quantified a 10% osteoid surface over bone surface in mice at 3 month of age (Potts *et al.* 2004). This indicates that the osteoid levels are higher

during initial growth and the number reduces once the growth rate slows down. As CD59a$^{-/-}$ mice contain larger bones, the growth rate might have reached the peak of osteoid formation earlier than WT mice. In contrast increased mineral apposition rate in CD59a$^{-/-}$ samples revealed enhanced OB activity and therefore could have resulted in faster bone growth (Erlebacher *et al.* 1998) and turnover (Shih and Norrdin 1986).

When examining osteoclast density in this study, tartrate resistant-acid phosphatase staining demonstrated increased osteoclast surface over bone surface in trabecular bone of CD59a$^{-/-}$ over WT mice at 8-10 and 20 weeks of age. As the data is in agreement with preliminary data by Dr Anwen Williams and *in vitro* findings, it is most likely that enhanced osteoclasts stimulated increased bone remodelling and therefore growth. In osteomalacia, where mineralisation is malfunctioning, it was discovered that enhanced bone remodelling resulted in thinner and more porous cortical bone and increased unmineralised osteoids that caused a drop in bone mineral density (Bhambri *et al.* 2006). Hence reduced cortical bone mineral density in this study could have resulted from a fast bone turnover that left osteoids partly unmineralised in growing mice. Once growth was finished accelerated osteoclastogenesis was followed by efficient bone formation. Bone growth has to be further investigated because bone development is dependent on chondrocyte actions which have not been considered here (Rauch 2005).

From *in vitro* data it was expected that increased osteoclastogenesis and possible decreased colony forming units would result in an osteoporotic phenotype. When bone phenotypes in CD59a$^{-/-}$ mice were analysed increased osteoclastogenesis was confirmed but osteoblast activity was also found up-regulated and more bone volume was demonstrated in trabecular and cortical bone in young male mice. Therefore osteoclastogenesis seems to be tightly coupled to osteoblast formation in CD59a$^{-/-}$ mice, suggesting that a potential mechanism for CD59 signalling could be found either in osteoclastogenesis itself or in a coupling mechanism, for example through TGFβ or BMPs (Matsuo and Irie 2008).

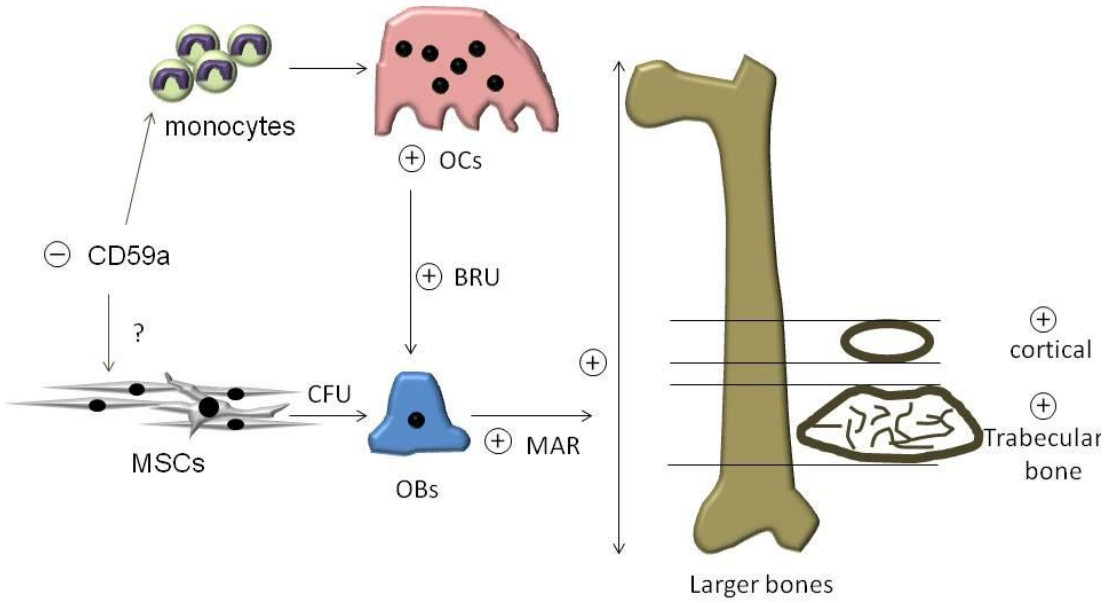

Figure 7.2 Schematic to summarise the role of CD59a in bone homeostasis in young adult male mice. CD59a deficiency increased osteoclast (OC) differentiation which is likely to enhance the bone remodelling unit (BRU) as seen by the mineral apposition (MAR). This results in a longer bone with more trabecular and cortical bone. The effect on mesenchymal stem cells (MSCs) and osteoblast (OB) formation needs to be further investigated.

7.5 Does Gender Have an Effect on Phenotypic Changes?

The effect of CD59a on osteoclastogenesis and most changes in bone architecture was restricted to male samples in young adult mice. The paroxysmal nocturnal haemoglobinuria phenotype in CD59a$^{-/-}$ mice was also exclusively present in male mice which was caused by higher haemolytic complement activity as explained in section 1.3.3 (Holt *et al.* 2001). Moreover, hormonal fluctuations were thought to be involved in gender specific effects of CD59a regulation in the brain during focal cerebral ischemia. Progesterone, for example, was mentioned to exhibit disease preventing effects in females (Harhausen *et al.* 2010).

Some architectural parameters such as bone mineral density was observed in female mice too, this effect in females could have been delayed or down-regulated by hormones such as oestrogen. Gender specific bone alterations were found in other murine knockout models. Leptin deficient mice, for example, presented a gender specific bone loss (effect in males only). This was due to 5 times higher free testosterone which resulted in modified androgen signalling (Cirmanova *et al.* 2008). Certainly, the gender specific effect of CD59a should be investigated to identify the interplay between oestrogen and CD59a signalling. Rat

models of ovariectomy and castration were reported to result in osteoporosis (Wink and Felts 1980; Gürkan *et al.* 1986; Wronski *et al.* 1989) and might be a model to determine alterations in androgen, oestrogen and testosterone levels in relation to CD59a. Additionally, oestrogen receptor knockouts have been generated (Dupont *et al.* 2000) and oestrogen treatment, for example 17b-estradiol as reported by Ito et al., are available and should be utilised to study the gender specific effect of CD59a in bone (Ito *et al.* 2001).

7.6 Is the Effect of CD59a Complement Dependent?

In vitro cultures of WT and CD59a$^{-/-}$ bone marrow preparations were performed in heat-inactivated foetal calf serum. Therefore, CD59a should not have been affected by complement within the serum suggesting that CD59a might have signalled through a complement independent pathway (Fig. 7.1). A ligand for CD59a is currently unknown, but proposed molecules include T-cell ligands such as CD2, natural killer cell proteins such as NKp46 or NKp30 and calreticulin (Kimberley *et al.* 2007). Mesenchymal stem cells have been shown to interact with CD2 on T-cells via leukocyte functional antigen 3 to inhibit their proliferation (Rasmusson *et al.* 2005). Moreover, calreticulin was found to regulate glucocorticoid receptor to decrease Wnt signalling by preventing nuclear concentration of β-catenin in osteoblasts (Olkku and Mahonen 2009). These findings suggest a link between mesenchymal stem cell regulation and CD59a which should be studied to widen mechanistic understandings of CD59 signalling.

Attempts to study this complement dependency were performed in C6$^{-/-}$ mice in this study. The data obtained was not sufficient to make definite conclusions and *in vivo* as well as *in vitro* changes should be monitored in single and double knockouts of C6 and CD59a in future studies. If C6$^{-/-}$ mice would present with the bone phenotype of WT mice and double knockouts were comparable to CD59a$^{-/-}$, this effect would be complement independent.

Alternatively *in vivo* imaging techniques should be used to dissect out complement dependency. Reagents to regulate membrane attack complex have been developed. BB5.1, for example, an anti-C5 antibody reduces complement mediated lysis by 80% (Peng *et al.* 2005). Recently a RNA antisense oligo against C6 was developed by Frank Baas's group to enhance membrane attack complex down-regulation (Fluiter *et al.* 2011). These should be tested in WT and CD59a$^{-/-}$ mice to determine mineral apposition utilising reagents such as Bone Tag (Licor), which can be monitored over time by *in vivo* fluorescent equipment, such as the Ivis

200 (Caliper Life Sciences 2009), that is available within the School of Medicine, Cardiff University.

Additionally, elevated or induced CD59a expression should be tested in WT and knockout models *in vitro* or *in vivo.* Many attempts to develop CD59a therapeutics have been made. The CD59-APT542 is a recombinant protein with a membrane associated tag developed in rats which was identified to be a 100 fold more active than soluble forms of CD59 in preventing complement mediated lysis *in vitro*. Intra-articular injection into Lewis rats prevented initiation of antigen induced arthritis (Fraser *et al.* 2003). More recently gene therapy has been utilised to enhance CD59a expression by injecting an adenovirus or adeno-associated virus, containing genetic information for sCD59a, into mice. This was tested in different disease models and was shown to also down-regulate complement lysis (Gandhi *et al.* 2011). These reagents should be utilised to determine complement dependency as well as therapeutic potential of CD59/CD59a on rodent bone homeostasis.

7.7 Role of CD59a in Osteoarthritis

Osteoarthritis treatment is somewhat limited to reducing disease progression and symptoms. The NHS supports patients by the mean of encouraging them to exercise and lose weight and supplying them with pain killers (paracetamol, NSAIDs, opioids, capsaicin cream) and intra-articular injection of corticosteroids (NHS-Choices 2010b). A treatment to prevent onset of osteoarthritis is not available yet (Wang *et al.* 2011). A recent paper observed for the first time that aging CD59a$^{-/-}$ mice developed spontaneous osteoarthritis. Deficiency in CD59a resulted in mild pathology characterised by diminished cartilage compared to WT mice at 18 month of age. Complement activation was shown in early osteoarthritis and deficiency in terminal pathway components protected from disease. Hence, the effect of CD59a was believed to be complement mediated (Wang *et al.* 2011). These changes suggested that CD59a protects from cell lysis in osteoarthritis. As cartilage degradation is a feature of osteoarthritis which is preceded by changes in bone structure, CD59a could have also functioned via a different mechanism. Early osteoarthritis was reported to be caused by accumulation of osteoclasts and cytokine production that resulted in a reduction in bone mass (Hayami *et al.* 2004). Up-regulation of osteoclastogenesis in CD59a$^{-/-}$ might be more readily amplified by pro-inflammatory cytokines than in WT mice and therefore cause more severe disease. If the effect of CD59a can be driven by the immune system it could have been influenced by macrophages. Induction of different subsets of macrophages M1 (T helper 1 cell activated) and M2b (immune complex and LPS activated) have been

shown to down-regulate CD59a expression (Luo *et al.* 2012). CD59a has also been shown to decelerate T-helper cell proliferation by interacting with the lipid raft associated kinases (section 1.3.1.1). Therefore, a deficiency in CD59a might have altered the interplay of T-cells and macrophages leading to inflammation as seen in osteoarthritis.

Furthermore, other parameters of osteoarthritis, such as cartilage, should be investigated. Tissue for this analysis was harvested and cartilage quality should be analysed utilising Safranin O staining (Kuroda *et al.* 2007). Furthermore joint space narrowing and pathology in the epiphysis, for example osteophytes, should be determined from microcomputed tomography images obtained here which include the knee joint (Abramson and Attur 2009). These would support the characterisation of CD59a$^{-/-}$ mice and consequently the aging induced osteoarthritis model.

7.8 Future Work

The characterisation of the bone phenotype of CD59a$^{-/-}$ mice should be finished by performing mechanical strength tests on femora to determine if changes demonstrated here reduce or enhance bone quality. Secondly, characterisation of mesenchymal stem cell differentiation *in vitro* should be repeated and resorption assays performed to determine functional potential of osteoclasts lacking CD59a. Thirdly, expression of transcription factors, hormones, mediators and receptors such as TAZ, BMPs for osteoblasts and CCL2/MCP-1, RANK for osteoclasts should be investigated to identify a mechanism for CD59a signalling. Moreover, it should be determined if CD59a acts complement dependent or independent by mechanisms described in section 7.6. Finally, the characteristics of osteoarthritis should be investigated to determine the possibility of CD59a as a therapeutic.

7.9 Conclusion

The complement regulator CD59a has been well classified in models of inflammatory diseases. I set out to investigate if CD59a$^{-/-}$ mice presented an osteoarthritic bone phenotype. The hypothesis was proved as osteoclastogenesis, a hallmark of early osteoarthritis, was up-regulated in young adult male CD59a$^{-/-}$ mice *in vitro* and *in vivo*. Furthermore, increased bone volume in cortical and trabecular bone was revealed as well as enhanced mineral apposition rate *in vivo* in absence of CD59a. These were an important finding as features of enhanced bone formation are also evident in osteoarthritis. Consequently, these studies highlight CD59a as a potential target for osteoarthritis treatment but more research needs to be performed to determine its mechanism of action.

8. REFERENCES

Abad, V., J. L. Meyers, M. Weise, R. I. Gafni, K. M. Barnes, O. Nilsson, J. D. Bacher and J. Baron (2002) The role of the resting zone in growth plate chondrogenesis. *Endocrinology*. **143**, 1851-1857.

Abramson, S. B. and M. Attur (2009) Developments in the scientific understanding of osteoarthritis. *Arthritis Res Ther*. **11**, 227.

Achilli, C., A. Ciana, C. Balduini, A. Risso and G. Minetti (2011) Application of gelatin zymography for evaluating low levels of contaminating neutrophils in red blood cell samples. *Analytical biochemistry*. **409**, 296-297.

Akashi, K., D. Traver, T. Miyamoto and I. L. Weissman (2000) A clonogenic common myeloid progenitor that gives rise to all myelold lineages. *Nature*. **404**, 193-196.

Alegretti, A. P., T. Mucenic, J. C. T. Brenol and R. M. Xavier (2009) The role of CD55/CD59 complement regulatory proteins on peripheral blood cells of systemic lupus erythematosus patients. *Brazilian Journal of Rheumatology*. **49**, 276-287.

Amoui, M., S. M. Suhr, D. J. Baylink and K. H. W. Lau (2004) An osteoclastic protein-tyrosine phosphatase may play a role in differentiation and activity of human monocytic U-937 cell-derived, osteoclast-like cells. *American Journal of Physiology-Cell Physiology*. **287**, C874-C884.

Andrades, J. A., M. E. Nimni, J. Becerra, R. Eisenstein, M. Davis and N. Sorgente (1996) Complement proteins are present in developing endochondral bone and may mediate cartilage cell death and vascularization. *Experimental cell research*. **227**, 208-213.

Anselme, K., B. Noėl, B. Flautre, M. C. Blary, C. Delecourt, M. Descamps and P. Hardouin (1999) Association of porous hydroxyapatite and bone marrow cells for bone regeneration. *Bone*. **25**, 51S-54S.

Arai, F., T. Miyamoto, O. Ohneda, T. Inada, T. Sudo, K. Brasel, T. Miyata, D. M. Anderson and T. Suda (1999) Commitment and differentiation of osteoclast precursor cells by the sequential expression of c-Fms and receptor activator of nuclear factor κB (RANK) receptors. *The Journal of experimental medicine*. **190**, 1741-1754.

Ariffin, S. H. Z., I. Z. Z. Abidin, M. D. Yazid and R. M. A. Wahab (2010) Differentiation analyses of adult suspension mononucleated peripheral blood cells of Mus musculus. *Cell Communication and Signaling*. **8**, 29.

Athanasou, N. A. (2011) The osteoclast—what's new? *Skeletal radiology*. **40**, 1137-1140.

Atkins, G. J., P. Kostakis, B. Pan, A. Farrugia, S. Gronthos, A. Evdokiou, K. Harrison, D. M. Findlay and A. C. Zannettino (2003) RANKL expression is related to the differentiation state of human osteoblasts. *Journal of Bone and Mineral Research*. **18**, 1088-1098.

Baalasubramanian, S., C. Harris, R. Donev, M. Mizuno, N. Omidvar, W. Song and B. Morgan (2004) CD59a is the primary regulator of membrane attack complex assembly in the mouse. *J Immunol*. **173**, 3684-92.

Bab, I., Y. Gabet, C. Haibi-Yonissi and R. Muller (2007) *Micro-tomographic atlas of the mouse skeleton*, 1st ed., Springer

Baba, A., T. Fujita and N. Tamura (1984) Sexual dimorphism of the fifth component of mouse complement. *The Journal of experimental medicine*. **160**, 411-419.

Bai, S., R. Kopan, W. Zou, M. J. Hilton, C. Ong, F. Long, F. P. Ross and S. L. Teitelbaum (2008) NOTCH1 regulates osteoclastogenesis directly in osteoclast precursors and indirectly via osteoblast lineage cells. *Journal of Biological Chemistry*. **283**, 6509-6518.

Baksh, D., R. Yao and R. S. Tuan (2007) Comparison of proliferative and multilineage differentiation potential of human mesenchymal stem cells derived from umbilical cord and bone marrow. *Stem cells*. **25**, 1384-1392.
Baramova, E., K. Bajou, A. Remacle, C. L'hoir, H. Krell, U. Weidle, A. Noël and J. M. Foidart (1997) Involvement of PA/plasmin system in the processing of pro-MMP-9 and in the second step of pro-MMP-2 activation. *FEBS letters*. **405**, 157-162.
Barsony, J., Y. Sugimura and J. G. Verbalis (2011) Osteoclast response to low extracellular sodium and the mechanism of hyponatremia-induced bone loss. *Journal of Biological Chemistry*. **286**, 10864.
Bartlett, D. W. and M. E. Davis (2006) Insights into the kinetics of siRNA-mediated gene silencing from live-cell and live-animal bioluminescent imaging. *Nucleic acids research*. **34**, 322-333.
Battaglino, R., J. Fu, U. Späte, U. Ersoy, M. Joe, L. Sedaghat and P. Stashenko (2004) Serotonin regulates osteoclast differentiation through its transporter. *Journal of Bone and Mineral Research*. **19**, 1420-1431.
Beamer, W., L. Donahue, C. Rosen and D. Baylink (1996) Genetic variability in adult bone density among inbred strains of mice. *Bone*. **18**, 397-403.
Beeton, C., S. Bord, D. Ireland and J. Compston (2006) Osteoclast formation and bone resorption are inhibited by megakaryocytes. *Bone*. **39**, 985-990.
Bellows, C., J. Heersche and J. Aubin (1992) Inorganic phosphate added exogenously or released from [beta]-glycerophosphate initiates mineralization of osteoid nodules in vitro. *Bone and mineral*. **17**, 15-29.
Bewig, B. and W. Schmidt (2000) Accelerated titering of adenoviruses. *Biotechniques*. **28**, 870.
Bhambri, R., V. Naik, N. Malhotra, S. Taneja, S. Rastogi, U. Ravishanker and A. Mithal (2006) Changes in bone mineral density following treatment of osteomalacia. *Journal of Clinical Densitometry*. **9**, 120-127.
Bhole, D. and G. L. Stahl (2004) Molecular basis for complement component 6 (C6) deficiency in rats and mice. *Immunobiology*. **209**, 559-568.
Bianco, P. (2011) Bone and the hematopoietic niche: a tale of two stem cells. *Blood*. **117**, 5281.
Bilezikian, J. P., A. Morishima, J. Bell and M. M. Grumbach (1998) Increased bone mass as a result of estrogen therapy in a man with aromatase deficiency. *New England Journal of Medicine*. **339**, 599-603.
Billiard, J., R. Moran, M. Whitley, M. Chatterjee Kishore, K. Gillis, E. Brown, B. Komm and P. Bodine (2003) Transcriptional profiling of human osteoblast differentiation. *Journal of cellular biochemistry*. **89**, 389-400.
Birrell, F. and D. Felson (2009) The age of osteoarthritis. *Age and ageing*. **38**, 2-3.
Biskobing, D. M., X. Fan and J. Rubin (1995) Characterization of MCSF-induced proliferation and subsequent osteoclast formation in murine marrow culture. *Journal of Bone and Mineral Research*. **10**, 1025-1032.
Bojkowska, K., F. SantoniádeáSio, I. Barde, S. Offner, S. Verp, C. Heinis, K. Johnsson and D. Trono (2011) Measuring InáVivo Protein Half-Life. *Chemistry & Biology*. **18**, 805-815.
Bone, H. G., S. L. Greenspan, C. McKeever, N. Bell, M. Davidson, R. W. Downs, R. Emkey, P. J. Meunier, S. S. Miller and A. L. Mulloy (2000) Alendronate and estrogen effects in postmenopausal women with low bone mineral density. *Journal of Clinical Endocrinology & Metabolism*. **85**, 720-726.
Boon, H. D. T., V. B. Yuri, K. T. Boon, H. W. Siew and L. Jinhua (2012) Complement C1q production by osteoclasts and its regulation of osteoclast development. *Biochemical Journal*.
Bora, N. S., S. Kaliappan, P. Jha, Q. Xu, B. Sivasankar, C. L. Harris, B. P. Morgan and P. S. Bora (2007) CD59, a complement regulatory protein, controls

choroidal neovascularization in a mouse model of wet-type age-related macular degeneration. *The Journal of Immunology*. **178**, 1783.
Borer, K. T., A. Pryor, C. A. Conn, R. Bonna and M. Kielb (1988) Group housing accelerates growth and induces obesity in adult hamsters. *American Journal of Physiology-Regulatory, Integrative and Comparative Physiology*. **255**, R128-R133.
Borniquel, S., N. García-Quintáns, I. Valle, Y. Olmos, B. Wild, F. Martínez-Granero, E. Soria, S. Lamas and M. Monsalve (2010) Inactivation of Foxo3a and Subsequent Downregulation of PGC-1α Mediate Nitric Oxide-Induced Endothelial Cell Migration. *Molecular and cellular biology*. **30**, 4035-4044.
Bowen, J., M. Noakes and P. M. Clifton (2004) A high dairy protein, high-calcium diet minimizes bone turnover in overweight adults during weight loss. *The Journal of nutrition*. **134**, 568.
Box, E., J. Gandolfi and C. Mitchell (2010) Maintaining safe mobility for the ageing population-the role of the private car.
Brandao-Burch, A., J. Utting, I. Orriss and T. Arnett (2005) Acidosis inhibits bone formation by osteoblasts in vitro by preventing mineralization. *Calcified tissue international*. **77**, 167-174.
Braun, J. and J. Sieper (2007) Ankylosing spondylitis. *The Lancet*. **369**, 1379-1390.
Breckpot, K., J. Corthals, C. Heirman, A. Bonehill, A. Michiels, S. Tuyaerts, C. De Greef and K. Thielemans (2004) Activation of monocytes via the CD14 receptor leads to the enhanced lentiviral transduction of immature dendritic cells. *Human gene therapy*. **15**, 562-573.
Bruckner, H. (1976) Effect of antibiotics on mice treated with cyclophosphamide. *Journal of the National Cancer Institute*. **57**, 1249.
Bruinink, A., U. Tobler, M. Hälg and J. Grünert (2004) Effects of serum and serum heat-inactivation on human bone derived osteoblast progenitor cells. *Journal of Materials Science: Materials in Medicine*. **15**, 497-501.
Buckwalter, J. and R. Cooper (1987) Bone structure and function. *Instr Course Lect*. **36**, 27-48.
Bull, M. J., A. S. Williams, Z. Mecklenburgh, C. J. Calder, J. P. Twohig, C. Elford, B. A. J. Evans, T. F. Rowley, T. J. Slebioda and V. Y. Taraban (2008) The Death Receptor 3–TNF-like protein 1A pathway drives adverse bone pathology in inflammatory arthritis. *The Journal of experimental medicine*. **205**, 2457-2464.
Burgess, T. L., Y. Qian, S. Kaufman, B. D. Ring, G. Van, C. Capparelli, M. Kelley, H. Hsu, W. J. Boyle and C. R. Dunstan (1999) The ligand for osteoprotegerin (OPGL) directly activates mature osteoclasts. *The Journal of cell biology*. **145**, 527.
Burns, J. C., T. Friedmann, W. Driever, M. Burrascano and J. K. Yee (1993) Vesicular stomatitis virus G glycoprotein pseudotyped retroviral vectors: concentration to very high titer and efficient gene transfer into mammalian and nonmammalian cells. *Proceedings of the National Academy of Sciences*. **90**, 8033.
Caliezi, C., W. Wuillemin, S. Zeerleder, M. Redondo, B. Eisele and C. Hack (2000) C1-esterase inhibitor: an anti-inflammatory agent and its potential use in the treatment of diseases other than hereditary angioedema. *Pharmacological reviews*. **52**, 91-112.
Caliper Life Sciences, I. (2009) IVIS | 200 Series
Calle, Y., G. E. Jones, C. Jagger, K. Fuller, M. P. Blundell, J. Chow, T. Chambers and A. J. Thrasher (2004) WASp deficiency in mice results in failure to form osteoclast sealing zones and defects in bone resorption. *Blood*. **103**, 3552-3561.
Cawthorn, W. P., A. J. Bree, Y. Yao, B. Du, N. Hemati, G. Martinez-Santibañez and O. A. MacDougald (2011) Wnt6, Wnt10a and Wnt10b inhibit adipogenesis

and stimulate osteoblastogenesis through a [beta]-catenin-dependent mechanism. *Bone*.
Cenni, E., S. Avnet, C. Fotia, M. Salerno and N. Baldini (2010) Platelet-rich plasma impairs osteoclast generation from human precursors of peripheral blood. *Journal of Orthopaedic Research*. **28**, 792-797.
Chang, Y. L., C. M. Stanford and J. C. Keller (2000) Calcium and phosphate supplementation promotes bone cell mineralization: Implications for hydroxyapatite (HA)-enhanced bone formation. *Journal of biomedical materials research*. **52**, 270-278.
Chau, D., R. J. Collighan, E. A. M. Verderio, V. L. Addy and M. Griffin (2005) The cellular response to transglutaminase-cross-linked collagen. *Biomaterials*. **26**, 6518-6529.
Chen, K. C., Y. S. Wang, C. Y. Hu, W. C. Chang, Y. C. Liao, C. Y. Dai and S. H. H. Juo (2011) OxLDL up-regulates microRNA-29b, leading to epigenetic modifications of MMP-2/MMP-9 genes: a novel mechanism for cardiovascular diseases. *The FASEB Journal*. **25**, 1718-1728.
Chen, L., X. Wei, B. Evans, W. Jiang and D. Aeschlimann (2008) IL-23 promotes osteoclast formation by up-regulation of receptor activator of NF-kappaB (RANK) expression in myeloid precursor cells. *Eur J Immunol*. **38**, 2845-54.
Chou, M. Y., D. Yan, T. Jafarov and E. Everett (2009) Modulation of murine bone marrow-derived CFU-F and CFU-OB by in vivo bisphosphonate and fluoride treatments. *Orthodontics & craniofacial research*. **12**, 141-147.
Choudhary, S., H. Huang, L. Raisz and C. Pilbeam (2008) Anabolic effects of PTH in cyclooxygenase-2 knockout osteoblasts in vitro. *Biochemical and biophysical research communications*. **372**, 536-541.
Cirmanova, V., M. Bayer, L. Starka and K. Zajickova (2008) The effect of leptin on bone: an evolving concept of action. *Physiol Res*. **57**, S143-S151.
Coelho, M. and M. Fernandes (2000) Human bone cell cultures in biocompatibility testing. Part II: effect of ascorbic acid,[beta]-glycerophosphate and dexamethasone on osteoblastic differentiation. *Biomaterials*. **21**, 1095-1102.
Contractor, T., B. Babiarz, A. J. Kowalski, S. R. Rittling, E. S. Sørensen and D. T. Denhardt (2005) Osteoclasts Resorb Protein-free Mineral (Osteologic™ Discs) Efficiently in the Absence of Osteopontin. *In Vivo*. **19**, 335-341.
Corisdeo, S., M. Gyda, M. Zaidi, B. S. Moonga and B. R. Troen (2001) New insights into the regulation of cathepsin K gene expression by osteoprotegerin ligand. *Biochemical and biophysical research communications*. **285**, 335-339.
Crafts, R. C. (1948) The effects of estrogens on the bone marrow of adult female dogs. *Blood*. **3**, 276-285.
Craig, A. (2009) An exploration of the potential of using adeno-associated virus vectors to transfer immunosuppressive genes to transplanted pancreatic islets, HOWARD UNIVERSITY
Crisp, M., K. J. Starkey, C. Lane, J. Ham and M. Ludgate (2000) Adipogenesis in thyroid eye disease. *Investigative ophthalmology & visual science*. **41**, 3249-3255.
Czepluch, F. S., S. J. F. Olieslagers and J. Waltenberger (2007) Monocyte function is severely impaired by the fluorochrome calcein acetomethylester. *Biochemical and biophysical research communications*. **361**, 410-413.
Davies, A., D. Simmons, G. Hale, R. Harrison, H. Tighe, P. Lachmann and H. Waldmann (1989) CD59, an LY-6-like protein expressed in human lymphoid cells, regulates the action of the complement membrane attack complex on homologous cells. *J Exp Med*. **170**, 637-54.
de Baat, P., M. Heijboer and C. de Baat (2005) [Development, physiology, and cell activity of bone]. *Ned Tijdschr Tandheelkd*. **112**, 258-63.
De Filippo, K., R. B. Henderson, M. Laschinger and N. Hogg (2008) Neutrophil chemokines KC and macrophage-inflammatory protein-2 are newly

synthesized by tissue macrophages using distinct TLR signaling pathways. *The Journal of Immunology*. **180**, 4308-4315.
De Schauwer, C., E. Meyer, G. R. Van de Walle and A. Van Soom (2011) Markers of stemness in equine mesenchymal stem cells: a plea for uniformity. *Theriogenology*. **75**, 1431-1443.
de Souza Malaspina, T. S., W. F. Zambuzzi, C. X. dos Santos, A. P. Campanelli, F. R. M. Laurindo, M. C. Sogayar and J. M. Granjeiro (2009) A possible mechanism of low molecular weight protein tyrosine phosphatase (LMW-PTP) activity modulation by glutathione action during human osteoblast differentiation. *Archives of Oral Biology*. **54**, 642-650.
de Vries, T. J., T. Schoenmaker, B. Hooibrink, P. J. M. Leenen and V. Everts (2009) Myeloid blasts are the mouse bone marrow cells prone to differentiate into osteoclasts. *Journal of leukocyte biology*. **85**, 919-927.
de Vrieze, E., F. Sharif, J. R. Metz, G. Flik and M. K. Richardson (2011) Matrix metalloproteinases in osteoclasts of ontogenetic and regenerating zebrafish scales. *Bone*. **48**, 704-712.
Derenne, S., M. Amiot, S. Barillé, M. Collette, N. Robillard, P. Berthaud, J. L. U. C. Harousseau and R. Bataille (1999) Zoledronate Is a Potent Inhibitor of Myeloma Cell Growth and Secretion of IL-6 and MMP-1 by the Tumoral Environment. *Journal of Bone and Mineral Research*. **14**, 2048-2056.
DIJK, V. (1999) Sex-limited protein: in vitro and in vivo functions. *Clinical & Experimental Immunology*. **116**, 395-400.
Dimai, H., T. Linkhart, S. Linkhart, L. Donahue, W. Beamer, C. Rosen, J. Farley and D. Baylink (1998) Alkaline phosphatase levels and osteoprogenitor cell numbers suggest bone formation may contribute to peak bone density differences between two inbred strains of mice. *Bone*. **22**, 211-216.
Dupont, S., A. Krust, A. Gansmuller, A. Dierich, P. Chambon and M. Mark (2000) Effect of single and compound knockouts of estrogen receptors alpha (ERalpha) and beta (ERbeta) on mouse reproductive phenotypes. *Development*. **127**, 4277-4291.
Duque, G. (2008) Bone and fat connection in aging bone. *Current opinion in rheumatology*. **20**, 429.
Efstratiadis, A. (1998) Genetics of mouse growth. *International Journal of Developmental Biology*. **42**, 955-976.
Ehrnthaller, C., A. Ignatius, F. Gebhard and M. Huber-Lang (2011) New insights of an old defense system: structure, function, and clinical relevance of the complement system. *Molecular Medicine*. **17**, 317.
Ehrnthaller, C., P. Lisson, R. Brenner, R. Blakytny, L. Kreja, L. Claes and A. Ignatius (2009) C5a receptor expression in bone cells and during fracture healing, Schattauer Biomechanics and Biology of Bone Regneration Symposium 2009
Engelke, D. R. and J. J. Rossi (2005) *RNA interference*, Elsevier Academic Press
Enlow, D. H. (1962) Functions of the Haversian system. *American Journal of Anatomy*. **110**, 269-305.
Erlebacher, A., E. H. Filvaroff, J. Q. Ye and R. Derynck (1998) Osteoblastic responses to TGF-β during bone remodeling. *Molecular biology of the cell*. **9**, 1903-1918.
Evans, J. F., J. K. Yeh and J. F. Aloia (2000) Osteoblast-like cells of the hypophysectomized rat: a model of aberrant osteoblast development. *American Journal of Physiology-Endocrinology And Metabolism*. **278**, E832-E838.
Fan, J., B. Wagner and D. McDonnell (1996) Identification of the sequences within the human complement 3 promoter required for estrogen responsiveness provides insight into the mechanism of tamoxifen mixed agonist activity. *Molecular Endocrinology*. **10**, 1605-1616.

Fanjul-Fernández, M., A. R. Folgueras, S. Cabrera and C. López-Otín (2010) Matrix metalloproteinases: evolution, gene regulation and functional analysis in mouse models. *Biochimica et Biophysica Acta (BBA)-Molecular Cell Research*. **1803**, 3-19.

Farkas, I., L. Baranyi, Y. Ishikawa, N. Okada, C. Bohata, D. Budai, A. Fukuda, M. Imai and H. Okada (2002) CD59 blocks not only the insertion of C9 into MAC but inhibits ion channel formation by homologous C5b-8 as well as C5b-9. *J Physiol*. **539**, 537-45.

Farkas, I., M. Sárvári, M. Aller, N. Okada, H. Okada, I. Likó and Z. Liposits (2012) Estrogen receptor alpha and beta differentially mediate C5aR agonist evoked Ca< sup> 2+</sup>-influx in neurons through L-type voltage-gated Ca< sup> 2+</sup> channels. *Neurochemistry International*.

Favus, M. a. C., S (2006) *Primer on the metabolic bone diseases and disorders of mineral metabolism*, 6th ed., ASBMR, Washington

Ferguson, V. L., R. A. Ayers, T. A. Bateman and S. J. Simske (2003) Bone development and age-related bone loss in male C57BL/6J mice. *Bone*. **33**, 387-398.

Fermentas-International-Inc (2011) Semi-dry Protein Transfer for Western Blotting, Thermo Fisher Scientific Inc.

Ferrari-Lacraz, S. and D. Burger (2010) RANKing bone resorption versus inflammation: Infection makes the decision. *IBMS BoneKEy*. **7**, 156-160.

Ferron, M., J. Wei, T. Yoshizawa, P. Ducy and G. Karsenty (2010) An ELISA-based method to quantify osteocalcin carboxylation in mice. *Biochemical and biophysical research communications*. **397**, 691-696.

Festy, F., L. Hoareau, S. Bes-Houtmann, A. M. Péquin, M. P. Gonthier, A. Munstun, J. J. Hoarau, M. Cesari and R. Roche (2005) Surface protein expression between human adipose tissue-derived stromal cells and mature adipocytes. *Histochemistry and cell biology*. **124**, 113-121.

Filgueira, L. (2009) Osteoclast Differentiation and Function. *Bone Cancer: Progression and Therapeutic Approaches*. Heymann, D. (ed.), pp 59-66, Elsevier Inc. London

Flanagan, A. M. and H. M. Massey (2003) Generating human osteoclasts in vitro from bone marrow and peripheral blood. *Methods Mol Med*. **80**, 113-128.

Fluiter, K., V. Ramaglia and F. Baas (2011) Antagonists of complement C6 affect neurodegeneration. *Molecular Immunology*. **48**, 1714-1714.

Foxwell, B., K. Browne, J. Bondeson, C. Clarke, R. De Martin, F. Brennan and M. Feldmann (1998) Efficient adenoviral infection with IκBα reveals that macrophage tumor necrosis factor α production in rheumatoid arthritis is NF-κB dependent. *Proceedings of the National Academy of Sciences*. **95**, 8211.

Franco, G. C. N., M. Kajiya, T. Nakanishi, K. Ohta, P. L. Rosalen, F. C. Groppo, C. W. O. Ernst, J. L. Boyesen, J. D. Bartlett and P. Stashenko (2011) Inhibition of matrix metalloproteinase-9 activity by doxycycline ameliorates RANK ligand-induced osteoclast differentiation in vitro and in vivo. *Experimental cell research*. **317**, 1454-1464.

Fraser, D. A., C. L. Harris, A. S. Williams, M. Mizuno, S. Gallagher, R. A. G. Smith and B. P. Morgan (2003) Generation of a Recombinant, Membrane-targeted Form of the Complement Regulator CD59. *Journal of Biological Chemistry*. **278**, 48921-48927.

Fritton, J., E. Myers, T. Wright and M. Van der Meulen (2005) Loading induces site-specific increases in mineral content assessed by microcomputed tomography of the mouse tibia. *Bone*. **36**, 1030-1038.

Froelich, S., A. Tai, K. Kennedy, A. Zubair and P. Wang (2011) Pseudotyping Lentiviral Vectors with Aura Virus Envelope Glycoproteins for DC-SIGN–Mediated Transduction of Dendritic Cells. *Human gene therapy*. **22**, 1281-1291.

Fromigué, O., Z. Hamidouche, S. Chateauvieux, P. Charbord and P. J. Marie (2008) Distinct osteoblastic differentiation potential of murine fetal liver and bone marrow stroma-derived mesenchymal stem cells. *Journal of cellular biochemistry*. **104**, 620-628.
Fuller, K., J. M. Owens and T. J. Chambers (1995) Macrophage inflammatory protein-1 alpha and IL-8 stimulate the motility but suppress the resorption of isolated rat osteoclasts. *The Journal of Immunology*. **154**, 6065-6072.
Fuller, K., J. L. Ross, K. A. Szewczyk, R. Moss and T. J. Chambers (2010) Bone is not essential for osteoclast activation. *PloS one*. **5**, e12837.
Gadjeva, M., S. Thiel and J. Jensenius (2001) The mannan-binding-lectin pathway of the innate immune response. *Curr Opin Immunol*. **13**, 74-8.
Galal, N., W. R. El-Beialy, Y. Deyama, Y. Yoshimura, K. Suzuki and Y. Totsuka (2007) Novel effect of estrogen on RANK and c-fms expression in RAW 264.7 cells. *International journal of molecular medicine*. **20**, 97-101.
Gale, D., C. Chaisson, S. Totterman, R. Schwartz, M. Gale and D. Felson (1999) Meniscal subluxation: association with osteoarthritis and joint space narrowing. *Osteoarthritis and Cartilage*. **7**, 526-532.
Gandhi, J., S. M. Cashman and R. Kumar-Singh (2011) Soluble CD59 Expressed from an Adenovirus In Vivo Is a Potent Inhibitor of Complement Deposition on Murine Liver Vascular Endothelium. *PloS one*. **6**, e21621.
Gein, S. V., M. S. Kuyukina, I. B. Ivshina, T. A. Baeva and V. A. Chereshnev (2011) In vitro cytokine stimulation assay for glycolipid biosurfactant from Rhodococcusruber: role of monocyte adhesion. *Cytotechnology*. **63**, 559-566.
Gelb, B. D., K. Moissoglu, J. Zhang, J. A. Martignetti, D. Brömme and R. J. Desnick (1996) Cathepsin K: isolation and characterization of the murine cDNA and genomic sequence, the homologue of the human pycnodysostosis gene. *Biochemical and molecular medicine*. **59**, 200-206.
Geurts, J. and V. Valderrabano (2012) Aging and Osteoarthritis: An Inevitable Encounter? *Journal of Aging Research*. **2012**.
Ghayor, C., R. M. Correro, K. Lange, L. S. Karfeld-Sulzer, K. W. Grätz and F. E. Weber (2011) Inhibition of Osteoclast Differentiation and Bone Resorption by N-Methylpyrrolidone. *Journal of Biological Chemistry*. **286**, 24458.
Gilbert, S. (2000a) Developmental Biology, Sunderland, MA: Sinauer Assoc, Inc
Gilbert, S. F. (2000b) Osteogenesis: the development of bones.
Giusti, I., S. D'Ascenzo, D. Millimaggi, G. Taraboletti, G. Carta, N. Franceschini, A. Pavan and V. Dolo (2008) Cathepsin B mediates the pH-dependent proinvasive activity of tumor-shed microvesicles. *Neoplasia (New York, NY)*. **10**, 481.
Goekoop, R., M. Kloppenburg, H. Kroon, L. Dirkse, T. Huizinga, R. Westendorp and J. Gussekloo (2011) Determinants of absence of osteoarthritis in old age. *Scandinavian Journal of Rheumatology*. **40**, 68-73.
Goodfellow, R., A. Williams, J. Levin, B. Williams and B. Morgan (2000) Soluble complement receptor one (sCR1) inhibits the development and progression of rat collagen-induced arthritis. *Clinical & Experimental Immunology*. **119**, 210-216.
Gorrill, R. and D. Hobson (1952) The agglutinating property of complement. *The Journal of Pathology and Bacteriology*. **64**, 257-263.
Gowen, L. C., D. N. Petersen, A. L. Mansolf, H. Qi, J. L. Stock, G. T. Tkalcevic, H. A. Simmons, D. T. Crawford, K. L. Chidsey-Frink and H. Z. Ke (2003) Targeted disruption of the osteoblast/osteocyte factor 45 gene (OF45) results in increased bone formation and bone mass. *Journal of Biological Chemistry*. **278**, 1998-2007.
Graham, G. G. (1972) Environmental factors affecting the growth of children. *The American Journal of Clinical Nutrition*. **25**, 1184-1188.

Granholm, S., P. Lundberg and U. H. Lerner (2008) Expression of the calcitonin receptor, calcitonin receptor-like receptor, and receptor activity modifying proteins during osteoclast differentiation. *Journal of cellular biochemistry*. **104**, 920-933.
Gressner, O., U. Meier, S. Hillebrandt, H. E Wasmuth, J. Kohl, T. Sauerbruch and F. Lammert (2007) Gc-globulin concentrations and C5 haplotype-tagging polymorphisms contribute to variations in serum activity of complement factor C5. *Clinical biochemistry*. **40**, 771-775.
Griesemer, A. D., M. Okumi, A. Shimizu, S. Moran, Y. Ishikawa, J. Iorio, J. S. Arn and K. Yamada (2009) Upregulation of CD59: potential mechanism of accommodation in a large animal model. *Transplantation*. **87**, 1308.
Griffin, X., F. Warner and M. Costa (2008) The role of electromagnetic stimulation in the management of established non-union of long bone fractures: What is the evidence? *Injury*. **39**, 419-429.
Grigoriadis, A. E., M. Kennedy, A. Bozec, F. Brunton, G. Stenbeck, I. H. Park, E. F. Wagner and G. M. Keller (2010) Directed differentiation of hematopoietic precursors and functional osteoclasts from human ES and iPS cells. *Blood*. **115**, 2769-2776.
Gropp, K., N. Weber, M. Reuter, S. Micklisch, I. Kopka, T. Hallström and C. Skerka (2011) 2-glycoprotein I, the major target in antiphospholipid syndrome, is a special human complement regulator. *Blood*. **118**, 2774-2783.
Gupta, K., M. Shukla, J. B. Cowland, C. J. Malemud and T. M. Haqqi (2007) Neutrophil gelatinase–associated lipocalin is expressed in osteoarthritis and forms a complex with matrix metalloproteinase 9. *Arthritis & Rheumatism*. **56**, 3326-3335.
Gürkan, L., A. Ekeland, K. M. Gautvik, N. Langeland, H. Rønningen and L. F. Solheim (1986) Bone changes after castration in rats. A model for osteoporosis. *Acta Orthopaedica*. **57**, 67-70.
Hadjidakis, D. and I. Androulakis (2006) Bone remodeling. *Ann N Y Acad Sci*. **1092**, 385-96.
Hahn-Dantona, E., J. F. Ruiz, P. Bornstein and D. K. Strickland (2001) The low density lipoprotein receptor-related protein modulates levels of matrix metalloproteinase 9 (MMP-9) by mediating its cellular catabolism. *Journal of Biological Chemistry*. **276**, 15498.
Hall, B. K. (2005) *Bone and Cartilage. Developmental and Evolutionary Skeletal Biology.*, Elsevier Academic Press
Halloran, B. P., V. L. Ferguson, S. J. Simske, A. Burghardt, L. L. Venton and S. Majumdar (2002) Changes in bone structure and mass with advancing age in the male C57BL/6J mouse. *Journal of Bone and Mineral Research*. **17**, 1044-1050.
Ham, A. W. and D. H. Cormack (1979) *Histophysiology of cartilage, bone, and joints*, Lippincott
Hamann, N., T. Kohler, R. Müller, G. P. Brüggemann and A. Niehoff (2012) The effect of level and downhill running on cortical and trabecular bone in growing rats. *Calcified tissue international*, 1-9.
Hamilton, J. A. (2008) Colony-stimulating factors in inflammation and autoimmunity. *Nature Reviews Immunology*. **8**, 533-544.
Hamlin, N. and P. Price (2004) Mineralization of decalcified bone occurs under cell culture conditions and requires bovine serum but not cells. *Calcified tissue international*. **75**, 231-242.
Harhausen, D., U. Khojasteh, P. F. Stahel, B. P. Morgan, W. Nietfeld, U. Dirnagl and G. Trendelenburg (2010) Membrane attack complex inhibitor CD59a protects against focal cerebral ischemia in mice. *J Neuroinflammation*. **7**, 15.
Harris, C. L., S. M. Hanna, M. Mizuno, D. S. Holt, K. J. Marchbank and B. P. Morgan (2003) Characterization of the mouse analogues of CD59 using novel

monoclonal antibodies: tissue distribution and functional comparison. *Immunology*. **109**, 117-126.
Hayami, T., M. Pickarski, G. A. Wesolowski, J. Mclane, A. Bone, J. Destefano, G. A. Rodan and L. T. Duong (2004) The role of subchondral bone remodeling in osteoarthritis: reduction of cartilage degeneration and prevention of osteophyte formation by alendronate in the rat anterior cruciate ligament transection model. *Arthritis & Rheumatism*. **50**, 1193-1206.
Hazama, R., X. Qu, K. Yokoyama, C. Tanaka, E. Kinoshita, J. He, S. Takahashi, K. Tohyama, H. Yamamura and Y. Tohyama (2009) ATP-induced osteoclast function: the formation of sealing-zone like structure and the secretion of lytic granules via microtubule-deacetylation under the control of Syk. *Genes to Cells*. **14**, 871-884.
Haÿ, E., E. Laplantine, V. Geoffroy, M. Frain, T. Kohler, R. Müller and P. J. Marie (2009) N-cadherin interacts with axin and LRP5 to negatively regulate Wnt/β-catenin signaling, osteoblast function, and bone formation. *Molecular and cellular biology*. **29**, 953-964.
He, J. Q., C. Wiesmann and M. van Lookeren Campagne (2008) A role of macrophage complement receptor CRIg in immune clearance and inflammation. *Molecular immunology*. **45**, 4041-4047.
Heinen, S., A. Hartmann, N. Lauer, U. Wiehl, H. M. Dahse, S. Schirmer, K. Gropp, T. Enghardt, R. Wallich and S. Hälbich (2009) Factor H–related protein 1 (CFHR-1) inhibits complement C5 convertase activity and terminal complex formation. *Blood*. **114**, 2439.
Helfrich, M. H. and S. Ralston (2003) *Bone research protocols*, Humana Pr Inc
Hermesh, T., B. Moltedo, T. M. Moran and C. B. López (2010) Antiviral instruction of bone marrow leukocytes during respiratory viral infections. *Cell host & microbe*. **7**, 343-353.
Hietala, M. A., I. M. Jonsson, A. Tarkowski, S. Kleinau and M. Pekna (2002) Complement deficiency ameliorates collagen-induced arthritis in mice. *The Journal of Immunology*. **169**, 454.
Hildebrand, T., A. Laib, R. Müller, J. Dequeker and P. Rüegsegger (1999) Direct Three-Dimensional Morphometric Analysis of Human Cancellous Bone: Microstructural Data from Spine, Femur, Iliac Crest, and Calcaneus. *Journal of Bone and Mineral Research*. **14**, 1167-1174.
Hoemann, C., H. El-Gabalawy and M. McKee (2009) In vitro osteogenesis assays: influence of the primary cell source on alkaline phosphatase activity and mineralization. *Pathologie Biologie*. **57**, 318-323.
Hoenderop, J. G. J., J. Van Leeuwen, B. C. J. van der Eerden, F. F. J. Kersten, A. van der Kemp, A. M. Mérillat, J. H. Waarsing, B. C. Rossier, V. Vallon and E. Hummler (2003) Renal Ca^ 2^+ wasting, hyperabsorption, and reduced bone thickness in mice lacking TRPV5. *Journal of Clinical Investigation*. **112**, 1906-1914.
Hoffmann, J., F. Kafatos, C. Janeway and R. Ezekowitz (1999) Phylogenetic perspectives in innate immunity. *Science*. **284**, 1313-8.
Hofmann, A., U. Ritz, M. Hessmann, C. Schmid, A. Tresch, J. Rompe, A. Meurer and P. Rommens (2008) Cell viability, osteoblast differentiation, and gene expression are altered in human osteoblasts from hypertrophic fracture non-unions. *Bone*. **42**, 894-906.
Hol, J., L. Wilhelmsen and G. Haraldsen (2010) The murine IL-8 homologues KC, MIP-2, and LIX are found in endothelial cytoplasmic granules but not in Weibel-Palade bodies. *Journal of leukocyte biology*. **87**, 501-508.
Holguin, M., L. Fredrick, N. Bernshaw, L. Wilcox and C. Parker (1989) Isolation and characterization of a membrane protein from normal human erythrocytes that inhibits reactive lysis of the erythrocytes of paroxysmal nocturnal hemoglobinuria. *J Clin Invest*. **84**, 7-17.

Holmes, S., K. Still, D. Buttle, N. Bishop and P. Grabowski (2004) Chemically modified tetracyclines act through multiple mechanisms directly on osteoclast precursors. *Bone*. **35**, 471-478.
Holt, D., M. Botto, A. Bygrave, S. Hanna, M. Walport and B. Morgan (2001) Targeted deletion of the CD59 gene causes spontaneous intravascular hemolysis and hemoglobinuria. *Blood*. **98**, 442-9.
Hong, J. H., E. S. Hwang, M. T. McManus, A. Amsterdam, Y. Tian, R. Kalmukova, E. Mueller, T. Benjamin, B. M. Spiegelman and P. A. Sharp (2005) TAZ, a transcriptional modulator of mesenchymal stem cell differentiation. *Science's STKE*. **309**, 1074.
HU, J. F. E. I., L. GILMER, R. Hopkins and J. LLOYD WOLFINBARGER (1989) Effects of antibiotics on cellular viability in porcine heart valve tissue. *Cardiovascular research*. **23**, 960-964.
Hu, Y. J., X. Wei, W. Zhao, Y. S. Liu and G. Q. Chen (2009) Biocompatibility of poly (3-hydroxybutyrate-co-3-hydroxyvalerate-co-3-hydroxyhexanoate) with bone marrow mesenchymal stem cells. *Acta biomaterialia*. **5**, 1115-1125.
Hughes, D. E., A. Dai, J. C. Tiffee, H. H. Li, G. R. Mundy and B. F. Boyce (1996) Estrogen promotes apoptosis of murine osteoclasts mediated by TGF–β. *Nature medicine*. **2**, 1132-1136.
Högler, W., C. Blimkie, C. Cowell, A. Kemp, J. Briody, P. Wiebe, N. Farpour-Lambert, C. Duncan and H. Woodhead (2003) A comparison of bone geometry and cortical density at the mid-femur between prepuberty and young adulthood using magnetic resonance imaging. *Bone*. **33**, 771-778.
Idris, A. I., E. Landao-Bassonga and S. H. Ralston (2010) The TRPV1 ion channel antagonist capsazepine inhibits osteoclast and osteoblast differentiation in vitro and ovariectomy induced bone loss in vivo. *Bone*. **46**, 1089-1099.
Idris, A. I., J. Rojas, I. R. Greig, R. J. van't Hof and S. H. Ralston (2008) Aminobisphosphonates cause osteoblast apoptosis and inhibit bone nodule formation in vitro. *Calcified tissue international*. **82**, 191-201.
Ignatius, A., P. Schoengraf, L. Kreja, A. Liedert, S. Recknagel, S. Kandert, R. Brenner, M. Schneider, J. Lambris and M. Huber Lang (2011) Complement C3a and C5a modulate osteoclast formation and inflammatory response of osteoblasts in synergism with IL 1ß. *Journal of Cellular Biochemistry*. **112**, 2594-2605.
Ishibashi, O., S. Niwa, K. Kadoyama and T. Inui (2006) MMP-9 antisense oligodeoxynucleotide exerts an inhibitory effect on osteoclastic bone resorption by suppressing cell migration. *Life sciences*. **79**, 1657-1660.
Ishida, N., K. Hayashi, M. Hoshijima, T. Ogawa, S. Koga, Y. Miyatake, M. Kumegawa, T. Kimura and T. Takeya (2002) Large Scale Gene Expression Analysis of Osteoclastogenesisin Vitro and Elucidation of NFAT2 as a Key Regulator. *Journal of Biological Chemistry*. **277**, 41147-41156.
Isogai, Y., T. Akatsu, T. Ishizuya, A. Yamaguchi, M. Hori, N. Takahashi and T. Suda (1996) Parathyroid hormone regulates osteoblast differentiation positively or negatively depending on the differentiation stages. *Journal of Bone and Mineral Research*. **11**, 1384-1393.
Ito, A., B. F. Bebo Jr, A. Matejuk, A. Zamora, M. Silverman, A. Fyfe-Johnson and H. Offner (2001) Estrogen treatment down-regulates TNF-α production and reduces the severity of experimental autoimmune encephalomyelitis in cytokine knockout mice. *The Journal of Immunology*. **167**, 542-552.
Izadpanah, R., C. Trygg, B. Patel, C. Kriedt, J. Dufour, J. M. Gimble and B. A. Bunnell (2006) Biologic properties of mesenchymal stem cells derived from bone marrow and adipose tissue. *Journal of cellular biochemistry*. **99**, 1285-1297.

Janeway, C. A., P. Travers, M. Walport and M. J. Shlomchik (2005) *Immunobiology - The immune system in health and disease*, 6th ed., Garland Science, London

Javazon, E. H., D. C. Colter, E. J. Schwarz and D. J. Prockop (2001) Rat Marrow Stromal Cells are More Sensitive to Plating Density and Expand More Rapidly from Single-Cell-Derived Colonies than Human Marrow Stromal Cells. *Stem cells*. **19**, 219-225.

Jiang, H., E. J. White, C. I. Ríos-Vicil, J. Xu, C. Gomez-Manzano and J. Fueyo (2011) Human adenovirus type 5 induces cell lysis through autophagy and autophagy-triggered caspase activity. *Journal of virology*. **85**, 4720-4729.

Jin, C. H., T. Shinki, M. Hong, T. Sato, A. Yamaguchi, T. Ikeda, S. Yoshiki, E. Abe and T. Suda (1992) 1 alpha, 25-dihydroxyvitamin D3 regulates in vivo production of the third component of complement (C3) in bone. *Endocrinology*. **131**, 2468.

Jones, J. and B. Morgan (1995) Apoptosis is associated with reduced expression of complement regulatory molecules, adhesion molecules and other receptors on polymorphonuclear leucocytes: functional relevance and role in inflammation. *Immunology*. **86**, 651.

Jung, K., M. Lein, C. Laube and R. Lichtinghagen (2001) Blood specimen collection methods influence the concentration and the diagnostic validity of matrix metalloproteinase 9 in blood. *Clinica chimica acta*. **314**, 241-244.

Kacena, M. A., C. M. Gundberg and M. C. Horowitz (2006) A reciprocal regulatory interaction between megakaryocytes, bone cells, and hematopoietic stem cells. *Bone*. **39**, 978-984.

Kamalia, N., C. McCulloch, H. Tenenbaum and H. Limeback (1992) Direct flow cytometric quantification of alkaline phosphatase activity in rat bone marrow stromal cells. *Journal of Histochemistry & Cytochemistry*. **40**, 1059.

Karieb, S. and S. W. Fox (2011) Phytoestrogens directly inhibit TNF-α-induced bone resorption in RAW264. 7 cells by suppressing c-fos-induced NFATc1 expression. *Journal of cellular biochemistry*. **112**, 476-487.

Karsdal, M., D. Leeming, E. Dam, K. Henriksen, P. Alexandersen, P. Pastoureau, R. Altman and C. Christiansen (2008) Should subchondral bone turnover be targeted when treating osteoarthritis? *Osteoarthritis and cartilage*. **16**, 638-646.

Kawamoto, T., C. Fan, R. J. Gaivin, M. A. Levine and S. A. Lietman (2011) Decreased SH3BP2 inhibits osteoclast differentiation and function. *Journal of Orthopaedic Research*.

Keaveny, T. M., E. F. Morgan, G. L. Niebur and O. C. Yeh (2001) Biomechanics of trabecular bone. *Annual review of biomedical engineering*. **3**, 307-333.

Kellgren, J. and J. Lawrence (1957) Radiological assessment of osteo-arthrosis. *Annals of the rheumatic diseases*. **16**, 494-502.

Khouja, H., A. Bevington, G. Kemp and R. Russell (1990) Calcium and orthophosphate deposits in vitro do not imply osteoblast-mediated mineralization: mineralization by betaglycerophosphate in the absence of osteoblasts. *Bone*. **11**, 385-391.

Kim, C., W. Wu, M. Wysoczynski, A. Abdel-Latif, M. Sunkara, A. Morris, M. Kucia, J. Ratajczak and M. Ratajczak (2011) Conditioning for hematopoietic transplantation activates the complement cascade and induces a proteolytic environment in bone marrow: a novel role for bioactive lipids and soluble C5b-C9 as homing factors. *Leukemia*.

Kim, M. S., C. J. Day and N. A. Morrison (2005) MCP-1 is induced by receptor activator of nuclear factor-κB ligand, promotes human osteoclast fusion, and rescues granulocyte macrophage colony-stimulating factor suppression of osteoclast formation. *Journal of Biological Chemistry*. **280**, 16163-16169.

Kim, N., M. Takami, J. Rho, R. Josien and Y. Choi (2002) A novel member of the leukocyte receptor complex regulates osteoclast differentiation. *The Journal of experimental medicine*. **195**, 201.
Kimberley, F., B. Sivasankar and B. Paul Morgan (2007) Alternative roles for CD59. *Mol Immunol*. **44**, 73-81.
Kinoshita, T. (1991) Biology of complement: the overture. *Immunol Today*. **12**, 291-5.
Kitami, S., H. Tanaka, T. Kawato, N. Tanabe, T. Katono-Tani, F. Zhang, N. Suzuki, Y. Yonehara and M. Maeno (2010) IL-17A suppresses the expression of bone resorption-related proteinases and osteoclast differentiation via IL-17RA or IL-17RC receptors in RAW264. 7 cells. *Biochimie*. **92**, 398-404.
Kleiner, D. E. and W. G. Stetlerstevenson (1994) Quantitative zymography: detection of picogram quantities of gelatinases. *Analytical biochemistry*. **218**, 325-329.
Knowles, H. and N. Athanasou (2009) Canonical and non-canonical pathways of osteoclast formation. *Histol Histopathol*. **24**, 337-346.
Kolodecik, T., F. Gorelick and E. Thrower (2009) GENETIC AND PHARMACOLOGIC MANIPULATION OF VACUOLAR ATPASE; EFFECTS ON ZYMOGEN ACTIVATION IN PANCREATIC ACINI. *Open access animal physiology*. **2009**, 1.
Komarova, S. V., M. F. Pilkington, A. F. Weidema, S. J. Dixon and S. M. Sims (2003) RANK ligand-induced elevation of cytosolic Ca2+ accelerates nuclear translocation of nuclear factor κB in osteoclasts. *Journal of Biological Chemistry*. **278**, 8286-8293.
Konttinen, Y. T., A. Ceponis, S. Meri, A. Vuorikoski, P. Kortekangas, T. Sorsa, A. Sukura and S. Santavirta (1996) Complement in acute and chronic arthritides: assessment of C3c, C9, and protectin (CD59) in synovial membrane. *Annals of the rheumatic diseases*. **55**, 888.
Koya, R. C., N. Kasahara, P. Favaro, R. Lau, H. Q. Ta, J. S. Weber and R. Stripecke (2003) Potent maturation of monocyte-derived dendritic cells after CD40L lentiviral gene delivery. *Journal of Immunotherapy*. **26**, 451.
Kudo, O., Y. Fujikawa, I. Itonaga, A. Sabokbar, T. Torisu and N. A. Athanasou (2002) Proinflammatory cytokine (TNFα/IL-1α) induction of human osteoclast formation. *The Journal of pathology*. **198**, 220-227.
Kukita, A., T. Kukita, K. Nagata, J. Teramachi, Y. J. Li, H. Yoshida, H. Miyamoto, S. Gay, F. Pessler and T. Shobuike (2011) The transcription factor FBI-1/OCZF/LRF is expressed in osteoclasts and regulates RANKL-induced osteoclast formation in vitro and in vivo. *Arthritis & Rheumatism*. **63**, 2744-2754.
Kumar, S., G. Mahendra and S. Ponnazhagan (2005) Determination of osteoprogenitor-specific promoter activity in mouse mesenchymal stem cells by recombinant adeno-associated virus transduction. *Biochimica et Biophysica Acta (BBA)-Gene Structure and Expression*. **1731**, 95-103.
Kuroda, R., K. Ishida, T. Matsumoto, T. Akisue, H. Fujioka, K. Mizuno, H. Ohgushi, S. Wakitani and M. Kurosaka (2007) Treatment of a full-thickness articular cartilage defect in the femoral condyle of an athlete with autologous bone-marrow stromal cells. *Osteoarthritis and cartilage*. **15**, 226-231.
Kähäri, V. M. and U. Saarialho-Kere (1997) Matrix metalloproteinases in skin. *Experimental dermatology*. **6**, 199-213.
Köhler, A., K. De Filippo, M. Hasenberg, C. van den Brandt, E. Nye, M. P. Hosking, T. E. Lane, L. Männ, R. M. Ransohoff and A. E. Hauser (2011) G-CSF–mediated thrombopoietin release triggers neutrophil motility and mobilization from bone marrow via induction of Cxcr2 ligands. *Blood*. **117**, 4349.
Laboratory, T. J. (1997) Helicobacter Infections in Laboratory Mice. *JAX Notes*

Lange, C., F. Cakiroglu, A. N. Spiess, H. Cappallo-Obermann, J. Dierlamm and A. R. Zander (2007) Accelerated and safe expansion of human mesenchymal stromal cells in animal serum-free medium for transplantation and regenerative medicine. *Journal of cellular physiology*. **213**, 18-26.

Larsson, T., R. Marsell, E. Schipani, C. Ohlsson, Ö. Ljunggren, H. S. Tenenhouse, H. Jüppner and K. B. Jonsson (2004) Transgenic mice expressing fibroblast growth factor 23 under the control of the α1 (I) collagen promoter exhibit growth retardation, osteomalacia, and disturbed phosphate homeostasis. *Endocrinology*. **145**, 3087-3094.

Lazarenko, O. P., S. O. Rzonca, L. J. Suva and B. Lecka-Czernik (2006) Netoglitazone is a PPAR-gamma ligand with selective effects on bone and fat. *Bone*. **38**, 74-84.

Lecaille, F., D. Brömme and G. Lalmanach (2008) Biochemical properties and regulation of cathepsin K activity. *Biochimie*. **90**, 208-226.

Lehmann, J. M., J. M. Lenhard, B. B. Oliver, G. M. Ringold and S. A. Kliewer (1997) Peroxisome proliferator-activated receptors α and γ are activated by indomethacin and other non-steroidal anti-inflammatory drugs. *Journal of Biological Chemistry*. **272**, 3406-3410.

Lehto, T., E. Honkanen, A. Teppo and S. Meri (1995) Urinary excretion of protectin (CD59), complement SC5b-9 and cytokines in membranous glomerulonephritis. *Kidney Int*. **47**, 1403-11.

Levi, M. and M. Popovtzer (1999) Disorders of phosphate balance. *Atlas of diseases of the kidney. Philadelphia: Currient Medicine*, 7.2-7.14.

Lewiecki, E. M., C. M. Gordon, S. Baim, M. B. Leonard, N. J. Bishop, M. L. Bianchi, H. J. Kalkwarf, C. B. Langman, H. Plotkin and F. Rauch (2008) International Society for Clinical Densitometry 2007 adult and pediatric official positions. *Bone*. **43**, 1115-1121.

Lewis, R. D., M. J. Perry, I. A. Guschina, C. L. Jackson, B. P. Morgan and T. R. Hughes (2011) CD55 Deficiency Protects against Atherosclerosis in ApoE-Deficient Mice via C3a Modulation of Lipid Metabolism. *The American journal of pathology*. **179**, 1601.

Leyva, F. J., J. J. Anzinger, J. P. McCoy and H. S. Kruth (2011) Evaluation of transduction efficiency in macrophage colony-stimulating factor differentiated human macrophages using HIV-1 based lentiviral vectors. *BMC biotechnology*. **11**, 13.

Li, W. A., Z. T. Barry, J. D. Cohen, C. L. Wilder, R. J. Deeds, P. M. Keegan and M. O. Platt (2010) Detection of femtomole quantities of mature cathepsin K with zymography. *Analytical biochemistry*. **401**, 91-98.

Lin, F., D. J. Salant, H. Meyerson, S. Emancipator, B. P. Morgan and M. E. Medof (2004) Respective roles of decay-accelerating factor and CD59 in circumventing glomerular injury in acute nephrotoxic serum nephritis. *The Journal of Immunology*. **172**, 2636.

Lindberg, M., S. Alatalo, J. Halleen, S. Mohan, J. Gustafsson and C. Ohlsson (2001) Estrogen receptor specificity in the regulation of the skeleton in female mice. *Journal of endocrinology*. **171**, 229-236.

Lindhe, J., D. Cecchinato, E. A. Bressan, M. Toia, M. G. Araújo and B. Liljenberg (2012) The alveolar process of the edentulous maxilla in periodontitis and non-periodontitis subjects. *Clinical Oral Implants Research*.

Lloyd, S. A. J., Y. Yuan, P. Kostenuik, M. Ominsky, A. Lau, S. Morony, M. Stolina, F. Asuncion and T. A. Bateman (2008) Soluble RANKL induces high bone turnover and decreases bone volume, density, and strength in mice. *Calcified tissue international*. **82**, 361-372.

Loeser, R. F. (2011) Aging and osteoarthritis. *Current Opinion in Rheumatology*. **23**, 492.

Lombardo, A., P. Genovese, C. M. Beausejour, S. Colleoni, Y. L. Lee, K. A. Kim, D. Ando, F. D. Urnov, C. Galli and P. D. Gregory (2007) Gene editing in human stem cells using zinc finger nucleases and integrase-defective lentiviral vector delivery. *Nature biotechnology*. **25**, 1298-1306.
Longhi, M. P., B. Sivasankar, N. Omidvar, B. P. Morgan and A. Gallimore (2005) Cutting edge: murine CD59a modulates antiviral CD4+ T cell activity in a complement-independent manner. *The Journal of Immunology*. **175**, 7098.
Lorenzo, J., Y. Choi and M. Horowitz (2010) *Osteoimmunology: Interactions of the Immune and Skeletal Systems*, Academic Press
Luo, C., M. Chen, A. Madden and H. Xu (2012) Expression of Complement Components and Regulators by Different Subtypes of Bone Marrow-Derived Macrophages. *Inflammation*, 1-14.
Luo, J., W. Zhou, X. Zhou, D. Li, J. Weng, Z. Yi, S. G. Cho, C. Li, T. Yi and X. Wu (2009) Regulation of bone formation and remodeling by G-protein-coupled receptor 48. *Development*. **136**, 2747-2756.
Lynch, C. C. (2011) Matrix metalloproteinases as master regulators of the vicious cycle of bone metastasis. *Bone*. **48**, 44-53.
Mamane, Y., C. C. Chan, G. Lavallee, N. Morin, L. J. Xu, J. Q. Huang, R. Gordon, W. Thomas, J. Lamb and E. E. Schadt (2009) The C3a anaphylatoxin receptor is a key mediator of insulin resistance and functions by modulating adipose tissue macrophage infiltration and activation. *Diabetes*. **58**, 2006-2017.
Mangham, D., D. Scoones and M. Drayson (1993) Complement and the recruitment of mononuclear osteoclasts. *Journal of clinical pathology*. **46**, 517.
Manni, J. A. and H. J. Müller-Eberhard (1969) The eighth component of human complement (C8): isolation, characterization, and hemolytic efficiency. *The Journal of experimental medicine*. **130**, 1145.
Marcenaro, E., R. Augugliaro, M. Falco, R. Castriconi, S. Parolini, S. Sivori, E. Romeo, R. Millo, L. Moretta and C. Bottino (2003) CD59 is physically and functionally associated with natural cytotoxicity receptors and activates human NK cell-mediated cytotoxicity. *European journal of immunology*. **33**, 3367-3376.
Marie, P. (2009) Bone cell–matrix protein interactions. *Osteoporosis international*. **20**, 1037-1042.
Marr, R. A., E. Rockenstein, A. Mukherjee, M. S. Kindy, L. B. Hersh, F. H. Gage, I. M. Verma and E. Masliah (2003) Neprilysin gene transfer reduces human amyloid pathology in transgenic mice. *The Journal of neuroscience*. **23**, 1992-1996.
Martin, M., A. Gottsäter, P. M. Nilsson, T. E. Mollnes, B. Lindblad and A. M. Blom (2009) Complement activation and plasma levels of C4b-binding protein in critical limb ischemia patients. *Journal of Vascular Surgery*. **50**, 100-106.
Matsuo, K. and N. Irie (2008) Osteoclast–osteoblast communication. *Archives of biochemistry and biophysics*. **473**, 201-209.
McLaren, J. E., C. J. Calder, B. P. McSharry, K. Sexton, R. C. Salter, N. N. Singh, G. W. G. Wilkinson, E. C. Y. Wang and D. P. Ramji (2010) The TNF-Like Protein 1A–Death Receptor 3 Pathway Promotes Macrophage Foam Cell Formation In Vitro. *The Journal of Immunology*. **184**, 5827.
Mead, R. J., J. W. Neal, M. R. Griffiths, C. Linington, M. Botto, H. Lassmann and B. P. Morgan (2003) Deficiency of the complement regulator CD59a enhances disease severity, demyelination and axonal injury in murine acute experimental allergic encephalomyelitis. *Laboratory investigation*. **84**, 21-28.
Medof, M., A. Gottlieb, T. Kinoshita, S. Hall, R. Silber, V. Nussenzweig and W. Rosse (1987) Relationship between decay accelerating factor deficiency, diminished acetylcholinesterase activity, and defective terminal complement

pathway restriction in paroxysmal nocturnal hemoglobinuria erythrocytes. *J Clin Invest*. **80**, 165-74.
Meri, S. and H. Jarva (1998) Complement regulation. *Vox sanguinis*. **74**, 291-302.
Meri, S., B. Morgan, A. Davies, R. Daniels, M. Olavesen, H. Waldmann and P. Lachmann (1990) Human protectin (CD59), an 18,000-20,000 MW complement lysis restricting factor, inhibits C5b-8 catalysed insertion of C9 into lipid bilayers. *Immunology*. **71**, 1-9.
Meri, S., H. Waldmann and P. Lachmann (1991) Distribution of protectin (CD59), a complement membrane attack inhibitor, in normal human tissues. *Lab Invest*. **65**, 532-7.
Michou, L. and J. P. Brown (2011) Genetics of bone diseases: Paget's disease, fibrous dysplasia, osteopetrosis, and osteogenesis imperfecta. *Joint Bone Spine*. **78**, 252-258.
Miller, L. M., W. Little, A. Schirmer, F. Sheik, B. Busa and S. Judex (2007) Accretion of bone quantity and quality in the developing mouse skeleton. *Journal of Bone and Mineral Research*. **22**, 1037-1045.
Minamitani, T., D. Iwakiri and K. Takada (2011) Adenovirus virus-associated RNAs induce type I interferon expression through a RIG-I-mediated pathway. *Journal of Virology*. **85**, 4035-4040.
Misso, M., K. Hewitt, W. Boon, Y. Murata, M. Jones and E. Simpson (2005) Cholesterol feeding prevents adiposity in the obese female aromatase knockout (ArKO) mouse. *Hormone and metabolic research*. **37**, 26-31.
Mittal, V. (2004) Improving the efficiency of RNA interference in mammals. *Nature reviews genetics*. **5**, 355-365.
Mizuno, M. and B. P. Morgan (2011) An Update on the Roles of the Complement System in Autoimmune Diseases and the Therapeutic Possibilities of Anti-Complement Agents. *Current Drug Therapy*. **6**, 35-50.
Mizuno, M., K. Nishikawa, R. M. Goodfellow, S. J. Piddlesden, B. P. Morgan and S. Matsuo (1997) The effects of functional suppression of a membrane-bound complement regulatory protein, CD59, in the synovial tissue in rats. *Arthritis & Rheumatism*. **40**, 527-533.
Moerman, E. J., K. Teng, D. A. Lipschitz and B. Lecka-Czernik (2004) Aging activates adipogenic and suppresses osteogenic programs in mesenchymal marrow stroma/stem cells: the role of PPAR-γ2 transcription factor and TGF-β/BMP signaling pathways. *Aging cell*. **3**, 379-389.
Mohan, S., C. Richman, R. Guo, Y. Amaar, L. R. Donahue, J. Wergedal and D. J. Baylink (2003) Insulin-like growth factor regulates peak bone mineral density in mice by both growth hormone-dependent and-independent mechanisms. *Endocrinology*. **144**, 929-936.
Moll, G., R. Jitschin, L. von Bahr, I. Rasmusson-Duprez, B. Sundberg, L. Lönnies, G. Elgue, K. Nilsson-Ekdahl, D. Mougiakakos and J. D. Lambris (2011) Mesenchymal stromal cells engage complement and complement receptor bearing innate effector cells to modulate immune responses. *PloS one*. **6**, e21703.
Monleon, I., M. J. Martínez-Lorenzo, A. Anel, P. Lasierra, L. Larrad, A. Piñeiro, J. Naval and M. A. Alava (2000) CD59 cross-linking induces secretion of APO2 ligand in overactivated human T cells. *European Journal of Immunology*. **30**, 1078-1087.
Morgan, B., J. Chamberlain-Banoub, J. Neal, W. Song, M. Mizuno and C. Harris (2006) The membrane attack pathway of complement drives pathology in passively induced experimental autoimmune myasthenia gravis in mice. *Clinical & Experimental Immunology*. **146**, 294-302.
Morgan, B. P. (1990) *Complement Clinical Aspects and Relevance to Disease*, Academic Press, London

Morgan, B. P. and C. L. Harris (1999) *Complement Regulatory Proteins*, Academic Press, London
Morley, B. J. and M. J. Walport (2000) *The Complement FactsBook*, Academic Press, London
Morriss-Kay, G., S. Iseki and D. Johnson (2001) The Molecular Basis of Skeletogenesis, Wiley, Chichester, UK
Murphy, K. and K. Campellone (2003) Lambda Red-mediated recombinogenic engineering of enterohemorrhagic and enteropathogenic E. coli. *BMC Molecular Biology*. **4**, 11.
Muto, A., T. Mizoguchi, N. Udagawa, S. Ito, I. Kawahara, Y. Abiko, A. Arai, S. Harada, Y. Kobayashi and Y. Nakamichi (2011) Lineage-committed osteoclast precursors circulate in blood and settle down into bone. *Journal of Bone and Mineral Research*.
Müller-Eberhard, H. (1988) Molecular organization and function of the complement system. *Annu Rev Biochem*. **57**, 321-47.
Nakashima, K., X. Zhou, G. Kunkel, Z. Zhang, J. M. Deng, R. R. Behringer and B. de Crombrugghe (2002) The novel zinc finger-containing transcription factor osterix is required for osteoblast differentiation and bone formation. *Cell*. **108**, 17-29.
Naldini, L., U. Blömer, P. Gallay, D. Ory, R. Mulligan, F. H. Gage, I. M. Verma and D. Trono (1996) In vivo gene delivery and stable transduction of nondividing cells by a lentiviral vector. *Science*. **272**, 263-267.
Nangaku, M., C. E. Alpers, J. Pippin, S. J. Shankland, K. Kurokawa, S. Adler, B. Morgan, R. J. Johnson and W. G. Couser (1998) CD59 protects glomerular endothelial cells from immune-mediated thrombotic microangiopathy in rats. *Journal of the American Society of Nephrology*. **9**, 590-597.
Negishi-Koga, T. and H. Takayanagi (2009) Ca2+-NFATc1 signaling is an essential axis of osteoclast differentiation. *Immunological reviews*. **231**, 241-256.
NHS-Choices (2010a) Rheumatoid Arthritis Treatment, Directgov
NHS-Choices (2010b) Treating Osteoarthritis, Directgov
Nicholson, G., M. Malakellis, F. Collier, P. Cameron, W. Holloway, T. Gough, C. Gregorio-King, M. Kirkland and D. Myers (2000) Induction of osteoclasts from CD14-positive human peripheral blood mononuclear cells by receptor activator of nuclear factor kappaB ligand (RANKL). *Clin Sci (Lond)*. **99**, 133-40.
Nilsson, K. E., M. Andrén, T. D. de Ståhl and S. Kleinau (2009) Enhanced susceptibility to low-dose collagen-induced arthritis in CR1/2-deficient female mice—possible role of estrogen on CR1 expression. *The FASEB Journal*. **23**, 2450-2458.
Nilsson, U. R. and H. J. Müller-Eberhard (1965) Isolation of ß1F-globulin from human serum and its characterization as the fifth component of complement. *The Journal of experimental medicine*. **122**, 277.
Nimura, A., T. Muneta, K. Otabe, H. Koga, Y. J. Ju, T. Mochizuki, K. Suzuki and I. Sekiya (2010) Analysis of human synovial and bone marrow mesenchymal stem cells in relation to heat-inactivation of autologous and fetal bovine serums. *BMC Musculoskeletal Disorders*. **11**, 208.
Novakofski, J. (2004) Adipogenesis: usefulness of in vitro and in vivo experimental models. *Journal of animal science*. **82**, 905-915.
Oka, Y., S. Iwai, H. Amano, Y. Irie, K. Yatomi, K. Ryu, S. Yamada, K. Inagaki and K. Oguchi (2012) Tea Polyphenols Inhibit Rat Osteoclast Formation and Differentiation. *Journal of Pharmacological Sciences*. **118**, 55-64.
Okamoto, M., J. Murai, Y. Imai, D. Ikegami, N. Kamiya, S. Kato, Y. Mishina, H. Yoshikawa and N. Tsumaki (2011) Conditional deletion of Bmpr1a in differentiated osteoclasts increases osteoblastic bone formation, increasing

volume of remodeling bone in mice. *Journal of Bone and Mineral Research*. **26**, 2511-2522.
Olkku, A. and A. Mahonen (2009) Calreticulin mediated glucocorticoid receptor export is involved in [beta]-catenin translocation and Wnt signalling inhibition in human osteoblastic cells. *Bone*. **44**, 555-565.
Omidvar, N., E. C. Y. Wang, P. Brennan, M. P. Longhi, R. A. G. Smith and B. P. Morgan (2006) Expression of glycosylphosphatidylinositol-anchored CD59 on target cells enhances human NK cell-mediated cytotoxicity. *The Journal of Immunology*. **176**, 2915.
Onan, D., E. H. Allan, J. M. W. Quinn, J. H. Gooi, S. Pompolo, N. A. Sims, M. T. Gillespie and T. J. Martin (2009) The chemokine Cxcl1 is a novel target gene of parathyroid hormone (PTH)/PTH-related protein in committed osteoblasts. *Endocrinology*. **150**, 2244-2253.
Otero, J. E., S. Dai, M. A. Alhawagri, I. Darwech and Y. Abu-Amer (2010) IKKβ activation is sufficient for RANK-independent osteoclast differentiation and osteolysis. *Journal of bone and mineral research*. **25**, 1282-1294.
Otto, F., A. P. Thornell, T. Crompton, A. Denzel, K. C. Gilmour, I. R. Rosewell, G. W. H. Stamp, R. S. P. Beddington, S. Mundlos and B. R. Olsen (1997) < i> Cbfa1</i>, a Candidate Gene for Cleidocranial Dysplasia Syndrome, Is Essential for Osteoblast Differentiation and Bone Development. *Cell*. **89**, 765-771.
Paessler, S., R. Z. Fayzulin, M. Anishchenko, I. P. Greene, S. C. Weaver and I. Frolov (2003) Recombinant Sindbis/Venezuelan equine encephalitis virus is highly attenuated and immunogenic. *Journal of virology*. **77**, 9278-9286.
Park-Min, K. H., J. D. Ji, T. Antoniv, A. C. Reid, R. B. Silver, M. B. Humphrey, M. Nakamura and L. B. Ivashkiv (2009) IL-10 suppresses calcium-mediated costimulation of receptor activator NF-κB signaling during human osteoclast differentiation by inhibiting TREM-2 expression. *The Journal of Immunology*. **183**, 2444-2455.
Peer, W. (2011) Plasma Membrane Protein Trafficking. *The Plant Plasma Membrane*, 31-56.
Pelch, K. E., S. M. Carleton, C. L. Phillips and S. C. Nagel (2011) Developmental Exposure to Low Dose Xenoestrogens Alters Femur Length and Tensile Strength in Adult Mice. *Biology of Reproduction*.
Peng, T., L. Hao, J. A. Madri, X. Su, J. A. Elias, G. L. Stahl, S. Squinto and Y. Wang (2005) Role of C5 in the development of airway inflammation, airway hyperresponsiveness, and ongoing airway response. *J Clin Invest*. **115**, 1590-1600.
Perez, J. T., A. Varble, R. Sachidanandam, I. Zlatev, M. Manoharan, A. García-Sastre and B. R. tenOever (2010) Influenza A virus-generated small RNAs regulate the switch from transcription to replication. *Proceedings of the National Academy of Sciences*. **107**, 11525.
Peter, S. J., C. R. Liang, D. J. Kim, M. S. Widmer and A. G. Mikos (1998) Osteoblastic phenotype of rat marrow stromal cells cultured in the presence of dexamethasone, β-glycerolphosphate, and L-ascorbic acid. *Journal of cellular biochemistry*. **71**, 55-62.
Philip, B. K., P. J. Childress, A. G. Robling, A. Heller, P. P. Nawroth, A. Bierhaus and J. P. Bidwell (2010) RAGE supports parathyroid hormone-induced gains in femoral trabecular bone. *American Journal of Physiology-Endocrinology And Metabolism*. **298**, E714-E725.
Picanço-C, V., R. C. E. M. de Sousa and D. Covas (2012) Advances in Lentiviral Vectors: A Patent Review. *Recent patents on DNA & gene sequences*.
Piccoli, A. K., A. P. Alegretti, L. Schneider, P. S. Lora and R. M. Xavier (2011) Expression of complement regulatory proteins CD55, CD59, CD35, and

CD46 in rheumatoid arthritis. *Revista Brasileira de Reumatologia*. **51**, 503-510.
Pobanz, J. M., R. A. Reinhardt, S. Koka and S. D. Sanderson (2000) C5a modulation of interleukin 1 induced interleukin 6 production by human osteoblast like cells. *Journal of periodontal research*. **35**, 137-145.
Potts, W., J. Bowyer, H. Jones, D. Tucker, A. J. Freemont, A. Millest, C. Martin, W. Vernon, D. Neerunjun and G. Slynn (2004) Cathepsin L-deficient mice exhibit abnormal skin and bone development and show increased resistance to osteoporosis following ovariectomy. *International journal of experimental pathology*. **85**, 85-96.
Price, C., B. C. Herman, T. Lufkin, H. M. Goldman and K. J. Jepsen (2005) Genetic variation in bone growth patterns defines adult mouse bone fragility. *Journal of Bone and Mineral Research*. **20**, 1983-1991.
Proff, P. and P. Römer (2009) The molecular mechanism behind bone remodelling: a review. *Clinical oral investigations*. **13**, 355-362.
Purpura, K. A., J. E. Aubin and P. W. Zandstra (2004) Sustained in vitro expansion of bone progenitors is cell density dependent. *Stem Cells*. **22**, 39-50.
Qiagen (2002) Effectene Transfection Reagent Handbook, Qiagen
Qin, X., A. Goldfine, N. Krumrei, L. Grubissich, J. Acosta, M. Chorev, A. Hays and J. Halperin (2004) Glycation inactivation of the complement regulatory protein CD59: a possible role in the pathogenesis of the vascular complications of human diabetes. *Diabetes*. **53**, 2653-61.
Qiu, P., E. F. Simonds, S. C. Bendall, K. D. Gibbs Jr, R. V. Bruggner, M. D. Linderman, K. Sachs, G. P. Nolan and S. K. Plevritis (2011) Extracting a cellular hierarchy from high-dimensional cytometry data with SPADE. *Nature biotechnology*.
Raisz, L. (1999) Physiology and pathophysiology of bone remodeling. *Clin Chem*. **45**, 1353-8.
Rajalin, A. M., H. Pollock and P. Aarnisalo (2010) ERRα regulates osteoblastic and adipogenic differentiation of mouse bone marrow mesenchymal stem cells. *Biochemical and biophysical research communications*. **396**, 477-482.
Ramaglia, V., R. H. M. King, B. P. Morgan and F. Baas (2009) Deficiency of the complement regulator CD59a exacerbates Wallerian degeneration. *Molecular immunology*. **46**, 1892-1896.
Rao, D. D., J. S. Vorhies, N. Senzer and J. Nemunaitis (2009) siRNA vs. shRNA: similarities and differences. *Advanced drug delivery reviews*. **61**, 746-759.
Rasmusson, I., O. Ringdén, B. Sundberg and K. Le Blanc (2005) Mesenchymal stem cells inhibit lymphocyte proliferation by mitogens and alloantigens by different mechanisms. *Experimental cell research*. **305**, 33-41.
Rauch, F. (2005) Bone growth in length and width: the Yin and Yang of bone stability. *Journal of Musculoskeletal and Neuronal Interactions*. **5**, 194.
Recker, R. R., L. G. Ste-Marie, B. Langdahl, D. Masanauskaite, D. Ethgen and P. D. Delmas (2009) Oral ibandronate preserves trabecular microarchitecture: micro-computed tomography findings from the oral ibandronate osteoporosis vertebral fracture trial in North America and Europe study. *Journal of Clinical Densitometry*. **12**, 71-76.
Reid, K. B. M. and R. R. Porter (1981) The proteolytic activation systems of complement. *Annual review of biochemistry*. **50**, 433-464.
Reynolds, J. (1996) Collagenases and tissue inhibitors of metalloproteinases: a functional balance in tissue degradation. *Oral diseases*. **2**, 70-76.
Riikonen, T., J. Westermarck, L. Koivisto, A. Broberg, V. M. Kähäri and J. Heino (1995) Integrin α2β1 is a positive regulator of collagenase (MMP-1) and collagen α1 (I) gene expression. *Journal of Biological Chemistry*. **270**, 13548-13552.

Ripoll, C. and B. Bunnell (2009) Comparative characterization of mesenchymal stem cells from eGFP transgenic and non-transgenic mice. *BMC cell biology*. **10**, 3.

Ritchlin, C. T., S. A. Haas-Smith, P. Li, D. G. Hicks and E. M. Schwarz (2003) Mechanisms of TNF-alpha-and RANKL-mediated osteoclastogenesis and bone resorption in psoriatic arthritis. *Journal of Clinical Investigation*. **111**, 821-832.

Rodan, G. A. and T. J. Martin (2000) Therapeutic approaches to bone diseases. *Science*. **289**, 1508.

Roman-Roman, S., T. Garcia, A. Jackson, J. Theilhaber, G. Rawadi, T. Connolly, S. Spinella-Jaegle, S. Kawai, B. Courtois and S. Bushnell (2003) Identification of genes regulated during osteoblastic differentiation by genome-wide expression analysis of mouse calvaria primary osteoblasts in vitro. *Bone*. **32**, 474-482.

Rosen, C. J. (2008) *Primer on the metabolic bone diseases and disorders of mineral metabolism*, Wiley

Rouas, R., R. Uch, Y. Cleuter, F. Jordier, C. Bagnis, P. Mannoni, P. Lewalle, P. Martiat and A. Van den Broeke (2002) Lentiviral-mediated gene delivery in human monocyte-derived dendritic cells: optimized design and procedures for highly efficient transduction compatible with clinical constraints. *Cancer gene therapy*. **9**, 715-724.

Rowling, M. J., C. Gliniak, J. E. Welsh and J. C. Fleet (2007) High dietary vitamin D prevents hypocalcemia and osteomalacia in CYP27B1 knockout mice. *The Journal of nutrition*. **137**, 2608-2615.

Rubin, J., Z. Schwartz, B. D. Boyan, X. Fan, N. Case, B. Sen, M. Drab, D. Smith, M. Aleman and K. L. Wong (2007) Caveolin-1 Knockout Mice Have Increased Bone Size and Stiffness. *Journal of Bone and Mineral Research*. **22**, 1408-1418.

Ruiz-Argüelles, A. and L. Llorente (2007) The role of complement regulatory proteins (CD55 and CD59) in the pathogenesis of autoimmune hemocytopenias. *Autoimmun Rev*. **6**, 155-61.

Saluja, S., S. Bhandari, S. Aggarwal and S. Kapoor (2009) Osteopetrosis: A rare cause of anemia-Review of literature. *Indian Journal of Pathology and Microbiology*. **52**, 363.

Samanna, V., T. Ma, T. Mak, M. Rogers and M. Chellaiah (2007) Actin polymerization modulates CD44 surface expression, MMP-9 activation, and osteoclast function. *Journal of cellular physiology*. **213**, 710-720.

Sanchez-Corral, P., O. Criado Garcia and S. Rodriguez de Cordoba (1995) Isoforms of human C4b-binding protein. I. Molecular basis for the C4BP isoform pattern and its variations in human plasma. *The Journal of Immunology*. **155**, 4030.

Sarma, K. V. R. (2009) Micronutrients–an essential aid to daily growth in children. *Indian Pediatrics*. **46**, S12-S19.

Sato, T., E. Abe, C. H. Jin, M. Hong, T. Katagiri, T. Kinoshita, N. Amizuka, H. Ozawa and T. Suda (1993) The biological roles of the third component of complement in osteoclast formation. *Endocrinology*. **133**, 397.

Sato, T., M. H. Hong, C. H. Jin, Y. Ishimi, N. Udagawa, T. Shinki, E. Abe and T. Suda (1991) The specific production of the third component of complement by osteoblastic cells treated with 1 [alpha], 25-dihydroxyvitamin D3. *FEBS letters*. **285**, 21-24.

Schambach, A., M. Galla, U. Modlich, E. Will, S. Chandra, L. Reeves, M. Colbert, D. A. Williams, C. von Kalle and C. Baum (2006) Lentiviral vectors pseudotyped with murine ecotropic envelope: increased biosafety and convenience in preclinical research. *Experimental hematology*. **34**, 588-592.

Scheller, E. L., J. Song, M. I. Dishowitz, F. N. Soki, K. D. Hankenson and P. H. Krebsbach (2010) Leptin functions peripherally to regulate differentiation of mesenchymal progenitor cells. *Stem Cells*. **28**, 1071-1080.
Scherer, L. J. and J. J. Rossi (2003) Approaches for the sequence-specific knockdown of mRNA. *Nature biotechnology*. **21**, 1457-1465.
Schiessl, H., H. Frost and W. Jee (1998) Estrogen and bone-muscle strength and mass relationships. *Bone*. **22**, 1-6.
Schmid, D., M. Pypaert and C. Münz (2007) Antigen-loading compartments for major histocompatibility complex class II molecules continuously receive input from autophagosomes. *Immunity*. **26**, 79-92.
Schüler, Y., C. Lee-Thedieck, K. Geiger, T. Kaiser, Y. Ino, W. K. Aicher and G. Klein (2012) Osteoblast-secreted factors enhance the expression of dysadherin and CCL2-dependent migration of renal carcinoma cells. *International Journal of Cancer*.
Scutt, A., L. Reading, N. Scutt and K. Still (2003) Mineralizing fibroblast-colony-forming assays. *Methods in Molecular Medicine*. **80**, 29-40.
Seeman, E. (2007) Is a change in bone mineral density a sensitive and specific surrogate of anti-fracture efficacy? *Bone*. **41**, 308-317.
Seeman, E. and P. D. Delmas (2006) Bone quality—the material and structural basis of bone strength and fragility. *New England Journal of Medicine*. **354**, 2250-2261.
Shevde, N. K., A. C. Bendixen, K. M. Dienger and J. Pike (2000) Estrogens suppress RANK ligand-induced osteoclast differentiation via a stromal cell independent mechanism involving c-Jun repression. *Proceedings of the National Academy of Sciences*. **97**, 7829.
Shih, M. S. and R. Norrdin (1986) PGE2 induces regional remodeling changes in haversian envelope: a histomorphometric study of fractured ribs in beagles. *Bone and mineral*. **1**, 227.
Shin, C. S., S. J. Her, J. A. Kim, D. H. Kim, S. W. Kim, S. Y. Kim, H. S. Kim, K. H. Park, J. G. Kim and R. Kitazawa (2005) Dominant Negative N-Cadherin Inhibits Osteoclast Differentiation by Interfering With β-Catenin Regulation of RANKL, Independent of Cell-Cell Adhesion. *Journal of Bone and Mineral Research*. **20**, 2200-2212.
Shockley, K. R., O. P. Lazarenko, P. J. Czernik, C. J. Rosen, G. A. Churchill and B. Lecka-Czernik (2009) PPARγ2 nuclear receptor controls multiple regulatory pathways of osteoblast differentiation from marrow mesenchymal stem cells. *Journal of cellular biochemistry*. **106**, 232-246.
Short, B., N. Brouard, T. Occhiodoro-Scott, A. Ramakrishnan and P. J. Simmons (2003) Mesenchymal stem cells. *Archives of medical research*. **34**, 565-571.
Siemionow, M. Z. (2006) *Tissue Surgery*, illustrated ed., Springer, London
Sigma-Aldrich (2010) Cell Quantification Sigma-Aldrich.com
Sivasankar, B., M. P. Longhi, K. M. E. Gallagher, G. J. Betts, B. P. Morgan, A. J. Godkin and A. M. Gallimore (2009) CD59 blockade enhances antigen-specific CD4+ T cell responses in humans: a new target for cancer immunotherapy? *The Journal of Immunology*. **182**, 5203.
Skyscan (2009) Morphometric Parameters in CT-Analyser
Slemenda, C. W., M. Peacock, S. Hui, L. Zhou and C. C. Johnston (1997) Reduced rates of skeletal remodeling are associated with increased bone mineral density during the development of peak skeletal mass. *Journal of Bone and Mineral Research*. **12**, 676-682.
Solomon, S., C. Kolb, S. Mohanty, E. Jeisy-Walder, R. Preyer, V. Schöllhorn and H. Illges (2002) Transmission of antibody-induced arthritis is independent of complement component 4 (C4) and the complement receptors 1 and 2 (CD21/35). *European journal of immunology*. **32**, 644-651.

Song, I., J. H. Kim, K. Kim, H. M. Jin, B. U. Youn and N. Kim (2009) Regulatory mechanism of NFATc1 in RANKL-induced osteoclast activation. *FEBS letters*. **583**, 2435-2440.
Spondylitis-Association-of-America (2011) MEDICATIONS USED TO TREAT ANKYLOSING SPONDYLITIS
AND RELATED DISEASES
Stanton, R. (2008) The AdZ adenovirus cloning system
Stenderup, K., J. Justesen, E. F. Eriksen, S. I. S. Rattan and M. Kassem (2001) Number and proliferative capacity of osteogenic stem cells are maintained during aging and in patients with osteoporosis. *Journal of Bone and Mineral Research*. **16**, 1120-1129.
Still, K. and A. Scutt (2001) Stimulation of CFU-f formation by prostaglandin E2 is mediated in part by its degradation product, prostaglandin A2. *Prostaglandins &Other Lipid Mediators*. **65**, 21-31.
Stolzing, A., E. Jones, D. McGonagle and A. Scutt (2008) Age-related changes in human bone marrow-derived mesenchymal stem cells: consequences for cell therapies. *Mechanisms of ageing and development*. **129**, 163-173.
Sundaram, K., R. Nishimura, J. Senn, R. F. Youssef, S. D. London and S. V. Reddy (2007) RANK ligand signaling modulates the matrix metalloproteinase-9 gene expression during osteoclast differentiation. *Experimental cell research*. **313**, 168-178.
Suva, L. J. (2006) PTH Expression, Not Always where You Think…. *Journal of Clinical Endocrinology & Metabolism*. **91**, 396.
Swartz, J. D. and L. A. Loevner (2008) *Imaging of the temporal bone*, Thieme Medical Pub
Szulc, J., M. Wiznerowicz, M. O. Sauvain, D. Trono and P. Aebischer (2006) A versatile tool for conditional gene expression and knockdown. *Nature methods*. **3**, 109-116.
Takahashi, N., N. Udagawa, S. Tanaka and T. Suda (2003) Generating murine osteoclasts from bone marrow. *Methods in molecular medicine*. **80**, 129-144.
Takahashi, S., S. Goldring, M. Katz, S. Hilsenbeck, R. Williams and G. Roodman (1995) Downregulation of calcitonin receptor mRNA expression by calcitonin during human osteoclast-like cell differentiation. *Journal of Clinical Investigation*. **95**, 167.
Take, I., Y. Kobayashi, Y. Yamamoto, H. Tsuboi, T. Ochi, S. Uematsu, N. Okafuji, S. Kurihara, N. Udagawa and N. Takahashi (2005) Prostaglandin E2 strongly inhibits human osteoclast formation. *Endocrinology*. **146**, 5204.
Talmage, D. W. (1957) Allergy and immunology. *Annual review of medicine*. **8**, 239-256.
Tanaka, S., T. Takahashi, H. Takayanagi, T. Miyazaki, H. Oda, K. Nakamura, H. Hirai and T. Kurokawa (1998) Modulation of Osteoclast Function by Adenovirus Vector-Induced Epidermal Growth Factor Receptor. *Journal of Bone and Mineral Research*. **13**, 1714-1720.
Teitelbaum, S. (2004) RANKing c-Jun in osteoclast development. *Journal of Clinical Investigation*. **114**, 463-465.
Teplyuk, N. M., Y. Zhang, Y. Lou, J. R. Hawse, M. Q. Hassan, V. I. Teplyuk, J. Pratap, M. Galindo, J. L. Stein and G. S. Stein (2009) The osteogenic transcription factor runx2 controls genes involved in sterol/steroid metabolism, including CYP11A1 in osteoblasts. *Molecular Endocrinology*. **23**, 849-861.
Terpos, E., M. Samarkos, C. Meletis, E. Apostolidou, M. Tsironi, K. Korovesis, D. Mavrogianni, N. Viniou and J. Meletis (2003) Unusual association between increased bone resorption and presence of paroxysmal nocturnal hemoglobinuria phenotype in multiple myeloma. *Int J Hematol*. **78**, 344-8.
The-Psoriasis-Association Treatments for Psoriatic Arthritis

Tian, X., R. Fu and L. Deng (2007) Method and conditions of isolation and proliferation of multipotent mesenchymal stem cells]. *Zhongguo xiu fu chong jian wai ke za zhi= Zhongguo xiufu chongjian waike zazhi= Chinese journal of reparative and reconstructive surgery*. **21**, 81.

Till, J. E. and E. A. McCulloch (1961) A direct measurement of the radiation sensitivity of normal mouse bone marrow cells. *Radiation research*. **14**, 213-222.

Tommasini, S. M., P. Nasser, M. B. Schaffler and K. J. Jepsen (2005) Relationship between bone morphology and bone quality in male tibias: implications for stress fracture risk. *Journal of Bone and Mineral Research*. **20**, 1372-1380.

Trentz, O., D. Arikketh, V. Sentilnathan, S. Hemmi, A. Handschin, B. de Rosario, P. Mohandas and P. V. A. Mohandas (2010) Surface proteins and osteoblast markers: characterization of human adipose tissue-derived osteogenic cells. *European Journal of Trauma and Emergency Surgery*. **36**, 457-463.

Trinchieri, G., M. Kobayashi, M. Rosen, R. Loudon, M. Murphy and B. Perussia (1986) Tumor necrosis factor and lymphotoxin induce differentiation of human myeloid cell lines in synergy with immune interferon. *The Journal of experimental medicine*. **164**, 1206.

Triolo, G., A. Accardo-Palumbo, L. Salli, F. Ciccia, A. Ferrante, L. Tedesco, S. Salli, E. Giardina, A. Pappalardo and G. Licata (2003) Impaired expression of erythrocyte glycosyl-phosphatidylinositol-anchored membrane CD59 in patients with psoriatic arthritis. Relation to terminal complement pathway activation. *Clinical and experimental rheumatology*. **21**, 225-228.

Tropel, P., D. Noël, N. Platet, P. Legrand, A. L. Benabid and F. Berger (2004) Isolation and characterisation of mesenchymal stem cells from adult mouse bone marrow. *Experimental cell research*. **295**, 395-406.

Tu, Z., H. Bu, J. E. Dennis and F. Lin (2010) Efficient osteoclast differentiation requires local complement activation. *Blood*. **116**, 4456.

Turner, C. H., Y. F. Hsieh, R. Müller, M. L. Bouxsein, D. J. Baylink, C. J. Rosen, M. D. Grynpas, L. R. Donahue and W. G. Beamer (2000) Genetic regulation of cortical and trabecular bone strength and microstructure in inbred strains of mice. *Journal of Bone and Mineral Research*. **15**, 1126-1131.

Uaesoontrachoon, K., H. J. Yoo, E. M. Tudor, R. N. Pike, E. J. Mackie and C. N. Pagel (2008) Osteopontin and skeletal muscle myoblasts: Association with muscle regeneration and regulation of myoblast function< i> in vitro</i>. *The international journal of biochemistry & cell biology*. **40**, 2303-2314.

Uveges, T. E., K. M. Kozloff, J. M. Ty, F. Ledgard, C. L. Raggio, G. Gronowicz, S. A. Goldstein and J. C. Marini (2009) Alendronate treatment of the brtl osteogenesis imperfecta mouse improves femoral geometry and load response before fracture but decreases predicted material properties and has detrimental effects on osteoblasts and bone formation. *Journal of Bone and Mineral Research*. **24**, 849-859.

van't Hof, R. J. (2012) Analysis of bone architecture in rodents using microcomputed tomography. *Methods in molecular biology (Clifton, NJ)*. **816**, 461.

Vidal, M. A., G. E. Kilroy, M. J. Lopez, J. R. Johnson, R. M. Moore and J. M. Gimble (2007) Characterization of Equine Adipose Tissue-Derived Stromal Cells: Adipogenic and Osteogenic Capacity and Comparison with Bone Marrow-Derived Mesenchymal Stromal Cells. *Veterinary Surgery*. **36**, 613-622.

Visse, R. and H. Nagase (2003) Matrix metalloproteinases and tissue inhibitors of metalloproteinases. *Circulation research*. **92**, 827-839.

Wada, T., T. Nakashima, A. J. Oliveira-dos-Santos, J. Gasser, H. Hara, G. Schett and J. M. Penninger (2005) The molecular scaffold Gab2 is a crucial component of RANK signaling and osteoclastogenesis. *Nature medicine*. **11**, 394-399.

Walport, M. (2001) Complement. First of two parts. *N Engl J Med*. **344**, 1058-66.
Wang, Q., A. L. Rozelle, C. M. Lepus, C. R. Scanzello, J. J. Song, D. M. Larsen, J. F. Crish, G. Bebek, S. Y. Ritter and T. M. Lindstrom (2011) Identification of a central role for complement in osteoarthritis. *Nature Medicine*.
Wang, Y., J. Kristan, L. Hao, C. S. Lenkoski, Y. Shen and L. A. Matis (2000) A role for complement in antibody-mediated inflammation: C5-deficient DBA/1 mice are resistant to collagen-induced arthritis. *The Journal of Immunology*. **164**, 4340.
Watkins, M. P., J. Y. Norris, S. K. Grimston, X. Zhang, R. J. Phipps, F. H. Ebetino and R. Civitelli (2012) Bisphosphonates improve trabecular bone mass and normalize cortical thickness in ovariectomized, osteoblast connexin43 deficient mice. *Bone*.
Watson, S. L., H. Marcal, M. Sarris, N. Di Girolamo, M. Coroneo and D. Wakefield (2010) The effect of mesenchymal stem cell conditioned media on corneal stromal fibroblast wound healing activities. *British Journal of Ophthalmology*. **94**, 1067.
Wehrli, F. W. (2007) Structural and functional assessment of trabecular and cortical bone by micro magnetic resonance imaging. *Journal of Magnetic Resonance Imaging*. **25**, 390-409.
Williams, A., M. Mizuno, P. Richards, D. Holt and B. Morgan (2004) Deletion of the gene encoding CD59a in mice increases disease severity in a murine model of rheumatoid arthritis. *Arthritis Rheum*. **50**, 3035-44.
Wilson, S. R., C. Peters, P. Saftig and D. Brömme (2009) Cathepsin K activity-dependent regulation of osteoclast actin ring formation and bone resorption. *Journal of Biological Chemistry*. **284**, 2584-2592.
Wink, C. S. and W. J. L. Felts (1980) Effects of castration on the bone structure of male rats: a model of osteoporosis. *Calcified tissue international*. **32**, 77-82.
Wronski, T., L. Dann, K. Scott and M. Cintron (1989) Long-term effects of ovariectomy and aging on the rat skeleton. *Calcified tissue international*. **45**, 360-366.
Xie, B., A. Laouar and E. Huberman (1998) Fibronectin-mediated cell adhesion is required for induction of 92-kDa type IV collagenase/gelatinase (MMP-9) gene expression during macrophage differentiation. *Journal of Biological Chemistry*. **273**, 11576-11582.
Xu, Y. and S. Lindquist (1993) Heat-shock protein hsp90 governs the activity of pp60v-src kinase. *Proceedings of the National Academy of Sciences*. **90**, 7074.
Yadav, M. C., A. M. S. Simão, S. Narisawa, C. Huesa, M. D. McKee, C. Farquharson and J. L. Millán (2011) Loss of skeletal mineralization by the simultaneous ablation of PHOSPHO1 and alkaline phosphatase function: a unified model of the mechanisms of initiation of skeletal calcification. *Journal of Bone and Mineral Research*. **26**, 286-297.
Yamashina, M., E. Ueda, T. Kinoshita, T. Takami, A. Ojima, H. Ono, H. Tanaka, N. Kondo, T. Orii and N. Okada (1990) Inherited complete deficiency of 20-kilodalton homologous restriction factor (CD59) as a cause of paroxysmal nocturnal hemoglobinuria. *New England Journal of Medicine*. **323**, 1184-1189.
Yameen, Z., D. Leavesley, Z. Upton and Y. Xiao (2009) Multilineage differentiation potential of bone and cartilage cells derived from explant culture. *The Open Stem Cell Journal*. **1**, 10-19.
Yang, H., K. I. Joo, L. Ziegler and P. Wang (2009) Cell type-specific targeting with surface-engineered lentiviral vectors co-displaying OKT3 antibody and fusogenic molecule. *Pharmaceutical research*. **26**, 1432-1445.

Yang, L. B., R. Li, S. Meri, J. Rogers and Y. Shen (2000) Deficiency of complement defense protein CD59 may contribute to neurodegeneration in Alzheimer's disease. *The Journal of Neuroscience*. **20**, 7505.
Yao, W., W. Dai, M. Shahnazari, A. Pham, Z. Chen, H. Chen, M. Guan and N. E. Lane (2010) Inhibition of the progesterone nuclear receptor during the bone linear growth phase increases peak bone mass in female mice. *PLoS One*. **5**, e11410.
Yao, Z., P. Li, Q. Zhang, E. M. Schwarz, P. Keng, A. Arbini, B. F. Boyce and L. Xing (2006) Tumor necrosis factor-α increases circulating osteoclast precursor numbers by promoting their proliferation and differentiation in the bone marrow through up-regulation of c-Fms expression. *Journal of Biological Chemistry*. **281**, 11846-11855.
Yarbro, C. H., M. H. Frogge and M. Goodman (2004) *Cancer symptom management*, Jones & Bartlett Learning
Yin, T. and L. Li (2006) The stem cell niches in bone. *Journal of Clinical Investigation*. **116**, 1195.
Yoshikawa, T., Y. Ueda, M. Koizumi, T. Ohmura and Y. Tanaka (2011) Treatment of fracture non-union with tissue-engineered bone grafts. *Stem Cell Studies*. **1**, e4.
Zee, E., I. Jansen, K. Hoeben, W. Beertsen and V. Everts (1998) EGF and IL-1α modulate the release of collagenase, gelatinase and TIMP-1 as well as the release of calcium by rabbit calvarial bone explants. *Journal of periodontal research*. **33**, 65-72.
Zeng, Z. S., A. M. Cohen and J. G. Guillem (1999) Loss of basement membrane type IV collagen is associated with increased expression of metalloproteinases 2 and 9 (MMP-2 and MMP-9) during human colorectal tumorigenesis. *Carcinogenesis*. **20**, 749.
Zhang, B., P. Metharom, H. Jullie, K. Ellem, G. Cleghorn, M. J. West and M. Q. Wei (2004) The significance of controlled conditions in lentiviral vector titration and in the use of multiplicity of infection (MOI) for predicting gene transfer events. *Genet Vaccines Ther*. **2**.
Zhang, F., S. I. Thornhill, S. J. Howe, M. Ulaganathan, A. Schambach, J. Sinclair, C. Kinnon, H. B. Gaspar, M. Antoniou and A. J. Thrasher (2007) Lentiviral vectors containing an enhancer-less ubiquitously acting chromatin opening element (UCOE) provide highly reproducible and stable transgene expression in hematopoietic cells. *Blood*. **110**, 1448-1457.
Zhang, J., C. Niu, L. Ye, H. Huang, X. He, W. G. Tong, J. Ross, J. Haug, T. Johnson and J. Q. Feng (2003) Identification of the haematopoietic stem cell niche and control of the niche size. *Nature*. **425**, 836-841.
Zhang, M., H. Ho, T. Sheu, M. D. Breyer, L. M. Flick, J. H. Jonason, H. A. Awad, E. M. Schwarz and R. J. O'Keefe (2011a) EP1−/− mice have enhanced osteoblast differentiation and accelerated fracture repair. *Journal of Bone and Mineral Research*. **26**, 792-802.
Zhang, M., S. Xuan, M. L. Bouxsein, D. von Stechow, N. Akeno, M. C. Faugere, H. Malluche, G. Zhao, C. J. Rosen and A. Efstratiadis (2002) Osteoblast-specific knockout of the insulin-like growth factor (IGF) receptor gene reveals an essential role of IGF signaling in bone matrix mineralization. *Journal of Biological Chemistry*. **277**, 44005-44012.
Zhang, W., G. Ou, M. Hamrick, W. Hill, J. Borke, K. Wenger, N. Chutkan, J. Yu, Q. S. Mi and C. M. Isales (2008) Age-Related Changes in the Osteogenic Differentiation Potential of Mouse Bone Marrow Stromal Cells. *Journal of Bone and Mineral Research*. **23**, 1118-1128.
Zhang, X., M. Hirai, S. Cantero, R. Ciubotariu, L. Dobrila, A. Hirsh, K. Igura, H. Satoh, I. Yokomi and T. Nishimura (2011b) Isolation and characterization of mesenchymal stem cells from human umbilical cord blood: reevaluation of

critical factors for successful isolation and high ability to proliferate and differentiate to chondrocytes as compared to mesenchymal stem cells from bone marrow and adipose tissue. *Journal of cellular biochemistry*. **112**, 1206-1218.

Zhang, Z., Z. Wang, H. Ren, M. Yue, K. Huang, H. Gu, M. Liu, B. Du and M. Qian (2011c) P2Y6 Agonist Uridine 5′-Diphosphate Promotes Host Defense against Bacterial Infection via Monocyte Chemoattractant Protein-1–Mediated Monocytes/Macrophages Recruitment. *The Journal of Immunology*. **186**, 5376.

Zhao, Q., Y. Jia and Y. Xiao (2009) Cathepsin K: A therapeutic target for bone diseases. *Biochemical and biophysical research communications*. **380**, 721-723.

Zhong, Z., C. R. Zylstra-Diegel, C. A. Schumacher, J. J. Baker, A. C. Carpenter, S. Rao, W. Yao, M. Guan, J. A. Helms and N. E. Lane (2012) Wntless functions in mature osteoblasts to regulate bone mass. *Proceedings of the National Academy of Sciences*. **109**, E2197-E2204.

Zipfel, P. F. and C. Skerka (1999) FHL-1/reconectin: a human complement and immune regulator with cell-adhesive function. *Immunology today*. **20**, 135-140.

Zipfel, P. F. and C. Skerka (2009) Complement regulators and inhibitory proteins. *Nature Reviews Immunology*. **9**, 729-740.

APPENDIX 1: Company Addresses

Abcam, Cambridge, UK

Akzo Nobel N. V., Amsterdam, Netherlands

Alpha Laboratories Ltd, Eastleigh, UK

Apollo Scientific Ltd, Bredbury, UK

Applied Biosystems, Life Technologies Ltd, Paisley, UK

Aperio Technologies Inc, Vista, US

BD Biosciences, Oxford, UK

BD Pharmingen UK Ltd, Cowley, Oxford, UK

Bioline Reagents Ltd, London, UK

Biomers.net GmbH, Ulm, Germany

Bio-Rad Laboratories Ltd, Hemel Hempstead, UK

Buehler GmbH, Düsseldorf, Germany

Caltag Laboratories Inc, Burlingame, US

Carestream Health, Inc., Rochester, US

Corning B.V Life Sciences, Amsterdam, Netherlands

Daido Sango Co. Ltd, Tokio, Japan

eBioscience, Inc., San Diego, USA

Embi Tech, San Diego, USA

Eurofins MWG Operon, London, UK

Fisher Scientific, Loughborough, UK

Fluka, Sigma-Aldrich, Dorset, UK

GE Healthcare, Chalfont, UK

Gibco, Life Technologies Ltd, Paisley, UK

GraphPad Software Inc, San Diego, CA, USA

Greiner, Stonehouse, Gloucestershire, UK

Invitrogen, Life Technologies Ltd, Paisley, UK

Jackson ImmuneResearch Europe Ltd, Suffolk, England

Knittel Gläser, Bielefeld, Germany

Leica Microsystems (UK) Ltd, Milton Keynes, UK

Lonza, Cambrex, Slough, UK

Macherey-Nagel, Düren, Germany

Merck Pharmaceuticals, West Drayton, UK

Menzel-Gläser, Braunschweig, Germany

Mesoscale Discovery, Gaithersburg, USA

Millipore (U.K.) Limited, Watford, UK

Miltenyi Biotec, Surrey, UK

MJ Research Inc., St. Bruno, Canada

Novochem Ltd, Budapest, Hungary

Nunc International, New York, USA

Oxoid Ltd, Cambridge, UK

Polysciences Europe GmbH, Eppelheim, Germany

Promega Ltd, Southhampton, UK

Qiagen, West Sussex, UK

R&D Systems, Abingdon, UK

Santa Cruz Biotechnology Inc., Heidelberg, Germany

Sanyo, Watford, UK

Skyscan, Kontich, Belgium

TAAB Laboratories Equipment Ltd, Berks, UK

The Scripps Research Institute, California, USA

Sigma-Aldrich**,** Dorset, UK

Scientific Laboratory Supplies Limited (SLS), Hessle, Yorkshire, UK

Source Bioscience Plc, Nottingham, UK

Thermo Scientific, Fisher Scientific, Waltham, USA

Vector Laboratories, Petersborough,UK

VWR International, Lutterworth, Leicestershire, UK